

Spring 1987

# GAMMA-RAY IMAGING OBSERVATIONS OF THE CRAB AND CYGNUS REGIONS

MARK LEWIS MCCONNELL

*University of New Hampshire, Durham*

Follow this and additional works at: <https://scholars.unh.edu/dissertation>

---

## Recommended Citation

MCCONNELL, MARK LEWIS, "GAMMA-RAY IMAGING OBSERVATIONS OF THE CRAB AND CYGNUS REGIONS" (1987). *Doctoral Dissertations*. 1512.

<https://scholars.unh.edu/dissertation/1512>

This Dissertation is brought to you for free and open access by the Student Scholarship at University of New Hampshire Scholars' Repository. It has been accepted for inclusion in Doctoral Dissertations by an authorized administrator of University of New Hampshire Scholars' Repository. For more information, please contact [nicole.hentz@unh.edu](mailto:nicole.hentz@unh.edu).

## **INFORMATION TO USERS**

While the most advanced technology has been used to photograph and reproduce this manuscript, the quality of the reproduction is heavily dependent upon the quality of the material submitted. For example:

- Manuscript pages may have indistinct print. In such cases, the best available copy has been filmed.
- Manuscripts may not always be complete. In such cases, a note will indicate that it is not possible to obtain missing pages.
- Copyrighted material may have been removed from the manuscript. In such cases, a note will indicate the deletion.

Oversize materials (e.g., maps, drawings, and charts) are photographed by sectioning the original, beginning at the upper left-hand corner and continuing from left to right in equal sections with small overlaps. Each oversize page is also filmed as one exposure and is available, for an additional charge, as a standard 35mm slide or as a 17"x 23" black and white photographic print.

Most photographs reproduce acceptably on positive microfilm or microfiche but lack the clarity on xerographic copies made from the microfilm. For an additional charge, 35mm slides of 6"x 9" black and white photographic prints are available for any photographs or illustrations that cannot be reproduced satisfactorily by xerography.

Order Number 8722436

**Gamma-ray imaging observations of the Crab and Cygnus  
regions**

McConnell, Mark Lewis, Ph.D.

University of New Hampshire, 1987

**U·M·I**  
300 N. Zeeb Rd.  
Ann Arbor, MI 48106

**PLEASE NOTE:**

In all cases this material has been filmed in the best possible way from the available copy. Problems encountered with this document have been identified here with a check mark .

1. Glossy photographs or pages \_\_\_\_\_
2. Colored illustrations, paper or print \_\_\_\_\_
3. Photographs with dark background \_\_\_\_\_
4. Illustrations are poor copy \_\_\_\_\_
5. Pages with black marks, not original copy \_\_\_\_\_
6. Print shows through as there is text on both sides of page \_\_\_\_\_
7. Indistinct, broken or small print on several pages
8. Print exceeds margin requirements \_\_\_\_\_
9. Tightly bound copy with print lost in spine \_\_\_\_\_
10. Computer printout pages with indistinct print \_\_\_\_\_
11. Page(s) \_\_\_\_\_ lacking when material received, and not available from school or author.
12. Page(s) \_\_\_\_\_ seem to be missing in numbering only as text follows.
13. Two pages numbered \_\_\_\_\_. Text follows.
14. Curling and wrinkled pages \_\_\_\_\_
15. Dissertation contains pages with print at a slant, filmed as received \_\_\_\_\_
16. Other \_\_\_\_\_  
\_\_\_\_\_  
\_\_\_\_\_

University  
Microfilms  
International

**GAMMA-RAY IMAGING OBSERVATIONS  
OF THE  
CRAB AND CYGNUS REGIONS**

**BY**

**MARK LEWIS McCONNELL**  
B.S., Case Western Reserve University, 1980

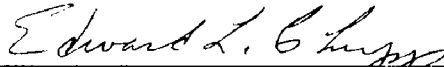
**A DISSERTATION**

**Submitted to the University of New Hampshire  
in Partial Fulfillment of  
the Requirements for the Degree of**

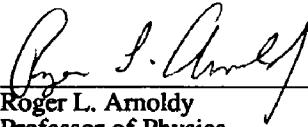
**Doctor of Philosophy  
in  
Physics**

**May, 1987**

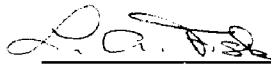
This dissertation has been examined and approved.



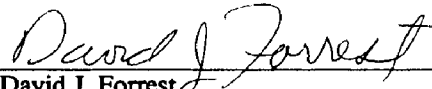
Edward L. Chupp, Dissertation Director  
Professor of Physics



Roger L. Arnoldy  
Professor of Physics



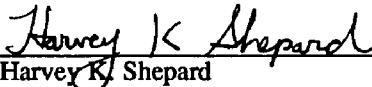
Lennard A. Fisk, Jr.  
Professor of Physics



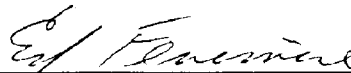
David J. Forrest  
Research Associate Professor of Physics



Jochen Heisenberg  
Professor of Physics



Harvey K. Shepard  
Professor of Physics



Edward E. Fenimore  
Los Alamos National Laboratory

2/20/87  
Date

**This dissertation is dedicated to the three most important people in my life - my wife, Chris, and my parents, Peggy and Burt. Without their love and support, this work might never have been completed.**

## **Acknowledgements**

I would like to thank my advisor, E. L. Chupp, for providing the opportunity to participate in this research program. Dave Forrest has provided valuable guidance, inspiration and support throughout the entire project. The continuing support of Phil Dunphy and Jon Googins made possible the successful development and operation of the DGT instrument. During the later stages of this work, the contributions of Alan Owens have been especially useful. Discussions with Tom Vestrand have been useful in elucidating some of the theoretical issues raised during the course of this research. In addition to those named above, there are numerous persons who have made contributions, both large and small, over the past seven years. Included among these are Dipen Bhattacharya, Indulis Gleske, Mogens Lauritzen, and Mark Popecki. The drafting work contained in this dissertation was provided by Sherry Palmer. Hank Dolben of the UNH Magnetosphere Research Lab kindly provided access to an Apple LaserWriter on which this dissertation was printed. Finally, the support of Albert G. Opp and the National Aeronautics and Space Administration (under NASA grant NGL30-002-021) is gratefully acknowledged.



## Publication List

McConnell, M. L., Forrest, D. J., Chupp, E. L., and Dunphy, P. P. 1982, *IEEE Trans. Nucl. Sci.*, **29**, 155. "A Coded Aperture Gamma-Ray Telescope."

McConnell, M. L., Dunphy, P. P., Forrest, D. J., and Chupp, E. L. 1983, in *Adv. Space Res.*, **3**, 105. "A Directional Gamma-Ray Telescope Using Coded Aperture Techniques."

McConnell, M. L., Dunphy, P. P., Forrest, D. J., Chupp, E. L., and Owens, A. 1987, to be published in *Ap. J.* "Gamma-Ray Observations of the Crab Region Using a Coded Aperture Telescope."

McConnell, M. L., Chupp, E. L., Dunphy, P. P., Forrest, D. J., and Owens, A. 1987, to be submitted to *Ap. J.* "Gamma-Ray Observations of the Cygnus Region with a Coded Aperture Telescope - Detection of MeV radiation from Cyg X-1."

Dunphy, P. P., McConnell, M. L., Chupp, E. L., Forrest, D. J., and Owens, A. 1987, to be submitted to *Nucl. Instr. Methods*. "A Balloon Borne Coded Aperture Telescope for Low-Energy Gamma-Ray Astronomy."

## TABLE OF CONTENTS

DEDICATION.....	iii
ACKNOWLEDGEMENTS.....	iv
PUBLICATION LIST.....	v
LIST OF TABLES.....	ix
LIST OF FIGURES.....	x
ABSTRACT.....	xv

CHAPTER	PAGE
INTRODUCTION.....	1
I. SCIENTIFIC BACKGROUND .....	8
Crab Nebula/Pulsar .....	8
Basic Theory.....	9
Gamma Ray Continuum Measurements.....	19
Gamma-Ray Line Emission.....	21
Cygnus X-1 .....	22
Basic Theory.....	22
Luminosity Variations.....	33
Spectral Observations.....	35
Other Sources .....	36
A0535+26.....	36
Anticenter Diffuse Emission.....	37
Cygnus X-3.....	38

<b>II. INSTRUMENTATION .....</b>	<b>40</b>
<b>Coded Aperture Imaging .....</b>	<b>40</b>
<b>Basic Concepts of Coded Aperture Imaging.....</b>	<b>42</b>
<b>Imaging Statistics.....</b>	<b>46</b>
<b>Background Systematics.....</b>	<b>47</b>
<b>Partial Mask Coding.....</b>	<b>55</b>
<b>The Directional Gamma-Ray Telescope .....</b>	<b>56</b>
<b>The Detector Array and Associated Electronics.....</b>	<b>56</b>
<b>The Coded Mask.....</b>	<b>63</b>
<b>Gondola and Pointing System.....</b>	<b>65</b>
<b>Telemetry and Ground Station.....</b>	<b>67</b>
<b>Instrumental Background.....</b>	<b>68</b>
<b>Sensitivity to Celestial Sources.....</b>	<b>72</b>
<b>III. OBSERVATIONS .....</b>	<b>76</b>
<b>Balloon Flight History .....</b>	<b>76</b>
<b>Summary of Flight 1379-P .....</b>	<b>77</b>
<b>Detector Anomalies.....</b>	<b>77</b>
<b>In-Flight Detector Tests.....</b>	<b>81</b>
<b>Source Observations.....</b>	<b>85</b>
<b>Pointing Accuracy and Stability.....</b>	<b>86</b>
<b>IV. DATA REDUCTION AND ANALYSIS .....</b>	<b>89</b>
<b>Reduction of Flight Data .....</b>	<b>90</b>
<b>Digitization of Telemetry Data.....</b>	<b>90</b>
<b>Image Data Processing.....</b>	<b>91</b>
<b>Image Analysis Procedures .....</b>	<b>98</b>

Point-Spread-Function of the Imaging System.....	98
Determination of Allowable Parameter Ranges.....	102
Determination of Source Photon Spectra .....	104
<b>V. RESULTS AND DISCUSSION .....</b>	<b>108</b>
<b>Crab Region (Galactic Anticenter) .....</b>	<b>108</b>
Observations.....	108
Crab Nebula/Pulsar.....	109
A0535+26.....	117
Galactic Anticenter Diffuse Emission.....	120
Cygnus Region .....	122
Cygnus X-1.....	124
Cygnus X-3.....	140
<b>VI. SUMMARY .....</b>	<b>144</b>
<b>APPENDICES .....</b>	<b>147</b>
<b>A. PROPERTIES OF A SINGLE IMAGE .....</b>	<b>148</b>
<b>B. PROPERTIES OF A COMPOSITE IMAGE .....</b>	<b>158</b>
<b>C. BOOTSTRAP SAMPLING STATISTICS .....</b>	<b>166</b>
<b>D. DGT RESPONSE FUNCTION .....</b>	<b>172</b>
<b>E. STATISTICS OF THE SOURCE SPECTRA .....</b>	<b>184</b>
<b>REFERENCES .....</b>	<b>190</b>

## List of Tables

II-1	Detection Properties of the DGT.....	56
III-1	Flight 1379-P Source Summary.....	86
III-2	Sample Sun Sensor Data.....	87
IV-1	DGT Energy Intervals.....	92
IV-2	Source Data Divisions.....	98
IV-3	Measured Widths of the Point-Spread-Function.....	102
V-1	Scans of Crab Region.....	109
V-2	Crab Spectral Results.....	112
V-3	Crab Region $1\sigma$ Upper Limits.....	118
V-4	Scans of Cygnus Region.....	122
V-5	Cygnus X-1 Spectral Results.....	128
V-6	Cygnus X-3 Upper Limits.....	141

## APPENDICES

B-1	Image Element Distribution Analysis.....	163
E-1	Crab Spectrum Statistics.....	186
E-2	Cygnus Spectrum Statistics.....	186
E-3	Crab Power-Law Model.....	188
E-4	Cyg X-1 Power-Law Model.....	188
E-5	Cyg X-1 Compton Model.....	189
E-6	Cyg X-1 Power-Law plus Compton Model.....	189

## List of Figures

II-1	Schematic diagram showing the principle components of a coded aperture telescope. ....	41
II-2	Cross-sectional view of the Directional Gamma-ray Telescope (DGT). ....	58
II-3	A sample $^{60}\text{Co}$ in-flight-calibration (IFC) spectrum obtained with the total integrated BGO array. Note that the two lines at 1.17 MeV and 1.33 MeV are not resolved by the BGO detectors. The detector threshold level is set at 0.16 MeV. ....	60
II-4	A schematic view of the side shield arrangement in the DGT. This view is that seen from the position of the mask looking down on the detector array. The shield references are UNH designations. ....	60
II-5	Functional block diagram of the DGT detector electronics. ....	62
II-6	Coded mask pattern used in the DGT. The outlined area near the center represents the basic URA pattern on which this mask is based. Each mask element is 5.6 cm by 5.6 cm in size. The shaded areas represent lead elements, each of which are 1.9 cm thick. ....	64
II-7	The nominal and legal (or fully-coded) fields-of-view for the DGT. Note that the outer half-elements of the nominal field are not fully coded. The partially-coded field-of-view extends outward from the legal field-of-view. ....	64
II-8	The measured and calculated background energy-loss spectrum at $3 \text{ gm cm}^{-2}$ over Palestine, TX. For comparison, the individual contributions to the detector counting rate are also shown. ....	70
II-9	The DGT $2\sigma$ upper limit sensitivities for continuum and narrow line fluxes compared with various observations. <b>Upper:</b> The narrow line sensitivity. Also shown are previously reported line fluxes from the Crab: CRAB(400 keV), Leventhal <i>et al.</i> (1977); CRAB(405 keV), Owens <i>et al.</i> (1985a). <b>Lower:</b> The continuum sensitivity. The spectra of other sources are shown for comparison [adapted from Dean and Ramsden (1981) for NGC 4151 and CG135+1, and Fichtel and Trombka (1981) for 3C273]. The spectrum denoted CRAB(UNH) is that reported here. ....	75
III-1	Atmospheric depth as a function of time during Flight 1379-P. The sharp increase in depth (corresponding to a decrease in altitude) which took place at ~25 hours UT resulted from the thermal effects of sunset on the balloon. ....	78
III-2	The fractional livetime of the experiment as a function of time during the flight. Note that the time is measured relative to 0 hrs UT on October 1. The minimum at ~15:30 is associated with the ascent through the Pfozter maximum. The slight increase in livetime at ~44 hours UT is associated with an abnormal upper-level threshold. ....	80

III-3	The Gaussian fit to the 0.511 MeV line of a $^{22}\text{Na}$ calibration source (with arbitrary normalization) compared to the feature observed in the DGT background spectrum. ....	82
III-4	The mean background spectrum resulting from local gamma-ray production in the DGT mask. The mask contribution ranges from 3% to 5% of the total detector background, with a maximum (at $\sim 0.511$ MeV) of $\sim 8\%$ . ....	84
III-5	A sample of the magnetometer data, which indicates the change of the detector azimuth angle from the null point of the magnetometer. ....	88
IV-1	Sequence which demonstrates the steps in producing a snapshot image. This data was accumulated during the DGT observation of the Crab. The location of the source is not obvious in this very short exposure image (64 seconds livetime); only by summing a number of such images does the source location become obvious. ....	94
IV-2	Two images of the Crab region, illustrating the efficacy of the background systematics correction. (Each view represents the reproduced gamma-ray intensity, in terms of the number of reproduced source counts per $0.95^\circ$ image element.) Figures IV-2a and IV-2b show the uncorrected and corrected data, respectively. The amplitude of the peak in Figure IV-2b corresponds to a significance in the detected flux of $10.6\sigma$ . The total source observation time was 12842 seconds ( $\sim 3.6$ hours). ....	97
V-1	Reproduced intensity contour of the Crab gamma-ray emission integrated over the energy range 200-600 keV. The contour values represent the number of reproduced gamma-ray events per $0.95^\circ$ pixel element. The data is consistent with a single point source located at the Crab. The inset shows the 90% confidence contour (as measured in the 160 keV to 1 MeV range). For comparison, the true position of the Crab is also shown. The location of A0535+26 is shown by the small square. (Note that due to the effect of source suppression, the average level of the non-source elements is approximately -80.) ....	111
V-2	The observed energy-loss spectrum of the Crab as derived from seven separate composite images, each covering a different energy range. For each energy range, the measured point-spread-function (PSF) was used to determine the total source response. The total integrated livetime for this observation is 12842 seconds. ....	113
V-3	The total Crab photon spectrum as measured by the DGT. The solid line represents the best fit to the DGT data using a power-law spectral model of the form $dN(E)/dE = A E^{-\alpha}$ . The inset shows the 90% confidence contour for the joint estimation of the two parameters $A$ and $\alpha$ . Other representative measurements are shown for comparison. ....	115

V-4	The upper limit flux levels from A0535+26 as derived from the DGT imaging data. Lower energy x-ray measurements (<100 keV), along with their extrapolation to higher energies, are shown for comparison. ....	119
V-5	The upper limit flux levels from the galactic anticenter diffuse emission (galactic longitude, $l = 175^\circ$ - $190^\circ$ ) as derived from the DGT imaging data. The measurements of Wheaton (1976) for $l = 240^\circ$ and those of Graser and Schönfelder (1982) for $l = 160^\circ$ - $197^\circ$ are shown for comparison. The calculations of Sacher and Schönfelder (1983) for the emission due to an $E^{-2.8}$ interstellar electron spectrum (Lebrun <i>et al.</i> 1982) are also shown. ....	121
V-6	Reproduced intensity contour map of the Cygnus region gamma-ray emission. The contour values represent the reproduced number of gamma-ray events per $0.95^\circ$ image element. This data is consistent with a single point source located at the position of Cygnus X-1. The inset shows the 90% confidence contour for the measured location of Cygnus X-1 (as measured in the 160 keV to 1 MeV range). For comparison, the true position of Cygnus X-1 is also shown. The location of Cygnus X-3 is noted by a small square. ....	125
V-7	The observed energy-loss spectrum of Cygnus X-1 as derived from eleven separate composite images, each covering a different energy range. For each energy range, the measured point-spread-function (PSF) was used to determine the total source response. The total integrated livetime for this spectrum is 13039 seconds. ....	126
V-8	The best-fit Cygnus X-1 power-law source spectrum. This model provides an acceptable representation of the data, with a $\chi^2$ of 1.71 for 9 degrees of freedom. ....	129
V-9	The minimum chi-square vs. annihilation temperature obtained from a fit of the 1-9.3 MeV data. The high temperature derived from this analysis is used to rule out a high-temperature annihilation feature as the source of the observed 1-9.3 MeV emission. ....	131
V-10	The photon spectrum of Cygnus X-1 derived from a model which consists of a power-law (fit to the data above 1 MeV) and an inverse Compton model. This model provides a reduced $\chi^2$ of 1.60 for 6 degrees of freedom. ....	132
V-11	The photon spectrum of Cygnus X-1 observed by the DGT is compared to other measurements, including those obtained by the EXOSAT satellite at energies below 50 keV. ....	137
V-12	A plot in Compton parameter space showing the constraint of the EXOSAT data (the solid line, based on a power-law index of -1.68) and the 68% ( $1\sigma$ ) confidence region based on the DGT results (the hatched area). ....	139
V-13	The upper limit flux levels for Cygnus X-3 as derived from the DGT imaging data. Other representative measurements are also shown for comparison. .	142



## APPENDICES

A-1	Sample image data obtained with the DGT during pre-flight calibrations with a $^{137}\text{Cs}$ source placed ~30 meters in front of the detector. ....	150
A-2	Imaging data for the case of a source lying at the corner of an image element. This data was taken under the same conditions as in Figure A-1. ....	151
A-3	A DGT image obtained by a sequence of exposures (of equal duration) to the same $^{137}\text{Cs}$ source located in different image elements. This demonstrates the ability of the DGT to image a spatially diffuse emission. ....	152
B-1	A schematic diagram demonstrating the definition of the location of a point (P) within the imaging field-of-view. ....	159
B-2	Spherical triangles which illustrate two cases for defining the location of point P within the field-of-view, based on Figure B-1. ....	159
B-3	Spherical triangle illustrating the determination of the azimuth and zenith for point P. ....	160
C-1	The bootstrap distribution for the measured intensity of the Crab in the 160 keV to 1 MeV energy range, based on 200 bootstrap samples. ....	170
C-2	A different representation of the bootstrap distribution for the Crab source counts in the 160 keV to 1 MeV energy range. This representation more readily permits the determination of confidence levels at any desired confidence. ....	170
C-3	The bootstrap distribution for the Crab source location, based on 200 bootstrap samples. ....	171
D-1	The absorption of incident photon flux by the lead contained in the DGT mask. The points are based on tabulated values of the total mass attenuation coefficient (Tsoufanidis 1983). The solid line represents the analytic fit which was used in the response function calculations. ....	176
D-2	The transmission of incident photon flux through the aluminum material contained in the DGT mask. The points are based on tabulated values of the total mass attenuation coefficient (Tsoufanidis 1983). The solid line represents the analytic fit which was used in the response function calculations. ....	177
D-3	The transmission of the incident photon flux through the aluminum in the detector housing. The points are based on tabulated values of the total mass attenuation coefficient (Tsoufanidis 1983). The solid line represents the analytic fit which was used in the response function calculations. ....	178

D-4	The photofraction of a 2" by 2 cm BGO crystal as compared to that of a standard 3" by 3" NaI(Tl) detector (Berger and Seltzer 1972). The data points are from Dunphy and Forrest (1985). .....	179
D-5	The full-energy-peak efficiency of the BGO array. The data points are based on the results of Dunphy and Forrest (1985). .....	180
D-6	The first escape peak fraction ( $P_1$ ) of BGO as a function of energy. The data points are measured points. The results for NaI are shown for comparison (Berger and Seltzer 1972). .....	181
D-7	The second escape peak fraction ( $P_2$ ) for BGO as a function of energy. The data points are measured points. The results for NaI are also shown for comparison (Berger and Seltzer 1972). .....	182
D-8	The measured energy resolution of the gain stabilized BGO array.....	183

## ABSTRACT

### GAMMA-RAY IMAGING OBSERVATIONS OF THE CRAB AND CYGNUS REGIONS

by

Mark Lewis McConnell

University of New Hampshire, May, 1987

This dissertation presents the results from a balloon-borne experiment, referred to as the Directional Gamma-Ray Telescope (DGT), which is designed to image celestial gamma-rays over the energy range 160 keV to 9.3 MeV. It utilizes a technique known as coded aperture imaging in order to obtain spatially resolved images of the sky with an angular resolution of  $3.8^\circ$ . This detector is the first flight-ready instrument of this type operating at energies above 160 keV. The first successful balloon flight of this instrument took place on 1984 October 1-2. During the thirty hours in which the payload remained at float altitude, imaging observations of a number of sky regions were obtained, including observations of the Crab and Cygnus regions.

The Crab Nebula/pulsar was observed to have a featureless power-law spectrum with a best fit form of  $5.1 \times 10^{-3} E_{\text{MeV}}^{-1.88}$  photons  $\text{cm}^{-2} \text{s}^{-1} \text{MeV}^{-1}$ , consistent with previous measurements. We have placed  $3\sigma$  upper limits on previously observed line emission at energies of 400 keV and 1049 keV; the results are  $3.0 \times 10^{-3}$  and  $1.9 \times 10^{-3}$  photons  $\text{cm}^{-2} \text{s}^{-1}$ , respectively. These upper limits lie below some previous measurements of this emission. We also place upper limits on the emission from the x-ray binary source A0535+26 and the anticenter diffuse emission.

Emission from Cyg X-1 was observed up to  $\sim 10$  MeV. At energies below 1 MeV, the data are consistent with a single-temperature inverse Compton model, with an electron temperature,  $kT_e$ , of  $\sim 80$  keV and an optical depth,  $\tau$ , of  $\sim 2.0$ . The inverse Compton model is often employed to explain the observed x-ray emission. In the 2-9.3 MeV range, the DGT results show emission which is not readily understood in the context of the inverse Compton model. We suggest that a second component, possibly produced by some non-thermal mechanism, may be necessary to explain the observations. Finally, upper limits are also derived for the flux from Cygnus X-3.

## Introduction

The field of gamma-ray astronomy has evolved relatively slowly over the past thirty years since Morrison (1958) first discussed the possibility of observing celestial gamma radiation. Ever since the publication of Morrison's paper, it has been recognized that the study of celestial gamma-ray emission has great potential significance for astrophysics. Cosmic gamma-rays are produced by a variety of physical processes. These processes include radioactive decay (resulting, for example, from nucleosynthesis), nuclear reactions (e.g., inelastic scattering of nuclei, spallation reactions or radiative capture reactions), antimatter annihilation, and interactions of charged particles with matter or electromagnetic fields.

The work in this dissertation involves the observation of low-energy gamma-ray emission in the energy range of 160 keV to 9.3 MeV. This spectral region is of particular interest, because it is this region in which not only continuum radiation, but also nuclear line emission, is observable (Chupp 1976). Only a handful of discrete extra-solar sources are known to be observable at these wavelengths. We can broadly classify these observed sources as either pulsars, which are observable primarily as a result of particle acceleration in a strong magnetic field, as accretion sources, which are observable as a result of very high plasma temperatures (and possibly particle acceleration), or as an accreting pulsar (combining both the pulsar and accretion phenomena). The study of low-energy gamma-ray emission therefore provides the opportunity to investigate both the pulsar and the accretion phenomena.

Pulsars are believed to be rapidly rotating magnetized neutron stars. The rapid rotation of a highly magnetized body is believed to result in a very efficient acceleration of charged particles. These particles are observable, in large part, due to their interaction with the strong magnetic field of the pulsar ( $\sim 10^{12}$  Gauss). Only one isolated pulsar, that

associated with the Crab Nebula, has been observed at these energies. There have been sporadic reports of line emission from the Crab, most notably at energies of  $\sim 77$  keV (electron cyclotron emission; e.g., Ling *et al.* 1979; Strickman *et al.* 1982) and  $\sim 400$  keV (possibly red-shifted electron-positron annihilation; e.g., Leventhal *et al.* 1977; Owens *et al.* 1985a). The study of the gamma-ray emissions from the Crab allows for an investigation of the particle acceleration mechanisms along with the study (via the line emissions) of the environment in which the acceleration takes place.

In discussing accretion sources, we can separately consider galactic and extragalactic sources. Accretion sources observable within our galaxy are generally a subset of a class of objects known as *binary x-ray sources*. These sources accrete matter from a main-sequence primary object onto some compact secondary (usually a neutron star or black hole), with the accretion process often occurring via the formation of an accretion disk. The gamma-ray emission results from the very high plasma temperatures which are characteristic of the accretion region. One example of this type of source is Cygnus X-1, which is believed to provide the best evidence for the existence of a black hole (e.g., Liang and Nolan 1984). The study of this relatively close system ( $\sim 2.5$  kpc) may provide important insights into the nature of the accretion process.

Accretion is also believed to be the major source of energy for the broad class of objects known as *active galactic nuclei* (or AGN), which include quasars and Seyfert galaxies. Instead of stellar-mass black holes, however, the accretion in these sources is believed to take place onto black holes with masses on the order of  $10^9 M_{\text{sol}}$  (where  $M_{\text{sol}}$  is one solar mass). NGC 4151 is an example of an AGN which has been observed in low-energy gamma-rays (Boella *et al.* 1984).

There are also sources which appear to consist of a pulsar located within a binary system. In such a situation, mass transfer to the pulsar (i.e., accretion) may take place. Such systems are also often considered part of the binary x-ray class. One notable source which may be of this type is Cygnus X-3. This object represents the most energetic

discrete source of gamma-rays, showing evidence of gamma-rays up to  $10^{15}$  eV in energy (Samorski and Stamm 1983). The acceleration of the particles which produce this emission may take place in the pulsar, but mass flow may also contribute to the overall gamma-ray emission.

In addition to discrete sources such as those discussed above, low-energy gamma-ray astronomy also deals with more diffuse sources. The interaction of cosmic rays with the interstellar medium leads to a flux of gamma-ray emission which appears to pervade the galaxy (e.g., Sacher and Schönfelder 1983). The study of this flux can lead to a better understanding of not only the distribution of interstellar matter, but also the spectrum, production and containment of interstellar cosmic rays.

The development of gamma-ray astronomy as a full-fledged branch of astronomy has been hindered not only by the development of suitable technology, but also by the need to observe from above the Earth's atmosphere. Early experimental results (using balloons and early satellite platforms in the 1960's) provided only marginal returns. In the past 15 years, many new results were reported based on numerous balloon and satellite experiments. Important results from balloon work included measurements of the 0.511 MeV line from the galactic center region along with the more recent measurements of  $^{26}\text{Al}$  emission (at 1.83 MeV). Notable satellite experiments of this time period included OSO-7 (first measurement of extraterrestrial gamma-ray lines, from a solar flare), SMM (further measurements of solar flare gamma-rays), HEAO-1 (four experiments covering the energy range 0.1 to 10 MeV), HEAO-3 (Ge detector array for the MeV energy range), SAS-2 (spark chamber for photon energies above 35 MeV) and COS-B (spark chamber experiment which provided a complete sky survey at energies above 50 MeV). (For a more complete review of the status of gamma-ray astronomy, see Ramaty and Lingenfelter 1982, and the references therein.)

Experimentally, this region of the electromagnetic spectrum suffers not only from very low source flux levels, but also very high background levels. The signal-to-

background ratio for even the strongest sources is generally on the order of 1-2%. In addition to the very high background levels which are encountered, present-day gamma-ray experiments suffer from very limited angular resolution. The ability to provide angular resolution for gamma-ray detectors is necessary in order to determine source counterparts in other regions of the electromagnetic spectrum. Furthermore, the ability to resolve nearby sources allows for unambiguous determination of source spectra. Source confusion is a common problem in gamma-ray astronomy.

Refraction or reflection optics are not practical at these energies, due to the low reflectivity of gamma-ray photons. Low-energy gamma-ray detectors usually rely on collimation techniques. This implies that the angular resolution is roughly equivalent to the field-of-view. Obviously, some method of "imaging" gamma-radiation would be of great importance to astrophysics. One means of imaging gamma radiation which has received considerable attention in recent years is the technique referred to as *coded aperture imaging*. Based on the idea of a simple pinhole camera, this procedure holds great promise for improving the angular resolution of gamma-ray detectors.

To date there have been only a handful of experiments carried out which make use of coded aperture imaging techniques. One of the earliest coded aperture experiments to image celestial photons was described by Blake *et al.* (1974). In this experiment, a random mask pattern was used to obtain x-ray images of the sun from a sounding rocket. Proctor *et al.* (1978) used a coded aperture x-ray telescope flown on a rocket to obtain imaging data of the galactic center over the energy range 2-20 keV. The same group has more recently flown an experiment on Spacelab 2 which operated in the range 2.5-30 keV (Willmore *et al.* 1984; Skinner *et al.* 1986).

A number of astronomical coded aperture experiments are presently under development for use in studying low-energy gamma-rays. A group at the California Institute of Technology has developed an instrument which utilizes an Anger camera for the detection plane and a Hexagonal Uniformly Redundant Array (or HURA; Cook *et al.* 1984;



Finger and Prince, 1985) for the mask pattern. In this balloon-borne experiment, known as the Gamma-Ray Imaging Payload (GRIP), the mask can be changed to an antimask by a simple rotation of  $60^\circ$ . This experiment operates in the energy range of 30 keV to 5 MeV and can image a  $20^\circ$  field-of-view with pixel elements of  $0.6^\circ$  (Cook *et al.* 1985; Althouse *et al.* 1985). Results from a recent successful balloon flight (fall, 1986) have not yet been published.

Gehrels *et al.* (1985) and Teegarden *et al.* (1985) have described an imaging experiment based on a  $5 \times 3$  Uniformly Redundant Array (URA; Fenimore and Cannon 1978) pattern which uses an array of seven coaxial germanium detectors in the detection plane. Known as the Gamma-Ray Imaging Spectrometer (GRIS), this balloon experiment represents a collaborative effort of NASA-Goddard Space Flight Center, Bell Laboratories and Sandia National Laboratory. It is designed to cover the 20 keV to 10 MeV range with a  $9^\circ$  by  $15^\circ$  field-of-view and  $3^\circ$  image elements.

Another balloon-borne experiment is being developed by a collaboration composed of scientists from UC San Diego, UC Berkeley, and CESR (France). The detection plane of this experiment is composed of an array of twelve Ge detectors operating in the energy range 10 keV to 10 MeV. Imaging is achieved via temporal aperture modulation (e.g., Proctor 1981; Durouchoux *et al.* 1983), a technique which is closely related to the spatial aperture modulation discussed in this dissertation. This telescope can image a  $12^\circ$  FWHM field-of-view with  $2.5^\circ$  angular resolution (Matteson *et al.* 1985).

The balloon experiment ZEBRA is being developed by a European collaboration involving groups from Great Britain and Italy (e.g., Butler *et al.* 1985). The detection plane of this telescope consists of an array of NaI(Tl) crystals, each of which has dimensions  $5 \times 5 \times 50$  cm. The mask pattern is based on a  $9 \times 7$  URA. The experiment can image photons in the energy range of 0.1-10 MeV with an angular resolution of  $\sim 1^\circ$ .

A French-Soviet collaboration is preparing a satellite experiment known as SIGMA (Mandrou 1984), which will incorporate a coded mask to image celestial radiation in the

energy range 30 keV to 2 MeV. Using a NaI(Tl) Anger camera in the detection plane, an angular resolution on the order of 2 arcminutes is expected. A launch date of late 1987 is presently scheduled.

At higher energies (>50 MeV), there are at least two instruments under development which will utilize coded aperture techniques to substantially improve the angular resolution. One such experiment is referred to as CAMTRAC (Coded Aperture Mask Track Chamber). This telescope, developed as a result of a collaboration between Case Western Reserve University and Southampton University, employs a drift chamber detection system in conjunction with a coded aperture mask. The angular resolution of this system is ~10 arc minutes (Frye *et al.* 1985).

Another French-Soviet collaboration is developing a high-energy instrument (GAMMA 1) which is also destined to be a satellite experiment. This device is similar to the CAMTRAC experiment, except that it utilizes a spark chamber for the detection system. Operating at energies above 50 MeV, an angular resolution of less than 20 arc minutes is expected (Akimov *et al.* 1985).

This thesis presents the first astrophysical results obtained with a coded aperture experiment in the energy region above 160 keV. In particular, we shall report on the development of an experiment which we call the Directional Gamma-Ray Telescope (DGT). This device operates over the energy range of 160 keV to 9.3 MeV with an intrinsic angular resolution of 3.8°.

The imaging results which are presented in this thesis are of two regions of the sky. The first sky region is an area centered on the Crab Nebula/pulsar and often referred to as the galactic anticenter region. Part of the motivation for observing the Crab was to provide an in-flight test of the characteristics of the DGT imaging system using a relatively strong source of celestial gamma-radiation. The scientific goals of this observation included a measurement of the total Crab spectrum (including a search for possible line emission) and an attempt to image the diffuse emission which had been observed by Graser and

Schönfelder (1982) at MeV energies. A confirming observation of the diffuse emission would be of great value.

The second set of imaging data involved an observation of a region centered on two well-known sources in the constellation of Cygnus - Cygnus X-1 and Cygnus X-3. Cyg X-1 is one of the best known candidates for a black hole (c.f., Oda 1977; Liang and Nolan 1984). The x-ray and gamma-ray emission is believed to be produced as a result of the accretion of matter onto the black hole. The study of these emissions provides a unique opportunity to investigate this important astrophysical process. Cyg X-3 has received much recognition in recent years as a result of its having been observed in ultra-high-energy (UHE) gamma-rays (e.g., Samorski and Stamm 1983). There are very few measurements of this source in the .1-10 MeV range. Past observations of either Cyg X-1 or Cyg X-3 in low energy gamma-rays usually had to contend with the proximity of these two sources (they are separated by only  $8.8^\circ$  in the sky). The DGT provides the unique opportunity to clearly resolve the emission spectra of these two sources.

The new imaging technology represented by the DGT is a potentially very important one for gamma-ray astrophysics. As discussed above, numerous investigators are already exploring the possibilities of the coded aperture technique for gamma-ray astronomy. In this sense, the DGT may represent the first of a long series of exciting new experimental developments in astrophysics.

## CHAPTER I

### Scientific Background

This dissertation deals with the analysis of two gamma-ray imaging observations obtained by the University of New Hampshire's Directional Gamma-ray Telescope (DGT). The first observation is of the region of the galactic anticenter, a region which is dominated by the Crab Nebula/pulsar. In addition to the Crab, however, this region also included the binary x-ray source A0535+26 and the diffuse galactic plane emission. A second observation, of the Cygnus region, encompassed both Cygnus X-1 and Cygnus X-3. In what follows, we review our present scientific knowledge of these sources in the context of their x-ray and gamma-ray emission.

#### Crab Nebula/Pulsar

This supernovae remnant is associated with a supernova reported as a "guest star" by Chinese astronomers in the year 1054 A.D (Smith 1977). During the 1950's, it became clear that much of the observed emission from the Crab Nebula (both radio and optical) could be explained in terms of synchrotron emission. Oort and Walraven (1956) carried out a detailed study of the Crab energetics and found that the radiative lifetimes of the particles responsible for the synchrotron emission are much shorter than the age of the Nebula itself. This implied some type of energy source within the nebula. The role of a rapidly rotating massive body was suggested for the source of both the nebular magnetic field (Piddington 1957) and the energetic particles (Wheeler 1966; Pacini 1967). Both Wheeler (1966) and Pacini (1967) specifically discussed rapidly-rotating neutron stars as the source of the Crab Nebula's energy. The discovery of pulsars by Hewish *et al.* (1968) soon led to the suggestion that the pulsar phenomenon involved a rapidly rotating neutron

star (Gold 1968). The subsequent discovery of the Crab pulsar, with a period of 33 ms, at both radio (Staelin and Reifenstein 1968) and optical (Cocke *et al.* 1969) wavelengths provided the resolution to the problem of the Crab Nebula energetics. Pulsed emission from the Crab has since been measured from radio frequencies (e.g., Rankin *et al.* 1970) to x-ray energies (e.g., Harnden and Seward 1984) to MeV gamma-rays (e.g., Orwig *et al.* 1971) to 100 MeV gamma-rays (e.g., Clear *et al.* 1986) up through  $10^{13}$  eV gamma-rays (e.g., Erickson *et al.* 1976).

At optical wavelengths, the Crab Nebula, subtends an angular size of  $4' \times 6'$ . This nebular emission represents expanding debris from the original supernova explosion. The distance to the Crab has been estimate to lie in the range of 1.3-2 kpc based on measurements of the radial velocities and proper motions of the  $H\alpha$  filaments in the Nebula (Apparao 1973; Shklovskii 1978). A distance in this range is also supported by studies of the original supernova light curve (Apparao 1973). A distance of 2 kpc has been suggested for general use (Apparao 1973) and is adopted here. At this distance, the linear extent of the nebula is  $2.3 \times 3.5$  pc. At increasing photon energies, the extent of the nebula decreases until, at x-ray energies ( $\sim 40$  keV), the emission extends over a region less than one arc-minute across (Pelling *et al.* 1986). At higher energies, the nebula has not yet been resolved due to the limited angular resolution of present detection systems.

The average magnetic field in the nebula can be inferred from a measurement of the break (at  $\sim 10^{13}$  Hz) in the synchrotron spectrum. The break frequency is related to the age of the nebula and the average magnetic field. A direct measurement of this break frequency was made for the first time by the Infrared Astronomy Satellite (IRAS). The results indicate that the nebula is permeated by a magnetic field with an average strength of  $3 \times 10^{-4}$  Gauss (Marsden *et al.* 1984).

### **Basic Theory**

Observed periods of pulsars lie in the range of 1.6 ms to 4.3 s. These periods are observed to increase very slowly in time, with period derivatives measured in nsec/day.

This behavior can be well-explained in the context of a rapidly spinning magnetized neutron star, which loses energy via the acceleration of charged particles and the emission of electromagnetic energy. The Crab period of 33 ms implies an emitting region less than  $\sim 10^5$  km. This size implies that the source must be associated with either a white dwarf, a neutron star, or a black hole. There are no models which predict periodic behavior of a black hole on these time scales (Shapiro and Teukolsky 1983). Models involving periodic emission from white dwarfs or neutron stars must involve either orbital motions, radial pulsations, or rotation. Although neutron star binary systems could have periods in the appropriate range, such systems would be copious emitters of gravitational radiation. The resultant loss of energy would lead to a *decrease* in the observed period, in contradiction with the observed period *increases* (Shapiro and Teukolsky 1983). Models for white dwarf pulsations reach periods as short as  $\sim 1$  s (Melzer and Thorne 1966; Ostriker and Tassoul 1968). This is not short enough to account for the Crab period. Predicted pulsation periods for neutron stars are found to lie in the range 1-10 ms (Melzer and Thorne 1966). These periods are *too* short for the observed pulsar periods. The shortest possible period for a rotating body occurs when it is rotating at the break-up velocity. This condition leads to (Smith 1977),

$$P_{\min} = (3\pi)^{1/2} (G\rho)^{-1/2} \quad (\text{I.1})$$

where  $\rho$  is the mean density of the rotating object. The density of a typical white dwarf is  $\sim 10^7$  gm cm<sup>-3</sup>. This corresponds to a minimum rotational period of 3.8 s, too long to account for the Crab's period. The typical density of a neutron star is  $\sim 10^{15}$  gm cm<sup>-3</sup>, which leads to a minimum period of 0.4 ms, a period sufficiently short to explain the observed pulsar periods. Hence, we must conclude from this analysis that only rotating neutron stars can adequately explain the entire range of observed pulsar periods.

The idea of a rotating neutron star forms the basis of a simple theory which can be used to explain the gross properties of the Crab pulsar (Pacini 1967, 1968; Gunn and Ostriker 1969). In this model, the neutron star is treated as a rotating magnetic dipole with

the dipole inclined at an angle  $\alpha$  to the rotation axis. Classical theory dictates that a time-varying dipole moment radiates energy at a rate given by,

$$\frac{dE}{dt} = - \frac{B_p^2 R^6 \Omega^4 \sin^2 \alpha}{6c^3} \quad (I.2)$$

where  $B_p$  is the strength of the dipole field at the magnetic pole,  $R$  is the radius of the neutron star, and  $\Omega$  is the angular frequency of rotation. Assuming that the energy lost is derived from the kinetic energy of rotation, then

$$\frac{dE}{dt} = I \Omega \frac{d\Omega}{dt} \quad (I.3)$$

A typical neutron star has a mass of  $M \approx 1.4 M_{\text{sol}} \approx 2.8 \times 10^{33}$  gm and a radius of  $R \approx 10^6$  cm (Smith 1977). This implies a moment of inertia of  $I = (2/5) MR^2 \approx 1.1 \times 10^{45}$  gm cm<sup>2</sup>. Given the observed values of  $\Omega$  ( $= 2\pi/P \approx 190.4$  s<sup>-1</sup>) and  $d\Omega/dt$  ( $\approx -2.435 \times 10^{-9}$  s<sup>-2</sup>), the calculated energy loss rate of the Crab pulsar is  $\approx 4.9 \times 10^{38}$  ergs s<sup>-1</sup>. This is roughly equivalent to the total observed energy requirements of the Crab Nebula/pulsar ( $\sim 10^{38}$  ergs s<sup>-1</sup>; Shklovskii 1978). Equation (I.2) can also be used to estimate the surface magnetic field of the Crab pulsar. Taking the observed value of  $\sim 10^{38}$  ergs s<sup>-1</sup> and setting  $\sin \alpha = 1$ , we obtain  $B_p \approx 3.5 \times 10^{12}$  Gauss. This result is the same order of magnitude which would result (based on magnetic flux conservation) in the collapse of a star with  $B \sim 100$  Gauss and  $R \sim 10^{11}$  cm to an object the size of a neutron star ( $R \sim 10^6$  cm). Furthermore, this field strength is comparable to that derived from the observations of cyclotron emission from the Crab ( $8.6 \times 10^{12}$  Gauss; e.g., Owens *et al.* 1985a), from Her X-1 ( $\sim 4-6 \times 10^{12}$  Gauss; Trümper *et al.* 1978) and from 4U 0115-63 ( $\sim 2 \times 10^{12}$  Gauss; Wheaton *et al.* 1979), all of which are believed to be sources which contain a neutron star.

A further prediction of this simple theory concerns the estimated age of the pulsar. If the pulsar's energy is, in fact, derived from the loss of rotational energy, then the estimated age of the pulsar is given by (Shapiro and Teukolsky 1983),

$$t \approx \frac{P}{2} \left( \frac{dP}{dt} \right)^{-1} \quad (I.4)$$

Using the values given by Lang (1980) of  $P = .03312965$  s and  $dP/dt = 36.526$  nsec/day, the estimated lifetime of the pulsar (for epoch 1971.75) is 1242 years. This result implies that the Crab supernova event took place in 730 A.D., not far from the known date of 1054 A.D.

The idealized model discussed above assumes that the neutron star lies in a vacuum. Goldreich and Julian (1969) pointed out, however, that the rapid rotation of a magnetized neutron star will generate an intense electric field at the surface of the neutron star. This electric field is sufficiently strong to overcome both the gravitational and binding forces of the neutron star material. This electric field will therefore strip charged particles (electrons or ions) off of the neutron star surface, thus creating a dense magnetosphere. This magnetosphere co-rotates with the neutron star out to a distance from the rotation axis which corresponds to a rotational velocity equal to the speed of light. This distance is given by,

$$R_{LC} = cP / 2\pi \quad (1.5)$$

The cylindrical surface defined by this condition is known as the *velocity-of-light cylinder*. ( $R_{LC}$  is roughly 16000 km in the case of the Crab pulsar.) The modeling of such a magnetosphere is a very complex theoretical problem. Indeed, an entirely self-consistent model of the pulsar magnetosphere has yet to be developed. (For a review, see Michel 1982.)

Despite the difficulties in the development of a complete model for the magnetosphere, various methods of pulsar particle acceleration have been discussed in the literature. These theories generally require the formation of some region in which particles are accelerated along open magnetic field lines. These acceleration regions, often referred to as *vacuum gaps*, are characterized as regions of charge-depletion in which  $\mathbf{E} \cdot \mathbf{B} \neq 0$  and across which a large electric potential ( $\sim 10^{14}$  volts) is developed.

Two principle theories have been developed to explain the formation of these gaps and the resultant particle acceleration. Those models which can be characterized as *polar*



*cap models* envision the formation of a vacuum gap near the polar surface of the neutron star with potential drops of  $\sim 10^{14}$  volts (Sturrock 1971; Ruderman and Sutherland 1974). A second class of models places the gap formation further out in the magnetosphere (Cheng and Ruderman 1977; Cheng *et al.* 1986a). These so-called *outer gap models* argue that vacuum gaps could exist in the outer magnetosphere with potential drops of  $10^{16}$  volts. In either case, the gap will discharge as a result of pair production within the gap (resulting from either photon-photon interactions or from photon interactions with the strong magnetic field). The discharge of the gap results in the injection of a beam of high-energy charged particles into the magnetosphere.

Given the energetic particle environment (electron energies of at least  $10^{14}$  eV) coupled with the strong magnetic field (up to  $\sim 10^{12}$  Gauss) expected near the pulsar, there are several production mechanisms which are expected to contribute to the Crab gamma-ray emission. The following discussion of these mechanisms is condensed from a number of references, including Ginzburg and Syrovatski (1964), Fazio (1967), Griesen (1971), Tucker (1975), Chupp (1976), Rybicki and Lightman (1979), and Lang (1980). These references should be consulted for further details.

An electron moving through a uniform magnetic field will spiral about the magnetic field line (assuming that there is some non-zero velocity component of the electron perpendicular to the field line). The angular frequency with which the electron gyrates about the magnetic field line is given by,

$$\omega_B = \frac{e B_{\perp}}{\gamma m c} \quad (I.6)$$

where  $B_{\perp}$  is the magnitude of the magnetic field perpendicular to the electron velocity and  $\gamma$  ( $\equiv E_e / mc^2$ ) is the relativistic Lorentz factor of the electron. This frequency is known as the *gyrofrequency*. At nonrelativistic energies (i.e.,  $\gamma \approx 1$ ) the gyrofrequency is also referred to as the *cyclotron frequency*. The corresponding radius of gyration (or *gyroradius*) is

$$r_B = m c^2 \gamma \beta / e B_{\perp} \quad (I.7)$$

where  $\beta \equiv v/c$ . For an energetic electron ( $E_e \approx 10$  MeV with  $\gamma \approx 19.6$  and  $\beta \approx 1.0$ ) in the pulsar magnetic field ( $10^{12}$  Gauss), the radius of gyration is  $\sim 3 \times 10^{-8}$  cm. In the nebular field ( $\sim 3 \times 10^{-4}$  Gauss), the same electron would have a radius of gyration of  $\sim 1 \times 10^8$  cm ( $\sim 1,000$  km).

The Lorentz acceleration resulting from this circular motion results in the emission of radiation by the electron. For the nonrelativistic case, the radiation is emitted at the cyclotron frequency and is termed *cyclotron radiation*. The corresponding photon energy of this emission is given by,

$$E_{\text{cycl}} = 1.15 \times 10^{-11} B_{\perp} \text{ (keV)} \quad (\text{I.8})$$

with  $B_{\perp}$  measured in Gauss. For a field strength of  $5 \times 10^{12}$  Gauss, the cyclotron "line" would appear at an energy of 57.5 keV (independent of the electron energy).

At relativistic energies ( $\gamma > 1$ ) the resulting radiation pattern produced in the "laboratory frame" by the electron is strongly beamed into a cone in the electron's forward direction with a half-angle of  $\sim 1/\gamma$ . The resulting radiation is termed *synchrotron radiation* (or *magnetobremstrahlung*). In this case, the spectrum from a single electron is quasi-continuous, being composed of a series of discrete lines, each corresponding to some harmonic of the gyrofrequency. The photon energy corresponding to the maximum of the intensity distribution is given by,

$$E_{\text{sync}} \equiv 5 \times 10^{-15} \gamma^2 B_{\perp} \text{ (MeV)} \quad (\text{I.9})$$

The production of a 1 MeV synchrotron photon in the nebular field of  $3 \times 10^{-4}$  Gauss requires an electron energy of  $4 \times 10^{14}$  eV. In the pulsar field of  $10^{12}$  Gauss, an electron of energy 7 MeV is required to produce 1 MeV synchrotron emission. It must be noted that the above synchrotron formula holds only under the condition  $\gamma \ll 10^8 B^{-1/2}$ .

It is instructive to look at the lifetime which corresponds to a typical electron in the Crab Nebula radiating principally via the synchrotron mechanism. The total synchrotron power radiated by an electron is given by,

$$\begin{aligned}
 P &\approx \frac{2}{3} \frac{e^4}{m^2 c^3} \gamma^2 B_{\perp}^2 & (I.10) \\
 &\approx 1.6 \times 10^{-15} \gamma^2 B_{\perp}^2 \text{ erg sec}^{-1}
 \end{aligned}$$

If the electron radiates solely by this mechanism, then the time required for the electron to lose a significant fraction of its energy is given by,

$$t_{\text{sync}} = E_e / P \approx (5 \times 10^8 / \gamma B_{\perp}^2) \text{ sec} \quad (I.11)$$

For the electrons in the nebula which radiate most of their energy at 1 MeV (from above),  $\gamma \sim 8 \times 10^8$ . By Equation (I.11), such an electron would have a synchrotron lifetime of  $\sim 82$  days. This is considerably less than the 930 year lifetime of the nebula itself. Clearly, if the nebula is producing such emission, then some type of secondary acceleration mechanism must be operating within the Nebula itself. The exact nature of this acceleration process is not clearly understood (e.g., Jung 1986; Pelling *et al.* 1986).

One very important feature of synchrotron emission is that, for a power-law distribution of electrons with a spectral index of  $\Gamma$ , the resulting synchrotron photon spectrum has the form,

$$I_{\text{synch}}(E) \propto E^{-\alpha} \quad (I.12)$$

with  $\alpha = (\Gamma + 1) / 2$ . In other words, a power-law electron spectrum produces a power-law photon spectrum. The spectrum of the Crab Nebula is well-described by a power-law (of energy spectral index = 0.26) from the radio to the infrared range. From the infrared all the way up to gamma-ray energies, the data follows a power-law of energy spectral index  $\sim 0.5$ . (See Marsden *et al.* 1984 for a summary.) The frequency at which the spectral break occurs is related to the age and average magnetic field of the Nebula. Specifically, the following relationship holds in a situation where there is a continuous injection of electrons into the nebula (Marsden *et al.* 1984),

$$\nu_b \approx 3.5 \times 10^8 B^{-3} t^2 \text{ Hz} \quad (I.13)$$

where  $B$  is in Gauss and  $t$  is in years. The reason for such a break in the spectrum lies in the fact that electrons which produce the radiation at frequencies below  $\nu_b$  have not lost any appreciable energy since the time the Nebula was created. These electrons include those which were initially injected into the Nebula. At higher frequencies, however, the electrons have lost a considerable fraction of their energy since the initial injection. All of the electrons responsible for this emission must have been created at some time after the initial event. The first *direct* measurement of the spectral break frequency (at  $\nu_b \sim 1 \times 10^{13}$  Hz) was obtained with the IRAS satellite (Marsden *et al.* 1984); this provides a value for the average nebular field of  $3 \times 10^{-4}$  Gauss.

Finally, we should note that synchrotron theory also predicts that the emission will be polarized in a plane perpendicular to the magnetic field. The Crab Nebula is known to exhibit a high degree of polarization from radio frequencies up to x-ray frequencies (e.g., Apparao 1973). This observation, in conjunction with the power-law spectra, provides strong support for the operation of the synchrotron mechanism in the Nebula.

It is also possible for electrons (or protons) with zero pitch angle (i.e., moving *along* a magnetic field line) to emit radiation if the field line is curved. Such radiation is analogous to synchrotron radiation and is termed *curvature radiation*. (Sturrock 1971). Due to the very strong and highly curved magnetic field lines near the surface of a neutron star, this mechanism may be quite important in the vicinity of a pulsar. The peak of the curvature radiation spectrum (for electrons) is defined by,

$$E_{\text{curv}} \approx 8.8 \times 10^{-12} \gamma^3 R_c^{-1} \text{ (MeV)} \quad (\text{I.14})$$

where  $R_c$  is the radius of curvature of the field lines. Near the pole of a pulsar, this is estimated to be  $R_c \sim 10^7$  (Sturrock 1971). In this case, an electron of energy  $E_e \approx 5 \times 10^{11}$  eV is required to produce a 1 MeV gamma-ray.

Another mechanism which is believed to operate in the Crab is the *inverse compton effect*. In this case, an energetic electron ( $\gamma \gg 1$ ) transfers energy to a photon. In the rest frame of the electron, this is just the standard compton interaction involving a transfer of

energy from the photon to the electron. An analysis of inverse Compton scattering first involves transforming to the rest frame of the electron, where the analysis can proceed using the standard Compton scattering formulation. Subsequent transformation back into the laboratory frame results in a net energy-gain for the photon. For the case in which  $\gamma E_0 \ll mc^2$  (where  $E_0$  is the initial photon energy and  $\gamma$ , as usual, refers to the electron), the cross-section for Compton scattering corresponds to the Thomson cross-section. In this case, the final photon energy ( $E_{\text{comp}}$ ) can be written as,

$$E_{\text{comp}} \approx (4/3) E_0 \gamma^2 \quad (\text{I.15})$$

For the situation in which  $\gamma E_0 \gg mc^2$ , the Klein-Nishina cross-section must be used and the resultant photon energy can be written as,

$$E_{\text{comp}} \approx \gamma mc^2 \quad (\text{I.16})$$

In order to produce a 1 MeV photon from an infrared photon ( $\sim 0.1$  eV), the required electron energy, as determined in the Thomson limit, is  $\sim 1.4 \times 10^9$  eV. Schlickeiser (1979, 1980) has discussed the application of this mechanism in the pulsar environment, where the Klein-Nishina formulation becomes important.

Finally, there is the possibility of gamma-ray line emission. There are various possible mechanisms which might produce observable line emission. One such mechanism (cyclotron radiation) has already been discussed. Another possible source is electron-positron annihilation at 0.511 MeV which would result from the creation of positrons in the pulsar magnetosphere (Varma 1977). Since models of pulsar magnetospheres generally predict a copious amount of positrons, this should be considered a very viable source of emission. (Indeed, as will be discussed below, such emission may already have been observed.) Theories of nucleosynthesis in supernovae suggest the potential for observable nuclear line emission from the Crab. In the case of the Crab, the strongest lines are expected to be  $< 1.0 \times 10^{-4} \text{ cm}^{-2} \text{ s}^{-1}$  (e.g., Clayton and Craddock 1965; Clayton *et al.* 1969).

Any line emission which originates in the vicinity of the pulsar itself (i.e., the neutron star) may be subject to a *gravitational redshift*. This results from the intense gravitational field of the compact object which acts to shift the observed energy of a line. This shift is usually expressed in terms of the quantity  $z$ , defined by (e.g., Narlikar 1983),

$$1 + z = \frac{\lambda}{\lambda_0} = \left(1 - \frac{2GM}{c^2 R}\right)^{-1/2} \quad (\text{I.17})$$

where  $\lambda_0$  is the un-shifted wavelength of the emission,  $\lambda$  is the shifted wavelength of the emission,  $M$  is the mass of the neutron star and  $R$  the distance between the center of the neutron star and the line source region. In terms of energy, this expression can be rewritten as,

$$E = E_0 \left(1 - \frac{2GM}{c^2 R}\right)^{1/2} \quad (\text{I.18})$$

where  $E$  and  $E_0$  are the shifted and unshifted line energies, respectively. As an example, consider an electron-positron annihilation line ( $E_0 = 511$  keV) produced at the surface of a neutron star of  $1 M_{\text{sol}}$  ( $R \sim 10^6$  cm). In this case, the line would be observed at an energy of  $0.84 E_0$  or 429 keV.

In general, the total gamma-ray spectrum of the Crab Nebula/pulsar can be considered as a superposition of two spectra. The first, that due to the Nebula, is believed to be dominated by synchrotron emission, generated by energetic electrons in a magnetic field of  $\sim 3 \times 10^{-4}$  Gauss. As mentioned previously, the required particle energies are such that a secondary acceleration mechanism must be acting within the nebula itself, possibly some type of Fermi acceleration (Jung 1986). A detailed study of the nebular spectrum requires an understanding of both the particle injection spectrum and the acceleration processes which take place within the nebula (Jung 1986; Pelling *et al.* 1986).

The second spectral component is that due to the pulsar itself. Models of the emission are generally based on the magnetospheric models discussed earlier. These theories must not only be able to explain the photon spectrum, but they must also be capable of explaining the apparent beaming of the emission (the so-called "lighthouse

effect") which leads to the pulsed emission. In the case of the vacuum gap models, the particles are presumed to be accelerated across the gap and out through the magnetosphere along open field lines. These particles then proceed to radiate via a combination of the curvature, synchrotron and inverse Compton processes. These initial particles (or the resultant photons) may undergo pair production processes, thus creating an electromagnetic cascade. The details of such models have been considered by numerous authors (e.g., Sturrock 1971; Ruderman and Sutherland 1974; Cheng and Ruderman 1977; Salvati and Massaro 1978; Scharlemann *et al.* 1978; Harding 1981; Cheng *et al.* 1986a,b).

We shall complete this discussion of pulsar emissions by mentioning two other models of high energy emission. The first model considers the relativistic beaming of the radiation emitted by a source located at the light-cylinder. In the case of these light-cylinder models, the relativistic velocity is not responsible for the radiation itself, but is responsible for the beaming of the radiation in a direction tangential to the velocity-of-light cylinder. This mechanism has been discussed by various authors, including, for example, Smith (1970, 1971), Zheleznyakov and Shaposhnikov (1972), and Ferguson (1981).

Finally, we note that large amplitude plasma waves may be able to accelerate charged particles in a region of the magnetosphere which lies outside the light cylinder, in the so-called *wind zone* (Kundt and Krotschek 1980). This mechanism may be capable of producing photon emission up to  $\sim 100$  MeV.

### **Gamma-Ray Continuum Measurements**

In the gamma-ray region, the Crab is one of the strongest and steadiest sources in the sky. Both its pulsed and unpulsed (i.e., steady) emission have been measured by a number of observers. Usually the assumption is made that the pulsed emission represents emission from the pulsar itself. Any steady, time-independent emission is assumed to emanate from the pulsar's surroundings (i.e., the nebula). The observations can generally be classified as being of the total (pulsed plus unpulsed) emission, the pulsed emission

(presumably due to the pulsar) and the unpulsed emission (presumably arising from the surrounding nebula).

Let us first consider the observations of the total Crab emission in the range of  $\sim 100$  keV up to  $\sim 100$  MeV. Numerous such observations have been made over the past 20 years. These include the measurements reported by Haymes *et al.* (1968), Laros *et al.* (1973), Baker *et al.* (1973), Helmken and Hoffman (1973), Kniffen *et al.* (1974), Walraven *et al.* (1975), Carpenter *et al.* (1976), Dolan *et al.* (1977), Leventhal *et al.* (1977), Ling *et al.* (1979), White *et al.* (1980), Graser and Schönfelder (1982), Strickman *et al.* (1982), Hameury *et al.* (1983), Owens *et al.* (1985a), Watanabe (1985), and Perotti *et al.* (1986). These observations are generally consistent with a single power-law photon spectrum of the form  $dN(E)/dE = A E^{-\alpha}$  throughout the entire energy range. The observed photon spectral index generally lies in the range of  $\alpha = 2.0 - 2.2$ . There are two important exceptions to this, however. Both Baker *et al.* (1973) and Gruber and Ling (1977) measured a considerable excess above the power-law in the 1-10 MeV range. This type of emission might be evidence for nuclear line emission. However, the available observations are generally in conflict with this so-called "MeV excess" (e.g., Schönfelder *et al.* 1975).

Spectral measurements of the Crab pulsar itself require that the data be time-binned at the pulsar frequency in order to determine the pulsed flux. Results for the pulsed emission in the energy range of  $\sim 100$  keV up to  $\sim 100$  MeV have been published by Kurfess (1971), Orwig *et al.* (1971), Albats *et al.* (1972), Bennett *et al.* (1977b), Strickman *et al.* (1982), Knight (1982), Hasinger *et al.* (1984), Mahoney *et al.* (1984), White *et al.* (1985), and Clear *et al.* (1986). These results indicate a photon spectral index of  $\sim 2.2$ . The fraction of the Crab's flux which is observed to be pulsed is  $\sim 20\%$  at 100 keV (Maurer 1979) and  $\sim 75\%$  at 100 MeV (Bennett *et al.* 1977b). The observed pulsar emission extends up to at least  $\sim 10^{13}$  eV (e.g., Erickson *et al.* 1976). It is interesting to note that the pulse shape and phase is fairly constant over the entire range of the spectrum, although



there is some evidence for time variability of the pulse shape at high energies (at  $\sim 100$  MeV; Clear *et al.* 1986).

Finally, we can consider the emission from the Crab Nebula itself. The ability to measure the nebular emission depends on the ability to observe the pulsar emission and then subtract that from the total observed spectrum. The spectrum as reported by Jung (1986) exhibits a break in the spectral index from  $\sim 2$  to  $\sim 2.5$  at an energy of  $\sim 150$  keV. A more complete discussion of the nebular emission is given by Jung (1986) and by Pelling *et al.* (1986).

### **Gamma-Ray Line Emission**

Although the measurements of the Crab spectrum are generally consistent with a power-law source spectrum, there have been occasional reports of narrow line emission, most notably at energies of  $\sim 78$  keV,  $\sim 400$  keV and 1049 keV (Leventhal *et al.* 1977; Ling *et al.* 1979; Yoshimori *et al.* 1979; Manchanda *et al.* 1982; Strickman *et al.* 1982; Ayre *et al.* 1983; Owens *et al.* 1985a; Watanabe 1985). Since the 78 keV emission is beyond the energy range of the DGT experiment, we shall not discuss these observations here.

The first reported detection of gamma-ray line emission from the Crab was made by Leventhal *et al.* (1977). Using a balloon-borne Ge(Li) detector, they detected a line at an energy of  $400 \pm 1$  keV with a flux of  $(2.24 \pm 0.65) \times 10^{-3}$  photons  $\text{cm}^{-2} \text{s}^{-1}$ . The width of this line was determined to be less than the instrumental resolution, i.e.,  $\leq 3$  keV. This line was interpreted as due to gravitationally redshifted electron-positron annihilation radiation with a redshift of  $z=0.28$ . The only other positive (i.e., greater than  $3\sigma$ ) detection of a line near this energy was made by Owens *et al.* (1985a). They found a line centered at 404.7 keV with an intensity of  $(7.2 \pm 2.1) \times 10^{-3}$  photons  $\text{cm}^{-2} \text{s}^{-1}$  and a line width of  $(3.5 \pm 1.4)$  keV. In addition to these measurements, Yoshimori *et al.* (1979) reported a marginal detection of a line at 400 keV with a line intensity of  $(7.4 \pm 5.4) \times 10^{-3}$  photons  $\text{cm}^{-2} \text{s}^{-1}$  and a line width of  $< 3$  keV. A number of observers have also placed upper limits on the flux from this energy region. These upper limits include those of Ling *et al.* (1979), Mahoney

*et al.* (1983) and Hameury *et al.* (1983) which are given (at the  $3\sigma$  level) by  $1.7 \times 10^{-3}$ ,  $1.8 \times 10^{-4}$ , and  $1.7 \times 10^{-3} \text{ cm}^{-2} \text{ s}^{-1}$ , respectively. These results, if not spurious, indicate time variability. Due to the limited statistical significance of the positive measurements, more measurements are needed in order to clarify this issue.

The detection of line emission at an energy of 1049.8 keV was reported by Owens *et al.* (1985a). They reported a feature with a measured width of  $(6.3 \pm 1.6)$  keV and an intensity of  $(2.0 \pm 0.5) \times 10^{-2}$  photons  $\text{cm}^{-2} \text{ s}^{-1}$ . There is no obvious mechanism for producing a line at this energy. This feature awaits confirmation.

## Cygnus X-1

Cyg X-1 was one of the earliest x-ray sources to be identified (Bowyer *et al.* 1965), as it is one of the brightest such sources in the sky. This object gained considerable prominence in March 1971 when the sudden appearance of an accurately located radio source coincided with a sudden change in the x-ray emission as observed by the Uhuru satellite (Tannanbaum *et al.* 1972). This correlated observation allowed for the identification of the x-ray source with a 5.6 day spectroscopic binary known as HDE 226868 (Bolton 1972). The association of Cyg X-1 and HDE 226868 was further confirmed by the detection of a 5.6 day modulation of the x-ray flux by an x-ray detector on board the Ariel V satellite (Holt *et al.* 1976). This was the first time that an x-ray source was found to be part of an optical binary system.

### Basic Theory

The optical star is a 9<sup>th</sup> magnitude O-type supergiant located at celestial coordinates  $\alpha(1950) = 19^{\text{h}} 56^{\text{m}} 29^{\text{s}}$ ,  $\delta(1950) = +35^{\circ} 03' 55''$ . The distance to HDE 226868 can be inferred based on its observed spectral classification (hence some known absolute magnitude) and the estimated interstellar extinction per unit distance along the line of sight.

Such studies conclude that the most probable distance is 2.5 kpc, with a minimum distance of 2 kpc (Margon *et al.* 1973; Bregman *et al.* 1973).

The radial velocity curve for the optical star can be measured using absorption lines in the observed spectrum, thus providing information on the orbital parameters of the system (Gies and Bolton 1982, 1986a). The period ( $P$ ) of the binary system (equivalent to the period of the radial velocity curve) is measured to be 5.600 days. The amplitude of the radial velocity curve ( $v_p$ ) is related to the quantities  $a_p$  (the distance of the primary from the system center-of-mass) and  $i$  (the inclination of the orbital plane to the line of sight) by the relation,

$$v_p = (2\pi/P) a_p \sin i \quad (\text{I.19})$$

Measurements indicate a value of  $a_p \sin i = (5.82 \pm 0.08) \times 10^6$  km. The radial velocity curve also provides a measure of the so-called *mass function* which depends only on the observables  $P$  and  $v_p$ . It is defined by,

$$f = (M_x \sin i)^3 / (M_x + M_p)^2 = P v_p^3 / 2\pi G \quad (\text{I.20})$$

where  $M_x$  and  $M_p$  refer to the mass of the x-ray companion and the optical primary, respectively. Based on measured values of  $P$  and  $V_p$ , the mass function is determined to be  $f = (0.252 \pm 0.010) M_{\text{sol}}$ . Given the mass of the primary star ( $M_p$ ) and an estimate of the orbital inclination ( $i$ ), this relation allows for an estimate of the mass of the x-ray companion. The observed luminosity of HDE 226868 and the estimated distance of  $\sim 2$  kpc require a star of at least  $8.5 M_{\text{sol}}$  (according to estimates based on stellar structure theory; Shapiro and Teukolsky 1983). Using this value for  $M_p$ , we can get a minimum mass estimate for the companion by setting  $\sin i = 1$ . This gives,

$$M_x \geq 3.3 M_{\text{sol}} \quad (\text{I.21})$$

A more detailed optical study of the Cyg X-1 system indicates minimum masses for the optical star and its companion of 20 and  $7 M_{\text{sol}}$  with probable values of 33 and  $16 M_{\text{sol}}$ , respectively (Gies and Bolton 1986a). The estimated mass of the secondary ( $> 7 M_{\text{sol}}$ ) implies that it may be a black hole, since this mass is well beyond the conventional upper

limit for a neutron star or white dwarf (the so-called Chandrasekhar limit of  $2-3 M_{\text{sol}}$ ; e.g., Joss and Rappaport 1984).

Based on optical data, it is generally (although not universally) agreed that Cyg X-1 consists of a compact secondary, presumably a black hole, in orbit about a main sequence primary. This makes Cyg X-1 one of a large class of x-ray emitting objects known as x-ray binaries. In such systems, the x-ray and gamma-ray emission is produced as a result of the accretion of matter from the primary (often considered to be a "normal" main sequence object) onto the compact secondary. Direct evidence for accretion in Cyg X-1 comes from optical observations of variable emission lines from the Balmer series of hydrogen and from He II; these lines are believed to indicate the presence of mass flow within the system (e.g., Bolton 1975; Gies and Bolton 1986b).

That accretion can be a very effective means of energy release can be seen by some very simple arguments. For spherical accretion of matter (at a rate  $dm/dt$ ) onto a compact object of mass  $M_x$ , the kinetic energy of the infalling matter will be converted into heat and radiation. If the efficiency of conversion into radiation is given by  $\eta$ , then the total luminosity will be given by,

$$L_x = \eta G (dm/dt) M_x / R_x \quad (I.22)$$

where  $R_x$  is the radius of the compact body. The conversion efficiency of a black hole has been estimated to be  $\eta \sim 0.1$  (Frank *et al.* 1985). For Cyg X-1, reasonable estimates of the other parameters are given by:  $dm/dt \approx 10^{-8} M_{\text{sol}} \text{ yr}^{-1} \approx 6 \times 10^{17} \text{ gm s}^{-1}$ ;  $M_x \approx 10 M_{\text{sol}} \approx 2 \times 10^{34} \text{ gm}$ ;  $R_x \approx 3 \times 10^6 \text{ cm}$  (Schwarzschild radius). The resulting luminosity is then estimated by this simple model to be  $L_x \sim 3 \times 10^{37} \text{ ergs s}^{-1}$ . This is, in fact, roughly equivalent to the observed x-ray luminosity of Cyg X-1 ( $\sim 4 \times 10^{37} \text{ ergs s}^{-1}$ ; Liang and Nolan 1984).

The maximum temperature at which the object will radiate as a result of accretion can be estimated. This maximum temperature corresponds to the total conversion of gravitational potential energy into thermal energy. For a given electron-proton pair

accreting onto the surface of a star of mass  $M_x$ , the potential energy which is released is given by  $E_{\text{grav}} \approx GM_x m_p / R_x$  where  $m_p$  is the proton mass. (The electron mass is negligible here.) This corresponds to a thermal energy of  $2 \times (3kT_{\text{th}}/2)$ . The resulting thermal temperature is then given by,

$$T_{\text{th}} \equiv GM_x m_p / 3kR_x \quad (\text{I.23})$$

Substitution of numbers corresponding to Cyg X-1 gives  $T_{\text{th}} = 1.8 \times 10^{12}$  K or  $kT_{\text{th}} \approx 150$  MeV. Obviously, this ideal model can readily produce emission in the MeV range. It must be stressed, however, that this is a maximum temperature and, in practice, is unlikely to be achieved.

There are two primary means of transferring mass from the primary to the secondary of an x-ray binary system. The first possibility is that the primary may develop an intense stellar wind, as is often the case for many early-type main-sequence stars. Mass loss rates from OB-type stars have been observed to lie in the range  $10^{-6}$  -  $10^{-5} M_{\text{sol}} \text{ yr}^{-1}$  (Gies and Bolton 1986a). For Cyg X-1, infrared measurements indicate a primary mass-loss rate of  $3.5 \times 10^{-6} M_{\text{sol}} \text{ yr}^{-1}$  (Persi *et al.* 1980). Some fraction of this mass may be captured by the secondary and accreted onto its surface. A second mass-transfer process takes place when the primary star expands to the point where the gravitational pull of the secondary can literally tear off material from the primary. This can occur only when the primary expands beyond its critical equipotential lobe and gas flows from the inner critical point of the system towards the compact object. For a co-rotating binary system, the critical lobe is known as the *Roche lobe* and the critical point is known as the *inner Lagrangian point* ( $L_1$ ).

Accretion onto the compact object can proceed in one of two ways (e.g., Frank *et al.* 1985). The simplest case is that of spherical accretion, i.e., radial inflow of the matter. This occurs in the case where the accreting material retains little, if any, angular momentum. If, on the other hand, the accreting matter has a sufficient amount of angular momentum, then this matter will accumulate to form an *accretion disk* around the companion object. In general, matter accreted via Roche lobe overflow will tend to form a

disk, whereas accretion resulting from a stellar wind may or may not result in the formation of an accretion disk. For Cyg X-1, it is believed that the accretion flow is intermediate between stellar wind accretion (Eardley *et al.* 1978) and Roche-lobe overflow (Bolton 1975; Gies and Bolton 1986b). We must therefore expect that at least some portion of the accreted material in the Cyg X-1 system will form a disk. Such a disk probably has a radius of  $R_d \leq 1.2 \times 10^5$  km (Liang and Nolan 1984).

The accretion structure can, in general, be determined from a set of conservation equations for mass, momentum, and energy (e.g., Shakura and Sunyaev 1973; Novikov and Thorne 1973; Shapiro and Teukolsky 1983; Frank *et al.* 1985). Also required are some type of viscosity law (in the case of a disk model), an equation of state, and a radiative transport equation. The resulting set of equations can then be solved algebraically to obtain functions of the various disk parameters as a function of radius. The important parameters to be determined from the model usually include the electron temperature ( $T_e$ ), the ion temperature ( $T_i$ ), the density ( $\rho$ ), and the pressure ( $P$ ). For disk models, the disk half-thickness ( $h$ ) is also determined. These models generally incorporate a number of simplifying assumptions. These assumptions include: no interactions between the accretion flow and the primary companion, no self-gravity interactions within the flow and no increase in mass of the central object due to accretion. The construction of accretion disk models also generally involve the *thin-disk approximation* (i.e., the disk thickness is much less than the disk radius); the theory regarding thick-disk models, which are probably more realistic, is not well developed at this time. Many accretion disk models relating to Cygnus X-1 also differ in the treatment of the central black hole. Many models (the so-called Newtonian disk models) are simplified by not taking into account the relativistic effects which may become important near the black hole (e.g., Shakura and Sunyaev 1973; Shapiro *et al.* 1976; Ichimaru 1977). These models represent a valid approximation as long as the black hole is non-rotating (Shapiro *et al.* 1976). For rotating black holes, however, the relativistic corrections become important, especially near the inner edge of the accretion

disk (Eilek 1980). The case of a rotating black hole may be important, because the higher densities and temperatures attained near its event horizon may be conducive to more energetic gamma-ray emission. Shapiro *et al.* (1976) suggested that measurements of gamma-ray emission may, in fact, provide a means of measuring the spin of a black hole. Disk accretion onto a rotating black hole has been treated by various authors (e.g., Novikov and Thorne 1973; Eilek 1980; Eilek and Kafatos 1983).

One of the first attempts to find a detailed self-consistent model of disk accretion onto a black hole was that of Shakura and Sunyaev (1973). This model is sometimes referred to as the *cool disk model*. The disk structure derived from this model was characterized by an optically-thick, relatively low temperature ( $10^6$  K) gas. Although reasonably successful in explaining the basic properties of the emission as seen from some accretion disk systems (e.g., cataclysmic variables), the model was not sufficiently hot to account for the hard x-ray emission which had been observed from Cyg X-1.

It was later pointed out (Thorne and Price 1975) that the emission at  $\sim 100$  keV might be explained by the presence of an optically-thin, high temperature region ( $T_e \sim 10^9$  K) in the inner portion of the accretion disk. The hard x-ray emission could then be explained by invoking the inverse Compton mechanism. This suggestion prompted Shapiro *et al.* (1976) to develop a self-consistent "hot disk" model (henceforth referred to as the SLE model) which was able to account for the higher-energy emission. Whereas the cool-disk model of Shakura and Sunyaev (1973) equated the electron and ion temperatures (i.e.,  $T_i = T_e$ ), the SLE model assumed these two quantities to be coupled only by collisional energy exchange. The result of this assumption is that, in general,  $T_i$  is greater than  $T_e$ . In particular, the application of this "two-temperature" disk model to Cyg X-1 results in  $T_e$  of  $\sim 10^9$  K and  $T_i$  of  $\sim 10^{12}$  K in the inner region of the disk. This temperature difference arises largely due to the more efficient cooling mechanisms (especially Compton cooling) for the electron population. Soft photons from the cool outer portion of the disk ( $T_e \sim 10^6$  K) diffuse into the inner disk region where they are Compton scattered by the hot electron

population ( $T_e \sim 10^9 \text{K}$ ). The resulting inverse Compton spectrum is of the form of a power-law from  $\sim 8 \text{ keV}$  up to a few hundred keV, above which it falls off exponentially.

Other "hot disk" models have been developed which differ from the SLE model in terms of the configuration of the hot gas component. For example, Eardley *et al.* (1978) suggested alternating hot and cold regions within a disk structure. Liang and Price (1977) developed a model in which a cool disk is surrounded by a hot corona. Both such models rely on soft photons from the cool disk region as input to the Compton process.

Spherical accretion models must rely on some type of turbulence mechanism for the efficient conversion of kinetic energy into thermal energy. Otherwise, the infalling matter would simply be absorbed at the Schwarzschild radius. Mészáros (1975) suggested that a suitable viscous dissipation mechanism is provided by magnetohydrodynamic and plasma turbulence. In a series of papers, Maraschi and co-workers have developed a detailed model of spherical accretion (Maraschi and Treves 1977; Maraschi *et al.* 1979; Maraschi *et al.* 1982; Colpi *et al.* 1984; Colpi *et al.* 1986). This model results in a two-temperature plasma similar to that in the SLE model. Soft photon input is provided by cyclotron radiation which results from the presence of a magnetic field ( $\sim 10^7 \text{ Gauss}$ ) within the accretion region.

Since the inverse Compton effect is a common feature of the models which have been proposed to explain the spectrum of Cyg X-1, it is worthwhile to review how this mechanism is applied. Based on the discussion earlier in this chapter, the two ingredients required to produce inverse Compton emission are 1) a supply of energetic electrons (at a temperature of  $T_e$ ) and 2) a supply of soft photons of energy  $h\nu_0 \ll kT_e$ . In the case of repeated scatterings of photons off of non-relativistic electrons, the evolution of the photon distribution function can be described by the *Kompaneets equation*. This equation was first derived by Kompaneets (1957) and can be written in the form (c.f., Sunyaev and Titarchuk 1980),



$$\frac{\partial n}{\partial y} = \frac{1}{x^2} \frac{\partial}{\partial x} x^4 \left( n + n^2 + \frac{\partial n}{\partial x} \right) \quad (\text{I.24})$$

where  $n$  is the photon occupation number ( $I_\nu = [2h\nu^3/c^2] n$ ),  $y = (4kT_e/m_e c^2) \sigma_T n_e c t$  is the Comptonization (or Kompaneets) parameter,  $\sigma_T$  is the Thomson cross-section and  $n_e$  is the electron number density. The Compton parameter is a useful measure of the energy exchange in the system. Physically, it represents the product of the average fractional energy change of the photon per scattering times the mean number of scatterings which it encounters as it traverses the medium. For  $y \geq 1$ , the energy of typical photon increases to  $\sim 3kT_e$  by repeated scatterings, at which point further scatterings will transfer no net energy from the electrons. This is the case of *saturated* Comptonization. For  $y \ll 1$  (*unsaturated* Comptonization), the total photon energy content (and, hence, the photon spectrum) is relatively unchanged. Solutions to this equation have been discussed by various authors, including Katz (1976), Shapiro *et al.* (1976), Rybicki and Lightman (1979), Sunyaev and Titarchuk (1980), and Liang and Nolan (1984).

Sunyaev and Titarchuk (1980) have applied the Kompaneets equation to the problem of a source of soft photons embedded in a spherical, isothermal plasma cloud. Their solution is valid for any spectral shape as long as the injected soft photons have an energy  $h\nu_0 \ll kT_e$ . The solution has the form,

$$\frac{dN}{dE} = A x^2 e^{-x} \int_0^\infty t^{n-1} e^{-t} \left( 1 + \frac{t}{x} \right)^{n+3} dt \quad (\text{I.25a})$$

where  $A$  is a constant,  $x = E / kT_e$ ,

$$n = -\frac{3}{2} + \left( \gamma + \frac{9}{4} \right)^{1/2} \quad (\text{I.25b})$$

$$\gamma = \frac{\pi^2 m_e c^2}{3kT_e \left( \tau + \frac{2}{3} \right)^2} \quad (\text{I.25c})$$

where  $\gamma$  as given here is appropriate for a spherical geometry. For a disk geometry, the factor 3 in front of  $kT_e$  in the denominator of equation (I.25c) should be changed to 12 (Shakura and Sunyaev 1980). At low energies ( $x \ll 1$ ) the solution can be represented as a power-law of the form  $dN/dE \sim x^{-(n+1)}$ . In the high-frequency limit ( $x \gg 1$ ), the spectrum is of the Wien type,  $dN/dE \sim x^2 e^{-x}$ . Note that this spectrum is characterized by two parameters - the electron temperature ( $T_e$ ) and the optical depth due to Thomson scattering ( $\tau$ ). Given that the emission spectrum is a single-temperature inverse Compton spectrum, then the electron temperature can be inferred from the roll-over energy; the optical depth can then be derived from the power-law index measured at low energies.

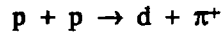
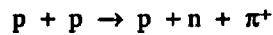
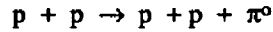
In some accretion models (e.g., the SLE model), the electron temperature is nearly independent of radius. In such a situation, it may be reasonable to model the emission as a single-temperature inverse Compton spectrum. However, there are models which predict an electron temperature ( $T_e$ ) which varies by nearly an order of magnitude within the accretion region (e.g., the spherical accretion model of Colpi *et al.* 1984). In such models, the electron temperature is a function of radius. Hence, the Comptonization region cannot be treated as an isothermal one. The spectrum must then be computed for a number of radii and the individual spectra summed (with appropriate attenuation corrections) in order to produce the total emergent spectrum. In the model of Colpi *et al.* (1984), for example, the resulting spectrum extends up to  $\sim 1$  MeV, with the exponential fall-off occurring above 1 MeV. A similar spectrum is also predicted in the model of Eilek and Kafatos (1983).

One of the predictions of the inverse Compton model is that, for a disk geometry viewed edge-on, there should exist a polarization of the observed x-ray emission. This polarization could reach 10% for a sufficiently high optical depth (Dolan 1986). Long *et al.* (1980) reported a marginal detection of 3-5% polarization in low energy x-rays. If this measurement is confirmed (and if the spectrum is indeed due to the inverse Compton effect), this would be a direct indication that disk accretion is taking place in the system.

Although the inverse Compton mechanism is generally believed to be the dominant mechanism for x-ray emission from Cyg X-1, other potential candidate mechanisms have been proposed. Mészáros (1983) has proposed a thermal bremsstrahlung model for the emission. Non-thermal models have also been suggested to account for some of the observed emission (e.g., Aharonian and Vardanian 1985).

Models of the Cyg X-1 x-ray emission which incorporate a hot electron population ( $T_e \geq 10^9$  K) may also require the incorporation of various relativistic effects. Svensson (1984) pointed out that at  $T_e \approx 10^9$  K ( $kT_e \approx 50$  keV  $\approx 0.1$  mc<sup>2</sup>), deviations from nonrelativistic analytical results (e.g., Sunyaev and Titarchuk 1980) are already large. Relativistic models of the Cyg X-1 emission are still in their infancy.

Another gamma-ray emission process was suggested by Shapiro *et al.* (1976) in the context of their two-temperature (SLE) model. Assuming a *thermalized* ion distribution at a temperature of  $T_i \sim 10^{12}$  K, the ions (protons) in the high-energy tail of the Maxwellian distribution will have sufficient energy to undergo p-p reactions (the threshold for which is at 290 MeV). The principle interactions would be,



These processes result in gamma-ray emission via two principle processes. The decay of neutral pions ( $\pi^0$ ) proceeds (in  $\sim 10^{-16}$  sec) via the emission of two gamma-rays, each with an energy of 68 MeV in the center-of-mass frame. In the laboratory frame, the spectrum is seen as a broad peak centered at 68 MeV. The charged pions decay (in  $\sim 10^{-8}$  sec) through a muon into an electron (or positron). The electrons and positrons then emit radiation via collisional bremsstrahlung. The entire pion production process may be enhanced for a rotating black hole due to the higher temperature and densities which are expected to exist just outside of a rotating event horizon. This mechanism has been investigated by various

authors (e.g., Dahlbacka *et al.* 1974; Collins 1979; Eilek 1980; Eilek and Kafatos 1983; Colpi *et al.* 1984; Colpi *et al.* 1986).

Finally, a discussion of potential gamma-ray emission mechanisms would not be complete without a discussion of line emission. There are two principal mechanisms for creating line emission: electron-positron annihilation and nuclear deexcitation. Liang (1979) discussed the importance of electron-positron pairs in models of accretion around black holes. Annihilation radiation from hot astrophysical plasmas has been discussed by Ramaty and Mészáros (1981). They find that for plasma temperatures greater than  $\sim 6 \times 10^9$  K (i.e.,  $kT_e > mc^2$ ), the mean line energy is given by  $E_m \approx 1.2 kT_e$  and the line has a FWHM  $\approx 2.61 kT_e$  (keV). This blue-shift of the peak emission results due to relativistic beaming effects.

The cross-sections for nuclear excitation generally reach a maximum in the energy range 10-30 MeV ( $T_i \sim 10^{11}$  K). Hence, while the conditions for pion production are somewhat marginal, there may be ample energy within the ion population for nuclear excitations to take place (Higdon and Lingenfelter 1977; Lingenfelter *et al.* 1978; Aharonian and Sunyaev 1984). Gamma-ray emission can therefore be expected from the deexcitation of the excited nuclei. The strongest line is expected to be that at 4.438 MeV from  $^{12}\text{C}^*$ . Other potentially observable lines are at 0.847 and 1.238 MeV from  $^{56}\text{Fe}$ , 1.369 MeV from  $^{24}\text{Mg}$ , 1.634 MeV from  $^{20}\text{Ne}$ , 1.779 MeV from  $^{28}\text{Si}$ , 2.313 MeV from  $^{14}\text{N}$ , and 6.129 MeV from  $^{16}\text{O}$ . In order for the line emission to be observable, the nuclear line emissivity must be at least of the order of the continuum emissivity. This requires a two-temperature plasma with  $T_e < 10^{10}$  K and  $T_i \geq 10^{10}$  (Lingenfelter *et al.* 1978; Aharonian and Sunyaev 1984). As discussed previously, such a plasma may be expected in the accretion region of Cyg X-1. However, at ion temperatures above  $\sim 10^{11}$  K spallation reactions can compete with the nuclear excitation reactions. Under such conditions, the destruction of nuclei via spallation can effectively suppress the nuclear line emission. It is expected that the total line

luminosity (from thermal plasma interactions) would then be  $\sim 10^{-4}$  of the total x-ray luminosity (Aharonian and Sunyaev 1984).

### **Luminosity Variations**

The x-ray emission from Cyg X-1 has been observed to be variable on timescales ranging from months down to milliseconds. Chaotic variability on a time scale of 0.3-1.2 seconds appears to be well-established at energies below  $\sim 20$  keV as a result of measurements made by a number of observers (e.g., Terrell 1972; Ogawara *et al.* 1977; Giles 1981; Meekins *et al.* 1984). Similar timescales have been measured for the variations in the 20-150 keV band (Doi 1980). Nolan *et al.* (1981b) measured variations on timescales from  $\sim 20$  seconds down to less than 80 ms based on measurements with the HEAO 1 satellite. Variation timescales as short as one millisecond have also been reported (Rothschild *et al.* 1974, 1977). These variations are all consistent with accretion disk models which predict no stable periodic x-ray emission with periods shorter than the 5.6 day orbital period. The millisecond variability has been interpreted as the orbital time scale of the innermost regions of an accretion disk, thus establishing an upper limit for the compact object of  $R \leq ct \sim 300$  km.

On longer timescales, the Cyg X-1 x-ray luminosity can generally be regarded as being in one of two states. The low-state (LS) is characterized by a relatively low flux of soft x-ray emission and a relatively high flux of hard x-ray emission. In the high-state (HS), the converse is true. (Note that the "state" is defined by the relative intensity of the soft x-ray emission and that the soft x-ray and hard x-ray emissions are anticorrelated.) Cyg X-1 appears to spend  $\sim 90\%$  of its time in the low x-ray state. Several transitions between states have also been observed since this bimodal behavior was first noticed in 1970 (Bleach *et al.* 1972; Tananbaum *et al.* 1972). For example, during a low-to-high state transition, the 1-10 keV flux is observed to increase by a factor of 3-5 within a one day

period; meanwhile, the hard x-ray flux decreases by a factor of 1.5. High state periods generally last for weeks to months before returning to the low state.

Ling *et al.* (1983) have presented evidence for a new state which they refer to as the "super-low" state (SLS). This state is characterized by relatively low fluxes in both the soft and hard x-ray regimes. Confirming evidence for this state has been reported by Perotti *et al.* (1986) based on balloon-borne measurements made by the MISO collaboration.

Most recently, Ling (1987) has claimed the existence of three separate states of gamma-ray emission during the low x-ray state. This assertion, based principally on data obtained from the HEAO-C gamma-ray experiment, implies more complex time variability than previously believed. Whether this behavior can be explained in the context of present models remains to be seen.

The general bimodal behavior has been ascribed to instabilities in the accretion disk structure (Lightman and Eardley 1974). Ichimaru (1977) developed an accretion disk model with an explicit formulation of the viscous stresses which predicted a bimodal behavior based on the mass accretion rate. The variations might also be explained by a change in the input of soft photons in the inverse Compton process (Nolan *et al.* 1981a; Ling *et al.* 1983). Mészáros (1975) has also suggested that a spherical accretion model with a variable accretion rate might also account for the bimodal behavior and the associated spectral changes.

Long-term periodic variations with a period of ~300 days have also been suggested (Manchanda 1983; Priedhorsky *et al.* 1983). Manchanda (1983) compiled all hard x-ray data (~30 keV) obtained between 1964 and 1982 and found evidence for a period of ~300 days. Priedhorsky *et al.* (1983) used data obtained from the Vela 5B (3-12 keV; 1969-1979) and Ariel V (3-6 keV; 1974-1980) satellites and found a period of  $294 \pm 4$  days. This periodicity was confirmed by Kemp *et al.* (1983) using optical photometry data. Priedhorsky *et al.* (1983) proposed three possible explanations for this period: the orbital period of a third body, precession of the accretion disk, or precession of the primary itself.

Manchanda (1983) also proposed a third body in the Cygnus X-1 system in order to explain this periodicity. Such a body may, in fact, eliminate the need for a massive compact companion in the system. Ling *et al.* (1983) note that their super-low state observations were obtained just after a 300 day minimum (based on the ephemeris of Priedhorsky *et al.* 1983). A second long-term period of 78 or 39 days reported by Kemp *et al.* (1978) based on optical and x-ray measurements has not been confirmed.

### Spectral Observations

The spectral data at energies below  $\sim 100$  keV is, in general, consistent with a single-temperature inverse Compton model. For example, Sunyaev and Trümper (1979) found that the hard x-ray spectrum (15-150 keV) obtained with the MPI/AIT balloon-borne experiment could be well-described by an inverse Compton model with a temperature of  $T_e = 2.5 \times 10^8$  K ( $kT_e = 27$  keV) and a Thomson optical depth of  $\tau_0 = 5$ . Additional data obtained with the MPI/AIT experiment yielded similar results (Steinle *et al.* 1982). Data obtained with the MISO balloon experiment (26 keV - 200 keV) were found to be well-fit by an inverse Compton model with  $T_e = 50 \pm 17$  keV and  $\tau_0 = 2.5 \pm 1.0$  (Perotti *et al.* 1986). At higher energies, the available data can be described in many instances by a power-law photon spectrum. Indeed the MISO data can also be equally-well represented by a power law with a photon spectral index of -1.92. Meegan *et al.* (1979) found a power-law fit with a spectral index of 2.26 in the 52 keV - 1.3 MeV range. In general, the emission appears to extend to  $\sim 1$  MeV with indications of a steep fall-off at  $\sim 1$  MeV (e.g., Nolan *et al.* 1981a). However, Mandrou *et al.* (1978) and Roques *et al.* (1985) reported on measurements obtained with the CESR experiment OPALE which indicate emission up to  $\sim 3$  MeV. They find a best-fit model consisting of a Compton spectrum ( $kT_e \sim 42$  keV,  $\tau \sim 2.8$ ) and a power-law at high energies (given by  $9.4 \times 10^{-3} E_{\text{MeV}}^{-1.3}$  photons  $\text{cm}^{-2} \text{s}^{-1} \text{MeV}^{-1}$ ). Emission above 1 MeV has also been reported by Baker *et al.* (1973).

There have been only two reports of possible gamma-ray line emission from Cyg X-1. The first is that of Nolan and Matteson (1983); they reported a possible broad

positron annihilation feature based on an analysis of data from HEAO 1. The measured location of the line was at  $500 \pm 75$  keV with an intensity of  $\sim 5 \times 10^{-3}$  cm<sup>-2</sup> s<sup>-1</sup> and a line width of  $\sim 400$  keV FWHM. The total significance of the line measurement is about  $3 \sigma$ . A line feature at 145 keV was reported by Watanabe (1985) based on data from a balloon-borne Ge(Li) detector. The measured intensity of the line was  $(1.34 \pm 0.31) \times 10^{-2}$  cm<sup>-2</sup> s<sup>-1</sup> with a width of 14.3 keV FWHM. The suggested source of this emission was a gravitationally redshifted line from <sup>56</sup>Co (nominal line energy of 158 keV). Neither of these two lines have been confirmed.

### Other Sources

#### A0535+26

This source was first discovered as a transient x-ray source by the rotation modulation collimator on board the Ariel V satellite in April, 1975 (Rosenberg *et al.* 1975). During this initial 16 day observation, it was observed to brighten to nearly twice the intensity of the Crab in the 3-7 keV range. Periodic variations with a period of 104 seconds were observed. Although the source remained visible to experiments on Ariel V until  $\sim$ September 20, the observed intensity had decayed considerably (to  $<10\%$  of the Crab) within about two months (Coe *et al.* 1975; Ricketts *et al.* 1975; Kaluziński *et al.* 1975; Rappaport *et al.* 1976). Since the initial observations, a number of outbursts have been observed (see Hameury *et al.* 1983 for a partial summary). There is evidence for a possible 111 day period between observed "high" states.

Subsequent outbursts observed by SAS-3 (Rappaport *et al.* 1976; Li *et al.* 1979) permitted a more accurate determination of the source location. These results led to the identification of A0535+26 with a 9<sup>th</sup> magnitude peculiar emission-line star HDE 245770 (Li *et al.* 1979). An analysis of the observed changes in the pulse period indicate that A0535+26 may be a member of a binary system (Li *et al.* 1979). The limited pulse arrival time data indicates a binary period of at least 20 days.



The rather complex shape of the pulsar light curve has been observed to vary considerably with energy (e.g., Frontera *et al.* 1985) and source intensity (Hameury *et al.* 1983). Variations in the pulse shape on time scales of  $\sim 10^3$  seconds have been reported by Frontera *et al.* (1985). These types of variations may provide further insight into the accretion process in x-ray binary systems. For example, Frontera *et al.* (1985) have pointed out that a study of the variation of the pulse profile with source luminosity may afford a unique opportunity to study the relation between accretion rate and pulse shape. The fraction of the emission which is pulsed appears to approach unity at 100 keV, indicating that strong beaming must be taking place.

To date, the spectral measurements of A0535+26 are limited to energies below 100 keV. The spectral data can be variably described with a blackbody spectrum (Coe *et al.* 1975; Frontera *et al.* 1982), a modified blackbody spectrum (Coe *et al.* 1975), an exponential (e.g., Hameury *et al.* 1983) or a power-law (e.g., Polcaro *et al.* 1982). Hameury *et al.* (1983) have suggested the need for data above 100 keV to help determine which of these models is most valid.

#### **Anticenter Diffuse Emission**

At high gamma-ray energies ( $E > 30$  MeV), satellite observations (especially those of SAS-2 and COS-B) have succeeded in mapping out a diffuse emission related to the galaxy (e.g., Fichtel *et al.* 1975; Mayer-Hasselwander *et al.* 1982; Strong *et al.* 1982). Much of this emission is undoubtedly associated with the interactions between energetic cosmic-rays and the ambient interstellar medium (e.g., Issa and Wolfendale 1981). This component is expected to be composed of primarily  $\pi^0$  decay, electron bremsstrahlung and inverse Compton emission. Some fraction of this emission (estimated to be anywhere from 5%-50%) may, however, be associated with unresolved point sources (e.g., Harding and Stecker 1981). The extent of this point source contribution is a subject of much discussion in the literature.

Due to the different spectral characteristics of cosmic-ray interactions and expected point source contributors, it is expected that observations at energies below 35 MeV would greatly facilitate the resolution of this problem. Observations of the galactic diffuse emission at these energies are rather incomplete at present. For the region of the galactic anticenter, only one observation exists at energies between 200 keV and 35 MeV; this is the imaging measurement made by Graser and Schönfelder (1982) with a balloon-borne Compton telescope. Sacher and Schönfelder (1983) have used different estimates of the interstellar electron spectrum to study this problem. They conclude that the electron spectrum derived by Lebrun *et al.* (1982) from higher-energy COS-B measurements would be able to explain most of the observed emission. However, other estimates of the electron spectrum (Webber *et al.* 1980; Webber 1982) would indicate that unresolved point sources must also contribute. Further measurements of the anticenter diffuse emission are clearly needed in order to resolve this problem with any degree of certainty.

### Cygnus X-3

Cygnus X-3 has been extensively observed from radio frequencies to ultra-high energy (UHE) gamma-rays (i.e., photons greater than  $10^{15}$  eV). A well-defined modulation of 4.8 hours has been found at both infrared and x-ray energies, although at radio wavelengths this modulation is not observed. At gamma-ray energies of 35-500 MeV, the 4.8 hour periodicity has been measured by the SAS II satellite (Lamb *et al.* 1977), but, surprisingly, no emission was detected by the COS-B satellite (Bennett *et al.* 1977a). At still higher energies ( $10^{12}$  eV), the 4.8 hour period shows up with the emission appearing in two narrow pulses at orbital phases of 0.2 and 0.8 (Danaher *et al.* 1981; Lamb *et al.* 1982; Weekes 1983; Dowthwaite *et al.* 1984). Samorski and Stamm (1983) and Lloyd-Evans *et al.* (1983) have reported the detection of emission  $>10^{15}$  eV. The modulation is generally interpreted to be due to orbital motion in a binary system.

The conventional binary model of the system (Vestrand and Eichler 1982) assumes that energetic particles accelerated by a young pulsar interact with the companion star.

These interactions produce the observable high-energy emission. The recent observation of pulsed emission at energies  $>10^{15}$  eV with a period of 12.6 ms (Chadwick *et al.* 1985) lends support to this model. Eichler and Vestrand (1984) have also argued that the accelerated particles must be ions which would imply that the system may be a significant source of nuclear line emission.

Cygnus X-3 also exhibits long term intensity/spectral variations at soft x-ray energies. At energies of 2-6 keV, there appear to be two distinct "states" (Leach *et al.* 1975). The "low state" displays a harder spectrum and is about a factor of three lower in intensity in this energy range. A possible x-ray period of 34.1 days has been reported (Molteni *et al.* 1980). At higher energies (10-100 keV), the status of the long-term behavior is not clear.

Observations of low energy gamma-ray emission from Cygnus X-3 are rather incomplete. At energies below  $\sim 200$  keV, a number of spectral measurements have been made (Rocchia *et al.* 1969; Peterson 1970; Matteson 1971; Ulmer *et al.* 1974; Pietsch *et al.* 1976; Reppin *et al.* 1979; Dolan *et al.* 1982; Willingale *et al.* 1985). At energies between 200 keV and 10 MeV, only one observation has been reported, that of Meegan *et al.* (1979). The measurement of Meegan *et al.* (1979) was made using a collimated NaI(Tl) scintillation detector with a field-of-view  $\sim 13^\circ$  FWHM. This field-of-view is comparable to the angular separation ( $8.8^\circ$ ) of Cygnus X-3 from the stronger source Cygnus X-1. The results for Cygnus X-3 indicated a statistically significant time variability, with an increasing flux towards zero phase (x-ray *minimum*). Meegan *et al.* (1979) could not rule out variability of Cygnus X-1 (which is known to be highly variable) as being responsible for the observed increase. Clearly, more data are needed for Cygnus X-3 above 200 keV in order to confirm the results of this single measurement.

## CHAPTER II

### Instrumentation

This chapter describes the University of New Hampshire's Directional Gamma-ray Telescope (DGT). This device, the operation of which is based on the idea of coded-aperture imaging, has been used to collect the data embodied in this thesis. Following a general review of the coded-aperture technique, the DGT experiment itself is described.

#### Coded Aperture Imaging

Classical imaging techniques (e.g., refraction or reflection optics) rely on the ability to modify the path of the incoming photons. The very low reflectivity of gamma-ray photons makes such procedures impractical at these wavelengths. These difficulties can be overcome, however, by the use of a pinhole camera, which consists of a single "pinhole" placed in front of a photon detection system. This type of imaging system is applicable to photons of any wavelength, as long as diffraction effects can be ignored. Diffraction effects are negligible as long as the diffraction pattern width ( $\sim 2f\lambda/d$ , where  $\lambda$  is the wavelength of the radiation; Jenkins and White 1950) is much less than the size of the pinhole ( $d$ ). Since this criterion is easily attained by gamma-ray photons for a reasonable size pinhole, a pinhole camera would be effective for gamma-ray measurements. The angular resolution ( $\Delta\phi$ ) of this system would be determined simply by the ratio of the pinhole size ( $d$ ) to the separation of the pinhole from the detection plane ( $f$ ); more specifically,  $\tan \Delta\phi = d/f$ . For astronomical applications, the flux levels are generally quite small. In this case, the limited throughput of a single pinhole small enough to achieve useful resolution would preclude its usefulness. A solution to this problem was first suggested by Dicke (1968) and, independently, by Ables (1968). The idea which they

proposed involved the use of a mask composed of multiple pinholes. Such a system, referred to as a "multi-pinhole" or *coded-aperture* telescope, would retain the desired angular resolution while providing the sensitivity which would be commensurate with the needs of the gamma-ray astronomer. (The concept of coded aperture imaging appears to have been first suggested by Mertz and Young (1961) using Fresnel zone plates.)

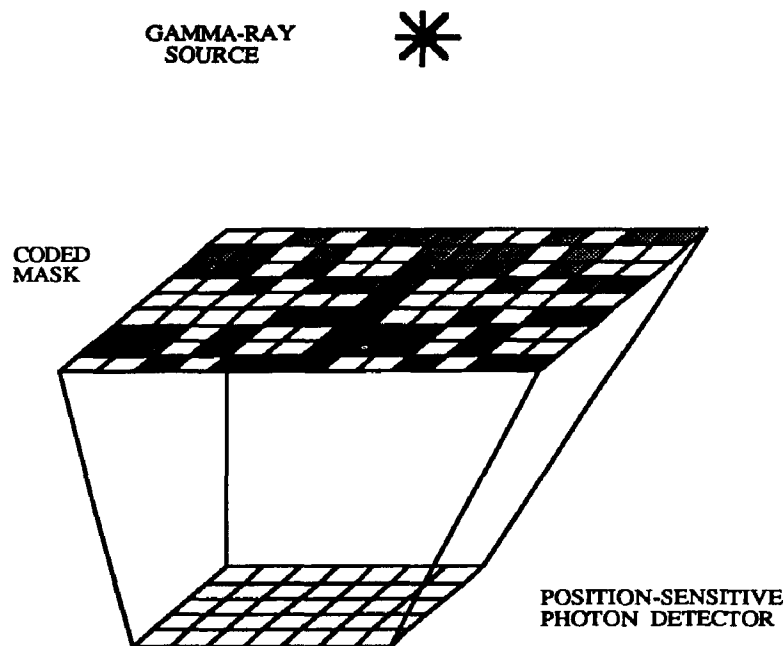


**FIGURE II-1:** Schematic diagram showing the principle components of a coded aperture telescope.

The principle elements of a coded aperture telescope are shown in Figure II-1. The first component is a position-sensitive photon detector (PSD), designed to measure the spatial distribution of the incident photons. The PSD might, for example, consist of photographic film, a gas-scintillation proportional counter, or, in the case of a gamma-ray experiment, some arrangement of scintillation or solid state detectors. Situated in front of, and parallel to, the PSD is some suitably coded aperture mask. The mask is composed of

both open (i.e., transparent) and closed (i.e., opaque) elements. Each transparent element acts as an independent "pinhole" camera and casts an image of the source (or source distribution) onto the detection plane. The resulting pattern detected by the PSD then consists of a superposition of a large number of independent images of the source distribution. A single image may then be reconstructed by some appropriate deconvolution technique.

One of the fundamental design criteria for a coded aperture imaging system is the choice of the pattern of elements which make up the coded mask. The use of a random pattern of pinholes was suggested by both Dicke (1968) and Ables (1968). For an infinitely large aperture, this type of pattern would prove ideal, in the sense that such a system would accurately reproduce the observed source distribution. In practice, however, the use of a finite aperture renders a random pattern less than ideal, due to artifacts in the imaging process. These artifacts (or "ghosts") arise when the response of the imaging system to a point source is not confined to the immediate vicinity of the reproduced source location. Fortunately, a number of finite aperture patterns have been suggested which do not produce such artifacts in the imaging process. In order to understand the derivation of such mask patterns, it is useful to first look at the imaging process in more detail.

### **Basic Concepts of Coded Aperture Imaging**

In order to describe the coded aperture imaging process, let us first define the following. Let  $A$  be the aperture transmission function which is equal to 1 for a perfectly transparent element and 0 for a perfectly opaque element. The distribution of the source emission (i.e., the source being imaged) will be described by the function  $S$ . The response of the photon detection plane, in terms of the spatial distribution of detected photons, will be represented by  $P$ . Finally, let  $B$  represent the spatial distribution of the background within the photon detection plane. The imaging process can then be described by the correlation of the source photon distribution ( $S$ ) and the aperture transmission function ( $A$ ),

$$P = S \otimes A + B \quad (\text{II.1a})$$

where  $\otimes$  is the correlation operator. These functions may also be represented in terms of discrete array elements. In this case, each element of the source distribution function (S) corresponds to an image resolution element or pixel, which is equivalent to the solid angle subtended by a single mask element as seen from the detection plane. Each element of A corresponds to a physical element in the aperture mask. For a source at infinity, each element of both the detector response (P) and the detector background (B) correspond to an area on the detection plane which is equivalent to the size of a mask element. In terms of these discrete elements, equation (II.1a) can be written as

$$P(k,l) = \sum_{i=1}^I \sum_{j=1}^J S(i,j) A(i+k,j+l) + B(k,l) \quad (\text{II.1b})$$

where the summations run over the number of elements in the detection plane.

The problem is then to determine the true source distribution (S) from knowledge of the detector response (P) and the aperture transmission function (A). Let us assume that the reconstructed image (which we will call S' in order to distinguish it from the true source distribution) can be obtained by correlating the detector response (P) with some suitably chosen *post-processing function*(G). This can be expressed mathematically as,

$$S' = P \otimes G \quad (\text{II.2a})$$

or, in terms of discrete array elements,

$$S'(i,j) = \sum_{k=1}^K \sum_{l=1}^L P(k,l) G(i+k,j+l) \quad (\text{II.2b})$$

The substitution of equation (II.1) into equation (II.2) results in the derivation of a fundamental requirement which may then be used in the selection of an appropriate mask pattern. The result of this substitution is,

$$S' = (S \otimes A) \otimes G + B \otimes G = RS \otimes (A \otimes G) + B \otimes G \quad (\text{II.3})$$

Here  $R$  denotes the reflection operator, i.e.,  $Rf(x) = f(-x)$ . Note that if the source ( $S$ ) is a point source (represented mathematically as a delta function), then the first term reduces to  $A \otimes G$ . The quantity  $A \otimes G$  is generally referred to as the system point-spread-function (PSF). For an ideal system, the PSF approximates a delta function and ensures the accurate reproduction of the observed source distribution. Therefore, in the selection of a mask pattern, we shall require the correlation of  $A$  and  $G$  to be a delta function, i.e.,

$$A \otimes G = \delta \quad (\text{II.4})$$

In this case, equation (II.3) reduces to,

$$S' = S + B \otimes G \quad (\text{II.5})$$

We see here that, under this condition, the procedure has reproduced the original source distribution ( $S$ ). The detector background ( $B$ ) has, however, added a spatially distributed noise to the image. (This background-induced noise term will be discussed in more detail below.)

Since  $G$  is normally derived directly from  $A$ , equation (II.4) represents a fundamental requirement on  $A$ , the coded aperture mask pattern. This requirement on  $A$  has provided the basis for research into the selection of the most appropriate mask pattern. In addition to this requirement, however, the mask pattern should also provide a suitable modulation transfer function (MTF; Fenimore 1980). One set of patterns which satisfy these criteria are the *Uniformly Redundant Arrays* (URA) of Fenimore and Cannon (1978).

The implementation of URA patterns has been extensively discussed by Fenimore and Cannon (1978) and by Fenimore (1978). URA patterns have dimensions of  $r$  by  $s$ , where  $r$  and  $s$  are prime numbers and  $r-s$  equals 2. In the preferred implementation of Fenimore and Cannon (1978), the mask consists of a 2 by 2 mosaic of a basic URA pattern; this insures that each point within the field-of-view contributes a complete cycle of the URA to the detector response. The opaque ( $A=0$ ) and transparent ( $A=1$ ) elements are determined from the following algorithm. Let  $A(i,j) = A(I,J)$ , where  $I = \text{mod}_r i$  and  $J = \text{mod}_s j$ . Then,



$$\begin{aligned}
 A(I,J) &= 0 \text{ if } I = 0, \\
 &= 1 \text{ if } J = 0, I \neq 0, \\
 &= 1 \text{ if } C_r(I) C_s(J) = 1, \\
 &= 0 \text{ otherwise}
 \end{aligned} \tag{II.6}$$

where

$$\begin{aligned}
 C_r(I) &= 1 \text{ if there exists an integer } x, 1 \leq x < r \\
 &\quad \text{such that } I = \text{mod}_r x^2 \\
 &= -1 \text{ otherwise.}
 \end{aligned} \tag{II.7}$$

Fenimore and Cannon (1978) also introduced the "balanced correlation method" of post-processing in which  $G$  is defined (in terms of discrete elements) as,

$$\begin{aligned}
 G(i,j) &= 1 \quad \text{if } A(i,j) = 1 \\
 &= -\rho / (1-\rho) \quad \text{if } A(i,j) = 0
 \end{aligned} \tag{II.8}$$

where  $\rho$  is the fraction of open elements in the mask pattern. (An alternative definition for  $G$  is given by Fenimore 1978.) For a URA pattern composed of  $N (= r \times s)$  elements,

$$\rho = (N + 1) / 2N \tag{II.9}$$

Combining this definition of  $G$  with the image reconstruction (eq. II.2b), one can see that each image element can be thought of as a sum of the measured counts in  $\rho N$  detectors ("source") minus the normalized sum of measured counts in the remaining  $(1-\rho)N$  detectors ("background"). Alternatively, one can note that for a source located in the center of an image element,  $\rho N$  detectors will be exposed to the source, while  $(1-\rho)N$  detectors will be blocked from the source by opaque mask elements.

Using these definitions of  $A$  and  $G$ , the point-spread-function (i.e.,  $A \otimes G$ ) is a delta function with flat, zero-level sidelobes. Therefore, a URA imaging system provides the desired capability of accurately reproducing the original source distribution without the introduction of any imaging artifacts. These particular advantages of a URA system were demonstrated by Fenimore *et al.* (1979). They used a mask based on a 137 X 139 URA pattern to obtain optical images of a laser driven compression of a Deuterium-filled glass microballoon at the Los Alamos National Laboratory. The resulting images clearly demonstrate the capabilities of a URA imaging system. For these reasons, a URA pattern was chosen for use in the present experiment.

### Imaging Statistics

In order to understand some of the practical concerns associated with coded aperture imaging, it is first useful to look at the statistics of the imaging process. In the following discussion we assume that the instrumental background is uniformly distributed across the detection plane. Let us also restrict ourselves to the case of discrete-element arrays; equation (II.2b) applies in this case,

$$S'(i,j) = \sum_{k=1}^K \sum_{l=1}^L P(k,l) G(i+k,j+l) \quad (\text{II.2b})$$

What we wish to determine is the variance of a given image element,  $S'(i,j)$ . Let us define this variance to be  $\sigma_S^2(i,j)$ . As can be seen in equation (II.2b), each reproduced image element is a sum of terms of the form  $p \times g$ , where  $p$  represents  $P(k,l)$  and  $g$  represents  $G(i+k,j+l)$ . Noting that these quantities are uncorrelated, the estimated error,  $\Delta(pg)$ , in each term of the summation is obtained from,

$$\left[ \frac{\Delta(pg)}{pg} \right]^2 = \left[ \frac{\Delta p}{p} \right]^2 + \left[ \frac{\Delta g}{g} \right]^2 \quad (\text{II.10})$$

Since the elements of the post-processing array ( $G$ ) are constants, the second term on the right-hand side of this expression is zero. The estimated error in each term then reduces to,

$$[\Delta(pg)]^2 = (\Delta p)^2 g^2 \quad (\text{II.11})$$

The variance of a given image element can now be derived from equation II.2b using standard propagation-of-error techniques (e.g., Bevington 1969). The result of such a calculation is given by,

$$\sigma_S^2(i,j) = \sum_{k=1}^K \sum_{l=1}^L \sigma_p^2(k,l) G^2(i+k,j+l) \quad (\text{II.12})$$

Assuming Poisson counting statistics,  $\sigma_p^2 = P(k,l)$ , we can rewrite equation (II.12) as,

$$\sigma_S^2(i,j) = \sum_{k=1}^K \sum_{l=1}^L P(k,l) G^2(i+k,j+l) \quad (\text{II.13})$$

We note here that if the fraction of open elements in the mask ( $\rho$ ) is equal to 0.5, all  $G^2$  elements are equal to 1, and the summations reduce to the sum of all of the counts registered in the detection plane (Fenimore 1978). The net result is,

$$\sigma_S^2(i,j) = \sum_{k=1}^K \sum_{l=1}^L P(k,l) = P_{\text{TOT}} \quad (\text{II.14})$$

where  $P_{\text{TOT}}$  represents the total number of detected counts. This expression then represents the best possible statistical precision for a coded aperture image. In practice, this is difficult to obtain (even if  $\rho$  is equal to 0.5) due to the presence of a nonuniform background distributed across the detection plane.

### Background Systematics

A major problem which can exist for any coded-aperture instrument is the presence of a (systematically) nonuniform background across the position-sensitive detection plane. In gamma-ray astronomy, the detector background arises from a number of sources, including diffuse cosmic gamma radiation, atmospheric gamma-rays, activation of the detector and surrounding material by protons and neutrons, and by natural radioactivity. Background nonuniformities may arise due to variations in the relative shielding within the detection plane, variations in photomultiplier tube gains, or, in the case of discrete detection elements, intrinsic differences among the individual detectors. Such nonuniformities (or *background systematics*) introduce nonstatistical noise into the reproduced image via the background term of equation (II.5). (One can think of this problem in terms of a fixed noise pattern within the field-of-view.) In many cases, the resulting image degradation cannot be tolerated and some method of eliminating (or at least reducing) the effects of these background systematics is required. For gamma-ray astronomy, the problem of

background systematics is especially acute because one normally deals with statistics which are background-dominated (i.e.,  $S \ll B$ ), so that even small relative background variations can prove detrimental.

In order to investigate more closely the problem of background systematics, let us look at the case of a field containing no sources, i.e., pure background. This is quite appropriate, since it is the background variations which create the systematics image noise; variations of source counts within the detection plane result in the reproduction of the actual source image. Let us define the response of a given detector by some factor, which we will call a *systematics factor* ( $\epsilon$ ), times the average background within the array ( $B_{ave}$ ). More specifically,

$$B(k,l) = \epsilon(k,l) B_{ave} \quad (\text{II.15a})$$

Furthermore, let us call  $\Delta\epsilon(k,l)$  the deviation of  $\epsilon$  from unity, so that equation (II.15a) can also be written as,

$$B(k,l) = \{1 + \Delta\epsilon(k,l)\} B_{ave} \quad (\text{II.15b})$$

Substituting  $B(k,l)$  for  $P(k,l)$  in equation (II.2b), we obtain,

$$S'(i,j) = \sum_{k=1}^K \sum_{l=1}^L B_{ave} G(i+k,j+l) + \sum_{k=1}^K \sum_{l=1}^L B_{ave} \Delta\epsilon(k,l) G(i+k,j+l) \quad (\text{II.16})$$

The first term in the above expression is zero, because the sum of all the  $G$  factors is defined (by the balanced correlation procedure) to be zero. Thus,

$$S'(i,j) = B_{ave} \sum_{k=1}^K \sum_{l=1}^L \Delta\epsilon(k,l) G(i+k,j+l) \quad (\text{II.17})$$

In general, this expression is non-zero and, in fact, represents the image noise created by the background systematics. Also, by inspection, it is apparent that the systematics noise is proportional to the variations in the relative background rates (via the  $\Delta\epsilon$ ). Based on data from the DGT experiment obtained at float altitude, it has been determined that the values of

$\Delta\epsilon$  range roughly between  $\pm 0.15$ . Hence, the magnitude of the individual terms in equation (II.17) are approximately 10-15% of the average background per detector.

In order to deal with this problem, two procedures have been developed. Both approaches depend on the assumption that the relative background rates do not vary with time. The first procedure uses an *antimask* to cancel out the effects of nonuniform background rates. The second approach involves the direct evaluation of the *relative* background rates of the detector elements within the detection plane and the subsequent correction of the detector count rates.

**Mask-Antimask Procedure.** The antimask approach produces two separate images. The first image is obtained with the initial mask pattern. A second image is then obtained with the antimask pattern using identical observational parameters (i.e., the same exposure time and pointing aspect). The antimask pattern is the complement of the mask pattern, i.e., it is the same pattern, but with the transparent and opaque elements interchanged. The (systematics) noise pattern in the antimask image is therefore the same as that obtained with the mask pattern, except that the "polarity" of the pattern is inverted. The direct addition of these two images cancels out the noise pattern. The resulting image suffers from statistical noise only.

We can show this property explicitly by first noting that the post-processing elements for the antimask are given by,

$$\begin{aligned} G_{AM}(i,j) &= \rho / (1 - \rho) & \text{if } A_{AM}(i,j) = 1 \\ &= -1 & \text{if } A_{AM}(i,j) = 0 \end{aligned} \quad (\text{II.18})$$

where  $\rho$  refers to the fraction of open elements in the *mask*. The normalization, as defined above, assures that both the mask and antimask reproduce any source distribution at the same intensity. More importantly, however, these post-processing elements are related to those of the mask by the simple relation,

$$G_{AM}(i,j) = -G_M(i,j) \quad (\text{II.19})$$

Using equations (II.15) and (II.2b), we can write down the explicit expression for the sum of the mask and antimask images as,

$$S'_{AM}(i,j) + S'_M(i,j) = \sum_{k=1}^K \sum_{l=1}^L \epsilon(k,l) B_{ave} \{G_{AM}(i+k,j+l) + G_M(i+k,j+l)\} \quad (II.20)$$

Here, we have once again assumed a pure background image. By comparison with equation (II.19), it can be seen that the quantity in brackets is equal to zero.

The effectiveness of the antimask procedure has been evaluated using both computer simulations and laboratory testing (McConnell *et al.* 1982). These tests have clearly demonstrated that the antimask is a viable approach for dealing with the background systematics problem.

The implementation of such a procedure on a balloon-borne experiment is not without its difficulties. Operating in the float-altitude environment of a balloon experiment is considerably more difficult than laboratory testing. The major problems are primarily mechanical in nature. Specifically,

- Some suitable means of changing between mask and antimask must be developed. For low-energy gamma-rays, these masks are necessarily very massive and the manipulation of such masks can be a non-trivial mechanical problem. One also needs to be concerned with the loss of effective instrumental livetime during the changeover procedure. This implies that the change should not only be smooth, but also as fast as possible. One possible solution to this problem is the use of a rotating hexagonal URA pattern; such patterns can be switched between mask and antimask by a 60° rotation of the mask pattern (Cook, et al., 1984).
- The need to maintain a fixed pointing aspect throughout the course of an image cycle (defined as one mask and one antimask image). By this we mean not just the pointing direction, but also the orientation of the FOV with respect to the sky. An equatorial mounting is therefore preferable to eliminate rotation of the FOV. It

should be stressed that knowing the aspect of the detector is not enough in this case (as it is for most gamma-ray payloads); it is necessary for the pointing to be fixed to within the spatial resolution of the imaging process throughout the entire imaging cycle. If this is not the case, then the cancellation of the mask and antimask image noise patterns will occur only by offsetting the imaged source distributions.

- Any changes in the mass distribution around the detector (especially in the forward aperture) may result in a change of the background distribution across the detection plane. Such an effect would reduce the antimask effectiveness.

The difficulty of mechanically implementing the antimask scheme on the present UNH gondola has led to the development of an alternative approach which eliminates the necessity of an antimask and associated mechanical requirements.

**Evaluation of Relative Background Rates.** A second technique for minimizing the effects of the background systematics involves the direct measurement of the *relative* background rates of the individual detector elements. If the relative background rates are constant in time, then this can be done to arbitrary precision, depending only on counting statistics. Once the systematics factors have been determined, then any set of imaging data can be corrected in order to eliminate the effects of the systematics. One might think of this as an evaluation of the noise pattern. Note that only the *pattern* need be determined. The intensity (or normalization) of the pattern is determined directly from a measurement of the background rate, which, by the nature of the coded-aperture process, is known at all times.

The first step in the procedure is to determine the systematic factors as defined by equation (II.15). This requires a collection of detector data. Ideally, this data would be pure background, i.e., it would contain no source counts. For a large field-of-view instrument, however, it may be difficult to eliminate this possibility. Fortunately, under some circumstances, it is feasible to determine the systematics even in the presence of source emission. This is possible in the background-dominated environment normally

encountered in gamma-ray astronomy experiments in which the source signal is much less than the background signal (e.g.,  $S/B < 2\%$ ). In this case, the *drift scan* observational procedure would be employed. The drift scan method allows the source under observation to drift through several image elements within the field-of-view. Hence, any source counts which are detected during the accumulation period would be randomly distributed throughout the detection plane. If the accumulation of the *systematics data* are made without correction for the aspect of the detector (i.e., the orientation of the field-of-view with respect to the source distribution), then the source counts constitute a nearly uniform DC response of the detection plane. Furthermore, given that source-to-background ratios for celestial gamma-ray sources in this energy range are generally less than 2%, we can, to first order, neglect the effects of any source contribution to the measurement of the background systematics.

The systematics data is accumulated for a time  $T_{sys}$ . From these data, the systematics factors are derived using equation (II.15). The variance associated with each systematic factor  $[\sigma_\epsilon(k,l)]$  is derived from the expression,

$$\left[ \frac{Q_\epsilon(k,l)}{\epsilon(k,l)} \right]^2 = \left[ \frac{\sigma_B(k,l)}{B(k,l)} \right]^2 + \left[ \frac{\sigma_{B_{ave}}}{B_{ave}} \right]^2 \quad (II.21)$$

which, upon substitution, reduces to,

$$\sigma_\epsilon^2(k,l) = \epsilon^2(k,l) \left( \frac{1}{B(k,l)} + \frac{1}{NB_{ave}} \right) \quad (II.22)$$

where  $N$  is defined as the number of elements in the detection plane (which is equivalent to the number of elements in the basic URA pattern).

Let us now consider a second set of data (*source data*) collected over a time  $T_{obs}$ . The number of counts measured by detector  $(k,l)$  is given by  $P(k,l)$ . These counts will, in general, consist of both a background component  $[b(k,l)]$  and a source component  $[s(k,l)]$ . The systematic factors can now be used to eliminate the systematics noise from this second



set of data. In order to accomplish this, we define a modified detector count total ( $P'(k,l)$ ) as,

$$P'(k,l) = \frac{P(k,l)}{\epsilon(k,l)} = b_{ave} + \frac{s(k,l)}{\epsilon(k,l)} \quad (II.23)$$

The correction process results in a normalized background term along with some modified source term. Since the background terms have been normalized to the same value, the effects of the background systematics have been suppressed. The important question is whether the modified source terms effect the total imaging response to the source. It is important to note that it is the *sum* of these source terms that represent the total response of the source. Since the average of the  $\epsilon(k,l)$  is 1, it can be expected that the sum of all of the source terms (summed over N detectors) is unchanged. Hence, we conclude that this procedure does not effect the source imaging results.

Although the above procedure succeeds in eliminating the image noise resulting from nonuniform background rates, the act of correcting the individual detector count sums results in a loss of statistical information relative to the ideal imaging case (eq. II.14). In order to ascertain how much information is lost, we first note that the variance associated with the determination of  $P'(k,l)$  is given by,

$$\sigma_{P'}^2(k,l) = \frac{1}{\epsilon^2(k,l)} \left\{ P(k,l) + P^2(k,l) \left( \frac{1}{B(k,l)} + \frac{1}{NB_{ave}} \right) \right\} \quad (II.24)$$

We can now proceed to derive an expression for the variance of image element (i,j) which results from using these modified detector data. The variance of the (i,j)<sup>th</sup> element of the reconstructed image (S') can be derived by substituting equation (II.24) for  $\sigma_{P'}^2(k,l)$  in equation (II.12). The following result can then be derived,

$$\sigma_{P'}^2(i,j) = \sum_{k=1}^K \sum_{l=1}^L \frac{G^2(i+k,j+l)}{\epsilon^2(k,l)} \left\{ P(k,l) + P^2(k,l) \left( \frac{1}{B(k,l)} + \frac{1}{NB_{ave}} \right) \right\} \quad (II.25)$$

In order to gain some insight into the meaning of this expression, we can make a number of simplifying approximations; namely,  $G^2 \approx 1$ ,  $\epsilon^2 \approx 1$ ,  $B(k,l) \approx B_{ave}$ ,  $P(k,l) \approx P_{ave}$ , and

$$\frac{P(k,l)}{B(k,l)} \approx \frac{P_{ave}}{B_{ave}} \approx \frac{T_{obs}}{T_{sys}} \quad (\text{II.26})$$

Using these approximations, we can write the average variance of the resulting image elements as,

$$\sigma^2 = P_{TOT} \left\{ 1 + \left( 1 + \frac{1}{N} \right) \frac{T_{obs}}{T_{sys}} \right\} \quad (\text{II.27a})$$

$$= P_{TOT} \left\{ 1 + 1.029 \frac{T_{obs}}{T_{sys}} \right\} \quad (\text{II.27b})$$

where  $P_{TOT}$  represents the total number of counts in the detection plane. This result can be directly compared to the ideal case (represented by eq. II.14) in which the average variance (which we shall call  $\sigma_o^2$ ) is given by  $\sigma_o^2 = P_{TOT}$ . The factor in parenthesis in equation (II.27) represents the loss of information resulting from the systematics correction procedure. The amount of information which is lost can be reduced by requiring  $T_{obs} \ll T_{sys}$ . From equation (II.27), it can be seen that the value of  $\sigma^2$  approaches the ideal value of  $P_{TOT}$  as  $T_{obs}/T_{sys}$  tends toward small values.

The preceding approach to the background systematics problem relies on the assumption that the systematics correction factors (the  $\epsilon$  factors in eq. II.15) remain constant in time. Equation (II.27) represents such an ideal situation. The available flight data from the DGT experiment suggests that, by and large, these factors remain constant. At some level, however, one expects to see variations of a nonstatistical nature. Analysis of the flight data from this experiment indicate that these variations take place on the order of 0.1% of the background level. These variations are not sufficiently large to influence the successful operation of the DGT experiment. The in-flight efficacy of this correction procedure will be discussed in Chapter IV.

### Partial Mask Coding

In a coded aperture telescope without a complete side shield, there exists a region in the sky surrounding the field-of-view (FOV) in which a source casts only a partial shadow of the mask onto the detection plane. (This effect is also sometimes referred to as vignetting, since it is analogous to vignetting in classical optics.) This results in spurious features in the reproduced image which are reproduced at an intensity corresponding to the true source reduced in proportion to the percentage of encoded data. The region of the sky in which this partial coding takes place is known as the "partially-coded" field-of-view (FOV). This is in contrast to the "fully-coded" FOV, which is the region of the sky in which a source will cast a complete shadow of the mask onto the detection plane. The size of the fully-coded (or "legal") FOV measures  $(A_x - D_x)/f$  by  $(A_y - D_y)/f$  radians where  $A_x, A_y$  are the dimensions of the aperture and  $D_x, D_y$  are the dimensions of the detection plane (Fenimore 1987). Obviously, the partially-coded FOV can be a problem, especially when observing a region of the sky (e.g., the galactic center) where there exists a large number of potential sources.

In principle, strong sources which are partially coded in this manner can be recognized by a direct examination of the data. Maggioli *et al.* (1984) discuss a means of evaluating, for any intensity source, whether a reproduced source arises from partial or complete coding of the source flux. Another simple method of partially coded source recognition is to allow the FOV to drift through the source field. Any partially coded sources would be recognizable by a change in either its reproduced intensity and/or its measured location (Charalambous *et al.* 1984). This, however, would require sufficient source statistics in the imaging process. More recently, Fenimore (1987) has discussed a technique referred to as *URA-tagging*, which allows one to reconstruct a spectrum for a given point in the field-of-view. This procedure avoids the problem of partially-coded images by considering only the fully-coded information for the given image element.

## The Directional Gamma-Ray Telescope

The original design of the Directional Gamma-ray Telescope (DGT) was motivated by the desire to obtain information on the spatial distribution of the galactic center 0.511 MeV positron annihilation radiation. The instrument's properties were therefore chosen so that its performance would be optimized at 0.511 MeV. The DGT design was based very heavily on a previous University of New Hampshire balloon experiment known as the Large Gamma-ray Telescope (LGT; see Dunphy *et al.* 1981). The detection properties of the DGT experiment are listed in Table II-1. A side view schematic is shown in Figure II-2. Here we see the two primary elements of the imaging system - the detector array and the coded mask. In addition to these components, however, there are several auxiliary components of the experiment, including the gondola structure and the Ground Station Electronics (GSE). In this chapter, we also discuss the background environment of the experiment and its sensitivity to source flux levels (both narrow line and continuum).

**Table II-1**  
**DETECTION PROPERTIES OF THE DGT**

PARAMETER	VALUE
Energy Range	160 keV - 9.3 MeV
Detection Area (geometric)	709.4 cm <sup>2</sup>
Full-energy Peak Efficiency	59% at 662 keV
Energy Resolution	19% FWHM at 662 keV
Legal Field-of-View	22.8° by 15.2°
Image pixel size	3.8°
Temporal resolution	~2 ms
Line sensitivity (1 $\sigma$ )	$< 1 \times 10^{-3} \text{ cm}^{-2} \text{ s}^{-1}$
Continuum sensitivity (1 $\sigma$ )	$< 1 \times 10^{-5} \text{ cm}^{-2} \text{ s}^{-1} \text{ keV}^{-1}$

### The Detector Array and Associated Electronics

One of the major design factors for a coded aperture telescope is the ability to isolate the location of a photon interaction in the detection plane. A discrete element array of scintillation crystals was chosen for the DGT as an effective means of achieving an

acceptable level of positional information. By using individual crystal elements, one can unambiguously locate the interaction site to a particular element. Hence, the positional resolution is roughly equivalent to the size of the each element. One advantage of a discrete-element array is the fact that the positional resolution is not a function of energy. This implies that the imaging properties (in terms of the point-spread-function) are, to first order, independent of energy.

The photon detection plane of the DGT is composed of a 7 by 5 rectangular array of individual bismuth germanate ( $\text{Bi}_4\text{Ge}_3\text{O}_{12}$ ) scintillation crystals. Each BGO crystal is a right-circular cylinder 5.1 cm in diameter by 2 cm thick. The detectors are arranged with a center-to-center spacing of 5.6 cm. A 2" EMI 9956B photomultiplier tube (PMT) is used to view each crystal. High-voltage DC to DC converters are mounted directly onto each photomultiplier tube base, thus forming an integral detector unit. Each high voltage converter is commandable (in 256 incremental steps) over a 300 volt range and incorporated into a  $^{60}\text{Co}$  gain stabilization system which is described below.

Since the imaging process requires that the response of the detectors be as uniform as possible, each individual detector in the array is continuously gain stabilized using an active  $^{60}\text{Co}$  calibration scheme. This procedure (Gleske and Forrest 1980) is analogous to that used on the Solar Maximum Mission Gamma-Ray Spectrometer (SMM-GRS; Forrest *et al.* 1980). Each decay event of  $^{60}\text{Co}$  produces coincident gamma-rays at energies of 1.17 and 1.33 MeV along with an associated  $\beta^-$  particle. The calibration scheme makes effective use of the  $\beta^-$  particle to electronically tag each event. Tagging signals originate from the decay of  $^{60}\text{Co}$  in the form of neutron-activated cobalt oxylate pellets encapsulated within four small (10 mm diameter by 7 mm thick) plastic scintillator "buttons." The buttons are mounted on individual 1.3 cm Hamamatsu R-647 photomultiplier tubes and placed equidistantly around the forward aperture of the detector array. The  $\beta^-$  particles originating in each decay event are detected in the plastic scintillator with an efficiency >95%. Events which are detected in the central array in coincidence with a  $^{60}\text{Co}$  decay are

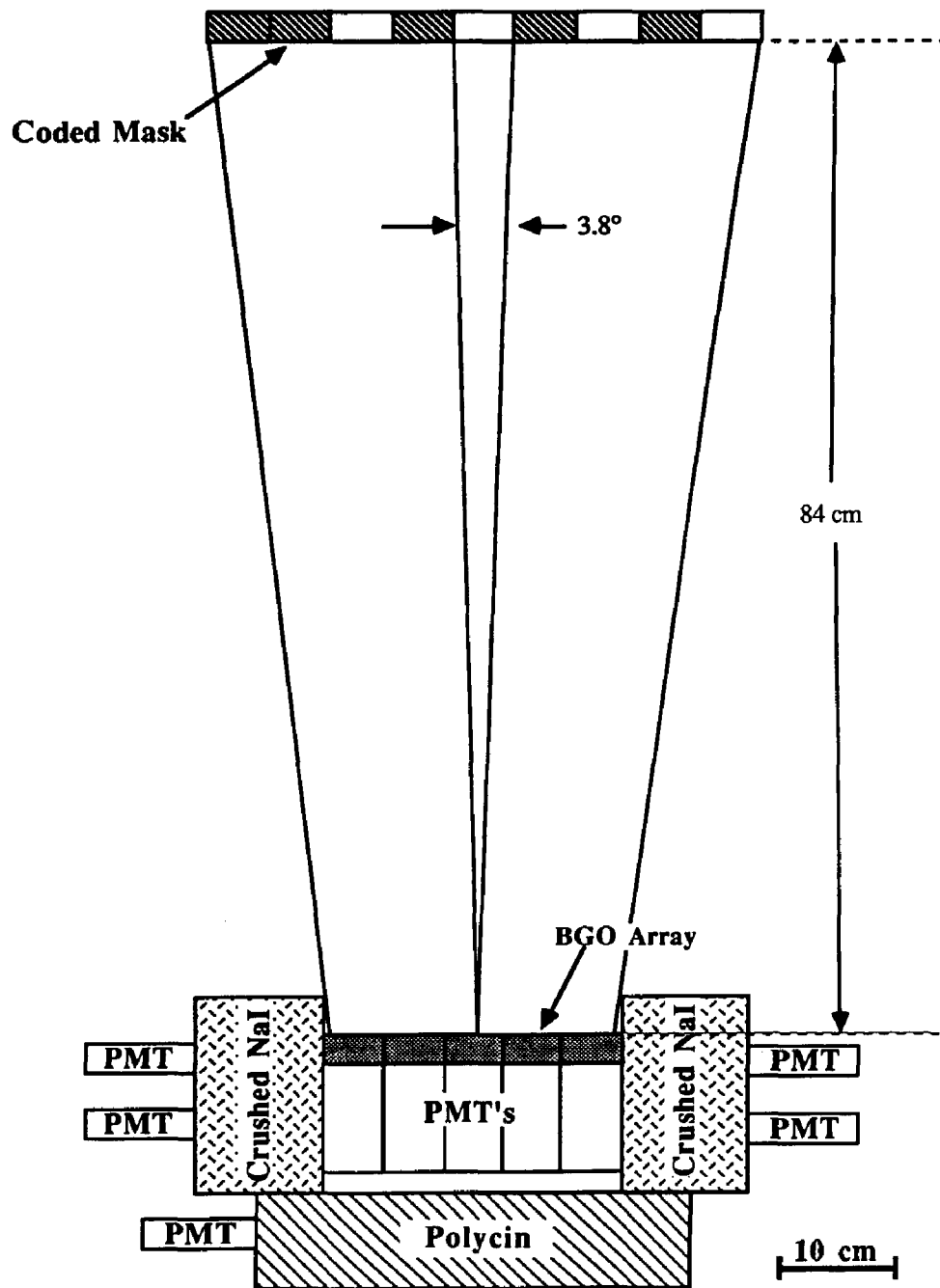


**FIGURE II-2:** Cross-sectional view of the Directional Gamma-ray Telescope (DGT).

electronically tagged as "in-flight calibration" (IFC) events. A given detector receives from 3 to 6 IFC events per second. Two broad pulse height windows (each covering about 30% of the total  $^{60}\text{Co}$  source spectrum) are set up in the logic electronics of each detector so that, when at the proper gain, each window will show the same  $^{60}\text{Co}$  counting rate. For each IFC event, the corresponding detector's high voltage is either incremented (if the pulse height falls in the lower window), decremented (if the pulse height falls in the upper window) or left unchanged (if the pulse height falls into neither window). Two slew modes are available. A "fast slew" mode uses larger high-voltage increments and is used when the detectors are turned on in order to rapidly reach a stable gain. The normal mode of operation uses a "slow slew" mode which involves much smaller high-voltage increments which are useful in maintaining the detector gain. A sample  $^{60}\text{Co}$  calibration spectrum, accumulated with the entire gain-stabilized array, is shown in Figure II-3.

The measured energy resolution of the gain-stabilized array is well-described by a power law of the form  $\Delta E/E = .158 (E_{\text{MeV}})^{-0.397}$ . The full energy peak efficiency of the BGO array has been determined using the photofraction measurements for a 2" by 2 cm BGO detector given by Dunphy and Forrest (1985). The photofraction ( $P_o$ ) is related to the full energy peak efficiency ( $\epsilon_p$ , in  $\text{cm}^2$ ) by the relation,

$$\epsilon_p = P_o \epsilon_T A \quad (\text{II.28})$$

where  $\epsilon_T$  is the total interaction efficiency and  $A$  is the total geometric area of the array. (More information on the response properties of the BGO array can be found in Appendix D.) BGO scintillation material was chosen in preference to the more traditional Alkali Halide detectors because of its higher sensitivity per unit volume. Since the background level of a scintillation material is, in general, proportional to its volume, the use of BGO provides a higher signal-to-background for an equivalent volume of detector material.

The detector array is mounted in a well-type NaI anticoincidence shield composed of 12 individual segments. Six segments make up the side shielding of the well, as shown in Figure II-4. Each of these six segments consist of a housing of 1/8" aluminum filled

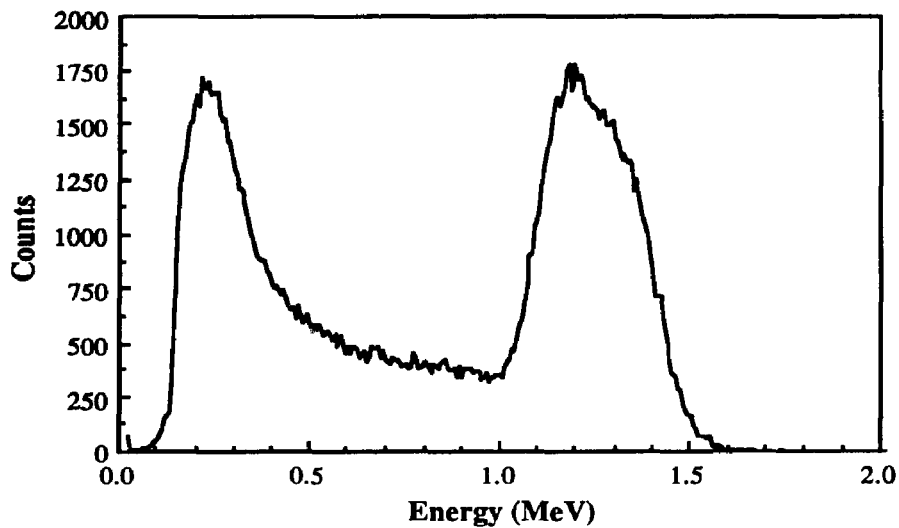


FIGURE II-3: A sample  $^{60}\text{Co}$  in-flight-calibration (IFC) spectrum obtained with the total integrated BGO array. Note that the two lines at 1.17 MeV and 1.33 MeV are not resolved by the BGO detectors. The detector threshold level is at 0.16 MeV.

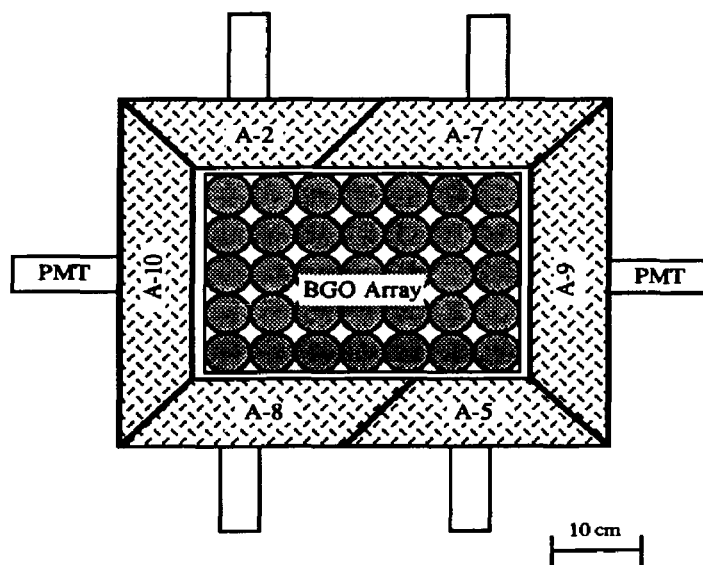


FIGURE II-4: A schematic view of the side shield arrangement in the DGT. This view is that seen from the position of the mask looking down on the detector array. The shield references are UNH designations.



with small (15-50 cm<sup>3</sup>) pieces of NaI scintillation crystals which are immersed in silicon oil. The silicon oil provides for optical transmission of the light produced in the NaI(Tl). Each of these side segments is viewed by two 1-1/2" RCA C70132D photomultiplier tubes with hemispherical photocathodes which are immersed in the silicon oil. These containers are 10 cm deep with a NaI(Tl) packing fraction of 70-80%, providing an effective NaI(Tl) thickness of 7.5 cm. The bottom of the anticoincidence well is comprised of 6 NaI Polycin™ bars each of length 36cm and 10 cm by 10 cm in cross section. Each bar is viewed by a single 1 1/2" photomultiplier at one end. The threshold level of the Polycin™ units are set at a level corresponding to a minimum energy deposition of ~250 keV. Due to the extremely poor energy resolution of the crushed NaI(Tl) segments the thresholds on these units could not be measured directly. Consequently, the thresholds for the side shields were set to provide the same counting rate per unit mass as the Polycin™ detectors. The entire anticoincidence well defines a forward opening aperture of ~120° FWHM.

Events which are detected in the central array are of two types. The so-called "main channel" (MC) events are those which are not associated with a <sup>60</sup>Co decay. These events are analyzed only if 1) they are associated with a single BGO detector (in order to insure the localization of the event and to minimize livetime losses due to telemetry limitations), 2) they are not coincident with a signal from the anticoincidence shielding, and 3) they lie within some predetermined energy-loss (i.e., voltage) range. As discussed previously, events which are associated with a <sup>60</sup>Co decay are termed IFC events. These events are analyzed the same way as MC events except that the shield veto signals are ignored.

A functional block diagram of the detector electronics is shown in Figure II-5. Anode signals from each detector's PMT are sent to individual preamplifier-discriminator circuits. The discriminator generates a logic pulse which is used in testing the various coincidence requirements for the event. The resolving time of the coincidence circuitry is 1.7μsec. The preamp circuitry also generates detector identification bits. Outputs from each of the 35 preamp circuits are sent to a common shaping amplifier. The output of the

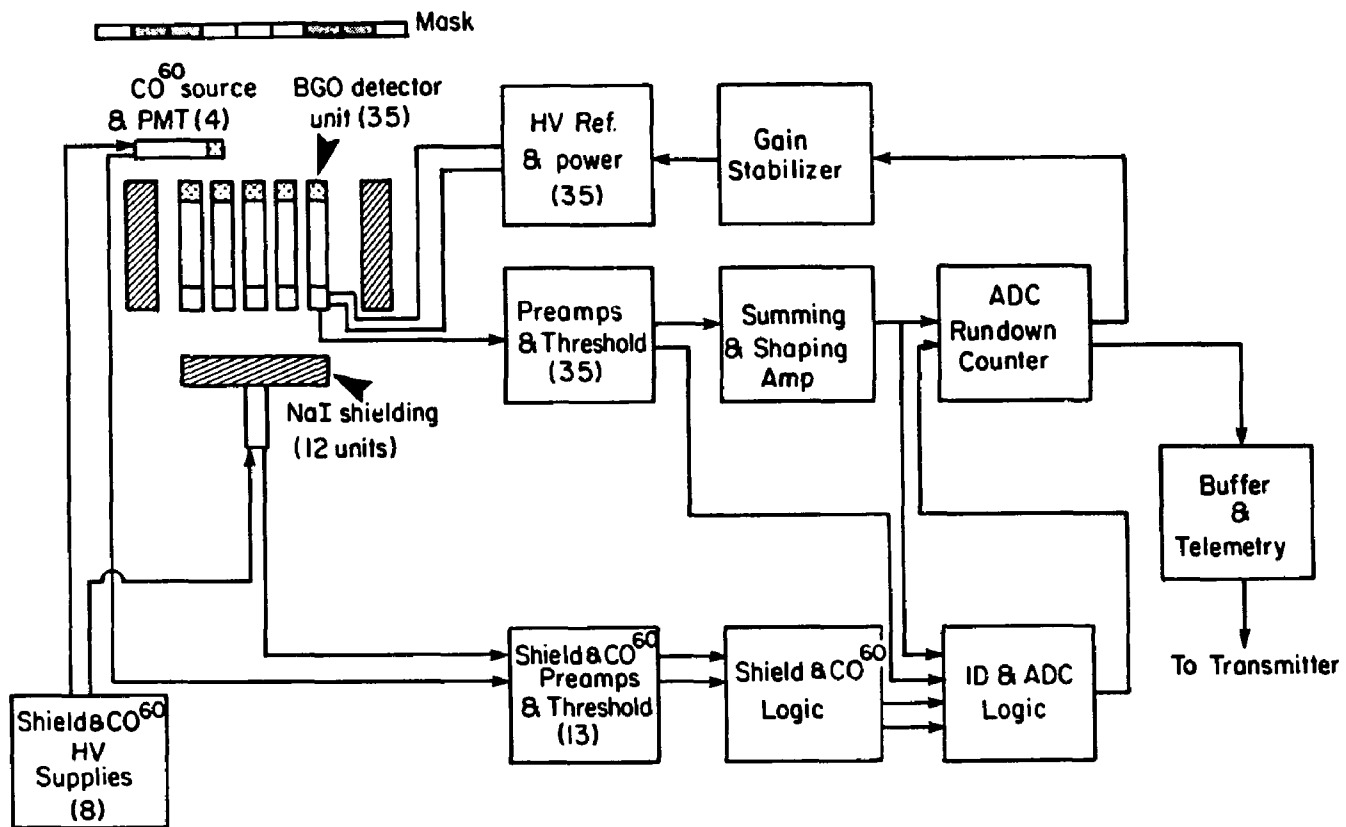
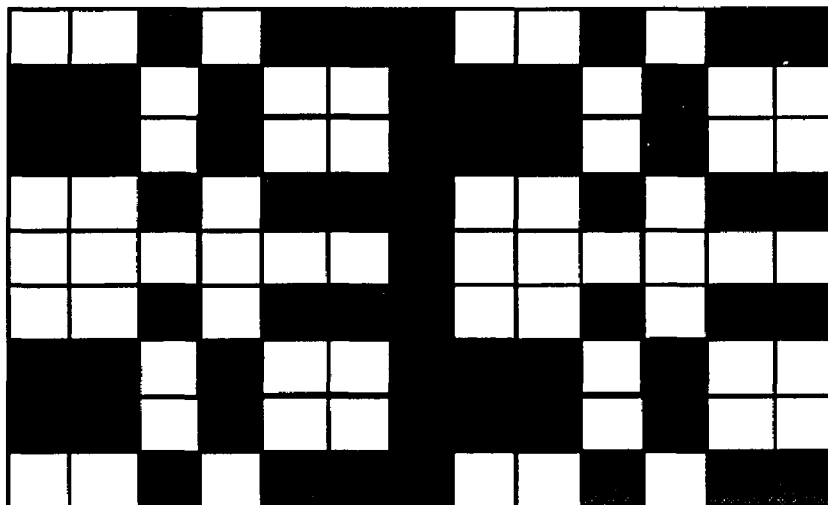


FIGURE II-5: Functional block diagram of the DGT detector electronics.

shaping amplifier is a bipolar pulse with an amplitude of from 0 to 10 volts. The amplitude of the leading (positive) lobe is used to insure that the event energy-loss lies within the predetermined range (160 keV to ~9.3 MeV). The negative lobe of the amplifier output is used for pulse height analysis with a 10-bit ADC rundown counter. The resulting 1024 channel pulse-height spectrum covers the energy range of 160 keV - 6.8 MeV, with a single channel width of 6.62 keV. Channel 1024 is an overflow channel which contains all events from the channel 1024 threshold (~6.8 MeV) up to the main channel maximum threshold (~9.3 MeV).

### **The Coded Mask**

The coded mask, composed of an array of opaque and transparent elements, has outside dimensions of 72.8 cm by 50.4 cm. Each opaque element of the array is composed of lead and measures 5.6 cm square by 1.9 cm thick. (Note that 5.6 cm corresponds to the center-to-center spacing of the detector elements.) The lead thickness is sufficient to attenuate 97% of the flux at 0.5 MeV and 60% at the attenuation minimum near 3 MeV (see Appendix D). The lead blocks are arranged on horizontal rails of 0.5mm aluminum and sandwiched between 0.5 mm thick sheets of aluminum. This provides for a rigid mask assembly with minimal absorption effects. The pattern of elements in the mask, shown in Figure II-6, is based on a 7 by 5 URA pattern ( $N = 35$  and  $\rho = 18/35 = 0.514$ ). The entire mask pattern of 9 by 13 elements is nearly a 2 by 2 repetition of the basic URA pattern. The separation between the mask and the detection plane is 84 cm. The solid angle subtended by a single element of the mask as seen from the detection plane dictates the solid angle of a single image element. For the DGT, each of the image elements measures  $3.8^\circ$  by  $3.8^\circ$ . The "nominal" field-of-view (i.e., that produced by a complete 2 by 2 cycle of the mask pattern) is an array of 7 by 5 image elements. For the DGT, this nominal field-of-view measures  $26.6^\circ$  by  $19.0^\circ$ . The lack of a complete 2 by 2 mask pattern, however, reduces the legal field-of-view down to  $22.8^\circ$  by  $15.2^\circ$ . The relationship between the nominal field-of-view and the legal field-of-view is shown in Figure II-7. The nominal



**FIGURE II-6:** Coded mask pattern used in the DGT. The outlined area near the center represents the basic URA pattern on which this mask is based. Each mask element is 5.6 cm by 5.6 cm in size. The shaded areas represent lead elements, each of which are 1.9 cm thick.

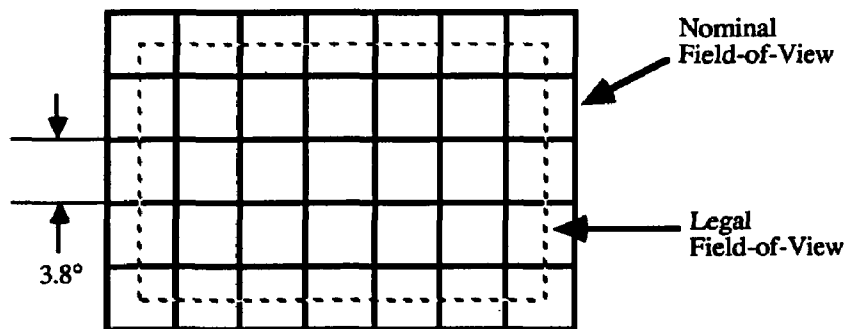


**FIGURE II-7:** The nominal and legal (or fully-coded) fields-of-view for the DGT. Note that the outer half-elements of the nominal field are not fully-coded. The partially-coded field-of-view extends outward from the legal field-of-view.

field is that reproduced by the image decoding procedure. Due to the fact that the field-of-view is centered on the detector symmetry axis, the outer elements of the decoded image are half in the legal field-of-view and half in the partially-coded field-of-view. For a source response in one of these outer elements, there exists an ambiguity as to whether or not the source is fully-coded. Only if the source location is known can this ambiguity be easily removed.

### **Gondola and Pointing System**

The main detector components (i.e., the BGO array, anticoincidence shielding and associated electronics) are contained within a 1/16" thick pressurized aluminum housing. The pressure inside this container is maintained at a minimum 5 psi during a balloon flight to reduce the potential of high voltage corona discharge. Temperature control within this container is maintained to within  $\pm 5^\circ$  of  $20^\circ$  C using foam insulation and internal heaters. Fans are also used to ensure the efficient removal of the internally-generated heat via convective airflow to the outer surface of the pressure vessel. Power for the experiment is provided by a stack of 100 lithium organic batteries having a total capacity of 200 amp-hours. Lithium organic batteries were chosen because of their high capacity (10 amp-hours at 200 mA) and small physical size. The average power consumption of the experiment is  $\sim 150$  W.

The pressurized container (or detector "can") is mounted onto a 0.75" thick support plate which, in turn, is mounted within the supporting arch on the gondola via a 1 1/2" horizontal shaft. This shaft also serves as the rotation axis of the central detectors. This mounting is such that the detector assembly can be moved independently in zenith angle over a range of  $0^\circ$  to  $85^\circ$  on either side of the supporting arch. The detector can is driven by a stepping motor in commandable increments. The mask is mounted, parallel to the detector, on a support arm which can be raised and lowered in elevation. In order to maintain a level gondola, a second (counterweight) arm is symmetrically mounted with respect to the mask arm and carries identical weight. Alignment of the mask with the

detector array is achieved by the use of infrared optical sensors. The zenith angles of the detector can and the mask/counterweight arms are determined with the use of calibrated potentiometers to an accuracy of  $\pm 0.25^\circ$ . The zenith reference is the local vertical and any offset of the gondola from level is determined by two precision inclinometers which measure pitch and yaw.

Azimuthal orientation of the experiment is obtained by setting an offset flux gate magnetometer to the desired azimuth and torquing an inertia wheel to null the magnetometer. The magnetometer angle is measured with a calibrated potentiometer to an accuracy of  $\pm 0.25^\circ$ . The inertia wheel drive signal is pulsed at a frequency determined by the offset angle and its rate of change. Due to both the effects of the balloon rotation and thermal (i.e., low-temperature) effects on the gondola support bearings, the experiment oscillates in azimuth about the magnetometer null point with an RMS amplitude of  $\sim 3.0^\circ$  (see Figure III-5). A second magnetometer, fixed with respect to the gondola, gives coarse verification of the pointing direction throughout the flight. The estimated uncertainty in the absolute pointing direction based on the pre-flight calibration is  $\pm 1^\circ$ .

Two sun sensors of different designs are used to periodically check the pointing zenith and azimuth during the daytime portion of the flight. Both of these sensors are mounted on the mask arm and require that they be pointed in the general direction of the sun in order to provide data. The first sensor had been used on previous UNH balloon flights of the LGT where pointing requirements were not as severe. This unit utilizes crossed photocells and requires a scanning observation in order to determine the sun's location to  $\pm 1^\circ$ . The second sun sensor was developed as a result of the increased pointing requirements of the DGT experiment. This detector is a two axis sensor, with each axis consisting of an independent unit. A thin slit placed above a photo-potentiometer comprises each unit. The photo-potentiometer consists of a resistive strip isolated from an adjacent conductive band by a thin layer of photo-resistive material. Light from the sun is collimated by the slit and falls on the photo-resistive material perpendicular to the photopot

axis, thus forming an electrical connection between the resistor and the conductor at that point. The impedance of the photopot is thus dependent on where the shaft of light intersects the plane of the photopot. Therefore, in principle, the impedance of the device will be a transcendental function of the sun angle. Two sun sensor units are mounted orthogonally to each other onto the mask support arm in order to measure both the sun's azimuth and zenith. The sensors are passive in that they only require that they be pointed to within  $\pm 15^\circ$  of the sun. This device can determine the pointing direction of the experiment to within 20 arc minutes.

The total gondola weight, including batteries, crash padding and NSBF electronics (telemetry) is 1735 pounds (790 kg). For Flight 1379-P (the subject of this thesis), a total of 600 pounds of ballast was carried for a total flight weight of 2435 pounds.

#### **Telemetry and Ground Station**

The telemetry rate of the DGT experiment is 25 kbits per second. These data are formatted into 25 bit data words, corresponding to a telemetry rate of 1000 words per second. Each word has the potential of containing the data for a single event in the central array (either main channel or IFC). The nominal event rate at float altitude over Texas is  $\sim 700 \text{ sec}^{-1}$  and the nominal livetime is 84%. Each data word includes 10 bits of detector pulse height information, six detector ID bits (three to define the row number and three to define the column number), a  $^{60}\text{Co}$  ID bit (to indicate whether the event is a calibration event or a main channel event), one bit for housekeeping information, and a parity bit. The data words are fed through a 32 word first-in-first-out (FIFO) buffer to decrease data losses from telemetry rate limitations. The data are transmitted on a Wide Band H channel in a biphasic-L format. During flight operations, the data are received by the NSBF ground equipment and fed directly into the Ground Station Electronics (GSE) and (simultaneously) recorded directly onto magnetic tape for later analysis.

Each 25-bit data word in the telemetry stream contains one bit of housekeeping data (or 1 bit every millisecond). This housekeeping information originates from many sources

within the experiment. This multiplexed (or MUX) data is in the form of 16-bit words, transmitted once every 16ms. The MUX data is organized into cycles consisting of eight major frames. Each major frame contains 8 MUX words. Every 125ms, a new major frame is begun and every second a MUX cycle is completed. The first word of each frame is always a MUX sync word which contains the number of that frame. This facilitates rapid resynchronization of the data stream in the event of momentary data loss. Critical pointing status bits are updated every 125ms. The livetime, pointing angles, inclinometer readings, sun sensor outputs and shield status bits are transmitted every second. Housekeeping information such as voltages, temperatures, pressures, shield rates, and detector rates are submultiplexed in the MUX data. The cycle time for this SUBMUX data is 32 seconds.

Data from the experiment can be directly interpreted by the GSE. The main component of the GSE is a custom-made computer system based on a 6502 microprocessor chip. This computer system uses a multi-tasking operating system for simultaneous data acquisition and display. The FORTH language is used to control data handling and display routines, many of which are, in turn, written in assembly language. As the telemetry data is fed into the GSE, the GSE hardware strips out the digital data and synchronizes onto the 25-bit data words. The multiplexed data (both MUX and SUBMUX) is also extracted by the GSE hardware. The multi-tasking ability of the GSE allows events to be accumulated into spectra and displayed on one terminal, while simultaneously showing the instrument pointing and housekeeping information on a second terminal. Accumulated data sets can also be transferred to an HP9825 desktop calculator which is used to produce hardcopy output of detector spectral and imaging data; this is especially useful during instrument calibration.

### **Instrumental Background**

Because of the low source fluxes and the high instrumental backgrounds typical of gamma-ray astronomy experiments, the minimum flux that can be measured is ultimately



limited by the level of the instrumental background. An understanding of the various background contributions is therefore essential in determining the limitations of the DGT design. The float-altitude background count rate of the DGT has been evaluated using semi-empirical and Monte-Carlo calculations. The details of these calculations are given in Owens *et al.* (1987); a summary of this work is given here for reference purposes. The results are shown in Figure II-8 in which we compare the calculated energy-loss spectrum at  $3 \text{ g cm}^{-2}$  with the experimentally determined spectrum. The typical uncertainty in these calculations is estimated to be  $\sim 30\%$ . The various contributions to the detector energy loss spectrum are described below.

**Atmospheric and cosmic diffuse flux.** This component is due to the atmospheric gamma-ray flux or the cosmic diffuse flux which enters the forward aperture of the experiment or which penetrates the anticoincidence shield undetected. (Any interactions between the incident photons and the shield must be such that the total energy loss is less than the shield threshold of 250 keV.) The large opening aperture of the DGT ( $\sim 120^\circ$ ) implies that this contribution will be important. The atmospheric gamma-ray flux and angular distribution used in the calculation were taken from Costa *et al.* (1984). The cosmic diffuse spectrum is that of Schönfelder *et al.* (1980).

**Neutron-induced components.** Neutrons interact with the detector and shield material to produce gamma-rays through the processes of capture or inelastic scattering. In the DGT, the neutron-induced background dominates the detector counting rate at energies  $> 2 \text{ MeV}$ . The principal contribution to the neutron induced counting rate arises from neutron interactions in the central array. In BGO, the contribution due to neutron capture reactions is approximately an order of magnitude smaller than that due to inelastic scattering and may, therefore, be neglected. Neutrons may also interact in the shield material to produce radioactive nuclei which subsequently decay by the emission of gamma-radiation. The main shield contribution arises from the reactions  $^{127}\text{I} (n,\gamma) ^{128}\text{I}$  and  $^{127}\text{I} (n,n') ^{128}\text{I}^*$ . The

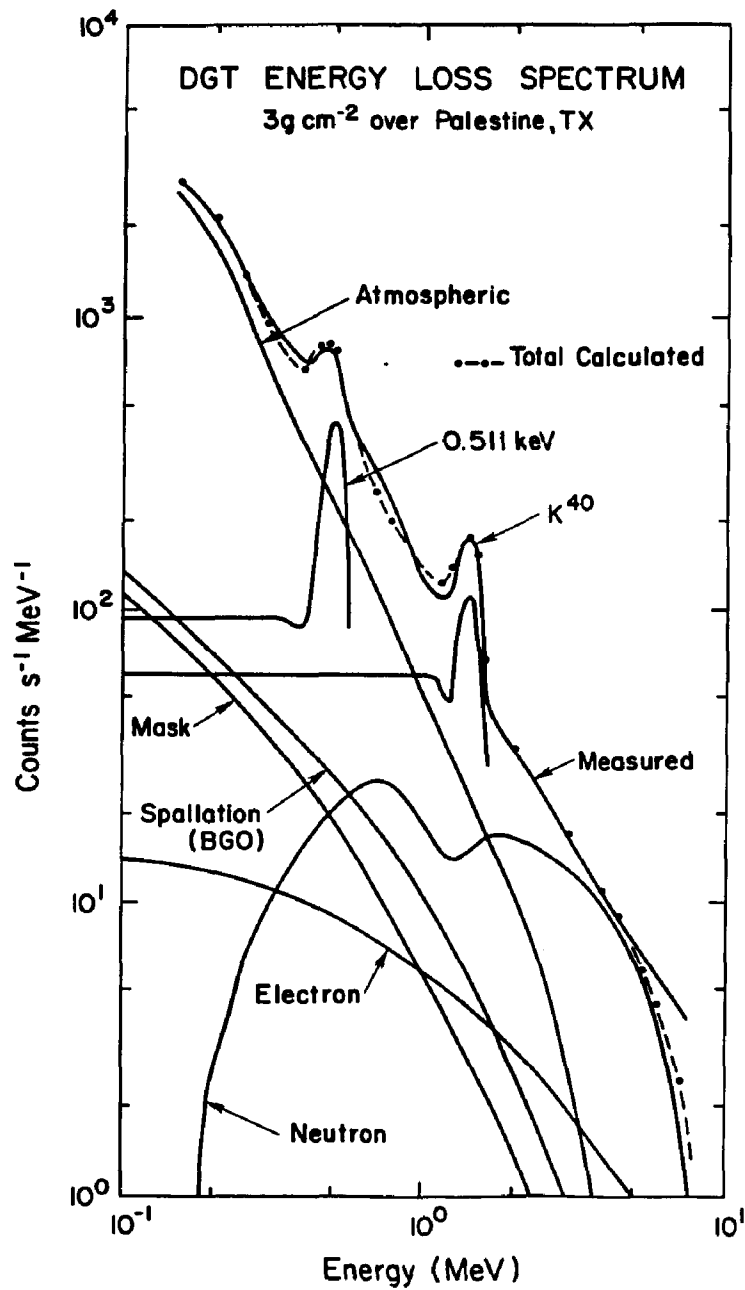


**FIGURE II-8:** The measured and calculated DGT background energy-loss spectrum at 3 gm cm<sup>-2</sup> over Palestine, TX. For comparison, the individual contributions to the detector counting rate are also shown.

atmospheric neutron flux values used in these calculations are those of Dean and Dipper (1981).

**Spallation component.** High-energy cosmic-rays may interact in the shield and central detector producing radioactive nuclides which decay in a time longer than the anticoincidence veto time of the instrument (about 1.7  $\mu$ sec). This component has been derived using the results of Fishman (1972).

**Mask production.** Neutrons and protons may also interact with the mask material to produce observable gamma-ray fluxes at the detection plane. High energy gamma-rays incident on the mask may Compton scatter or produce pairs within the mask material. The electron(s) can then produce secondary photons by bremsstrahlung or, if an electromagnetic cascade develops, by the secondary or tertiary electrons. A fraction of these secondary photons may then escape from the mask and interact in the detection plane. The resulting gamma-ray spectrum at the detection plane was calculated using the empirical formula given in Owens *et al.* (1985b).

**Charged-particle component.** Primary and secondary electrons and protons may enter the forward aperture and deposit energy in the central array. In the case of the DGT, the electron background contribution (derived from the electron flux given by Daniel and Stephens 1974) is significant only at lower energies. The contribution due to soft albedo protons may be neglected since the incident flux is at least two orders of magnitude smaller than that of the electrons.

**Natural radioactivity.** All materials which are commonly used in gamma-ray astronomy experiments contain the natural radionuclides  $^{40}\text{K}$ , Ra and  $^{228}\text{Th}$  which produce numerous emissions, both continuous and discrete, at gamma-ray energies. For example,  $^{40}\text{K}$  (which produces a dominate feature in the DGT background spectrum) decays by  $\beta^+$  emission to  $^{40}\text{Ca}$  or, alternatively, to  $^{40}\text{Ar}$  by  $\beta^+$ /EC decay resulting in gamma-ray emission at 1.46 MeV.

From Figure II-8, it can be seen that the calculated and measured energy-loss spectra are in reasonable agreement. Also apparent in the figure are the presence of two strong background lines in the measured background spectrum. One line is located at a mean energy of ~492 keV. This line is a superposition of activation lines of  $^{23}\text{Na}$  and  $^{127}\text{I}$  along with the atmospheric electron-positron annihilation line. A second line feature appears at 1.46 MeV and is due to radioactive  $^{40}\text{K}$  which appears to originate in the BGO photomultiplier tubes.

### Sensitivity to Celestial Sources

The measured flight background can be used to derive estimates of the DGT sensitivity to narrow line and continuum source emissions. Knowledge of the source sensitivity is important in that it can help to determine the limitations of the present configuration of the DGT experiment.

**Flux sensitivity - general case.** In general, we can define the statistical significance of a gamma-ray observation as,

$$n_{\sigma} = S / \sigma \quad (\text{II.30})$$

where  $S$  is the total number of modulated source counts and  $\sigma$  is the standard deviation error of the measurement. Let us consider the ideal case of a source located at the center of an image element, so that the response is entirely confined to that element. The appropriate expression for  $\sigma$  to be used here is that given in equation (II.27). Substitution of this expression into equation (II.30) yields,

$$n_{\sigma} = \frac{S}{\sqrt{(S + B) \left\{ 1 + 1.029 \left( \frac{T_{\text{obs}}}{T_{\text{sys}}} \right) \right\}}} \quad (\text{II.31})$$

where  $B$  is the total number of background counts,  $T_{\text{obs}}$  is the source observation time,  $T_{\text{sys}}$  is the systematics observation time and we have used  $N = 35$  for the DGT.

We can write down explicit expressions for S and B based on the (energy-dependent) instrument parameters. Note that the fraction of the source flux which is transmitted through the "closed" mask elements (i.e., the fraction of unmodulated flux) acts as a contribution to the background in this analysis. The expressions for S and B are given by,

$$\begin{aligned} S &= F T_{\text{obs}} (\epsilon_p A) \tau_{\text{Al}} \rho (1 - \tau_{\text{Pb}}) \\ B &= F T_{\text{obs}} (\epsilon_p A) \tau_{\text{Al}} \tau_{\text{Pb}} + R_B T_{\text{obs}} \end{aligned} \quad (\text{II.32})$$

where,

- F = the source flux ( $\text{cm}^{-2} \text{s}^{-1}$ )
- $\epsilon_p A$  = the effective photopeak area of the unmasked array ( $\text{cm}^2$ )
- $\tau_{\text{Al}}$  = the fractional transmission of Al in front of the array (0.26 cm thick)
- $\tau_{\text{Pb}}$  = the fractional transmission of Pb in mask elements (1.9 cm thick)
- $\rho$  = the fraction of open mask elements (= 0.514)
- $R_B$  = the background rate ( $\text{s}^{-1}$ ) from all sources in the specified energy range

We can now substitute the definitions (II.32) into Equation (II.31) and solve for the flux level corresponding to an  $n_\sigma$  observation. Assuming background-dominated statistics, i.e.,  $S \ll B$ , we obtain,

$$F \approx \frac{n_\sigma}{(\epsilon_p A) \rho \tau_{\text{Al}} (1 - \tau_{\text{Pb}})} \sqrt{\frac{R_B}{T_{\text{obs}}} \left( 1 + 1.029 \frac{T_{\text{obs}}}{T_{\text{sys}}} \right)} \quad (\text{II.33})$$

This is a very general expression which can be used to predict the instrument sensitivity to either narrow line or continuum fluxes. This represents the minimum detectable flux at the detector. In practice, it may also be necessary to correct for atmospheric absorption between the source and the detector.

**Narrow line flux sensitivity.** In the present context, we define "narrow" to be a width comparable to or less than the instrumental energy resolution. We can determine the narrow line sensitivity if we make use of the measured energy resolution of the BGO array,

$$\Delta E / E = 0.158 E_{\text{MeV}}^{-0.397} \quad (\text{II.34})$$

The measurement of a narrow line flux is made over an energy range equal to the line width at the given energy. Knowledge of the line width (via the energy resolution, eq. II.34) can be used along with the known instrumental background to determine the corresponding background counting rate ( $R_B$ ) at any given energy. We have calculated the corresponding narrow line flux sensitivity, assuming observational parameters roughly equivalent to those which pertain to the Crab observation performed by the DGT (see Chapter III). More specifically, we have chosen a mean atmospheric pathlength of  $3 \text{ gm cm}^{-2}$ ,  $T_{\text{obs}} = 12842$  seconds, and  $T_{\text{sys}} = 18250$  seconds. The background used in the calculations is that measured over Palestine, TX at a float altitude of  $3 \text{ gm cm}^{-2}$ . The results of the calculations are shown in the upper panel of Figure II-9.

**Continuum flux sensitivity.** Equation (II.33), in conjunction with measured float-altitude background rates, could also be used to determine the continuum flux sensitivity, i.e., the sensitivity to source flux over a much wider energy range than that given by the instrument's energy resolution. Instead of proceeding in this fashion, however, we have used the results of the DGT observations of the Crab (see Chapter V) to directly determine the continuum flux sensitivities. More specifically, the  $1\sigma$  errors in the derived Crab flux represent the minimum flux which can be measured by the DGT at the  $1\sigma$  level. In this way, the sensitivity estimates are much more accurate in that they incorporate the various non-ideal aspects of a true source measurement. The data has been converted into  $2\sigma$  flux sensitivities and is displayed in the lower panel of Figure II-9. Also shown are various representative source spectra.

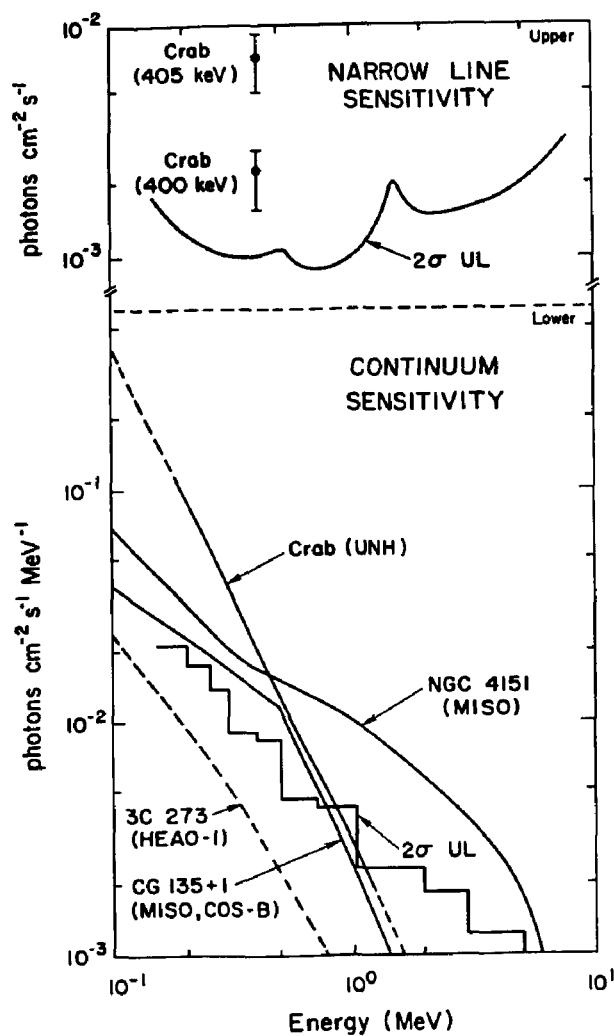


**FIGURE II-9:** The DGT  $2\sigma$  upper limit sensitivities for continuum and narrow line fluxes compared with various observations.

**Upper -** The narrow line sensitivity. Also shown are previously reported line fluxes from the Crab: CRAB(400 keV), Leventhal *et al.* (1977); CRAB(405 keV), Owens *et al.* (1985a).

**Lower -** The continuum sensitivity. The spectra of other sources are shown for comparison [adapted from Dean and Ramsden (1981) for NGC 4151 and CG135+1, and Fichtel and Trombka (1981) for 3C273]. The spectrum denoted CRAB(UNH) is that reported here.

## **CHAPTER III**

### **Observations**

This chapter provides an overview of the DGT balloon flights along with a description of the only successful DGT balloon flight (NASA Flight 1379-P). A summary of the observations obtained during this latter flight is presented.

#### **Balloon Flight History**

To date there have been three balloon flights of the Directional Gamma-ray Telescope (DGT). All three flights were launched from the National Scientific Balloon Facility (NSBF) in Palestine, TX, a facility presently operated by the National Aeronautics and Space Administration (NASA). The first two flights were unsuccessful due to catastrophic balloon failures. The third flight represents the only successful flight of the DGT.

##### **Flight 1311-P**

The first flight of the DGT took place on 1982 September 30. Launched at 00:36 UT, the balloon suffered a catastrophic failure during ascent through the tropopause (at 78mb residual atmosphere) at 01:42 UT. No useful scientific data was obtained. Attempts to extrapolate the observed background rates to those expected at float altitude met with limited success.

##### **Flight 1340-P**

The second balloon flight of the DGT was launched on 1983 September 23 at 23:43 UT. A catastrophic balloon failure took place at 02:36 UT. At the time of the balloon failure, the package (still slowly ascending) was just reaching float altitude



(3.1mb). There was insufficient time near float altitude to obtain any useful scientific data, although important float-altitude background data was collected for the first time.

### **Flight 1379-P**

The third flight attempt of the DGT took place on 1-2 October 1984 and proved extremely successful. Since the data obtained during this flight have provided the basis for the work presented in this thesis, an expanded summary of this flight is presented below.

### **Summary of Flight 1379-P**

The launch of Flight 1379-P took place on 1 October 1984 at 14:25 UT. The balloon successfully negotiated the tropopause and reached 3mb float altitude at approximately 17:00 UT. The instrument remained at float altitude for roughly 30 hours. As can be seen in Figure III-1, the altitude of the payload generally varied between 2.5 and 3.5 gm cm<sup>-2</sup>. The balloon remained well within the ~300 mile telemetry limit of Palestine throughout the entire flight. Termination of the flight took place (upon command) at 22:35 UT on October 2. The package was recovered some 65 miles northwest of Palestine, TX.

### **Detector Anomalies**

In general, the detector system performed well during the flight. There were, however, a few instrumental problems which required attention during post-flight data processing and analysis. Each of these problems is discussed briefly below.

**Detector gain changes.** Despite the use of an active gain stabilization system, substantial changes in the gain of the BGO detectors were observed during the flight. One detector, in particular, showed large variations (about 15%) in gain throughout the flight. The other 34 detectors showed better than 2% gain stability, with much of this variation attributed to a sudden shift in the zero-energy channel about 6 hours after launch. As a result of these variations, gain corrections were required to be implemented during the data

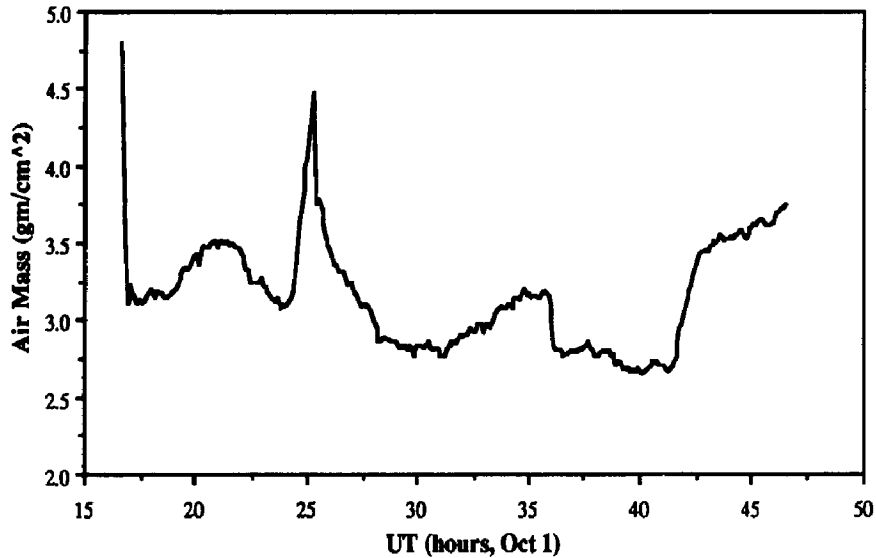


**FIGURE III-1:** Atmospheric depth as a function of time during Flight 1379-P. The sharp increase in depth (corresponding to a decrease in altitude) which took place at ~25 hours UT resulted from the thermal effects of sunset on the balloon.

analysis. Individual detector energy calibrations (for each of the 35 detectors) were determined at roughly 25 minute intervals throughout the flight. Measurement of the detector energy vs. pulse-height channel was facilitated by the presence of a group of background lines centered at 0.492 MeV (produced by the atmospheric 0.511 MeV electron-positron annihilation line along with instrumental activation lines) and a single instrumental background line at 1.46 MeV (due to <sup>40</sup>K, which is apparently contained in the BGO photomultiplier tubes). The use of these two lines provided a two-point energy calibration. This calibration procedure proved much more effective than the use of the <sup>60</sup>Co due to the limited ability of the BGO detectors to resolve the two <sup>60</sup>Co lines at 1.17 and 1.33 MeV. The resulting gain corrections provided an effective gain stability of better than 1%.

**Anticoincidence shield high-voltage supply.** About four hours into the flight, the instrumental livetime suddenly changed from an average level of 90% to an average level of 84%. A thorough review of the flight data indicated that this transition was associated with a change in the counting rate of two side shield sections (sections A-5 and A-9 in Figure II-5). Comparisons with other similar shield sections showed the A-5/A-9 shield counting rate to be nominal *after* this transition, i.e., when the instrumental livetime was at 84%. The fact that sections A-5 and A-9 were correlated in this behavior indicates that the problem was caused by an intermittent high voltage supply, since they were supplied by the same high voltage unit. Since the instrumental livetime is dominated by the normally high counting rates in the anticoincidence shields, any large drop in the shield rates would be expected to be associated with a higher percentage livetime. This is precisely what is seen in the data. The extent of this shield problem is readily seen in Figure III-2, which shows a plot of the percentage livetime as a function of time during the flight. Note that during the first few hours after reaching float (i.e., after ~17:00 UT), the shields remained fairly stable in the "abnormal" state. After the transition (at ~20:30 UT), the shields acted erratically for another five hours. After 25:00 UT (1:00 UT on October 2), the shield problem appears to have resolved itself. There was no evidence of any substantial problems after this time. The effects of the loss in shield efficiency can also be seen in the distribution of the BGO count rates; those near the A-5 and A-9 shield sections tend to show higher count rates during the 90% livetime period. To date, the data collected during the "abnormal" state has not been analyzed due to poorly behaved systematics. Data accumulated during the "erratic" phase were selected based on the livetime; any one second data record which showed greater than 85.5% livetime was rejected from the imaging analysis.

**Loss of PHA upper-level threshold.** Late in the flight (from ~19:40 - 20:00 UT on Oct. 2), there was a noticeable decrease in the main channel event rate. (The corresponding slight increase in livetime can be seen in Figure III-2.) Closer inspection of the data shows that the count rate fell first in the higher channels. Gradually, the lower channel count rates

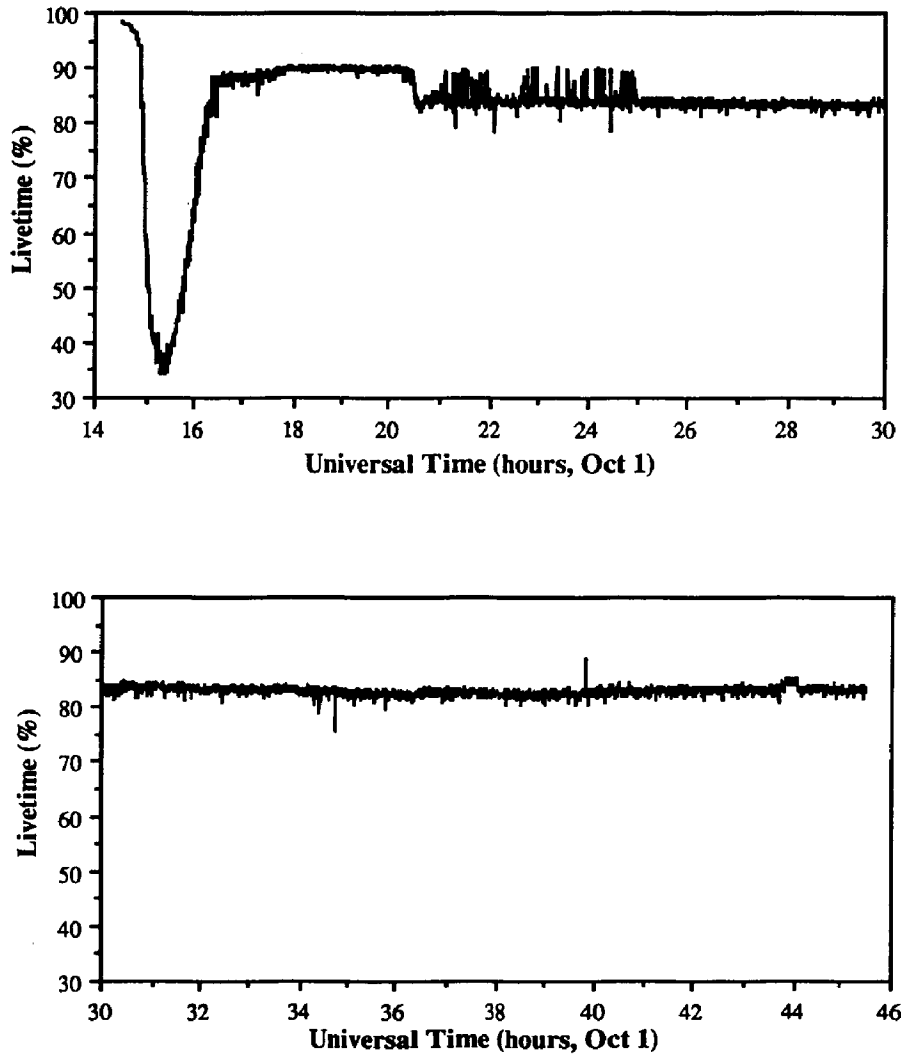


**Figure III-2:** The fractional livetime of the experiment as a function of time during the flight. Note that the time is measured relative to 0 hours UT on October 1. The minimum at ~15:30 is associated with the ascent through the Pfozter maximum. The slight increase in livetime at ~44 hours UT is associated with an abnormal upper-level threshold.

also fell. The apparent explanation of this anomaly is that the upper-level threshold on the PHA circuit gradually fell to a very low level. This effectively prevented the analysis of a large fraction of the incoming photon events. Although the initial drop of this threshold was very slow, the return to nominal level (as measured by the total counting rate) was very abrupt. An analysis of the count rate versus time in the highest pulse height channels indicates that this problem was entirely confined to this brief interval.

**Abnormal pulse-height spectrum in detector #4.** One of the 35 BGO detectors (detector #4) displayed an abnormal spectrum above  $\sim 3$  MeV energy loss. Below  $\sim 3$  MeV, the spectrum of this detector was very similar in shape and intensity with surrounding detectors. Above this point, however, detector #4 showed a much higher rate, displaying a very broad peak with a FWHM  $\sim 4$  MeV. There are two possible explanations for this effect. One plausible explanation is a malfunction of the detector preamp; any effects in the detector preamp would be specific to that particular detector. A second explanation involves an erratic high voltage supply for the photomultiplier tube of detector #4. It is not possible, based on the telemetry data, to determine which of these two explanations is most likely. In processing the data above 3 MeV, the response of detector #4 (in terms of observed counts) was replaced by the average response of the other 34 detectors. Charalambous *et al.* (1984) has discussed the problem of lost detector elements and conclude that such an averaging procedure is an efficient means of recovering much of the lost data. In any case, we have "lost" only one out of 35 detectors, or 2.9% of the detection plane. A correction for this loss of detection efficiency is made during the response function analysis.

### **In-Flight Detector Tests**

A few tests were performed during the flight with the goal of better understanding the in-flight performance of the detector system.

**$^{22}\text{Na}$  calibration source.** One such test involved the measurement of a  $^{22}\text{Na}$  calibration source. Past experience with UNH balloon-borne experiments indicated that the

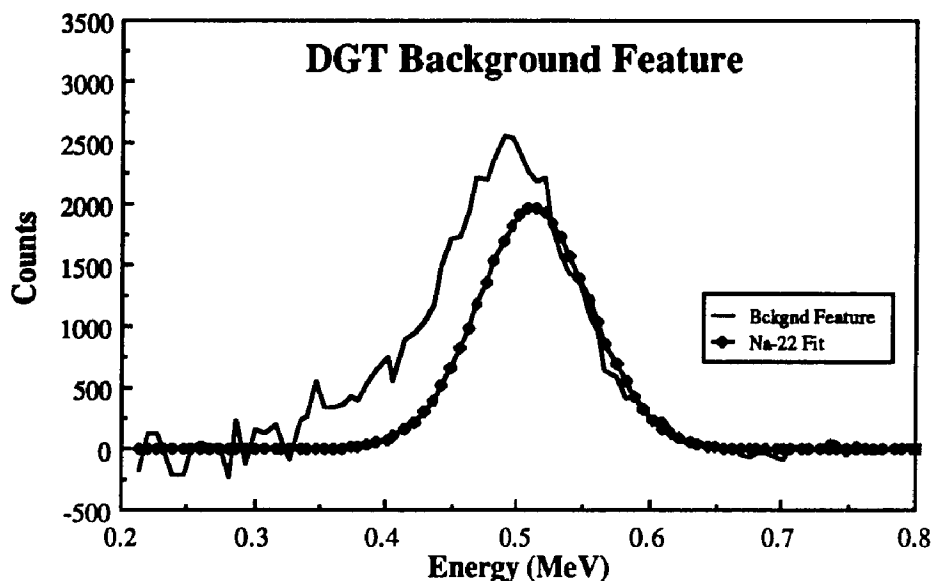


**FIGURE III-3:** The Gaussian fit to the 0.511 MeV line of a  $^{22}\text{Na}$  calibration source (with arbitrary normalization) compared to the feature observed in the DGT background spectra.

peak location of the atmospheric 0.511 MeV line appeared at a lower-than-expected energy. Was this an artifact of the fitting procedures used or was this some real physical effect, resulting from the presence of unresolvable line emission? In order to resolve this question, a spectrum was obtained at float of a calibrated source of 0.511 MeV photons. The  $^{22}\text{Na}$  source was mounted, using a spring-loaded device, on the counterweight arm and placed so as to protrude from behind the lead counterweight. Immediately upon reaching float, a spectrum of the  $^{22}\text{Na}$  source was accumulated. Afterwards, the source was released and allowed to fall behind the lead counterweight. A subsequent "background" spectrum accumulation was later used in extracting the  $^{22}\text{Na}$  source spectrum. (This background spectrum also confirmed that the source did fall behind the lead and hence did not affect the scientific observations which followed.) The peak corresponding to the 0.511 MeV line from  $^{22}\text{Na}$  was fit using a Gaussian function. The resulting function is shown (with arbitrary normalization) in Figure III-3. Also shown in

the figure is the background feature (less the underlying background continuum) observed in the DGT background spectra. It is obvious that the background feature cannot be explained as a single line at 0.511 MeV. The low-energy "tail" which is seen implies that other lower-energy background lines must contribute. Potential contributors include lines from the reactions  $^{23}\text{Na} (n,n'\gamma) ^{23}\text{Na}$  (with  $E_\gamma=0.439$  MeV) and  $^{127}\text{I} (n,n'\gamma) ^{127}\text{I}$  (with  $E_\gamma=0.440$  and 0.490 MeV). These reactions would presumably take place in the large volume of Polcin™ located beneath the main detector array. Similar line features were observed in the previous LGT experiment.

**Mask background spectrum.** Another test was an attempt to measure the effect of the lead mask on the detector background. Many gamma-ray experimenters had expressed considerable concern that the presence of such a massive weight within the open aperture of the detector would increase the background to an intolerable level. This would render the coded aperture technique useless unless some type of active mask was employed. Based on data collected during the first two (unsuccessful) balloon flights of the DGT, it did not appear as though the background level would be intolerable. It was apparent that the mask contribution to the background, if any, would not prohibit the success of the experiment. During Flight 1379-P an attempt was made to directly measure the mask background by maintaining the detector at its lowest possible zenith angle ( $\sim 20^\circ$ ) while moving the mask (independently) to its largest possible zenith angle ( $\sim 90^\circ$ ). In this way, the mask was as far removed from the detector aperture as possible. Spectra were accumulated both with the mask in front of the detector and with the mask removed. After accounting for the attenuating effects of the mask on the atmospheric flux (based on the atmospheric component in Figure II-8), the spectrum due to local production in the mask could be determined. The results for the mean background spectrum due to the mask are shown in Figure III-4. These results show a continuum which agrees quite well with the calculated contribution shown in Figure II-8. On top of this continuum is a line feature consistent with 0.511 MeV photons along with indications of a possible 1.022 MeV component.

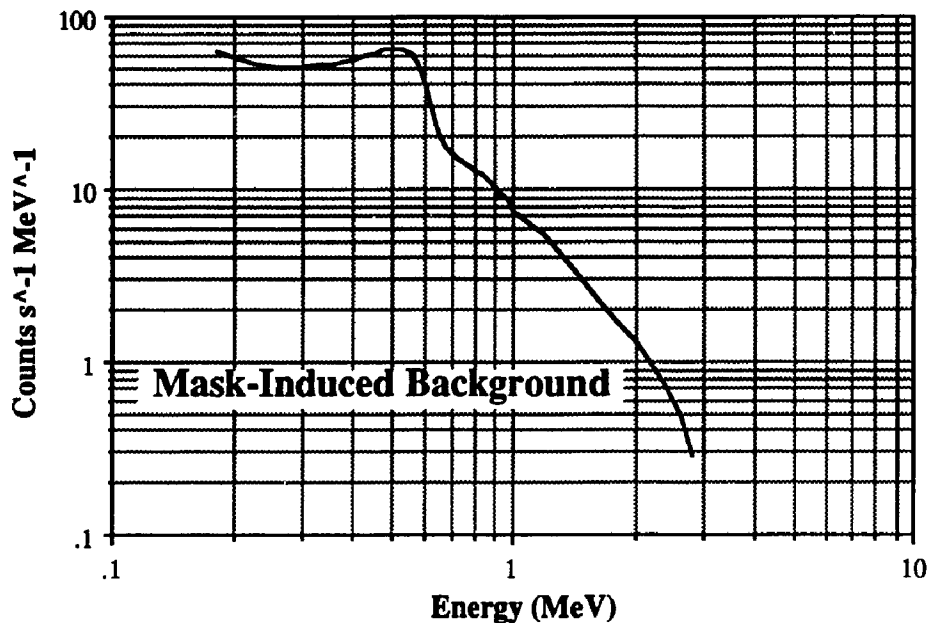


**FIGURE III-4:** The mean background spectrum resulting from local gamma-ray production in the DGT mask. The mask contribution ranges from 3% to 5% of the total detector background, with a maximum (at  $\sim 0.511$  MeV) of  $\sim 8\%$ .

(Line features were not included in the background calculations discussed in Chapter II.) The fraction of the total background which is attributable to the mask is generally in the range 3-5%, with a maximum (at  $\sim 0.511$  MeV) of  $\sim 8\%$ . An important result from this analysis is that the mask shows no appreciable contribution to the detector background at energies greater than 1 MeV.

**Upper-level energy threshold.** As discussed in Chapter II, the last channel (channel 1024) in the DGT pulse-height spectrum represents an overflow channel. The upper limit on the acceptable input photon energy was believed to be in the range of 9-10 MeV based on pre-flight calibrations with an electronic pulser fed into the detector electronics. Due to the inaccuracy with which this upper threshold was known, it was of interest to use the flight data to determine the upper threshold. This was achieved by assuming that the background spectrum at high-energies extended as a power-law to about 10 MeV. By



fitting the measured response of the overflow channel, the upper threshold was determined to be at  $\sim 9.3$  MeV. This is the value which was used throughout the data analysis. For the spectral analysis, the data was normally integrated from 6 MeV to the upper limit in order to obtain a single data point. The error in the derived energy range for such a data point is estimated to be no more than 10%; such an error is well below the error on any flux measurement in this energy range.

### Source Observations

The long duration of this balloon flight permitted observations of a number of astrophysically interesting sources. These source observations are summarized in Table III-1. The primary targets of this flight were the Crab region, the Cygnus region (encompassing both Cyg X-1 and Cyg X-3) and the region around NGC 4151. Secondary sources included 2CG135+1, 3C273 and SS433. Each source was tracked using a modified *drift-scan* technique. This procedure involves pointing the experiment ahead of the source (in terms of its diurnal motion) and allowing the source to drift through several image elements within the field-of-view. (This modified procedure is in contrast to the standard drift scan procedure in which the source is generally allowed to pass completely through the field-of-view in order to obtain both source and background measurements.) During the DGT observations, this drift period was normally about 30 minutes, i.e., the pointing direction of the experiment was updated every 30 minutes. Due to the inability of the DGT to point to within  $\sim 20^\circ$  of the zenith, about two hours of source observation time was generally lost as the source passed through the local meridian. Each source was, in general, observed during both the ascending and descending part of its transit. Also listed in Table III-1 is the total integrated livetime covered by the processed observations. These times are generally much shorter than one would expect based on the fractional livetime of the experiment ( $\sim 84\%$  during nominal operation at float); this is largely due to the various restrictions that were placed on the data during post-flight processing. (The various selection criteria will be discussed in more detail in Chapter IV.)

The work embodied in this thesis deals with principally with the Crab and Cygnus observations. The observations of NGC 4151 and CG135+1 have been processed, but not completely analyzed. The data pertaining to the observations of SS433 and 3C273 have not yet been processed.

**Table III-1**  
**FLIGHT 1379-P SOURCE SUMMARY**

TARGET	DATE (Oct)	OBSERVATION PERIOD (UT)	INSTRUMENTAL LIVETIME (secs)
Crab	2	7:30 - 10:00	12842
	2	12:30 - 15:00	
Cygnus	1-2	21:30 - 0:30	13039
	2	3:30 - 6:00	
NGC 4151	1	19:00 - 21:00	5559
	2	15:30 - 16:30	
	2	19:00 - 21:00	
CG 135+1	2	6:00 - 7:30	11097
	2	10:00 - 12:30	
SS433	1-2	00:30 - 3:30	---
	2	21:24 - 22:17	
3C273	1	17:30 - 19:00	---
	2	17:00 - 18:30	

### Pointing Accuracy and Stability

One of the important mechanical requirements of this experiment was the need to have accurate information on the detector pointing direction. (Note that the detector pointing *direction* is not the same as the pointing *aspect*; we define the detector aspect as the orientation of the field-of-view relative to the source distribution.) Based on pre-flight calibration data, we expected that the DGT pointing direction would be known to  $\pm 1.0^\circ$ . Some in-flight confirmation of this was, however, required in order to ensure the quality of the flight data. Consequently, a series of tests were performed during the flight using the

two sets of sun sensors described in Chapter II. The essential idea of these tests was to assess our ability to point the mask arm at the sun based on the available pointing information. A total of three separate tests were performed at various times throughout the flight, each lasting roughly 30 minutes. Some sample data from the photopot sun sensor is shown in Table III-2. The sun sensor output is used along with the knowledge of the sun's zenith and azimuth to calculate the corresponding pointing direction of the mask arm. The zenith and azimuth encoders, in conjunction with pre-flight calibration data, also permits a determination of the mask pointing direction. Results of an analysis of this data indicate that the orientation system was, in general, accurate to  $\pm 1.0^\circ$ .

**Table III-2**  
**SAMPLE SUN SENSOR DATA**

TIME (UT, Oct 1)	SUN SENSOR		ENCODERS		DIFF (degs)
	ZENITH (degs)	AZIMUTH (degs)	ZENITH (degs)	AZIMUTH (degs)	
21:20:30	54.7	245.2	55.5	245.9	1.06
21:21:00	54.7	243.6	55.5	243.8	0.82
21:21:30	54.7	245.3	56.0	245.3	1.30
21:22:00	54.7	247.0	55.5	247.0	0.80
21:22:30	54.7	247.8	55.5	247.6	0.82
21:23:00	54.7	246.4	55.3	246.8	0.72
21:23:30	54.7	244.2	55.5	244.9	1.06
21:24:00	54.7	244.6	56.0	244.7	1.30

The stability of the pointing platform was also a determining factor in the development of the data analysis procedures. Although the knowledge of the pointing direction at any given moment in time was known to  $\pm 1.0^\circ$ , the pointing direction itself varied continuously throughout the flight. This was due largely to the oscillation of the balloon payload about its vertical axis. The extent of this oscillation could be measured directly by the readout of the magnetometer signal. As shown in Figure III-5, this oscillation was sinusoidal in nature with a period of roughly 30 seconds. During the flight, the amplitude of this azimuthal oscillation varied between  $\pm 3^\circ$  and  $\pm 4^\circ$ , with a direct

dependence on the ambient temperature. This temperature dependence of this oscillation would indicate that the amplitude grew larger as the payload thrust bearings (which supported the entire payload weight) became less able to respond quickly to the effects of the orientation platform's inertia wheel. During the processing of the DGT imaging data, this motion was accounted for by creating separate images based on the range of the maghi readout.

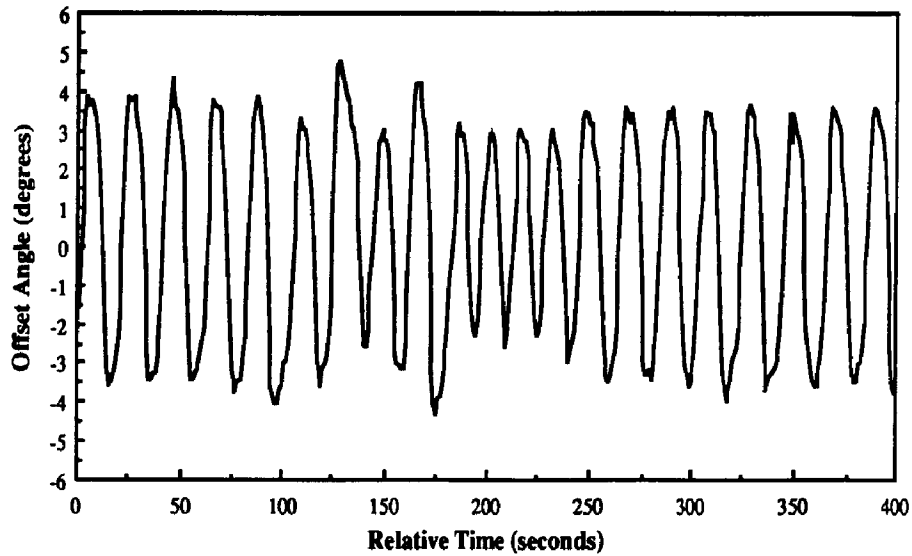


**FIGURE III-5:** A sample of the magnetometer data, which indicates the change of the detector azimuth angle from the null point of the magnetometer.

## CHAPTER IV

### Data Reduction and Analysis

The DGT database presented an analysis problem which differed greatly from other, more traditional, gamma-ray experiments. Collimated detectors were commonly used in past measurements of low-energy gamma radiation. In this case, a measurement of the source intensity could be derived by subtracting a "background" accumulation from a "source" accumulation. Corrections were generally made for the estimated time variability of the background counting rate. The net result was a spectrum representing the sum of all sources present in the field-of-view during the "source" measurement. If there were more than one known source in the field-of-view, then the time-dependent exposure of the sources (given the angular response of the detector and some assumed source distribution) could be used to unfold the individual source spectra. The analysis of the DGT database required a radically different approach due to the imaging nature of the experiment. For this reason, the procedures developed for the DGT shall be reviewed in detail.

In this chapter, we shall first describe the data reduction process, followed by the steps which are required to process and analyze the imaging data. The image analysis takes place in three steps. First, the decoded sky images are assembled from the flight data. Next, the resulting images are analyzed to determine the source distribution and the associated intensity (i.e., number of gamma-ray counts measured by the DGT) as a function of detector energy loss. The detector energy-loss spectra are then used (in the final step) to extract the corresponding source photon spectra, using the known instrument response function.

## Reduction of Flight Data

The primary computational tools used in the post-flight data reduction and analysis were two Zenith Z-100 microcomputers. Each was equipped with a 10 Mbyte hard disk. A 1/4" cartridge tape backup system facilitated the storage of large amounts of processed data. The processing procedures developed for the DGT database were dictated in large part by the limitations of the microcomputer hardware. Although it may have been preferable to use a larger mainframe computer for the data processing and analysis, the use of microcomputers offered greater accessibility and substantial economic savings.

### Digitization of Telemetry Data

The first step in the flight data processing is the digitization of the analog telemetry data tapes which were recorded during the flight. An AMPEX tape recorder was used to record this data and is also used for playback purposes. A custom-made interface allows the signal from the telemetry tapes to be fed directly into the Z-100 microcomputer. This interface converts the analog telemetry into the corresponding digital data stream, synchronizes to the digital data stream and strips out the individual 25-bit data words. The 25-bit data words are in turn buffered into 32-bit words and dumped sequentially onto the Z-100 hard disk. Once this raw data is on the Z-100's hard disk, it is reformatted into one second data records which permit ready access to any desired data from the experiment. In this fashion, a maximum of about 1540 seconds (or ~26 minutes) of formatted data could be produced at a time. The files of formatted data produced in this manner are referred to as *flight files*. These flight files are stored on 1/4" cartridge tape from which they could be retrieved by the Z-100 as desired. Due to the size of these flight files (~4 Mbytes), two such flight files could be placed onto the hard disk simultaneously. This meant that, during data analysis, a maximum of ~50 minutes of flight data could be directly available at any given time.

All housekeeping and other diagnostic data are read directly from the flight files. The sun sensor data, for example, could be stripped out of the flight tapes for further study. Detector spectra (either main channel or IFC) could be accumulated directly from these tapes. Further data processing, however, was required in order to extract the imaging information.

### **Image Data Processing**

The basic procedure required to create an image is as follows. The detector data (i.e., the number of photon events in each BGO detector) are accumulated over some brief time period (on the order of tens of seconds). The accumulated data must meet certain requirements which deal primarily with the instrument pointing direction and experimental status. The length of the accumulation period is chosen so as to minimize the effects of the experiment's motion and the effects of diurnal motion. The resulting detector response (or detector "map") is then correlated with the DGT post-processing function in order to create the corresponding sky image. The resulting sky image is transformed into some detector-independent coordinate frame (based on celestial coordinates). A number of such images are accumulated, transformed and summed together to create the final sky image.

In practice, however, this procedure is complicated by the need to incorporate the energy-dependent systematics corrections. This means that each individual energy range must be processed separately in order to incorporate these corrections. Ideally, one would create an image for each channel in the DGT pulse height spectrum. This was not only impractical, due to the limited computational facilities, but also unnecessary. Since the energy resolution of the BGO detectors was generally much greater than the 6.62 keV channel width, many channels could be combined without appreciable loss of spectral information. Furthermore, the low flux levels of the sources under observation meant that wide channel bands were desirable to obtain reasonable source statistics (i.e., measured data points with greater than  $1\sigma$  statistical significance). In order to facilitate this energy-dependent analysis, a number of standard energy ranges were set up. These energy ranges,

referred to as *energy intervals*, are tabulated in Table IV-1. Also listed in the table, for reference purposes, is the average background rate for each energy interval.

**Table IV-1**  
**DGT ENERGY INTERVALS**

INTERVAL	ENERGY (keV)	BCKGND RATE (sec <sup>-1</sup> )
1	160-200	93.64
2	180-200	
3	200-250	85.54
4	250-300	61.68
5	300-400	87.11
6	400-600	137.42
7	600-800	49.87
8	800-1000	33.53
9	1000-2000	98.36
10	2000-3000	23.16
11	3000-6000	26.37
12	200-600 (w/o sys corr)	371.75
13	3000-4000	12.09
14	4000-5000	8.40
15	5000-6000	5.92
16	6000-9318	12.23

For the purposes of the Flight 1379-P data analysis, only one set of systematics correction factors have been used. The correction factors were derived from a very long accumulation of detector data spread over various portions of the flight. Due to the large opening aperture (~120° FWHM) of the DGT, it was impractical to expect that the accumulation of the systematics data would not contain at least some source contribution. Indeed, based on the discussion in Chapter II, it is expected that the systematics data could be secured even in the presence of source counts. The systematics correction factors (the  $\epsilon(k,l)$  in eq. II.15a) which have been used in this analysis are derived from data obtained during observations of CG135+1, SS433 and 3C273. These three sources are expected to have an especially small signal-to-background ratio (<1%) and thus represent the about the best available approximation to a "pure background" measurement. The systematics



correction factors are calculated from a direct accumulation of this data, i.e., there were no corrections for changes in the pointing aspect of the experiment. This procedure insures that any source counts are randomly distributed throughout the array. The total instrumental livetime for the systematics data accumulation ( $T_{sys}$ ) was 18,250 seconds. As discussed earlier (c.f., Chapter II), the effectiveness of this systematics reduction procedure relies on the assumption that the background systematics (in terms of the  $\epsilon_i$ ) are independent of time. Based on an analysis of the DGT flight database, it has been determined that the  $\epsilon_i$  are variable on a level which is less than 0.1% of the background for any given energy range. Such a variability is less than the statistical uncertainty of the imaging measurements.

The first step in the image formation process is to divide the source observation period into *data segments*, each of which consist of a contiguous set of data on the same flight tape and with the same primary pointing parameters (i.e., detector zenith and azimuth). These data segments vary from 5 to 25 minutes in length. The motivation behind the creation of these data segments was the desire to eliminate the data between pointing transitions when the detector aspect was changing at a rapid rate. This greatly simplified the data reduction software.

Each data segment was then processed into one or more *data intervals*. The actual accumulation of detector pulse-height data takes place within the data intervals. In order to minimize the blurring effects of the Earth's diurnal motion during a single image exposure, the data intervals are limited to five minutes in length. (Five minutes translates into a diurnal motion of  $1.25^\circ$  at  $\delta=0^\circ$  or  $1.08^\circ$  at  $\delta=30^\circ$ .) Due to the azimuthal instability of the experiment (c.f., Chapter III), four separate sets of data are accumulated within each data interval. Each of the four sets of data (also referred to as *snapshots*) are associated with a given range of the magnetometer output, hence some specific azimuth angle correction. This procedure reduces the effective azimuthal instability of the analysis to  $\pm 1^\circ$ . The data accumulated within each snapshot is corrected using the systematics correction factors and

then correlated with the post-processing function (c.f., Equation II-2b) to create a single image consisting of a 5 by 7 array of  $3.8^\circ$  pixel elements. These snapshot images generally represent about 60 seconds of instrumental livetime and are referenced to the azimuth and zenith angles which correspond to the center of the field-of-view.

SNAPSHOT IMAGE DEVELOPMENT						
138.5	141.6	143.4	126.1	129.2	162.6	127.9
137.9	137.0	177.3	153.5	162.5	158.9	149.4
149.5	139.2	157.5	165.6	164.8	181.8	155.1
149.3	140.7	166.1	153.2	142.2	162.8	133.0
154.1	136.8	128.1	143.6	132.3	151.0	139.0
a) accumulated detector map						
0.878	0.925	0.956	0.994	0.941	1.007	0.935
0.938	0.983	1.065	1.083	0.994	1.121	0.993
0.969	0.999	1.066	1.121	1.037	1.090	1.038
0.977	0.973	1.091	1.110	1.016	1.079	1.010
0.906	0.913	0.985	1.014	0.900	0.977	0.917
b) systematics correction factors						
157.7	153.1	150.0	134.0	137.3	161.5	136.8
147.0	139.4	166.5	141.7	163.5	141.7	150.4
154.3	139.3	147.7	147.7	158.9	166.8	149.4
152.8	144.6	152.2	138.0	140.0	150.9	131.7
170.1	149.8	130.0	141.6	147.0	154.5	151.6
c) corrected detector map						
-64.6	-22.3	150.0	60.9	-9.7	-44.5	-40.7
10.1	37.7	-35.5	-52.2	-60.8	-45.7	-36.4
-87.9	16.1	-67.7	113.7	75.3	-27.5	127.1
-22.9	-3.4	-15.9	53.5	-26.6	-13.8	92.3
-76.1	74.4	-52.6	69.7	-2.7	-70.0	-1.2
d) final snapshot image						

**FIGURE IV-1:** Sequence which demonstrates the steps in producing a snapshot image. This data was accumulated during the DGT observation of the Crab. The location of the source is not obvious in this very short exposure image (64 seconds livetime); only by summing a number of such images does the source location become obvious.

The formation of a snapshot image is demonstrated in Figure IV-1. This sample data was collected over the energy range 200-250 keV during the DGT observations of the Crab region. The total integrated livetime represented by this data is 64.0 seconds. The

image is associated with a particular azimuth and zenith pointing direction (corresponding to the center of the field-of-view); these quantities are used to transform the image into a common coordinate frame (see below). The raw accumulated detector map is displayed in Figure IV-1a. In this representation, each of the 35 numbers corresponds to the total number of counts in a given detector. (This array is equivalent to the P array discussed in Chapter II.) In Figure IV-1b, the systematics correction factors for each detector are shown. These factors are then used to correct the raw detector map (c.f., Equation II.23). This results in the corrected detector map (P' in the notation of Chapter II) shown in Figure IV-1c. Finally, the detector map is correlated with the DGT's post-processing function (c.f., Equation II.2b) in order to create the final snapshot image (Figure IV-1d).

During the accumulation of the snapshot data, care was taken to insure that the data met certain requirements. These requirements were imposed to insure that the experiment was in a stable configuration and not, for example, in transition between pointing directions. Therefore, during the accumulation process, various orientation status bits were checked for each one second data record. A given one second record was rejected if any one of the following conditions were met :

- Arm 1 motor on (arm driving up or down)
- Arm 2 motor on (arm driving up or down)
- Detector zenith motor on
- Detector not aligned with mask
- Mask-detector alignment mode not enabled
- Azimuth correction drive not enabled
- Azimuth motor on

These requirements resulted in the rejection of some data. For example, at times near sunrise or sunset, reflections of the sun seemed to interact with the detector alignment system in such a manner as to set up oscillations of the detector assembly. (These oscillations were eliminated real time by briefly disabling the mask alignment and allowing the system to stabilize.) Furthermore these requirements also assured that any data taken during a transition from one pointing direction to another was eliminated from the analysis.

The final step in the image formation process is to assemble the final *composite image* from the individual snapshot images. This is accomplished by transforming each snapshot image into a common coordinate frame and then, within that frame, summing all of the images together. The common coordinate system is based on the celestial coordinates of right ascension and declination. More specifically, if we define the center of a composite image by the celestial coordinates  $(\alpha_0, \delta_0)$ , then the common (*skymap*) coordinate frame is defined by,

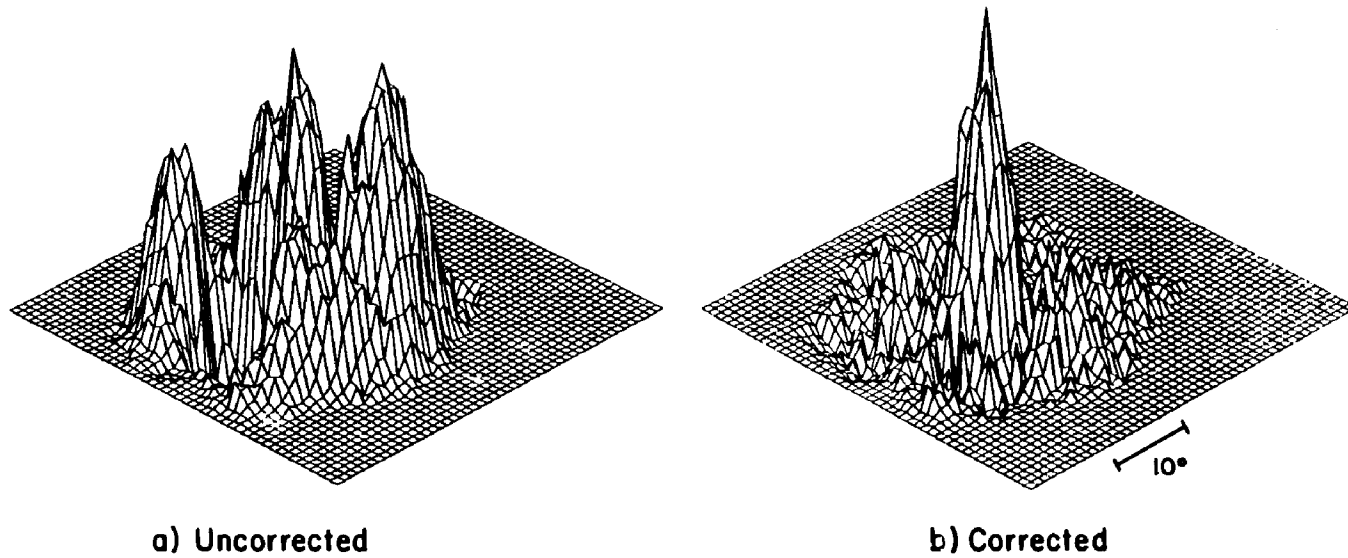
$$x = (\alpha - \alpha_0) \cos \delta \quad (\text{IV.1})$$

$$y = \delta - \delta_0 \quad (\text{IV.2})$$

where the origin of the (x,y) coordinate system is also located at the center of the composite image.

Each snapshot image is associated with specific values of Universal Time, balloon location (latitude and longitude), magnetic declination, encoder output values (for both azimuth and zenith) and average magnetometer output (indicating the azimuth offset from null). All of these parameters are used in the transformation of the snapshot image into the skymap coordinate frame. In order to facilitate this transformation procedure, each snapshot image is divided into smaller pixel elements, each of which is  $0.95^\circ$  by  $0.95^\circ$  in size. (Each  $3.8^\circ$  image element is split into a four by four array.) Each  $0.95^\circ$  pixel is assigned a value 1/16 that of the original  $3.8^\circ$  pixel from which it was derived, thus conserving the total source counts. The resulting *segmented image* is now a 28 by 20 array. Each  $0.95^\circ$  image element of the segmented image is independently transformed into the skymap coordinate frame and added into an array which represents the composite source image. A similar array also keeps track of the livetime for each element in the skymap array. (Full details of the transformation into the skymap coordinate frame are given in Appendix B.)

Figure IV-2 demonstrates not only the results of the image composition, but also the efficacy of the systematics corrections. Here we show two images which have been



### Crab Region 200-600 keV

**FIGURE IV-2:** Two images of the Crab region, illustrating the efficacy of the background systematics correction. (Each view represents the reproduced gamma-ray intensity, in terms of the number of reproduced source counts per  $0.95^\circ$  image element.) Figures IV-2a and IV-2b show the uncorrected and corrected data, respectively. The amplitude of the peak in Figure IV-2b corresponds to a significance in the detected flux of  $10.6 \sigma$ . The total source observation time was 12842 seconds ( $\sim 3.6$  hours).

produced using the Crab data integrated over the energy range 200-600 keV. Both images were processed in exactly the same way except that Figure IV-2a was not corrected for the effects of the background systematics. In Figure IV-2b we see that the Crab signal, previously lost in the background noise level, stands out clearly at the  $10.6 \sigma$  level. It is also quite obvious from this figure that the problem of background systematics is indeed a serious one which must be dealt with in a gamma-ray telescope of this type.

For reference purposes, the total number of data segments, data intervals and data snapshots for each of the source observations are listed in Table IV-2.

**Table IV-2**  
**SOURCE DATA DIVISIONS**

SOURCE	DATA SEGMENTS	DATA INTERVALS	DATA SNAPSHOTS
Crab	21	59	236
Cygnus	22	69	276
NGC 4151	8	26	103
CG135+1	16	54	216

### **Image Analysis Procedures**

In analyzing the imaging data, the desire was to extract as much information as possible regarding the source distributions and associated intensities. In addition to the best-fit (or most probable) values of the parameters which describe the source distribution, it was also important to determine the range of values for each of these parameters which is statistically allowed by the data.

#### **Point-Spread-Function of the Imaging System**

In order to extract both spatial and spectral information from the imaging data, the response of the DGT imaging system to a point source of gamma-ray emission must be

fully understood. More precisely, one needs to obtain information on the point-spread-function (PSF) of the imaging system. Knowledge of the PSF allows one to predict the system response to any arbitrary source distribution. As discussed in Chapter II, the PSF for a single image is a function of the location of a source relative to the center of an image element. The behavior of this PSF was confirmed with laboratory imaging measurements. The PSF for a composite image, on the other hand, is a complicated function of many factors, including the detailed time history of the instrument pointing aspect. As such, the composite image PSF could best be measured using data obtained during an actual balloon flight.

The measurement of the composite image PSF was one of the tasks assigned to the first balloon flight of the DGT. The Crab Nebula/pulsar was considered to be an ideal target for this purpose. Based on data obtained at various wavelengths (c.f., Chapter I), the gamma-ray emission is expected to emanate from a region less than 1 arc minute in size, a size which is negligible relative to the basic  $3.8^\circ$  pixel size of the DGT imaging system. For the purposes of this experiment, therefore, the Crab could be treated as a point source of gamma-ray emission. Furthermore, the Crab is one of the brightest sources in the sky at these energies with a fairly stable, well-defined power-law photon spectrum. These characteristics make the Crab an ideal target for evaluating the in-flight imaging properties of the DGT. More importantly, the Crab observation permitted a direct assessment of the in-flight PSF.

The analysis of the imaging data required some functional form to represent the imaging response to a point source. A logical first choice for such a function would be a Gaussian function of the form,

$$f(x,y) = \frac{S_T}{2\pi \alpha_x \alpha_y} \exp \left\{ -\frac{1}{2} \left[ \left( \frac{x-\mu_x}{\alpha_x} \right)^2 + \left( \frac{y-\mu_y}{\alpha_y} \right)^2 \right] \right\} \quad (IV.3)$$

where  $\mu_x$  and  $\mu_y$  define the source location and  $\alpha_x$  and  $\alpha_y$  are a measure of the width of the Gaussian peak.  $S_T$  defines the total imaging response (in terms of the number of

reproduced counts) to the source. This function is, more precisely, a bivariate normal distribution function with zero correlation between  $x$  and  $y$ . An alternative to this function might then be to include a non-zero correlation, thus adding a fifth parameter ( $\rho_c$ , representing the correlation between  $x$  and  $y$ ) to the fitting function. In this case, we would have,

$$f(x,y) = \frac{S_T}{2\pi \alpha_x \alpha_y} \frac{1}{\sqrt{1-\rho_c^2}} \times \quad (IV.4)$$

$$\exp \left\{ -\frac{1}{2(1-\rho_c^2)} \left[ \left( \frac{x-\mu_x}{\alpha_x} \right)^2 - 2\rho_c \left( \frac{x-\mu_x}{\alpha_x} \right) \left( \frac{y-\mu_y}{\alpha_y} \right) + \left( \frac{y-\mu_y}{\alpha_y} \right)^2 \right] \right\}$$

Another variant on the Gaussian function would be to allow the powers in the exponential to be variable. This would then be a six parameter function given by,

$$f(x,y) = \frac{S_T}{2\pi \alpha_x \alpha_y} \exp \left\{ -\frac{1}{2} \left[ \left( \frac{x-\mu_x}{\alpha_x} \right)^{\alpha_x} + \left( \frac{y-\mu_y}{\alpha_y} \right)^{\alpha_y} \right] \right\} \quad (IV.5)$$

where  $\alpha_x$  and  $\alpha_y$  are now also allowed to be free parameters. The alternative functions (eqs. IV.4 and IV.5) were also used to fit some of the imaging data. These latter functions increased the complexity of the analysis and offered no statistically significant improvement in the fitting results. For the sake of simplicity, therefore, equation (IV.3) was chosen for use in the analysis.

In addition to the term represented by equation (IV.3) above, a representation of the imaging PSF also required an additional correction term due to the effect which we call *source suppression*. Source suppression (which is discussed more thoroughly in Appendix A) results from there being an average non-source image element level of less than zero. As a consequence of this negative DC level, a summation of images (with the source lying, in general, within a different pixel element for each image) produces a response to the source, part of which falls below the zero level of the image. The net result is a need to



include an additional term in the PSF. The full PSF expression then becomes (c.f., Appendix B),

$$f(x,y) = \frac{R_{\text{fit}}}{2\pi \sigma_x \sigma_y} \exp \left\{ -\frac{1}{2} \left[ \left( \frac{x - \mu_x}{\sigma_x} \right)^2 + \left( \frac{y - \mu_y}{\sigma_y} \right)^2 \right] \right\} - \frac{R_{\text{fit}}}{560} \quad (\text{IV.6a})$$

where  $R_{\text{fit}}$  is related to the total imaging response ( $S_T$ ) by,

$$S_T = (34/35) R_{\text{fit}} \quad (\text{IV.6b})$$

The above expression (eq. IV.6) is valid for a single point source within the field-of-view. For more than one source, the value for  $R_{\text{fit}}$  in the second term is replaced by the sum of all such values for each source within the field-of-view.

The functional form given by equation (IV.6) has been successfully used in the analysis of the imaging data obtained during Flight 1379-P. Acceptable fits of this function (in terms of the associated  $\chi^2$ ) have been made to the imaging data of both the Crab and of Cygnus X-1. (A measurement of the Crab response in the 180-400 keV range gave a reduced  $\chi^2$  of 1.005 for 116 degrees of freedom.) Initially, the quantities of interest include the source location ( $\mu_x$  and  $\mu_y$ ) and the imaging PSF ( $\sigma_x$  and  $\sigma_y$ ). All four of these quantities are independent of energy. The location of the source within the resulting image is a result of the source-detector aspect; the PSF is independent of energy due, in large part, to the lack of any energy-dependence in the ability of the DGT to locate a photon interaction within the detection plane. It is therefore appropriate to measure these quantities using data integrated over an energy range which provides the best possible source statistics. For the DGT data, this range was chosen to be 160 keV to 1 MeV (energy intervals 1 and 3-8 in Table IV-1).

The results obtained from an analysis of both the Crab and Cygnus X-1 indicate statistically equivalent values of  $\sigma_x$  and  $\sigma_y$ , as can be seen in Table IV-3. The fact that this function provides an acceptable fit with similar results for each source gives us great confidence that this function accurately represents the true PSF of the imaging system. The measured width of the PSF,  $\sim 4.8^\circ$  full-width at half-maximum (FWHM), is consistent with

reasonable estimates of what can be expected. The minimum expected width of the PSF is  $3.8^\circ$ , corresponding to the size of the basic DGT image element. The true PSF is expected to be broadened beyond this value by the effects of the Earth's rotation ( $\sim 1^\circ$ ), the pointing instability ( $\sim 2^\circ$ ) and the estimated pointing error ( $\sim 1^\circ$ ). These numbers indicate that the expected PSF should have a width of  $\sim 4.5^\circ$ , a result which is consistent with the measured value.

**Table IV-3**  
**MEASURED WIDTHS OF THE POINT-SPREAD-FUNCTION**

SOURCE	$\sigma_x$	$\sigma_y$	<FWHM>
Crab	$2.06^\circ \pm .15^\circ$	$2.04^\circ \pm .13^\circ$	$4.83^\circ \pm .36$
Cygnus X-1	$2.08^\circ \pm .12^\circ$	$2.21^\circ \pm .16^\circ$	$5.04^\circ \pm .36$

Once the source location and PSF parameters are known for a given observation, then these quantities are used, along with equation (IV.6), to determine the source intensity for any given energy range. The source energy-loss spectrum may then be derived from measurements of the source intensity for a number of different energy intervals.

#### Determination of Allowable Parameter Ranges

In any experiment, it is more important to ascertain which models can be ruled out by the data. In this context, it is necessary to determine the statistically-allowable range of a given parameter as well as the most probable (or best-fit) value. The problem of determining allowable parameter ranges is therefore an important one in experimental science.

The best-fit value for a given parameter can be determined from a minimization of either the  $\chi^2$  or the variance of the data with respect to a particular model. (Minimization of the experimental variance is appropriate only when the model uncertainties for each data point are equivalent; to first order, this is the case with the DGT imaging data.) The

estimation of allowable parameter ranges can also be accomplished using a  $\chi^2$  technique, where one varies the parameter of interest (in some predetermined fashion) in order to effect some desired change in the value of  $\chi^2$ . A general prescription for this  $\chi^2$  procedure is given by Lampton *et al.* (1976). Initially, a  $\chi^2$  approach was used to determine the allowable ranges of the parameters which were measured in the DGT imaging data. A couple of difficulties arose in the application of this procedure to the DGT database. A model had been developed which predicted the variance of the pixel elements for a single DGT image. Subsequent extension to the composite image case was subject to some uncertainty. A second, more serious difficulty arose when the statistical uncertainties in the PSF parameters ( $\sigma_x$  and  $\sigma_y$ ) and the uncertainties in the source location ( $\mu_x$  and  $\mu_y$ ) were to be incorporated into the determination of the source intensity in a given energy interval. The means of accounting for uncertainties in parameters derived from calibration data was not apparent based on the limited discussions in the literature (e.g., Cline and Lesser 1970; Lampton *et al.* 1976; Avni 1976). Various options seemed available, but the choice of the appropriate procedure was not immediately obvious. The solution to this problem was the use of an alternative approach known as *bootstrap sampling*. This method provided an independent means of ascertaining the most appropriate use of the  $\chi^2$  technique.

The concept of bootstrap sampling (Efron 1979; Diaconis and Efron 1983; Simpson and Mayer-Hasselwander 1986) is based on the idea that the parent distribution of any experimentally-determined parameter can be determined by repeating the experiment a large number of times. In order to "repeat" the experiment, simulated datasets are derived directly from the measured dataset. These simulated datasets are obtained by randomly sampling the measured dataset with replacement. The distribution of the parameters as measured from a large collection of simulated datasets provides the best estimate of the parent distribution of the parameters. From this estimated distribution, confidence levels can easily be derived. Note that the best-fit values are still derived directly from the measured dataset; the bootstrap procedure simply provides information on the most-

probable *distribution* of the parameters. (See Appendix C for more details about the bootstrap approach.)

In the application of this procedure to the DGT imaging data, the individual data points are represented by the snapshot images ( $N_s$  snapshots for each energy interval). A complete DGT bootstrap sample consists of a simulated (or bootstrap) image for each energy interval along with a sum image which represents the sum of all bootstrap images over the energy range 160 keV to 1 MeV. If we have a total of  $N_{\text{NRG}}$  energy ranges in the spectral analysis, we obtain a total of  $N_{\text{NRG}} + 5$  parameters from a single bootstrap sample. These parameters include the best-fit values of  $\mu_x$ ,  $\mu_y$ ,  $\sigma_x$ ,  $\sigma_y$ , and source intensity as determined from the sum image, along with the  $N_{\text{NRG}}$  intensity values from each of the individual bootstrap images. A large number of such samples were measured for each source (200 for the present analysis). The resulting distribution for each of the bootstrap parameters provides direct information on the allowable range for each parameter. It is important to note that this procedure automatically incorporates the uncertainties in the values of  $\mu_x$ ,  $\mu_y$ ,  $\sigma_x$  and  $\sigma_y$ . As mentioned above, this was a major difficulty of the  $\chi^2$  procedure and one of the primary motivations for our use of the bootstrap.

Although the bootstrap approach provides a very simple algorithm for extracting confidence levels, the requirement of generating a large number of simulated datasets necessarily implies a large amount of computer time. For example, the generation of one bootstrap sample (for  $N_{\text{NRG}} = 7$ ) required roughly one hour on the Z-100. A study of the required number of bootstrap samples was carried out by studying the measured variance of a given parameter versus number of bootstrap samples. It was found that after 200 samples, the measured variance reached an asymptotic value.

### **Determination of Source Photon Spectra**

The actual measurement that one makes with a scintillation detector system is a photon energy-loss spectrum. Due to the various energy-loss mechanisms involved

(primarily the photoelectric, Compton and pair production mechanisms), the energy-loss (or pulse-height) spectrum generally bears little resemblance to the photon spectrum which was incident on the detector. The problem is therefore to determine the incident photon spectrum based only on the measured energy-loss spectrum and the known properties of the detection system. These detector properties are incorporated into what is known as a *response function* which can predict the energy-loss spectrum which would be observed by the detector for a known incident photon spectrum (see Appendix D). The response function is a crucial tool for understanding the measurements made by the detection system. The extent to which a response function is known may, to some degree, dictate the true capability of the experiment.

The problem at hand can best be understood by considering four separate spectra. The first spectrum is that which is emitted by the celestial source. The second spectrum is the spectrum which is incident on the experiment, having been modified by the energy-dependent atmospheric attenuation. The third spectrum is that which actually interacts in the BGO scintillation crystals; this spectrum has been modified by the absorptive effects of the detector enclosure and by the modulation of the coded aperture mask. Finally, the last spectrum is the pulse-height spectrum which is observed by the BGO scintillation detectors.

For the DGT, a response function has been developed which not only incorporates the relevant detector properties, but also accounts for the time-dependent source attenuation by the Earth's atmosphere. This time-dependence is derived directly from the in-flight pointing history of the experiment.

Given the observed pulse-height spectrum, the problem is to determine the spectrum of the observed celestial source. The solution of this problem is an iterative one which makes use of the known response function of the experiment. We start by choosing a trial source spectrum (e.g., a power law). We then proceed through a complete response function (including the effects of atmospheric attenuation, material absorption and mask

modulation) to obtain the corresponding pulse height spectrum. In this fashion, a library of response spectra (i.e, energy-loss spectra) can be generated for various values of the source spectrum parameters. A statistical comparison of the modeled pulse height spectra to that which is actually observed allows a determination of the most probable source spectrum. In a similar fashion, one can proceed to obtain confidence contours in parameter space for the parameters which define the spectral model.

In order to display the experimental spectral data, it is common practice to convert the data points of the energy-loss spectrum into points in "photon-space." This unfolding process is a non-trivial problem. The solution depends directly on the form of the model photon spectrum being used. If the model source spectrum is modified in any way, then the resulting data points will move around in photon-space (an effect sometimes referred to as the *obligance*; Fenimore *et al.* 1983). This effect arises due largely to the fact that, for scintillation detectors, the detector response at a given energy loss depends on the photon spectrum not only at that energy, but also on the photon spectrum at higher energies. For x-ray detectors, where the photoelectric cross-section dominates the detection process, this is not a serious problem; in this case, there exists a unique photon spectrum which can be unfolded using simple matrix techniques.

For the DGT analysis, the conversion of the energy-loss data points into photon-space is achieved in a manner analogous to the procedure used by the SMM GRS experimenters. This procedure assumes that the ratio of counts to flux is the same whether we are concerned with the true data or with modeled data obtained from the response function. More specifically, if we are given the observed counts in the energy loss spectrum ( $\text{Counts}_{\text{obs}}$ ), the predicted counts based on the best-fit photon spectrum ( $\text{Counts}_{\text{pred}}$ ) and the predicted flux based on the best-fit photon spectrum ( $\text{Flux}_{\text{pred}}$ ), then the "observed flux" can be expressed as,

$$\text{Flux}_{\text{obs}} = \text{Flux}_{\text{pred}} \times (\text{Counts}_{\text{obs}} / \text{Counts}_{\text{pred}}) \quad (\text{IV.7})$$

The statistical errors obtained for the data points in energy-loss space are propagated through this expression in order to obtain the corresponding errors for the flux values in photon space.

## CHAPTER V

### Results and Discussion

In this chapter, we review the results obtained from an analysis of the Crab and Cygnus imaging data collected during Flight 1379-P.

#### Crab Region (Galactic Anticenter)

Observations of the galactic anticenter region were motivated, in part, by the desire to use the Crab Nebula/pulsar to evaluate the DGT imaging characteristics. The Crab is one of the brightest and best-studied gamma-ray sources in the sky. It would therefore serve as an ideal "calibration" source for the DGT. In terms of scientific objectives, the search for gamma-ray lines from the Crab is of interest, due to sporadic reports of such emission. The anticenter observation would also permit a study of the diffuse emission which had previously been imaged by Graser and Schönfelder (1982) using the MPE Compton telescope. Finally, this observation provided an opportunity to place constraints on the gamma-ray emission from the x-ray binary A0535+26. (We should also note that the high energy source CG195+4, also known as "Geminga", lies in this region of the sky, but received poor exposure in the DGT imaging data.)

#### Observations

The Crab region was observed by the DGT on two separate occasions during Flight 1379-P. Relevant observational parameters for each of these observations (or "scans") are given in Table V-1. As discussed in Chapter III, a modified drift scan technique was used to collect these data. Pointing updates were sent to the experiment once every 30 minutes; this corresponded to an average source drift (due to diurnal motion) of  $\sim 8^\circ$ . The total



integrated exposure of both Crab scans amounted to 12842 seconds of instrumental livetime, providing an effective exposure of  $3.41 \times 10^6 \text{ cm}^2 \text{ s}$  at 511 keV.

**Table V-1**  
**SCANS OF CRAB REGION**

SCAN	DATE	TIME (UT)	ATM DEPTH ( $\text{gm cm}^{-2}$ )	CRAB ZENITH ANGLE (degrees)	LIVETIME (secs)
1	Oct 2	7:30 - 10:00	2.85 - 3.08	49.0 - 19.0	6375
2	Oct 2	12:30 - 15:00	2.76 - 2.86	21.0 - 52.0	6467

The Crab observations were made during the early morning hours, just around sunrise (which took place at  $\sim 12:10$  UT). It was during this period that the gondola experienced the coldest ambient temperature of the flight. As a result of these cold temperatures (around  $-50^\circ \text{ C}$ ), the response of the inertial orientation system was considerably reduced. The resulting azimuthal instability of the experiment was larger ( $\pm 4^\circ$ ) than at any other time during the flight. Each snapshot image was therefore accumulated to include an effective azimuth range of  $2^\circ$ . A total of 236 snapshot images were derived from the dataset.

#### **Crab Nebula/Pulsar**

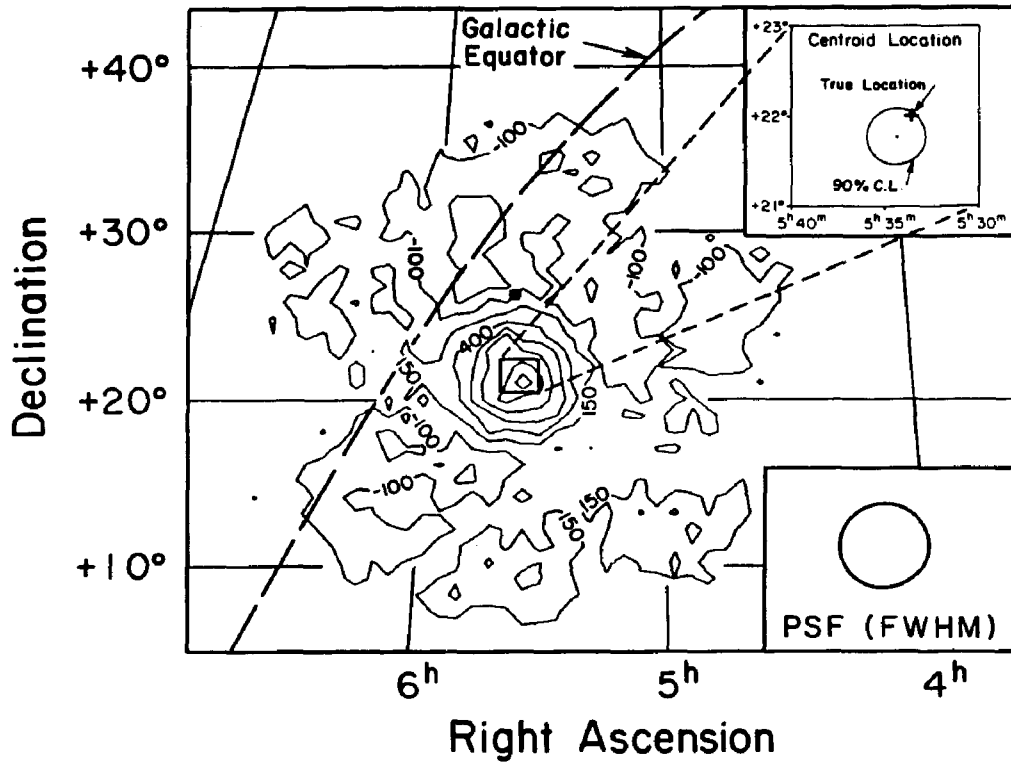
The data accumulated in the 200-600 keV energy range has been used to create the composite image shown in Figure V-1. The image is represented as a contour plot showing the number of reproduced gamma-ray events per  $0.95^\circ$  pixel element. It must be stressed that this does not represent the true distribution of the gamma-ray emission, but rather the true gamma-ray fluence folded through the imaging point-spread-function (PSF) of the instrument. The strong peak reproduced near the center of the image is associated with the emission of the Crab itself.

The in-flight PSF of the imaging system was measured directly using similar imaging data integrated over the energy range 160 keV to 1 MeV. This energy range was chosen so as to optimize the available source statistics. The measurement was accomplished by fitting the peak region using the functional form given in equation (IV.6), thereby allowing the PSF parameters ( $\sigma_x$  and  $\sigma_y$ ), the source location ( $\mu_x$  and  $\mu_y$ ) and the source intensity (number of measured photon counts) to be measured simultaneously. The statistically allowable range (or error) for each of these parameters were determined from a set of 200 bootstrap samples, as outlined in Chapter IV. The total number of reproduced source counts in the peak region, integrated over the energy range 160 keV to 1 MeV, is determined to be  $59715 \pm 4971$  (corresponding to the parameter  $S_T$  in eq. IV.6b). This gives a significance of  $12.0\sigma$  for the Crab measurement in this energy range (with a signal-to-background ratio of 0.9%). The resulting values for  $\sigma_x$  and  $\sigma_y$  determined for the Crab response are statistically equivalent with an average value of  $2.05^\circ \pm 0.20^\circ$ , indicating a symmetric response. This corresponds to a full width at half-maximum (FWHM) of  $4.83^\circ \pm 0.47^\circ$ . For comparison with the imaging data, the full width at half-maximum of the measured PSF is shown in Figure V-1.

The ability to measure the position of a celestial gamma-ray source depends primarily on the measured source statistics and the width of the instrumental PSF. Since the PSF can be approximated by a Gaussian, the estimated centroid location error can be written as,

$$\sigma_{\text{loc}} \equiv \sigma_{\text{PSF}} / n_\sigma \quad (\text{V.1})$$

where  $\sigma_{\text{loc}}$  is the error on the source location,  $\sigma_{\text{PSF}}$  refers to the width of the measured PSF and  $n_\sigma$  is the significance of the measurement (in terms of the number of standard deviations of the source signal above the mean background level). The inset of Figure V-1 shows the 90% confidence contour for the Crab centroid location, based on the bootstrap analysis. This confidence contour is roughly circular with a radius of 19 arc minutes. At



## Crab Region 200-600 keV

**FIGURE V-1:** Reproduced intensity contour of the Crab gamma-ray emission integrated over the energy range 200-600 keV. The contour values represent the number of reproduced gamma-ray events per  $0.95^\circ$  pixel element. The data is consistent with a single point source located at the Crab. The inset shows the 90% confidence contour (as measured in the 160 keV to 1 MeV range). For comparison, the true position of the Crab is also shown. The location of A0535+26 is shown by the small square. (Note that due to the effect of source suppression, the average level of the non-source elements is approximately -80.)

the 68% ( $1\sigma$ ) confidence level, the source is located to an accuracy of  $\pm 12$  arc minutes. From equation (V.1) and the measured values of  $\sigma_{\text{PSF}} = 2.05^\circ$  and  $n_\sigma = 12.0$ , we expect an error of  $\pm 10.3$  arc minutes (at the 68% confidence level), in good agreement with the measured error. The true Crab location (marked with a cross in the insert of Figure V-1) is offset from the measured location by an amount which is consistent with our estimated uncertainty in the pointing system of  $\pm 30$  arc minutes.

In order to construct a spectrum of the Crab, we have produced a total of seven composite images, each covering a different energy interval. The total energy range covered by these observations is 160 keV to  $\sim 9.3$  MeV. From each image, the total number of observed counts was determined by fitting equation (IV.6) to the imaging response of the source, with the source location and PSF parameters fixed at the values determined from fitting the 160 keV to 1 MeV data. Errors on the derived source intensity are determined using a bootstrap analysis. This process allows us to construct an energy-loss spectrum (i.e., number of detected counts as a function of energy) for the Crab. This data is presented in Table V-2 and plotted in Figure V-2.

**Table V-2**  
**CRAB SPECTRAL RESULTS**

ENERGY (keV)	BACKGND COUNTS (12842 seconds)	SOURCE COUNTS (12842 seconds)	MEASURED FLUX ( $\text{cm}^{-2} \text{s}^{-1} \text{MeV}^{-1}$ )
160-200	$1.2025 \times 10^6$	$12359 \pm 1931$	$(1.15 \pm 0.18) \times 10^{-1}$
200-250	$1.0985 \times 10^6$	$16231 \pm 2175$	$(1.16 \pm 0.16) \times 10^{-1}$
250-300	$7.9209 \times 10^5$	$8640 \pm 1596$	$(6.04 \pm 1.12) \times 10^{-2}$
300-400	$1.1187 \times 10^6$	$8037 \pm 1828$	$(2.85 \pm 0.65) \times 10^{-2}$
400-800	$2.4052 \times 10^6$	$12887 \pm 2839$	$(1.29 \pm 0.28) \times 10^{-2}$
800-2000	$1.6937 \times 10^6$	$7850 \pm 2650$	$(4.42 \pm 1.49) \times 10^{-3}$
2000-9300	$7.9312 \times 10^5$	$1172 \pm 1479$	$(1.50 \pm 1.89) \times 10^{-4}$

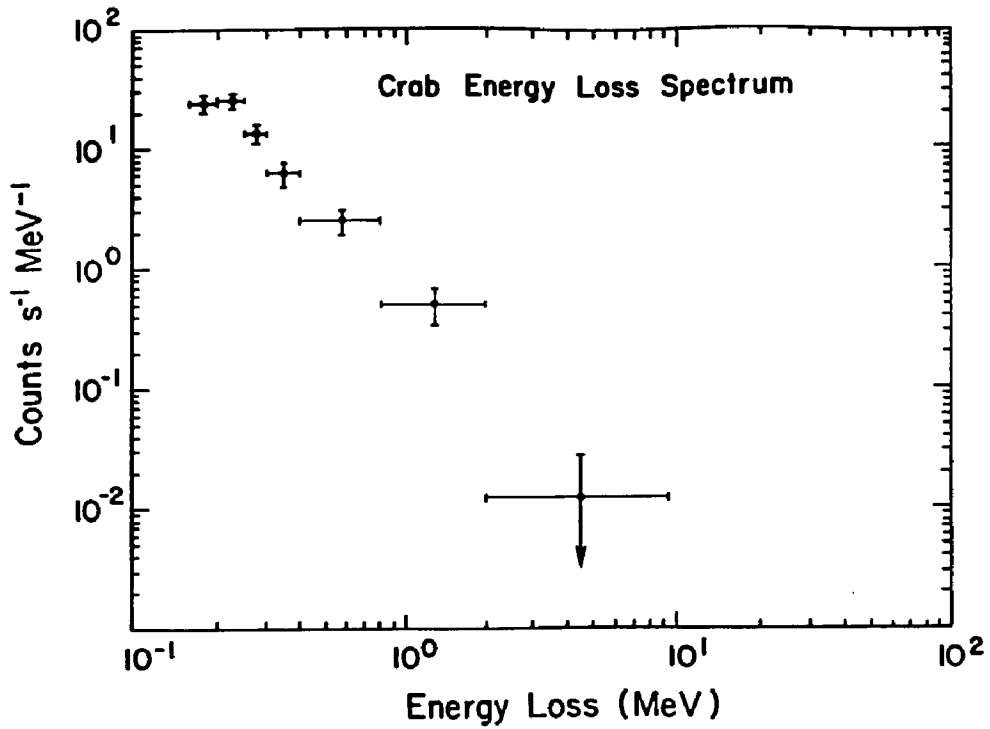


**FIGURE V-2:** The observed energy-loss spectrum of the Crab as derived from seven separate composite images, each covering a different energy range. For each energy range, the measured point-spread-function (PSF) was used to determine the total source response. The total integrated livetime for this observation is 12842 seconds.

The consistency of the Crab spectral data has been studied by dividing the entire Crab dataset into four equal intervals of time, each spanning roughly 1-1/2 hours. (Each scan listed in Table V-1 is split into two equal time periods.) For each energy range used in the analysis, the measured counts in each time frame were corrected to common livetime and zero atmospheric depth. In this way, the response for each time interval could be directly compared. A  $\chi^2$  analysis was used to test the resulting data for time variability within each energy range. The results are consistent with a constant mean count rate throughout the entire observation period. Furthermore, the power-law photon spectral parameters derived from these four energy-loss spectra were consistent at the 99% confidence level.

The measured energy-loss spectrum for the entire dataset has been used to derive the best-fit power-law source spectrum using the known response function of the DGT (see Appendix D). The best-fit photon spectrum is given by  $5.1 \times 10^{-3} E_{\text{MeV}}^{-1.88}$  photons  $\text{cm}^{-2} \text{s}^{-1} \text{MeV}^{-1}$ . This form gives a reduced  $\chi^2$  of 1.50 for 5 degrees of freedom (probability of exceeding  $\chi^2$ ,  $P_{\chi^2}$ , of 0.19). (A closer look at the  $\chi^2$  analysis is given in Appendix E.) Each data point in the energy-loss spectrum has been converted into a photon flux value using this best-fit photon spectrum. The results are given in Table V-2 and Figure V-3. Figure V-3 also shows the 90% confidence contour for the joint estimation of the two parameters  $A$  and  $\alpha$ .

The DGT results for the total Crab spectrum (i.e., pulsed plus unpulsed) are consistent with previous spectral measurements in this energy range, as evidenced by the representative data from other experiments which are plotted in Figure V-3. Due to the lack of precise timing information for each event in the DGT datastream, we have been unable to extract the pulsar spectrum. The derived spectrum therefore represents the total (i.e., pulsed plus unpulsed) spectrum of the Crab.

In addition to the measurement of the Crab continuum radiation, we have also performed a search of the Crab data for line emission at 404.7 keV and 1049.8 keV. The

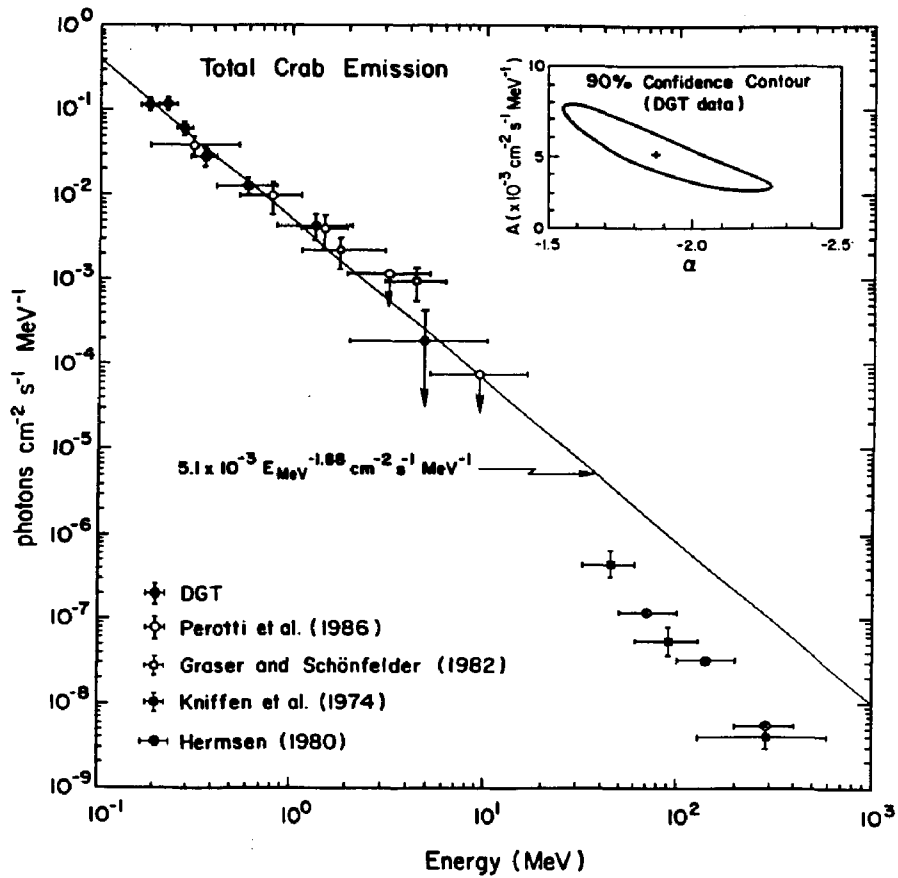


**FIGURE V-3:** The total Crab photon spectrum as measured by the DGT. The solid line represents the best fit to the DGT data using a power-law spectral model of the form  $dN(E)/dE = A E^{-\alpha}$ . The inset shows the 90% confidence contour for the joint estimation of the two parameters  $A$  and  $\alpha$ . Other representative measurements are shown for comparison.

search was accomplished by producing composite images integrated over three energy ranges for each line energy - one range centered on the line location and one on either side of the line location. The flux of the candidate line was determined by comparing counts in the center bin with the average source continuum on either side of the central bin. Each energy range corresponds to 1.2 times the FWHM of the detector energy resolution at the line energy; it has been shown (Jacobson *et al.* 1975) that this is the optimum bin width (in terms of signal-to-noise) with which to detect a line in the presence of a background continuum. The measured residuals are consistent with zero flux, allowing us to place  $3\sigma$  upper limits on line emission at 404 and 1049 keV of  $3.0 \times 10^{-3}$  and  $1.9 \times 10^{-3}$  photons  $\text{cm}^{-2} \text{s}^{-1}$ , respectively. These results can be compared with the recent positive measurements of Owens *et al.* (1985a) which are given by intensities of  $(7.2 \pm 2.1) \times 10^{-3}$  and  $(2.0 \pm 0.5) \times 10^{-2}$  photons  $\text{cm}^{-2} \text{s}^{-1}$  for line emission at 404.7 and 1049.8 keV, respectively. The DGT upper limits lie below both of these flux values. For the emission at  $\sim 400$  keV, positive measurements have also been made by Leventhal *et al.* (1977) and Yoshimori *et al.* (1979), with measured flux values given by  $(2.24 \pm 0.65) \times 10^{-3}$  photons  $\text{cm}^{-2} \text{s}^{-1}$  and  $(7.4 \pm 5.4) \times 10^{-3}$  photons  $\text{cm}^{-2} \text{s}^{-1}$ , respectively. The origin of this feature is generally presumed to be due to gravitationally-redshifted electron-positron annihilation near the surface of the pulsar. The measurements would correspond to redshifts of  $z = 0.27$  (Owens *et al.* 1985a) or  $z = 0.28$  (Leventhal *et al.* 1977; Yoshimori *et al.* 1979). In addition to these positive measurements, a number of observers have reported upper limits on the flux at this energy (e.g., Ling *et al.* 1977; Hameury *et al.* 1983; Mahoney *et al.* 1984); all of these upper limits lie below the positive measurements given above. At present, there is no general agreement regarding the flux level (or even the existence) of this feature. In addition, there is as yet no viable explanation for the line emission observed at 1049.8 keV. Further observations will be required in order to establish the existence of both of these features.



Our measurement of the total Crab photon spectrum is consistent with a power law source spectrum showing no evidence for any features to within the energy resolution of the experiment. In addition to the line limits given above, we find no evidence for any broad-band excess emission over the power-law at energies  $>1$  MeV, as had been reported by some previous observers (Baker *et al.* 1973; Gruber and Ling 1977). Gruber and Ling suggested that this emission might be due to the nearby source A0535+26. However, the DGT detected no measurable flux from this object (see below), indicating that A0535+26 does not contribute to the observed Crab spectrum at MeV energies. Ayre *et al.* (1983) suggested that the narrow line emission observed at 1049.8 keV might account for the observed "MeV excess." The present results do not support this hypothesis.

The extension of the DGT power-law spectrum to high energies does not, at first, appear to agree with the measured data points from the SAS-2 or COS-B satellites (see Figure V-3). It should be noted, however, that the allowable parameter ranges for the DGT spectral fit are quite large. A single power law can, in fact, be used to simultaneously describe the DGT and COS-B data. The best fit for such a model is given by  $2.67 \times 10^{-3} E_{\text{MeV}}^{-2.33}$  photons  $\text{cm}^{-2} \text{s}^{-1} \text{MeV}^{-1}$ , giving a reduced  $\chi^2$  of 1.71 for 9 degrees of freedom ( $P_\chi = 0.08$ ). We conclude that the DGT data is not inconsistent with a single power law spectrum extending over this entire energy range.

#### **A0535+26**

In addition to the Crab Nebula/pulsar, the image of the Crab region also contains two other sources of interest. The first such source is the flaring x-ray binary source A0535+26, whose angular separation from the Crab is only  $4.4^\circ$ . Its location is shown as a small black square in Figure V-1. An analysis of the imaging data shows no evidence for this source. Upper limits on the flux level from A0535+26 have been derived using a procedure which fits both the Crab and A0535+26 simultaneously. This procedure incorporated the measured PSF and the known location of A0535+26 (corrected by the

offset between the measured and known Crab locations). The  $1\sigma$  upper limits which were derived are given in Table V-3 and in Figure V-4.

Past observations of A0535+26 (see Hameury *et al.* 1983 and references therein) suggest a 111-day period between successive "high" states, at which times it can attain a flux level five times that of the Crab at 20 keV. Based on the 111 day period and extrapolating from the high-state observations of 5 October 1980 (e.g., Hameury *et al.* 1983; Frontera *et al.* 1982), we find that the DGT observation took place only 14 days after the time of predicted peak activity. We cannot determine with any degree of certainty, however, which state the source was in at the time of the observations. As shown in Figure V-4, the DGT upper limits are inconsistent with power-law extrapolations of x-ray data obtained in both the low state (Polcaro *et al.* 1982) and the high state (e.g., Hameury *et al.* 1983). Although not conclusive, this result tends to support the interpretation of the A0535+26 photon spectrum as being best described by either an exponential (e.g., Hameury *et al.* 1983) or a thermal (e.g., Frontera *et al.* 1982) spectrum. Such a spectrum is consistent with the types of spectra which are generally observed for binary x-ray pulsars (Joss and Rappaport 1984).

Table V-3  
CRAB REGION  $1\sigma$  UPPER LIMITS

ENERGY (keV)	A0535+26 ( $\text{cm}^{-2} \text{s}^{-1} \text{MeV}^{-1}$ )	DIFFUSE EMISSION ( $\text{cm}^{-2} \text{s}^{-1} \text{rad}^{-1} \text{MeV}^{-1}$ )
160-200	$2.22 \times 10^{-2}$	$3.15 \times 10^{-1}$
200-250	$1.60 \times 10^{-2}$	$1.91 \times 10^{-1}$
250-300	$1.12 \times 10^{-2}$	$1.34 \times 10^{-1}$
300-400	$6.50 \times 10^{-3}$	$7.76 \times 10^{-2}$
400-800	$2.80 \times 10^{-3}$	$3.34 \times 10^{-2}$
800-2000	$1.49 \times 10^{-3}$	$1.78 \times 10^{-2}$
2000-9300	$2.49 \times 10^{-4}$	$2.97 \times 10^{-3}$

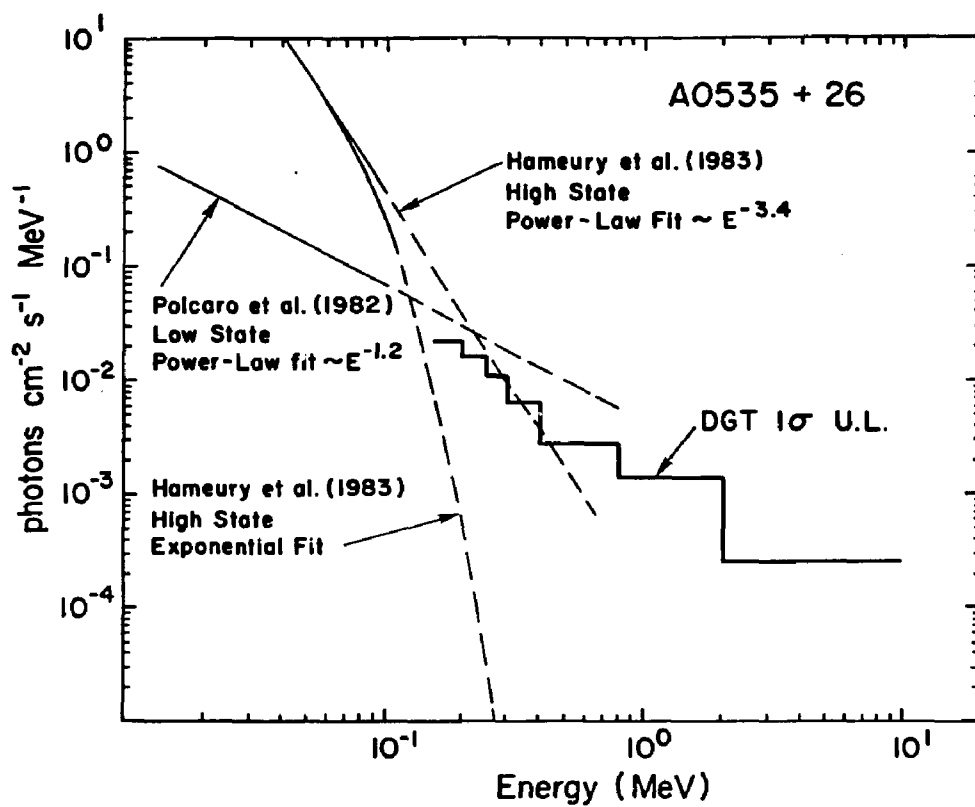


**FIGURE V-4:** The upper limit flux levels from A0535+26 as derived from the DGT imaging data. Lower energy x-ray measurements (<100 keV), along with their extrapolation to higher energies, are shown for comparison.

### **Galactic Anticenter Diffuse Emission**

The third and final source of interest in this image is the anticenter diffuse flux. This is a spatially distributed flux which has been measured in the 1-10 MeV range by Graser and Schönfelder (1982). This emission, located near the Crab, was observed to lie along the galactic equator with a FWHM scale height relative to the galactic plane of roughly  $4^\circ$ . The DGT image of this region shows no evidence for such emission. The imaging data has therefore been used to set upper limits on the diffuse flux. The emission has been modeled using a series of point sources distributed along  $15^\circ$  of the galactic plane (galactic longitude range,  $l = 175^\circ$ - $190^\circ$ ), thus approximating the distribution observed by Graser and Schönfelder (1982). The resulting upper limits are given in Table V-3 and in Figure V-5. These upper limits lie above the data points of Graser and Schönfelder (1982) for  $l = 160^\circ$ - $197^\circ$  as well as the theoretical calculations of Sacher and Schönfelder (1983) for the interactions of cosmic ray electrons in the interstellar medium. The calculations are based on a  $E^{-2.8}$  interstellar electron spectrum, as derived from COS-B data (Lebrun *et al.* 1982).

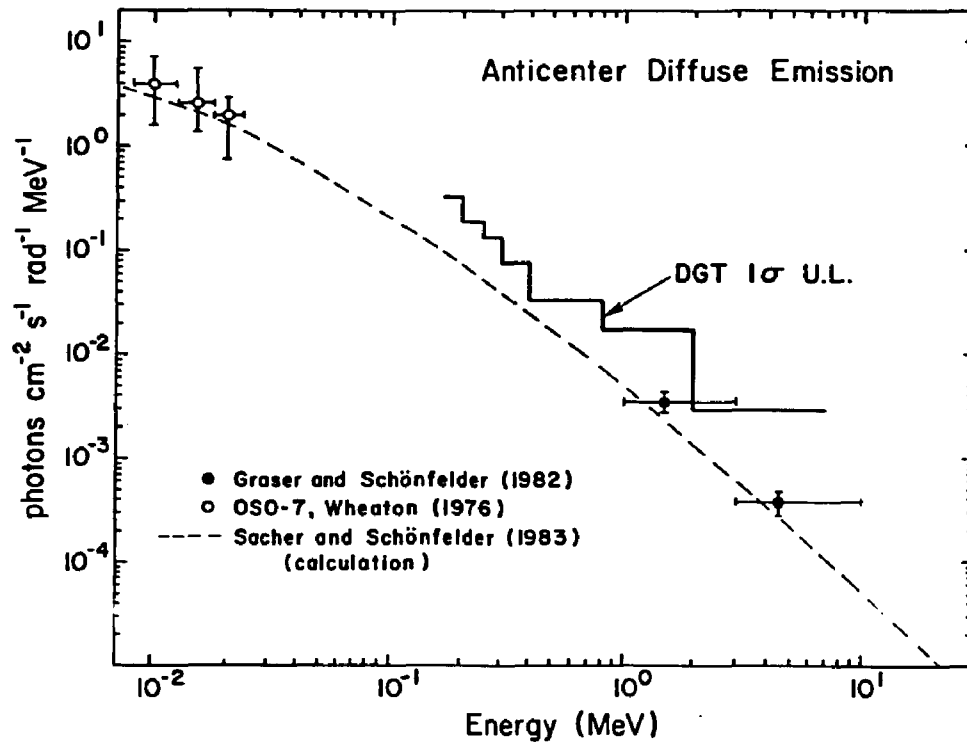


**FIGURE V-5:** The upper limit flux levels from the galactic anticenter diffuse emission (galactic longitude,  $l = 175^\circ$ - $190^\circ$ ) as derived from the DGT imaging data. The measurements of Wheaton (1976) for  $l = 240^\circ$  and those of Graser and Schönfelder (1982) for  $l = 160^\circ$ - $197^\circ$  are shown for comparison. The calculations of Sacher and Schönfelder (1983) for the emission due to an  $E^{-2.8}$  interstellar electron spectrum (Lebrun *et al.* 1982) are also shown.

## Cygnus Region

An observation of the Cygnus region permitted the simultaneous observation of two important high-energy sources - Cygnus X-1 and Cygnus X-3. Separated by only  $8^\circ$ , past experiments could not always clearly resolve the emission from these two sources. The imaging capability of the DGT provided a unique opportunity to obtain clearly resolved spectra from these two sources. From the experimental point of view, such an observation would provide a good demonstration of the ability of the coded aperture technique to resolve nearby sources.

### Observations

The DGT data for the Cygnus region were obtained during two time periods of the flight. The relevant parameters for these two observations are given in Table V-4. As with the Crab data, the Cygnus data were collected using a modified drift scan technique. The pointing requirements of this observation were, however, more stringent due to the desire to maintain both Cyg X-1 and Cyg X-3 within the imaging field-of-view. Pointing updates were provided to the experiment once every 20 minutes (instead of once every 30 minutes, as with the Crab measurements). The total integrated exposure of both Cygnus scans amounted to 13039 seconds, providing an effective exposure of  $1.39 \times 10^7 \text{ cm}^2 \text{ s}$  at 511 keV.

**Table V-4**  
**SCANS OF CYGNUS REGION**

SCAN	DATE	TIME (UT)	ATM DEPTH ( $\text{gm cm}^{-2}$ )	CYG X-1 ZENITH ANGLE (degrees)	LIVETIME (secs)
1	Oct 1-2	21:30 - 00:30	3.09 - 3.50	51.0 - 19.0	6008
2	Oct 2	3:30 - 6:00	2.78 - 3.10	24.0 - 54.0	7031

Two special considerations were involved in the analysis of the Cygnus data. First, there were times during the observations when Cyg X-1 was within  $1.9^\circ$  of the outside edge of the nominal field-of-view. (This resulted from the attempt to maintain both Cyg X-1 and Cyg X-3 within the field-of-view.) Recall (from Chapter II) that the region of the field-of-view which is within  $1.9^\circ$  (one-half image element) of the edge of the nominal field is not fully coded (i.e., not part of the legal field-of-view). For this reason, any Cygnus data collected when Cyg X-1 was in this region of the field-of-view was excluded from the image analysis. A total of  $\sim 900$  seconds of data were rejected as a result of this problem. Some appropriate analysis procedure may, however, be able to recover much of this data.

During the first of the two Cygnus scans, the shield high-voltage supply was behaving erratically. As discussed in Chapter III, the shield problem was noticeable primarily due to the change in instrumental livetime from  $\sim 84\%$  (normal) to  $\sim 90\%$  (abnormal). It had been determined that the background systematics varied between these two shield states. Since all data analysis (including the determination of the background systematics) took place during normal shield state, it was decided to selectively accumulate this erratic data. Each one second record of flight data was either accepted or rejected based on the measured livetime for that one second. If the livetime was measured to be greater than  $85.5\%$ , then the one second record was rejected from the analysis. This selection criterion resulted in the rejection of  $\sim 1300$  seconds of Cygnus data. A study of the systematics using this same selection requirement indicated that the resulting systematics were statistically equivalent to those measured during the normal shield state.

The azimuthal instability during this period was observed to be  $\pm 3^\circ$ . This was as good as at any other time during the flight. Since four snapshot images are used to cover the entire range of the instability (see Chapter IV), the resulting snapshot images were integrated over an azimuth range of  $1.5^\circ$ . A total of 276 snapshot images were derived from the Cygnus dataset.

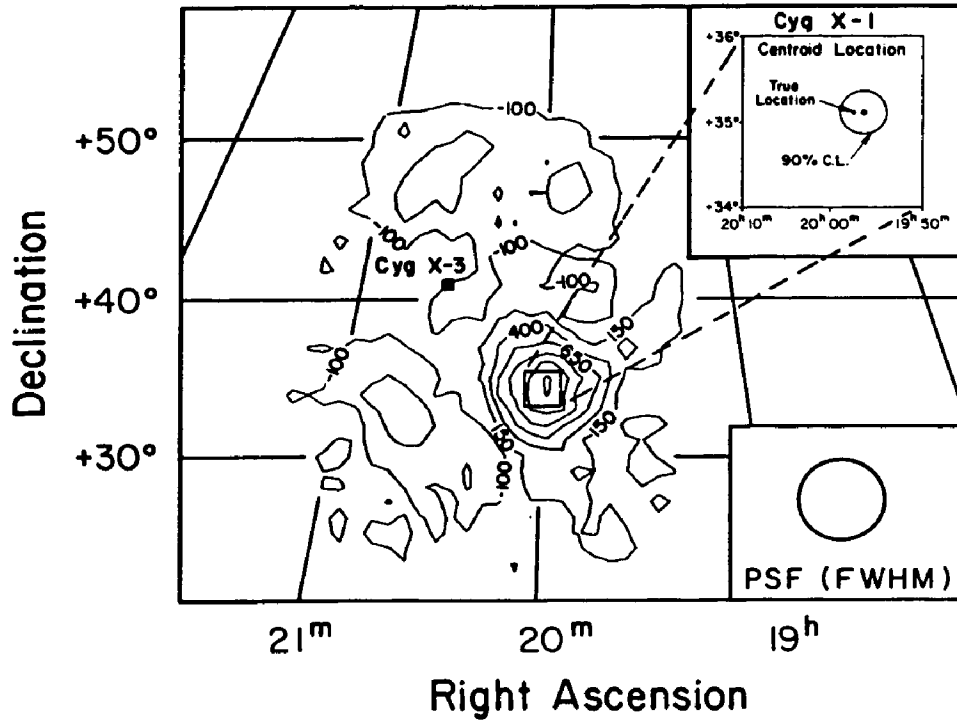
### Cygnus X-1

The total Cygnus dataset (13039 seconds of instrumental livetime) integrated over the energy range of 200-600 keV has been used to create the composite image shown in Figure V-6. As with Figure V-1, this contour map represents the number of reproduced gamma-ray events per  $0.95^\circ$  pixel element. Cyg X-1 stands out in this image as the prominent peak just to the lower right of the image center. On the other hand, Cyg X-3 (whose position is denoted by a small square) shows no measurable counting rate excess. The data are consistent with a single point source at the location of Cyg X-1.

As with the Crab data, the source location and PSF parameters were determined using imaging data integrated over the energy range 160 keV to 1 MeV. A fit of equation (IV.6) provided values for the source location ( $\mu_x$  and  $\mu_y$ ), the PSF parameters ( $\sigma_x$  and  $\sigma_y$ ) and the integrated source counts. Errors on these five parameters were obtained using a bootstrap analysis with 200 bootstrap samples. The total number of reproduced source counts in the peak region of Cyg X-1, integrated over the energy range 160 keV to 1 MeV, has been determined to be  $78910 \pm 7052$ . This corresponds to a total source significance of  $11.2\sigma$  in this energy range, with a source-to-background ratio of 1.1%. The measured values for  $\sigma_x$  and  $\sigma_y$  are statistically equivalent with an average value given by  $2.15^\circ \pm 0.10^\circ$ . The 90% confidence contour for the peak centroid location of Cyg X-1 is shown in the insert of Figure V-6. The corresponding  $1\sigma$  (i.e., 68% confidence level) uncertainty in the measured Cyg X-1 source location is  $\pm 9.7$  arc minutes; this can be compared with the expected error (c.f., eq. V.1) of  $\pm 11.5$  arc minutes. As in the case of the Crab results, the measured location of Cyg X-1 is offset from the true location by an amount which is consistent with the estimated pointing uncertainty of the experiment.

The Cyg X-1 energy-loss spectrum has been determined from a set of 11 independent composite images of the Cygnus region. As before, the total number of counts reproduced in a given image were determined by fitting equation (IV.6) to the imaging response of the source, with the source location ( $\mu_x$  and  $\mu_y$ ) and PSF parameters





### Cygnus Region 200-600 keV

**FIGURE V-6:** Reproduced gamma-ray intensity contour map of the Cygnus region. The contour values represent the reproduced number of gamma-ray events per 0.95° image element. These data are consistent with a single point source located at the position of Cygnus X-1. The insert shows the 90% confidence contour for the measured location of Cygnus X-1 (as measured in the 160 keV to 1 MeV range). For comparison, the true position of Cygnus X-1 is also shown. The location of Cygnus X-3 is noted by a small square.

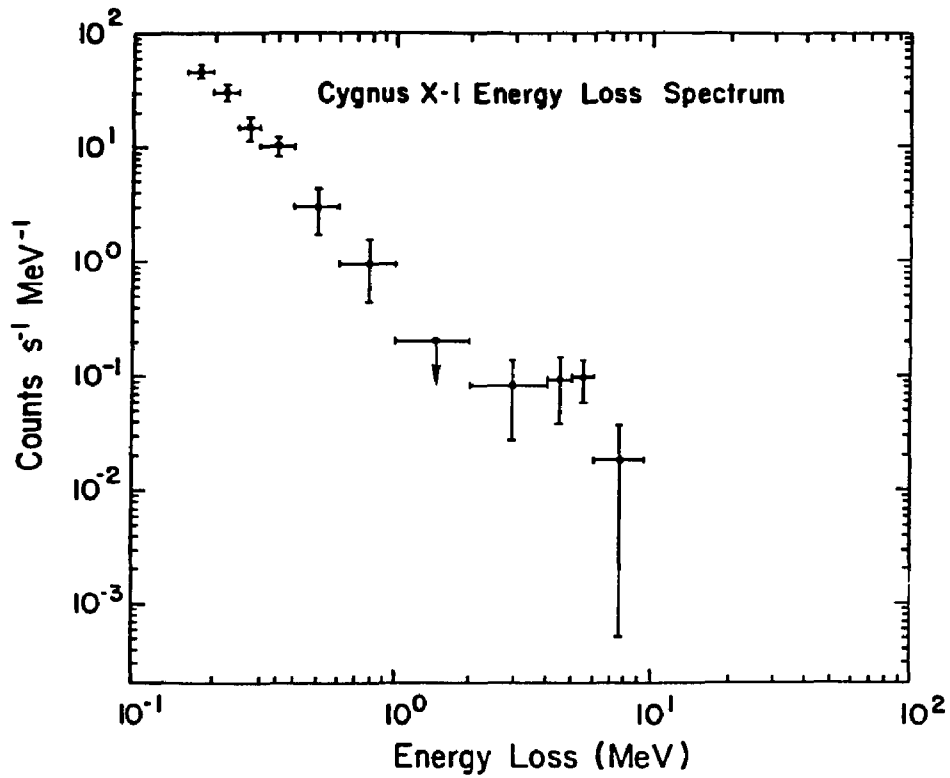


**FIGURE V-7:** The observed energy-loss spectrum of Cyg X-1 as derived from eleven separate composite images, each covering a different energy range. For each energy range, the measured point-spread-function (PSF) was used to determine the total source response. The total integrated livetime for this spectrum is 13039 seconds.

( $\sigma_x$  and  $\sigma_y$ ) fixed at the values measured in the 160 keV to 1 MeV energy range. Errors on the derived source intensities are determined using a bootstrap analysis technique with 200 bootstrap samples. The resulting energy-loss data is given in Table V-5 and displayed in Figure V-7.

The Cyg X-1 spectral data has been checked for consistency by studying the measured energy-loss spectra in four separate time intervals. We found marginal evidence for time variability in one of the 11 energy intervals, that corresponding to the 200-250 keV energy range. In this energy range, the derived value for the reduced  $\chi^2$  (under a constant count rate hypothesis) is 4.15 for 3 degrees of freedom ( $P_\chi = .006$ ). This implies a 0.6% probability that the count rate was constant in this energy range. Alternatively, one can state that there is evidence for time variability at roughly the  $3\sigma$  level. Given the limited energy resolution which has been used in this analysis, we can not rule out the possibility of some transient line feature. In the analysis which follows, we have treated this variability as a statistical effect. The Cyg X-1 count rates at all other energies (including those above 2 MeV) were found to be consistent with a constant mean count rate.

We have tested various parameterized source photon spectral models using the total energy-loss spectrum. The simplest photon spectral model is that of a pure power-law spectrum. The DGT data taken by itself is consistent with a single featureless power-law given by  $3.73 \times 10^{-3} E_{\text{MeV}}^{-2.35}$  photons  $\text{cm}^{-2} \text{s}^{-1} \text{MeV}^{-1}$ . This provides a marginally acceptable fit with a reduced  $\chi^2$  of 1.71 for 9 degrees of freedom ( $P_\chi = 0.08$ ). The largest contributions to the  $\chi^2$  come from the data points above 1 MeV (see Appendix E). The spectrum derived from this fit is given in Table V-5 and displayed in Figure V-8. This power-law spectrum, extended to x-ray energies, is not consistent with the x-ray data for Cyg X-1; the x-ray data generally follows a much harder power-law index of about -1.6 (see discussion below). The DGT power-law is also inconsistent with the upper limit derived from SAS-2 data at energies above 100 MeV (Fichtel *et al.* 1975). Furthermore, the data points above 1 MeV (which contribute the most to the measured  $\chi^2$ ) indicate the

possibility of a flattening of the spectrum at these energies. We conclude, therefore, that although this power-law may be used to describe the DGT data, its extension beyond the DGT energy range is inconsistent with available data. Tests using other spectral models are therefore warranted.

**Table V-5**  
**CYGNUS X-1 SPECTRAL RESULTS**

ENERGY (keV)	BACKGND COUNTS (13039 secs)	SOURCE COUNTS (13039 secs)	Power-Law FLUX ( $\text{cm}^{-2} \text{s}^{-1} \text{MeV}^{-1}$ )	Pwr-Law plus Compton FLUX ( $\text{cm}^{-2} \text{s}^{-1} \text{MeV}^{-1}$ )
160-200	$1.2210 \times 10^6$	23800±2750	$(2.13 \pm 0.25) \times 10^{-1}$	$(2.26 \pm 0.26) \times 10^{-1}$
200-250	$1.1154 \times 10^6$	19560±3138	$(1.34 \pm 0.22) \times 10^{-1}$	$(1.41 \pm 0.23) \times 10^{-1}$
250-300	$8.0425 \times 10^5$	9549±2198	$(6.60 \pm 1.52) \times 10^{-2}$	$(6.78 \pm 1.56) \times 10^{-2}$
300-400	$1.1358 \times 10^6$	13255±2454	$(4.59 \pm 0.85) \times 10^{-2}$	$(4.62 \pm 0.86) \times 10^{-2}$
400-600	$1.7918 \times 10^6$	7824±3425	$(1.52 \pm 0.67) \times 10^{-2}$	$(1.36 \pm 0.59) \times 10^{-2}$
600-1000	$1.0875 \times 10^6$	4922±3120	$(6.20 \pm 3.93) \times 10^{-3}$	$(4.89 \pm 3.10) \times 10^{-3}$
1000-2000	$1.2825 \times 10^6$	-3815±2695	$< 2.22 \times 10^{-3}$	$< 1.88 \times 10^{-3}$
2000-4000	$4.5962 \times 10^5$	2135±1430	$(1.46 \pm 0.98) \times 10^{-3}$	$(9.96 \pm 6.67) \times 10^{-4}$
4000-5000	$1.0953 \times 10^5$	1193±699	$(2.00 \pm 1.17) \times 10^{-3}$	$(1.20 \pm 0.70) \times 10^{-3}$
5000-6000	$7.7191 \times 10^4$	1265±535	$(2.09 \pm 0.89) \times 10^{-3}$	$(1.31 \pm 0.55) \times 10^{-3}$
6000-9300	$1.5947 \times 10^5$	805±783	$(4.05 \pm 3.94) \times 10^{-4}$	$(2.83 \pm 2.76) \times 10^{-4}$

X-ray observations of Cyg X-1 are generally described in terms of a single-temperature inverse Compton model (Sunyaev and Titarchuk 1980) with electron temperatures in the range of 20-80 keV and optical depths of 2-5 (e.g., Sunyaev and Trümper 1979; Nolan *et al.* 1981; Steinle *et al.* 1982). The inverse Compton model explains many of the observed x-ray features of Cyg X-1, including not only the observed spectrum, but also the spectral changes which result from changes in the overall luminosity. An attempt to fit the entire DGT spectrum with a single-temperature inverse Compton spectrum resulted in best-fit parameters of  $kT_e = 177$  keV and  $\tau = 0.6$ . This model results in a reduced  $\chi^2$  of 1.96 for 8 degrees of freedom ( $P_\chi = 0.045$ ), indicating an unacceptable fit. (Values of  $P_\chi$  outside of the range 0.05-0.95 are considered to be

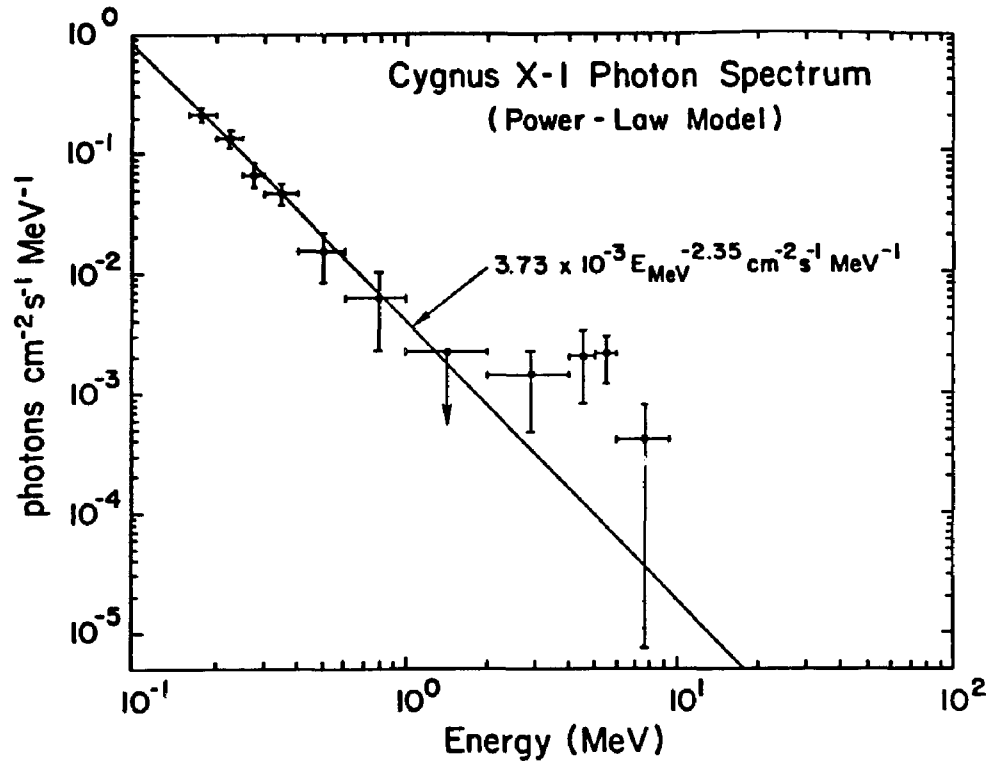


**FIGURE V-8:** The best-fit Cygnus X-1 power-law source spectrum. This model provides an acceptable representation of the data, with a  $\chi^2$  of 1.71 for 9 degrees of freedom.

unacceptable.) Although the emission below 1 MeV can be adequately described by such a model, the model falls far short of the data points above 2 MeV (see Appendix E). Based on these results, a single-temperature inverse Compton model is ruled out as an explanation for the entire DGT energy-loss spectrum.

The success of the inverse Compton model in explaining not only the x-ray measurements, but also the DGT data *below* 1 MeV (along with the sound theoretical basis for such a model) leads us to the conclusion that the DGT results *above* 1 MeV must arise due to some other production mechanism. Based on the discussion in Chapter I, at least three possibilities present themselves in the context of current models of Cyg X-1: 1) a high-temperature, blue-shifted annihilation line (Ramaty and Mészáros 1981), 2) electron bremsstrahlung resulting from the decay of charged pions in the accretion flow (e.g., Eilek and Kafatos 1980) or 3) continuum nuclear line emission. In what follows, we shall consider each of these models in the context of the present observations.

We have first investigated the possibility that the data points above 1 MeV can be described in terms of a high-temperature annihilation line. Such a line can be modeled (based on Ramaty and Mészáros 1981) as a Gaussian with a mean photon energy of  $1.2 kT_e$  and a FWHM of  $2.61 kT_e$ . (Although the model of Ramaty and Mészáros (1981) predicts that the annihilation feature will be asymmetric, the symmetric Gaussian used here is sufficient for the purposes of estimating the annihilation temperature, especially given the limited statistics of our data.) This model photon spectrum has been successfully fit to the DGT data between 1 and 9.3 MeV. The results of this analysis are displayed in Figure V-8 in which the minimum  $\chi^2$  is plotted versus the corresponding electron plasma temperature. Based on this data, the most probable temperature for such an annihilation feature is 3.5 MeV, with a reduced  $\chi^2$  of 1.4 for 4 degrees of freedom ( $P_\chi = 0.20$ ). At the  $2.6\sigma$  (99% confidence) level, these results would constrain the electron temperature ( $T_e$ ) of such an annihilation region to be greater than 1.5 MeV. (Any effects resulting from a gravitational redshift would imply that the true temperature of the annihilation region is even higher than

the 3.5 MeV quoted here.) The derived temperature is inconsistent with the electron temperatures (<100 keV) which are required to explain the low energy emissions via the inverse Compton process. This discrepancy might be reconciled by assuming that the annihilation region is spatially distinct from that which produces the low-energy continuum. Although the present data cannot exclude this possibility, we consider this to be an unlikely explanation for the observed 2-9.3 MeV emission.

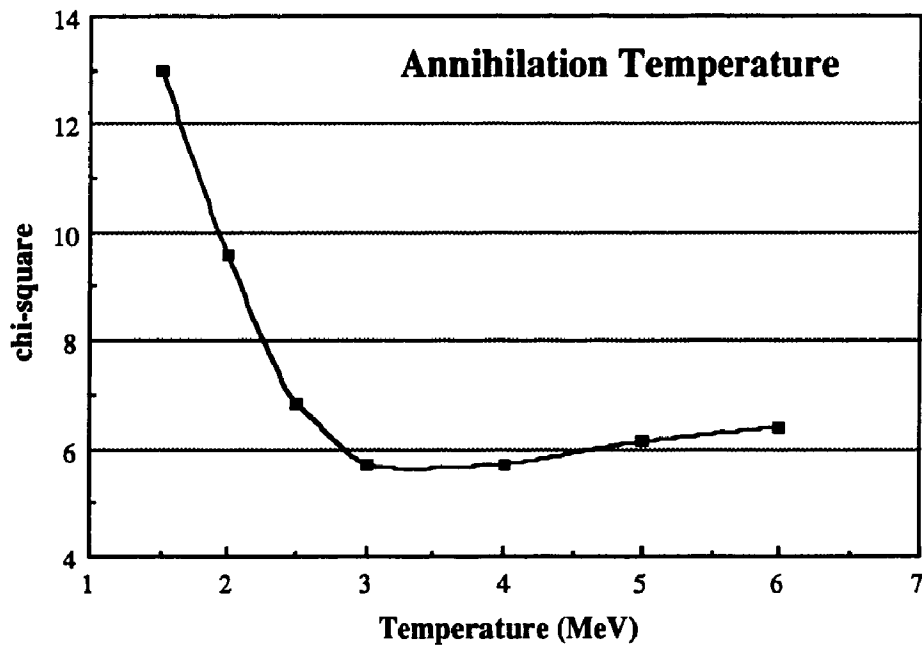


**FIGURE V-9:** The minimum chi-square vs. the electron temperature of the annihilation region. These results were obtained from a fit of the 1-9.3 MeV data. The high temperature implied by these results is inconsistent with the electron temperatures required to explain the observed x-ray emission.

In order to derive reasonable estimates of the photon flux above 1 MeV, the high-energy data (1-9.3 MeV) have been fit with a single power-law model. Given the limited statistical quality of the DGT data above 1 MeV, a power-law model can be used to represent either an electron bremsstrahlung spectrum or a nuclear line continuum. The

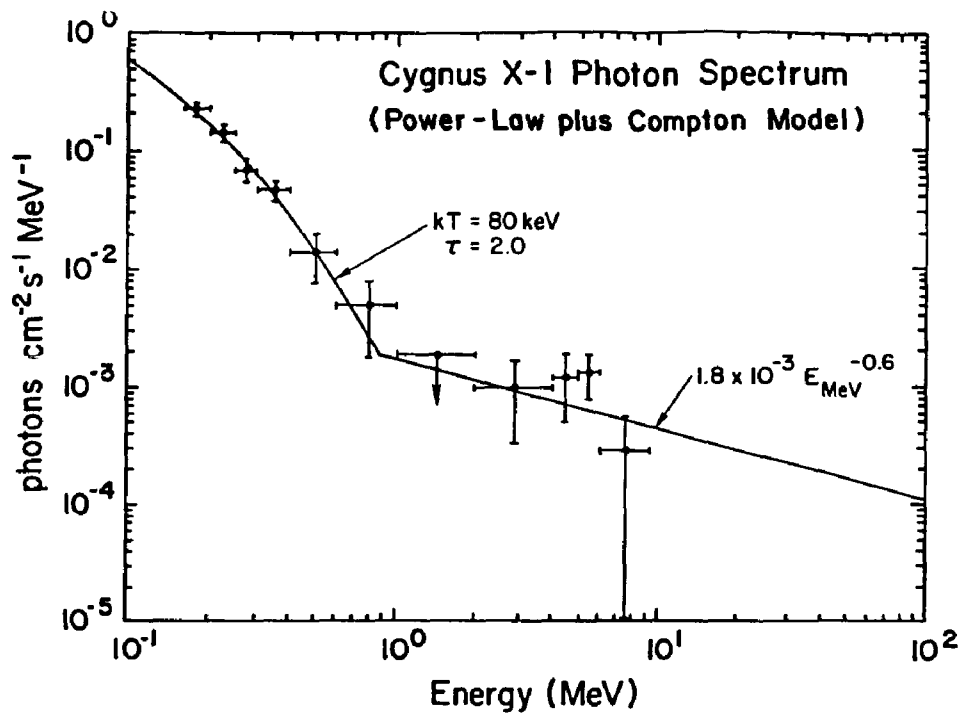


**FIGURE V-10:** The photon spectrum of Cygnus X-1 derived from a model which consists of a power-law (fit to the data above 1 MeV) and an inverse Compton model. This particular model provides a reduced  $\chi^2$  of 1.60 for 6 degrees of freedom.



resulting best-fit power-law is of the form  $1.8 \times 10^{-3} E_{\text{MeV}}^{-0.6}$  photons  $\text{cm}^{-2} \text{s}^{-1} \text{MeV}^{-1}$ , providing a reduced  $\chi^2$  of 2.40 for 3 degrees of freedom ( $P_\chi = 0.07$ ). In order to obtain an acceptable fit to the entire DGT energy-loss spectrum, we have constrained this high-energy power-law to its best-fit value (given above), extended this to the low energy end of the spectrum and included an inverse Compton model in order to adequately fit the data below 1 MeV. This composite model gives best-fit inverse Compton parameters of  $kT_e \approx 175$  keV and  $\tau \approx 0.6$ , with a reduced  $\chi^2$  of 1.45 for 6 degrees of freedom ( $P_\chi = 0.20$ ). A photon spectrum has been derived from this model using the Compton parameters  $kT_e = 80$  keV and  $\tau = 2.0$ . These parameters lie within the 68% ( $1\sigma$ ) confidence contour for the fit to the DGT data and are in reasonable agreement with low-energy x-ray data (see Figure V-12 below). The photon spectrum which is derived from these parameters is tabulated in Table V-5 and displayed in Figure V-10. (See Appendix E for more detailed information on the  $\chi^2$  results.)

Let us first look at the implications of the derived flux values for the possibility of pion production in the accretion region. As discussed in Chapter I, this pion production would arise due to p-p interactions within the hot (thermalized) ion population ( $T_i \sim 10^{12}$  K). These interactions lead to both the production of neutral pions ( $\pi^0$ ) and charged pions ( $\pi^\pm$ ). The neutral pions decay and produce gamma-ray emission with a broad peak centered at  $\sim 68$  MeV. The charged pions decay into muons which, in turn, decay into an electron or a positron. The resulting  $e^\pm$  particles can then radiate via collisional bremsstrahlung. It is this bremsstrahlung emission which might provide an explanation for the observed 2-9.3 MeV flux. If this is the case, however, we should be able to predict the associated  $\pi^0$  flux and compare that estimate with gamma-ray results from the SAS-2 satellite.

In order to determine the corresponding  $\pi^0$  flux, we can make use of the model proposed by Eilek and Kafatos (1980) for a disk which is optically thin to  $\gamma\text{-}\gamma$  pair production. Normalizing their modeled photon spectra (based on their Figure 2) to the

measured DGT flux at 1 MeV, we find the estimated  $\pi^0$  flux between 100 and 150 MeV to be  $\sim 3.5 \times 10^{-3}$  photons  $\text{cm}^{-2} \text{s}^{-1}$ . This number can be directly compared with experimental results from the SAS-2 satellite. These results provide an upper limit for Cyg X-1 at energies above 100 MeV of  $2.7 \times 10^{-6}$  photons  $\text{cm}^{-2} \text{s}^{-1}$  (Fichtel *et al.* 1975). This measured upper limit is three order of magnitudes lower than the  $\pi^0$  flux predicted under the assumption that the 2-9.3 MeV emission observed by the DGT is electron bremsstrahlung resulting from the decay of charged pions. Unless the pion production process is highly time-variable (which cannot be ruled out since the DGT and SAS-2 results were obtained at different times), it would appear that the DGT data can be explained as resulting from pion production within an accretion disk which is optically thin to  $\gamma$ - $\gamma$  pair production. Eilek and Kafatos (1983) have also suggested that if the accretion region is optically thick to  $\gamma$ - $\gamma$  pair production, then the  $\pi^0$  peak may be degraded in energy to below 10 MeV. The resulting spectrum which was estimated by Eilek and Kafatos (1983) bears some resemblance to the DGT measurements. The details of such a model, however, have apparently not been developed. One potential problem in the application of this model to Cyg X-1 may be the lack of a sufficiently high photon density.

We must emphasize that a lack of pion production does not rule out the possibility of a two-temperature plasma in the accretion region, as discussed by Shapiro *et al.* (1976). Under ideal circumstances (i.e., total conversion of gravitational potential energy to thermal energy), the maximum possible ion temperature is  $\sim 1.8 \times 10^{12}$  K (or 180 MeV). This is well below the pion production threshold of 290 MeV. In order for pion production to take place, the ion population must thermalize before it reaches the black hole event horizon. In this case, the ions in the tail of the Maxwellian distribution would have sufficient energy to initiate pion production. In other words, the pion production models require that the thermalization time scale of the ion plasma must be less than the free-fall time scale. Theoretically, it is not clear whether this requirement for pion production will be met. The

results obtained here suggest that, if such a two-temperature plasma exists, then the free-fall time scale may be less than the ion thermalization time-scale.

A third possibility for the 2-9.3 MeV emission is that it represents the emission from one or more nuclear lines. Given the very high ion temperature ( $T_i \sim 10^{12}$  K) which is generally predicted for the accretion region, there is more than the minimum amount of energy required for nuclear levels to be excited ( $\sim 10$  MeV). (The thermalization of the ion population is not necessary in this case.) The strongest line which is to be expected in this type of astrophysical environment is that at 4.438 MeV due to the deexcitation of  $^{12}\text{C}^*$  (Higdon and Lingenfelter 1977). The emissivity of this line peaks at an ion temperature of  $\sim 10^{11}$  K. The predicted width of this line at a temperature of  $T_i \sim 10^{12}$  K is 0.9 MeV (Higdon and Lingenfelter 1977). The 2-9.3 MeV data from the DGT can be roughly described as a broad line centered at  $\sim 4$ -5 MeV with a FWHM  $\sim 3$ -4 MeV. A single (thermally broadened) line due to  $^{12}\text{C}^*$  is therefore not capable of producing the observed emission. It is therefore suggested that the emission may be due to more than one nuclear line. The feature observed here in the Cyg X-1 spectrum bears a resemblance to solar flare data obtained from the SMM Gamma-Ray Spectrometer; in the case of solar flares, the emission is known to result from a series of nuclear lines. It can also be noted that the DGT data appears to fall off in intensity above 6 MeV; this would be consistent with the nuclear cutoff at  $\sim 7$  MeV. Qualitatively, the data suggests the possible presence of a nuclear line continuum.

The argument for observable nuclear line emission in the standard models of Cyg X-1 does not, however, have a sound basis in theory. Although some authors (Higdon and Lingenfelter 1977; Lingenfelter *et al.* 1978) have discussed the possibility of observable line emission, Aharonian and Sunyaev (1984) have pointed out the importance of spallation effects in hot astrophysical plasmas ( $T_i \geq 10^{11}$  K). They argue that, as the plasma falls towards the event horizon, spallation competes with thermal excitation and acts so as to destroy the nuclei. Although spallation itself may result in prompt gamma-ray

emission (from the spalled nuclei), the removal of the nuclei from the population inhibits the *repeated* thermal excitation of the nuclei. The observability of line emission, to a great extent, relies on the *repeated* excitation of the nuclei. The net result of this process is that, according to Aharonian and Sunyaev (1984), the nuclear line luminosity cannot exceed  $\sim 10^{-4}$  of the total luminosity. The 2-9.3 MeV emission observed by the DGT implies a total 2-9.3 MeV luminosity of  $\sim 3 \times 10^{37}$  ergs  $s^{-1}$ , as compared to a total x-ray luminosity (1 keV to 1 MeV) of  $\sim 2.5 \times 10^{37}$  ergs  $s^{-1}$ . Based on the theoretical results of Aharonian and Sunyaev (1984), we conclude that it is unlikely that the emission observed by the DGT in the 2-9.3 MeV range is due to nuclear line emission resulting from *thermal* excitation of nuclei.

The above discussion has concentrated on thermal mechanisms which might account for the observed MeV radiation. None of these mechanisms appear to be strong candidates. Another possibility is that this radiation is produced by some *nonthermal* process. Nonthermal processes (e.g., Aharonian and Vardanian 1985) would involve some type of acceleration mechanism within (or near) the accretion region. More research (both theoretical and experimental) is clearly dictated in order to determine the origin of the 2-9.3 MeV emission.

We have also compared the DGT spectral results with those that have obtained from observations made by the European Space Agency's EXOSAT satellite (Owens 1986). This data was obtained with EXOSAT's MEDA experiment (described by Turner *et al.* 1981). This experiment consists of two collimated proportional counters, one an Argon-based detector which covers the energy range 1-15 keV, the other a Xenon-based detector covering the range 15-32 keV. (The detector response actually extends up to 50 keV, but the response above  $\sim 30$  keV is not well understood at this time.) EXOSAT observed Cyg X-1 on six occasions during the period from the beginning of 1984 to early 1985. For each of these observations, we have obtained photon spectra covering the energy range 1-30 keV. These data have been fit using a model composed of a power-law continuum and

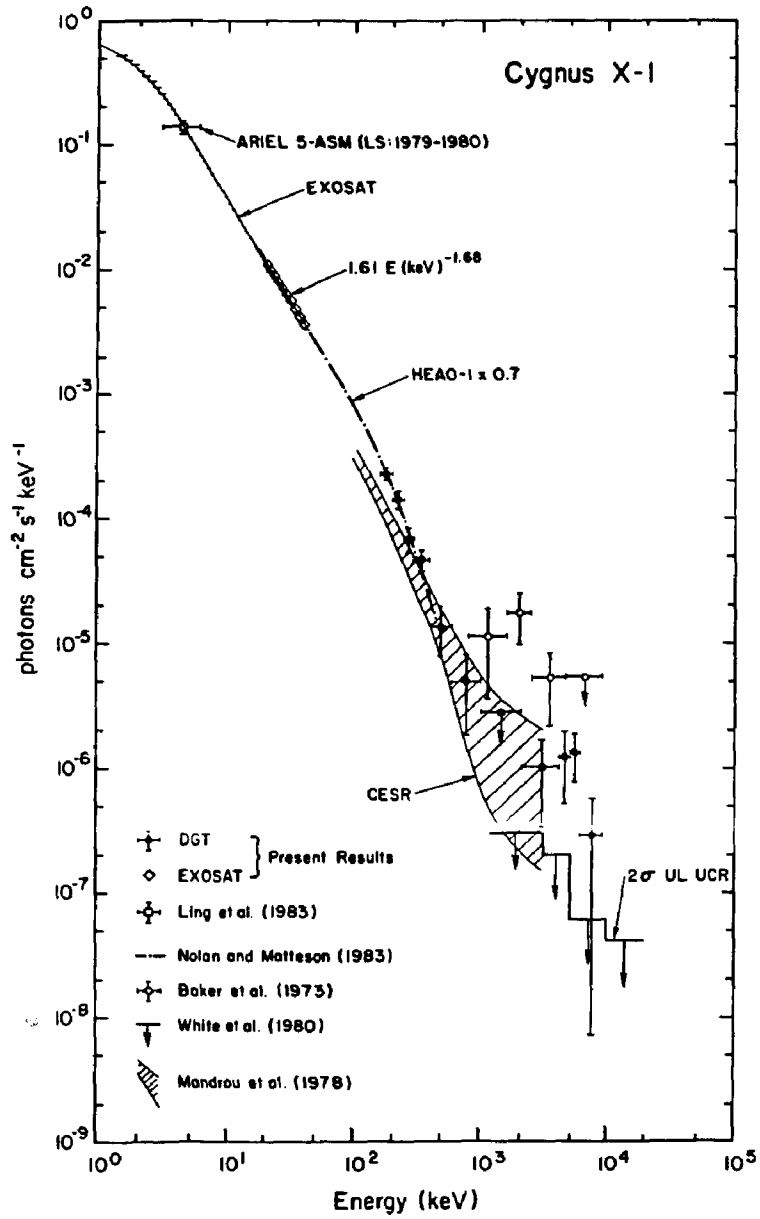


**FIGURE V-11:** The photon spectrum of Cygnus X-1 observed by the DGT is compared to other measurements, including those obtained by the EXOSAT satellite at energies below 50 keV.

a Compton-redshifted iron K line (Barr *et al.* 1985). All of these EXOSAT observations indicate that Cyg X-1 was in its low x-ray state, based both on the observed flux and the observed spectrum. (The average power-law index for all six observations is given by -1.63.)

The EXOSAT observations nearest the DGT flight were those secured on 1984 July 24 (day 206) and 1984 November 2 (day 307). The DGT balloon flight took place on day 275-276. Based on all of the available EXOSAT measurements, we must assume that Cyg X-1 was in its low x-ray state at the time of the DGT observations. Even within its low state, the x-ray emission from Cyg X-1 can be quite variable. Indeed, the relative x-ray intensity between days 206 and 307 increases by roughly 50%. In order to compare the DGT data to the x-ray spectrum, we derived a normalization based on an interpolation of the x-ray intensity between these two dates. The resulting x-ray spectrum (with a best-fit power-law index of -1.68) can then be compared directly with the DGT spectrum. This is done in Figure V-11, where we also include various other reported measurements (taken at various epochs). It can be seen that the normalized HEAO-1 spectrum (see below) provides a smooth connection between the DGT and the EXOSAT spectra. We can look more closely at the agreement between the DGT and EXOSAT results by studying how the two sets of data constrain the inverse Compton spectral fits in  $(kT_e, \tau)$  parameter space. The x-ray spectral index does not, by itself, constrain either the electron temperature ( $kT_e$ ) or the optical depth ( $\tau$ ). Based on Equations (I.25b) and (I.25c), we can derive a relationship for  $\tau$  in terms of  $kT_e$  and the x-ray power-law index ( $n+1$ ). The resulting function is plotted in Figure V-12 below (where we ignore the small errors in the determination of the x-ray power-law). On the same plot, we have placed the 68% confidence contour (the hatched area in Figure V-12) based on the DGT data. If the Cyg X-1 spectral model used for the DGT (i.e., the power-law at high energies coupled with the inverse Compton model at lower energies) is appropriate *and* if the data below 1 MeV can be described by a *single* comptonization temperature, then we can expect agreement in

parameter space between these two sets of data. As can be seen, the two data sets are not inconsistent with one another. Taken together, they indicate most-probable Compton parameters of approximately  $kT_e \approx 80$  keV and  $\tau \approx 2.0$ .

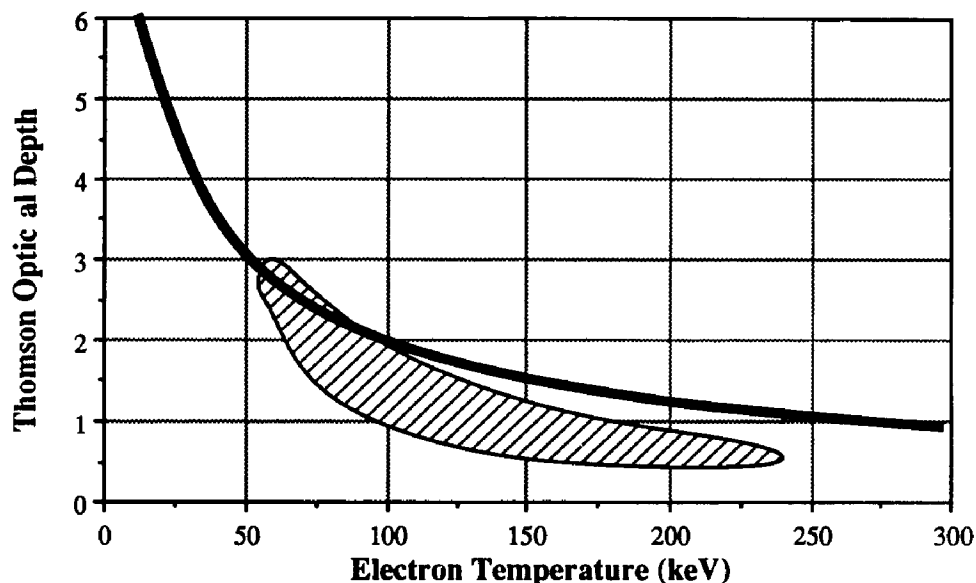


**FIGURE V-12:** A plot in Compton parameter space showing the constraint of the EXOSAT data (the solid line, based on a power-law index of -1.68) and the 68% ( $1\sigma$ ) confidence region based on the DGT results (the hatched area).

The EXOSAT-DGT results are compared with previously reported spectra in Figure V-11. At low energies (<300 keV), the spectrum of HEAO-1 (Nolan and Matteson 1983) is normalized to the EXOSAT data. The Cyg X-1 spectrum was not observed to vary in shape below  $\sim 300$  keV during intensity changes, so such a normalization is permissible (Nolan and Matteson 1983). At energies above 100 keV, we find that the data of Mandrou *et al.* (1978) agrees well with the DGT data points, especially around 1 MeV. Indeed, that dataset has been described (Roques *et al.* 1985) in terms of a Compton plus power-law spectrum, just as has been done for the DGT data; they find a power-law index of -1.3 best

fits the high-energy data points. The results of Baker *et al.* (1973) are in conflict with the present results. We also find that the upper limits of White *et al.* (1980) are well below the DGT data points. These results may be explained by variability, as might be expected at these energies based on data from HEAO-3 (Ling 1987).

Based on the DGT results, we find that the Cyg X-1 data is consistent with a single temperature inverse Compton model plus a second, higher energy component which is necessary to explain the emission above 1 MeV. Various interpretations of the data above 1 MeV have been studied. These results tend to exclude the feasibility of a high-temperature annihilation line (Ramaty and Mészáros 1981) or the possibility of electron bremsstrahlung resulting from charged pion decay (Eilek and Kafatos 1980). It is also suggested that this MeV emission might originate from a series of nuclear lines, but it is unlikely that this emission would be produced by a thermal mechanism. The results imply that some nonthermal mechanism may be involved. Despite the relatively low statistical significance of the observed MeV emission ( $2.9\sigma$ ), we are confident that the observation is not some instrumental artifact. No known instrumental effect could produce the type of emission which is observed. Furthermore, the spectrum of the Crab shows no similar feature at these energies. Nonetheless, it will be important for future measurements to establish the reality and the origin of this feature.

### Cygnus X-3

No measurable flux from Cyg X-3 was found in the imaging data. Since the emission may be dependent on the orbital phase of the binary system, the ephemeris of Parsignault *et al.* (1977) has been used to determine the binary phase for the time of the DGT observations. During scan #1 the phase varied from 0.54 to 0.17. During scan #2 the phase varied from 0.79 to 0.31. Hence, the data collectively covers nearly a full cycle of the 4.8 hour binary system; only phases from 0.31 to 0.54 are not covered by the dataset. (The peak emission which is seen in very-high-energy and ultra-high-energy gamma-rays is observed during phases 0.20-0.30 and 0.50-0.70.)



Upper limits on the flux level from Cyg X-3 were derived in the same way as for A0535+26. The procedure fits both Cyg X-1 and Cyg X-3 simultaneously using the measured PSF and the known location of Cyg X-3 (corrected for the measured offset between the observed and known locations of Cyg X-1). The resulting  $1\sigma$  upper limits are given in Table V-6 and plotted, along with other representative observations, in Figure V-13. These upper limits were derived assuming an  $E^{-2.2}$  power-law source spectrum for Cyg X-3 (as was measured by Meegan *et al.* 1979).

**Table V-6**  
**CYGNUS X-3 UPPER LIMITS**

ENERGY (keV)	$1\sigma$ UPPER LIMIT ( $\text{cm}^{-2} \text{s}^{-1} \text{MeV}^{-1}$ )
160-200	$2.60 \times 10^{-2}$
200-250	$3.12 \times 10^{-2}$
250-300	$1.57 \times 10^{-2}$
300-400	$1.61 \times 10^{-2}$
400-600	$1.07 \times 10^{-2}$
600-1000	$4.05 \times 10^{-3}$
1000-2000	$2.28 \times 10^{-3}$
2000-3000	$1.72 \times 10^{-3}$
3000-6000	$5.14 \times 10^{-4}$
6000-9300	$3.19 \times 10^{-4}$

The upper limits obtained from the DGT data are marginally inconsistent with the measurements of Meegan *et al.* (1979). This may be an indication of a change in the source intensity. Long term variations of the Cyg X-3 intensity have been measured at x-ray energies (<10 keV) by the Japanese Tenma satellite (Kitamoto 1985). However, at energies above 23 keV data from the OSO-8 satellite (Dolan *et al.* 1982) showed no long-term variations during the 1975-1977 period.

It is important to note that the DGT measurements, unlike those of Meegan *et al.* (1979), can clearly resolve Cyg X-3 and Cyg X-1. Indeed, Meegan *et al.* (1979) state that

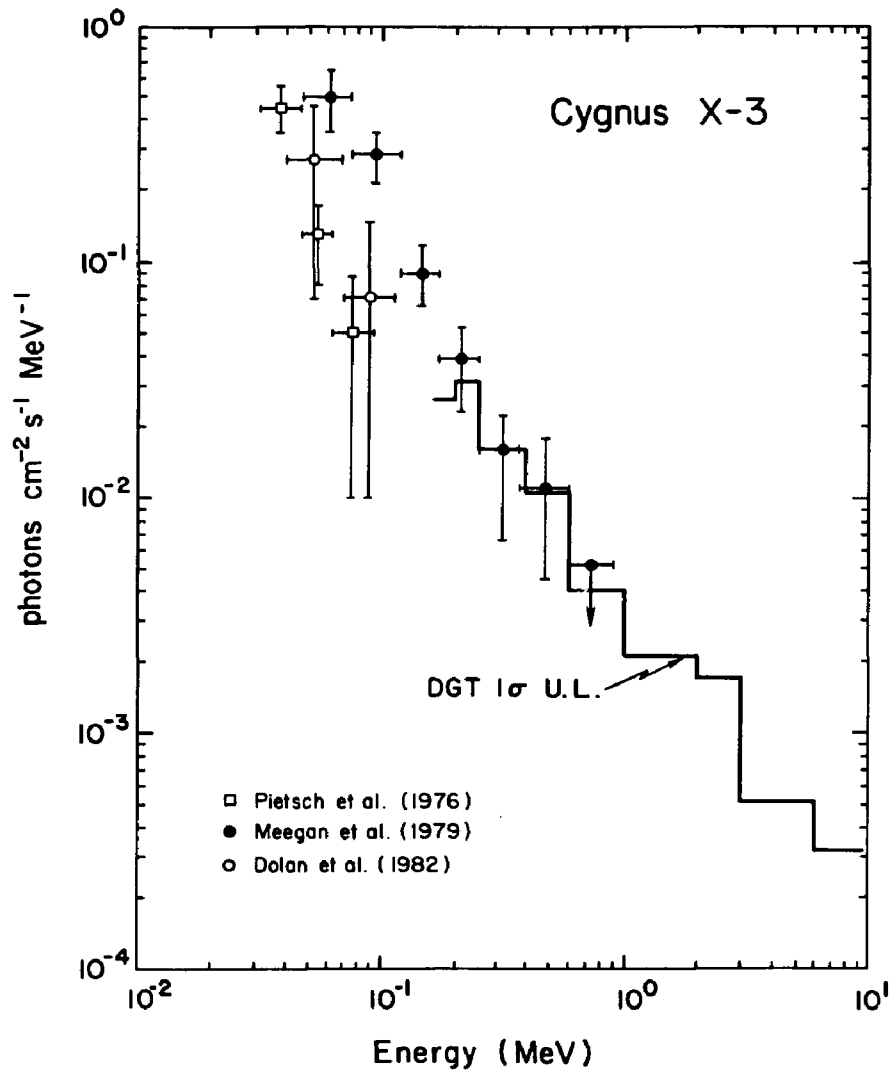


**FIGURE V-13:** The upper limit flux levels for Cyg X-3 as derived from the DGT imaging data. Other representative measurements are also shown for comparison.

they cannot rule out Cyg X-1 as being responsible for intensity changes which they interpreted as being due to Cyg X-3. Further positive measurements of Cyg X-3 in this energy band are needed in order to determine the source spectrum with any degree of certainty.

## CHAPTER VI

### Summary

In this dissertation, I have presented results obtained from a balloon flight of a new gamma-ray telescope employing the coded aperture technique. This instrument, referred to as the Directional Gamma-ray Telescope (DGT), operates over the energy range 160 keV to 9.3 MeV. The 30 hour balloon flight (which took place on 1-2 October 1984) permitted the observation of a number of sky regions. Each observation encompassed an area of the sky of  $\sim 400$  square degrees. Of the regions which were observed, two were chosen here for analysis.

The first observation which has been considered was centered on the Crab Nebula/pulsar, a region sometimes referred to as the galactic anticenter. The total observation represents  $\sim 3.6$  hours of accumulated data. The Crab Nebula/pulsar is clearly seen in the resulting image. The Crab spectrum has been measured from 160 keV up to at least 2 MeV. The data is well-described by a single power-law spectrum of the form  $A E_{\text{MeV}}^{-\alpha}$  photons  $\text{cm}^{-2} \text{s}^{-1} \text{MeV}^{-1}$ , where  $A = (5.1^{+2.4}_{-1.6}) \times 10^{-3}$  and  $\alpha = (1.88 \pm 0.22)$ . Within the limitations of the DGT energy resolution, there is no evidence for any discernible structure in the spectrum. In particular, we have placed  $3\sigma$  upper limits on the flux levels from previously reported line emission at energies of  $\sim 400$  keV and 1049.8 keV. Those levels are given by  $3.0 \times 10^{-3}$  and  $1.9 \times 10^{-3}$  photons  $\text{cm}^{-2} \text{s}^{-1}$ , respectively. In addition to gamma-ray emission from the Crab, we have also looked for emission from two other sources in this field. These two sources are the flaring x-ray binary A0535+26 and the diffuse emission which has been observed from the direction of the galactic anticenter. Neither source shows a positive response in the DGT imaging data. We have placed upper limits on the flux from both of these sources.

The second observation discussed here is that of the Cygnus region. This region contains two high-energy sources - Cygnus X-1 and Cygnus X-3. Cyg X-1 dominates the image obtained from this region. Its spectrum has been measured from 160 keV up to ~9.3 MeV. Emission in the energy range 2-9.3 MeV is detected at the 2.9  $\sigma$  level. The data is consistent with a two-component model which is composed of an inverse Compton model at low energies (with  $kT_e = 80$  keV and  $\tau = 2.0$ ) coupled with a power-law to accommodate the high-energy points (>2 MeV). The inverse Compton model is commonly used to explain x-ray measurements of this source. It is also consistent with the present theoretical picture in which Cyg X-1 contains a black hole in orbit about a main-sequence primary. The high-energy emission results from the accretion of matter onto the black hole (possibly via an accretion disk). We have investigated various explanations for the emission above 2 MeV. The possibility of a high-temperature (blue-shifted) annihilation line is considered unlikely, since the implied temperature of ~3.5 MeV is inconsistent with the inverse Compton model which successfully explains the low energy data. Although the presence of two distinct emission regions is possible, it is considered to be an unlikely scenario. Pion production in a hot ion plasma ( $T_i \sim 10^{12}$ K) appears to be ruled out based on the lack of observable emission at ~100 MeV, although a time-variable process may account for this inconsistency. Nuclear line emission in a thermal plasma is considered, but this possibility is considered improbable based on theoretical arguments. We are led to the conclusion that the emission cannot easily be accounted for within the framework of present accretion models. Its explanation may require some type of non-thermal mechanism, the exact nature of which remains unclear. As for Cygnus X-3, no emission was detected and upper limits were placed on the flux levels from this source.

In addition to the scientific results discussed above, the experimental aspects of this project are also noteworthy. Although the coded aperture technique is being developed by numerous groups involved in gamma-ray astronomy, the DGT represents the first operational detector which can image celestial photons at energies above 160 keV. We

have successfully demonstrated a means for dealing with the problems induced by a nonuniform background rate within the detection plane of the experiment. The results presented here demonstrate the future potential of this experimental approach to gamma-ray astronomical research.

## **APPENDICES**

## APPENDIX A

### Properties of a Single DGT Image

This appendix discusses the imaging properties which are characteristic of the DGT. For the sake of this discussion, it is important to distinguish between the basic imaging properties of a single DGT image and the properties related to a composite image. Here, we consider a *single image* as one obtained with a fixed detector-source geometry. This would be the case for images obtained in the laboratory or the snapshot images discussed in Chapter IV. The properties of such an image are therefore fundamental properties of the actual imaging process. A *composite image*, on the other hand, is an image obtained with a variable detector-source geometry. Such is the case when observing a region of the sky, for example. The variable geometry dictates that an image must be compiled from a number of individual single (or snapshot) images, with each snapshot approximating a fixed geometry situation. The properties of the resulting composite image are, in general, quite different than those of a single snapshot image.

#### Basic Properties of a Single Image

A single DGT image consists of 35 *image elements* (or *pixels*). Each element represents the reproduced intensity contained within a  $3.8^\circ$  by  $3.8^\circ$  region of the field-of-view. For a point source within the field-of-view, anywhere from one to four image elements will exhibit a positive response, depending on the source location relative to the center of an image element. For a source at the center of an image element, the imaging response will be entirely confined to that element. If a source lies on a line joining the centers of two adjacent elements, the imaging response will be split between those two



elements with the relative response of the two elements depending on the source location. The extreme case is that of a source lying at the corner of an image element; in this case, the imaging response will show up in the four adjacent elements. In any of these cases, the relative response of those elements involved in the imaging response can be used to determine the location of the source.

The imaging process is best described by an example. A set of sample imaging data is shown in Figure A-1. This data was obtained during pre-flight calibrations prior to the second balloon flight attempt (Flight 1340-P in September, 1983). In this case, a  $^{137}\text{Cs}$  calibration source was placed  $\sim 100$  feet in front of the detector. Such a large detector-source distance was required to minimize image deformities resulting from an "unfocused" image. The image was integrated for 200 seconds and processed on the DGT ground station. Figure A-1a shows the integrated response of the detection plane (the *detector map*), which represents the number of counts in each of the 35 detectors. This view corresponds to that which would be seen by an observer in front of the detector. The reproduced image (or *image map*), obtain using equation (II.2b), is displayed in Figure A-1b. Here, the display represents the number of reproduced counts in the image and is equivalent to the view seen by the detection system. (These perspectives were adopted as the logical views which the experimenter would encounter.) The source is seen to be located in the  $i = 4, j = 2$  element.

We can use the data shown in Figure A-1 to point out some of the basic features of a DGT image. First, we note that the pattern of "on" and "off" detectors seen in the detector map corresponds to the URA pattern in Figure II-6. There are 18 "on" detectors which are exposed to the source, showing an average response of  $2200 \pm 73$  counts. The 17 "off" detectors (blocked from the source by lead mask elements) contain an average of  $980 \pm 61$  counts. If we treat the "on" and "off" detectors as source and background measurements, respectively, we calculate a total of  $18(2200) - (18/17) \times 17(980) = 21956$  counts. This is the same result achieved by the imaging process. In a similar manner, the spectrum of the

---

**SAMPLE DGT IMAGING DATA**


---

970.0	2249.0	2171.0	1012.0	951.0	1027.0	2223.0
2078.0	2236.0	2220.0	867.0	2162.0	2358.0	2262.0
1014.0	2240.0	2190.0	991.0	1068.0	1024.0	2303.0
2105.0	997.0	1030.0	1024.0	2186.0	2202.0	1044.0
2177.0	918.0	896.0	962.0	2072.0	2160.0	873.0

## a) DETECTOR MAP

-845.4	-1360.1	-1162.4	-855.6	-450.1	-1143.9	-1547.4
-318.3	-384.2	-765.1	-822.7	97.6	-779.5	-1180.9
-225.6	-565.4	-454.2	114.1	-830.9	-723.9	89.4
-299.8	-390.4	-600.4	21956.1	-754.8	-964.8	-833.0
-213.3	-1030.6	72.9	-688.9	-550.9	-927.7	-660.1

## b) IMAGE MAP

---

**FIGURE A-1:** Sample image data obtained with the DGT during pre-flight calibrations, using a  $^{137}\text{Cs}$  source placed ~30 meters in front of the detector.

source could be reconstructed by adding and subtracting detector spectra. Another main feature of this image, is that the average non-source image element has a value less than zero; in this case, the average number of counts in the non-source elements is  $-646 \pm 415$  counts. Finally, we note that the variance of these non-source elements represents the variance of the source element as well. By equation II.13, we expect the variance to be approximately the square root of the total number of counts in the array. This leads to an expected variance of 237, considerably smaller than that actually observed. This difference is due to the presence of nonuniformities in the detector background (i.e., systematics). These nonuniformities result, in large part, due to the scattering environment in which these measurements were made. (We neglect these nonuniformities in this discussion, since the images are source dominated with a source-to-background ratio of 35%.)

In the above example, the source was purposely positioned in the center of an image element. In this case, the imaging response is entirely confined to that one element. In

Figure A-2, the imaging results for a source located at a corner of an image element are displayed. This data also represents a 200 second accumulation under the same conditions as above.

SOURCE LOCATED AT THE CORNER OF A PIXEL						
1512.0	1635.0	1652.0	1330.0	1192.0	1539.0	1540.0
1801.0	1952.0	2246.0	1563.0	1252.0	1719.0	1802.0
1866.0	1862.0	2163.0	1729.0	1277.0	1650.0	1899.0
1606.0	1619.0	1770.0	1474.0	1222.0	1478.0	1520.0
1719.0	1413.0	939.0	921.0	1291.0	2190.0	1687.0
a) DETECTOR MAP						
-1526.5	-836.8	-1407.1	-567.1	579.7	-1227.9	-1475.0
561.2	87.6	-1065.3	-1281.5	361.5	-1149.7	-707.1
-1147.6	-941.8	-816.2	4639.7	5800.9	229.7	-105.9
-700.9	-770.9	-1127.1	4557.4	4995.9	137.1	-118.2
-272.6	-482.6	-313.8	-1250.6	-803.8	-1520.3	-334.3
b) IMAGE MAP						

**FIGURE A-2:** Imaging data for the case of a source lying at the corner of an image element. This data was taken under the same conditions as in Figure A-1.

The image of Figure A-2 is not as simple as that in Figure A-1. Note that there is no clearly defined pattern in the detector map. The idea of "on" and "off" detectors has become somewhat confused. Nonetheless, the image which results from the correlation process (i.e., eq. II.2b) reproduces a response which is distributed approximately equally between four adjacent image elements. This is the expected result for a source at the corner of an image element. An important feature of this image is that the sum of the four source elements is 19994 counts, a value which is ~10% lower than that in the image of Figure A-1. Since these images represent the same accumulation time, the number of reproduced source counts should be the same in the two images. The reason for this discrepancy can be traced to the existence of the negative response for the non-source image elements. This

effect, which we call *source suppression*, is described in more detail in the next section. It should also be noted that the statistical precision of this measurement is reduced by a factor of two as compared to the result in Figure A-1, since four image elements must be summed together instead of just the single element as in the previous case.

One final example will serve to illustrate the capability of the DGT to image spatially diffuse emission. In this case (shown in Figure A-3), the diffuse emission has been simulated by a sequence of seven exposures (each 50 seconds in duration) using the same  $^{137}\text{Cs}$  source as in the above examples. The source was located at the center of a different image element for each exposure. The result was the simulation of a diffuse "ridge" of emission. The total number of reproduced source counts in this image is 31942.3. This is well below the value expected (from Figure A-1) of  $(7/4) \times 21956 = 38423$ . Again, this discrepancy results from the source suppression effect discussed below.

---

**IMAGING OF DIFFUSE EMISSION**

---

2484.0	2674.0	2461.0	2652.0	2683.0	2659.0	2556.0
3387.0	3678.0	3639.0	3451.0	3519.0	3675.0	3502.0
2597.0	2659.0	2835.0	2691.0	2731.0	2698.0	2723.0
2676.0	2591.0	2619.0	2732.0	2747.0	2764.0	2508.0
2619.0	2580.0	2546.0	2650.0	2413.0	2640.0	2358.0

a) DETECTOR MAP

-998.9	-1531.6	-1810.1	-2948.6	-1342.7	-1392.1	-1565.1
-471.8	-1194.5	-885.6	-1217.1	-66.2	-2013.9	-589.2
-572.7	-786.8	-869.2	-671.5	-885.6	-1289.2	471.1
4807.0	4722.6	3678.8	5276.4	3888.8	4092.6	5476.1
-949.5	-2001.5	-381.2	-1175.9	-1818.3	-1740.1	-1262.4

b) IMAGE MAP

---

**FIGURE A-3:** A DGT image obtained by a sequence of exposures (of equal duration) to the same  $^{137}\text{Cs}$  source located in different image elements. This demonstrates the ability of the DGT to image a spatially diffuse emission.

### Source Suppression in DGT Images

One of the properties of a single DGT image (demonstrated in Figure A-1) is that the average level of the non-source image elements is less than zero. This is an effect which must be accounted for in order to extract the true response of the imaging system to a source within the field-of-view.

In order to understand this problem, we will first look at the case of a single source located in the center of an image element. Next, we shall look at what happens to the reproduced source intensity when the source response is spread among more than one image element.

#### Single Source in a Single Image Element

Let  $S$  be the total number of modulated source counts which are measured in the detection plane,  $B$  the total number of background counts (which includes the unmodulated source counts),  $\rho$  the fraction of open elements in the mask and  $N$  the total number of detector elements (which is also equal to the number of elements in the basic URA mask pattern). There are therefore  $\rho N$  detector elements which measure  $S/(\rho N)$  source counts. All  $N$  detectors also measure  $B/N$  background counts. For the image element containing the source, the response is given by (c.f., eq. II.2b),

$$\begin{aligned}
 S' &= \sum_{i=1}^{\rho N} \left( \frac{B}{N} + \frac{S}{\rho N} \right) + \sum_{i=1}^{(1-\rho)N} \left( \frac{-\rho}{1-\rho} \right) \frac{B}{N} & (A.1) \\
 &= \rho N \left( \frac{B}{N} + \frac{S}{\rho N} \right) - (1-\rho)N \left( \frac{\rho}{1-\rho} \right) \frac{B}{N} \\
 &= S
 \end{aligned}$$

As expected, this image element reproduces the total source counts.

In the case of a non-source element, the correlation process associates 1/2 of those  $(\rho N)$  detectors exposed to the source with a  $G$  value of +1 and the rest of the exposed

detectors with a G value of  $-\rho/(1-\rho)$ . There will be  $\rho N$  background terms associated with a G value of +1 and  $(1-\rho)N$  background terms associated with a G value of  $-\rho/(1-\rho)$ . The resulting summation is given by,

$$\begin{aligned}\Delta &= \sum_{i=1}^{\rho N/2} \left( \frac{S}{\rho N} - \frac{\rho}{1-\rho} \frac{S}{\rho N} \right) + \sum_{i=1}^{\rho N} \frac{B}{N} + \sum_{i=1}^{(1-\rho)N} \left( \frac{-\rho}{1-\rho} \right) \frac{B}{N} \quad (\text{A.2}) \\ &= \frac{S}{2} - \frac{\rho}{1-\rho} \frac{S}{2} + \rho B - \rho B \\ &= \left( \frac{1-2\rho}{1-\rho} \right) \frac{S}{2}\end{aligned}$$

Note that the average level of the non-source image elements depends only on  $\rho$  (the fraction of open elements in the mask) and  $S$  (the total source counts). For URA patterns, the fraction of open elements is given by equation (II.9),

$$\rho = (N + 1) / 2N \quad (\text{A.3})$$

Substitution of (A.3) into (A.2) shows that, for a mask based on a URA pattern composed of  $N$  elements, we expect an average level for non-source elements given by,

$$\Delta = -S / (N-1) \quad (\text{A.4})$$

For large  $N$ , the level of the non-source elements approaches zero and the problem of source suppression becomes negligible. For the DGT (with  $N=35$ ), however, we find,

$$\Delta(\text{DGT}) = -.0294 S \quad (\text{A.5})$$

In this case, the effect can be of the same order as the errors on the source measurement. As an example, we can consider the imaging data of Figure A-1. Here we find that  $S = 21956$  with a measured average value for the non-source elements of  $-646$ . By equation (A.5), we expect a value of  $\Delta = -.0294 \times 21956 = -646$ , which corresponds precisely to the measured average.

As a result of this discussion, we see that for a single source located at the center of an image element (so that the imaging response is confined to that single image element),

the following holds. First, the system will reproduce the total source counts in the source image element. Second, for non-source image elements, there will be an average DC level given by equation (A.2). For  $\rho > 0.5$ , the average non-source image level will be less than zero. For  $\rho < 0.5$ , the average non-source image level will be greater than zero. Only for  $\rho = 0.5$  will the non-source level lie at exactly zero.

### Source Counts Spread Among More than One Image Element

The imaging process is a linear one in the sense that the imaging of more than one source can be thought of as a sum of images, with one image for each source. Furthermore, for a single source whose response is divided among  $n$  image elements, then the resulting image can also be thought of as a sum of  $n$  images. Each of these  $n$  source images has the characteristics as outlined above. If we sum  $n$  individual images, then the source response of one image is added to the (negative) non-source level of the other  $n-1$  images. The net result is that the response from that one source will be "suppressed" below its true value. More specifically, for the case of a URA mask pattern (with  $\Delta$  defined by eq. A.4), we can write the (net positive) response of the  $i^{\text{th}}$  source element ( $R_i$ ) as,

$$R_i = S_i - \frac{1}{N-1} \sum_{\substack{j=1 \\ i \neq j}}^n S_j = S_i - \frac{1}{N-1} (S_T - S_i) \quad (\text{A.6})$$

$$R_i = \frac{N S_i - S_T}{N-1}$$

where  $S_T$  is the total number of source counts modulated by the imaging system and  $S_i$  is the number of such counts corresponding to the  $i^{\text{th}}$  source element. If we now sum equation (A.6) over all  $n$  source image elements, we can get an expression for the total (positive) source response in the image. This becomes,

$$R_T = \sum_{i=1}^n R_i = \left( \frac{N-n}{N-1} \right) S_T \quad (\text{A.7})$$

Here we see directly that the larger  $n$  is (i.e., the greater the number of source image elements), the more source suppression exists. We can compare this result to the imaging data of Figure A-2. In that image,  $R_T = 19994$  counts, which corresponds to  $S_T = (34/31) \times 19994 = 21929$ . This can be compared to the known value of  $S_T$  (based on Figure A-1) of 21956.

For the sum image, the non-source image level can be expressed, using equation (A.4), as,

$$\Delta = \sum_{i=1}^n \Delta_i = \frac{-1}{N-1} \sum_{i=1}^n S_i = \frac{-1}{N-1} S_T \quad (\text{A.8})$$

It is important to note here that  $S_T$  represents the *true* response of the imaging system, while  $R_T$  represents the *net positive* response of the imaging process. Results from Figure A-2 provide a value for  $\Delta = -645$ . From equation (A.8), we would expect a value of  $\Delta = -.0294 \times 21929 = -645$ .

### Solution to the Source Suppression Problem

In the previous section, we demonstrated that there existed a difference between the *true* response of the imaging system and the *net positive* imaging response. The problem at hand is to determine the *true* source intensity, based only on a knowledge of the net positive response in the image. Normally, one would expect to use the zero level as a baseline in measuring the image response. This, however, would give erroneous results, as demonstrated above. Let us instead use the average level of the non-source image elements ( $\Delta$ ) as a baseline. If we were to fit the image response using this baseline, we would obtain,

$$R_{\text{fit}} = R_T + n|\Delta| = \frac{N-n}{N-1} S_T + n \frac{S_T}{N-1} = \frac{N}{N-1} S_T \quad (\text{A.9})$$

We see from this result that, in order to obtain the desired quantity ( $S_T$ ), we need only to add the value of the average non-source image element ( $\Delta$ ). In other words,



$$S_T = R_{fit} + \Delta = ((N-1)/N) R_{fit} \quad (A.10)$$

For the imaging data of Figure A-2,  $R_{fit} = 19994 + 4(645) = 22574$ . It then follows (eq. A.10) that  $S_T = 22574 - 645 = 21929$ . A second example comes from Figure A-3. In this case, the value of  $\Delta$  is -1140.8 and the total number of positive source counts is 31942. This gives a value for  $R_{fit}$  of  $31942 + 7(1141) = 39929$ . From equation (A.10) we obtain  $S_T = 39929 - 1141 = 38788$ , which can be compared to the expected value (see previous section) of 38423. These same results can be obtained from equation (A.7), except in this case it is not necessary to know how many elements are involved in the imaging response to the source. This makes the latter approach a more general one. This procedure makes intuitive sense if we note that each of the  $n$  image elements involved in the source response contributes a total of

$$\frac{1}{N-1} \frac{S_T}{n} \quad (A.11)$$

So, in order to effectively deal with the problem of source suppression, the appropriate procedure is as follows. First, measure the response of the source relative to the average non-source element level (the level defined by eq. A.4). This measurement provides a value of  $R_{fit}$  (eq. A.9). Next, in order to correct for the suppression effects, we must add to  $R_{fit}$  a quantity ( $\Delta$ ) which corresponds to the average non-source image element level. This procedure (eq. A.10) results in a quantity ( $S_T$ ) which represents the true number of reproduced source counts.

Another possible solution to the problem of source suppression may involve a more suitable choice for the post-processing function. Our choice (eq. II.8) was, in part, dictated by the desire to reproduce the correct source counts in the case of a single source located at the center of an image element (as in Figure A-1). In hindsight, a choice of  $G$  which would provide a positive DC level in the resulting image may be easier to work with in terms of image analysis. We have not, however, explored these options in the present work.

## APPENDIX B

### Properties of a Composite Image

In this Appendix, we review the procedures necessary to produce a composite DGT image. This is followed by a discussion of the general properties of a composite image.

#### Formation of a Composite Image

As discussed in Chapter IV, a composite image is composed of a large number of individual snapshot images. Each snapshot image (see Figure IV-1) is a 5 by 7 image, with each element corresponding to a region of the sky  $3.8^\circ$  by  $3.8^\circ$  in size. In order to combine a large number of such images, each snapshot image is broken down into a 20 by 28 array (each element  $0.95^\circ$  by  $0.95^\circ$  in size) and then transformed into some common coordinate frame. The obvious choice for a coordinate system was some system based on celestial coordinates - right ascension ( $\alpha$ ) and declination ( $\delta$ ). Here we review the necessary procedures required to perform this transformation. The problem is divided into four parts. First, we must define some point (which we call point P) within the DGT field-of-view (FOV). Next, we determine the zenith ( $\theta$ ) and azimuth (A) of point P. The corresponding right ascension and declination ( $\alpha, \delta$ ) can then be calculated. These coordinates are then transformed into what we call *skymap coordinates*, which are the coordinates used for the display and analysis of DGT imaging data.

#### Defining the Location of a Point Within the Field-of-View

The zenith and azimuth coordinates which are provided by the experiment refer to the center of the FOV. Let us refer to these coordinates as the *pointing zenith* ( $\theta_0$ ) and *pointing azimuth* ( $A_0$ ). Let point O define the center of the FOV. For any point (such as

point P) within the FOV, we must have some means of defining its location relative to point O. The problem is defined in the following figure,

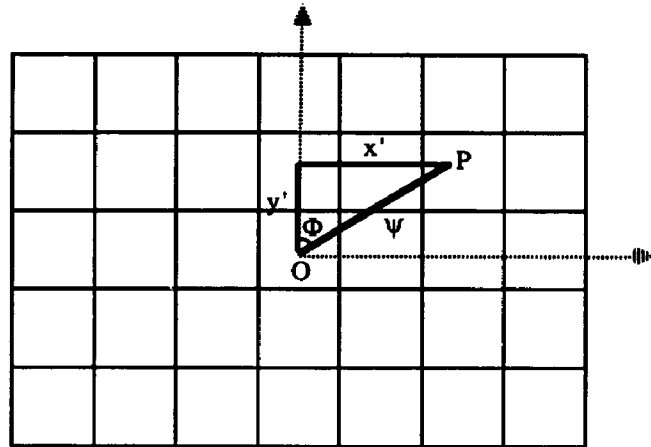


**FIGURE B-1:** A schematic diagram demonstrating the definition of the location of a point (P) within the imaging field-of-view.

For small angles, the relationships of standard trigonometry can be used in order to solve the relevant triangle. In general, however, it is more appropriate in this case to use spherical trigonometry. In order to solve the spherical triangle, we can distinguish two cases, depending on the relative values of the pointing zenith angle ( $\theta_0$ ) and the zenith angle ( $\theta$ ) of point P. These two cases are illustrated below,

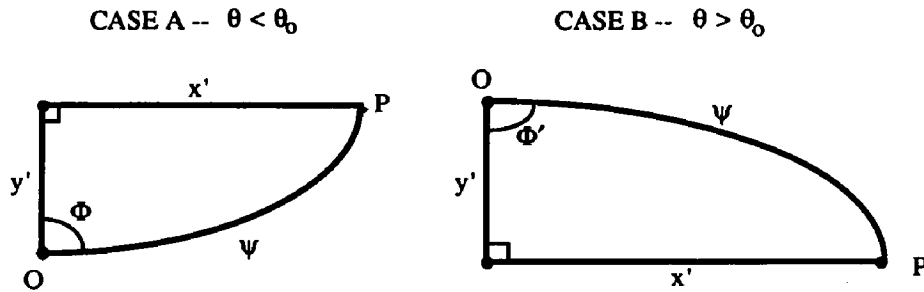


**FIGURE B-2:** Spherical triangles which illustrate two cases for defining the location of point P within the field-of-view, based on Figure B-1.

Note that  $\Phi' = 180^\circ - \Phi$ . For either case, the following relations hold true,

$$\cos \psi = \cos x' \cos y' \quad (\text{B.1})$$

$$\sin \Phi = \sin x' \sin \psi \quad (\text{B.2})$$

The quantities  $(\psi, \Phi)$  can now be used to define point P.

### Azimuth and Zenith of a Point Within the Field-of-View

The results of the last section can now be used to derive the azimuth and zenith coordinates corresponding to point P. The problem can be solved using the following spherical triangle,

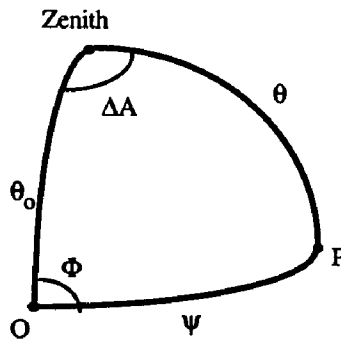


**FIGURE B-3:** Spherical triangle illustrating the determination of the azimuth and zenith for point P.

where  $\Delta A$  is defined by the relationship,

$$A = A_0 - \Delta A \quad (\text{B.3})$$

The following relationships, based on spherical trigonometry, now hold,

$$\cos \theta = \cos \psi \cos \theta_0 + \cos \Phi \sin \psi \sin \theta_0 \quad (\text{B.4})$$

$$\cos \Delta A = \{ \cos \psi - \cos \theta_0 \cos \theta \} / \{ \sin \theta_0 \sin \theta \} \quad (\text{B.5})$$

From these relationships, the zenith ( $\theta$ ) and azimuth ( $A$ ) of point P can be obtained. The next step is to convert these horizon coordinates to celestial coordinates.

### Horizon to Celestial Coordinates

The procedures for converting from horizon to celestial coordinates can be found in many references. Two that are especially useful are Smart (1972) and Duffett-Smith (1981). In order to convert from horizon to celestial coordinates, we need to know not only the zenith ( $\theta$ ) and azimuth ( $A$ ) for the given point, but also the observer's latitude ( $\phi$ ) and the local sidereal time (LST). The LST can, in turn, be derived from the observer's longitude ( $\lambda$ ), the present Universal Time (UT) and a knowledge of the sidereal time at Greenwich for 0<sup>h</sup> UT on the day in question ( $\tau_0$ ).

The first step is to convert from ( $\theta, A$ ) to declination ( $\delta$ ) and hour-angle ( $H$ ). These quantities are related by the following,

$$\sin \delta = \cos (90-\theta) \sin \phi + \sin (90-\theta) \cos \phi \cos A \quad (\text{B.6})$$

$$\cos H = \{ \cos (90-\theta) - \sin \phi \sin \delta \} / \{ \cos \phi \cos \delta \} \quad (\text{B.7})$$

At this point, the measured hour-angle ( $H$ ) is converted into right ascension ( $\alpha$ ). This requires a knowledge of the local sidereal time (LST). The LST is given by,

$$\text{LST} = \tau_0 + 1.002738 \text{ UT} - \lambda \quad (\text{B.8})$$

The quantity 1.002738 is used to convert units of Universal Time into units of sidereal time. The value of  $\tau_0$  can be obtained from the Astronomical Almanac. Note that all quantities need to be given in angular measure (using  $15^\circ = 1$  hour). The value of  $\alpha$  is then given by,

$$\begin{aligned} \alpha &= \text{LST} - H \\ &= \tau_0 + 1.002738 \text{ UT} - \lambda - H \end{aligned} \quad (\text{B.9})$$

### Conversion to Skymap Coordinates

The composite DGT images are created within a 50 by 50 element *skymap array*. Each element of this array represents the usual  $0.95^\circ$  by  $0.95^\circ$  region. We shall define the coordinates of point P within the skymap array as ( $x, y$ ). The origin of the skymap array is situated in the center of the array and is defined by the celestial coordinates ( $\alpha_0, \delta_0$ ). The

relations between the  $(\alpha, \delta)$  coordinates of point P and the  $(x, y)$  coordinates of point P are as follows,

$$x = (\alpha - \alpha_0) \cos \delta \quad (\text{B.10})$$

$$y = \delta - \delta_0 \quad (\text{B.11})$$

In terms of FORTRAN array elements (I,J), these  $(x, y)$  coordinates become,

$$I = (x + 23.75) / 0.95 + 0.5 \quad (\text{B.12})$$

$$J = (y + 23.75) / 0.95 + 0.5 \quad (\text{B.13})$$

The actual image analysis (source fitting, etc.) is done in terms of the array elements (I,J).

### Composite Image Statistics

It is worthwhile to compare the Crab and Cygnus imaging data, which clearly show evidence for source emission, with other images which show no evidence for detectable source emission. Two other imaging observations, along with the Crab and Cygnus results, have been used in such a comparison; these are the observations of NGC 4151 and of 2CG135+1.

One potentially useful means of testing for the presence of a source within the field-of-view is to look at the frequency distribution of the image element responses, i.e., the response of each  $0.95^\circ$  element in terms of the number of standard deviations ( $n_\sigma$ ). For an image containing no source emission, this distribution would be roughly Gaussian in shape and symmetric about a mean value of zero. When source emission is present within the field-of-view, the distribution will develop a tail on the high end; the peak which corresponds to the non-source elements will peak at a slightly negative value.

The *image element distribution* for a given composite image is set up by calculating the standard deviation of each image element (based on eq. II.27) using the livetime for that element and the total systematics observation time ( $T_{sys}$ ). Since each skymap image element results from dividing the original elements by 16, the calculation of the standard

deviation must also include this factor. The significance ( $n_{\sigma}$ ) of each element is determined by dividing the element response by the calculated standard deviation. The frequency distribution of these  $n_{\sigma}$  values corresponds to the image element distribution.

The image element distributions of the four sets of imaging data have been studied using three basic statistics of the distribution - the standard deviation ( $s$ ), the *skewness* and the *peakedness* (or *kurtosis*). For an image with no source, we expect the standard deviation to be 1, the skewness to be 0 and the peakedness would be 3. For an image containing source response, we would expect the standard deviation to be greater than 1, the skewness to be positive (indicating that the majority of the *large* deviations are on the positive side) and the peakedness to be something other than 3. In order to demonstrate the potential of this line of analysis, we have looked at the four sets of imaging data in the energy range 200-600 keV. The results of this analysis are presented in Table B-1.

**Table B-1**  
**IMAGE ELEMENT DISTRIBUTION ANALYSIS**

	CRAB	CYGNUS	NGC 4151	CG135+1
N	1114	973	1078	1135
$\mu$	-.069	.086	.014	.134
s	1.614	1.536	.990	1.140
skewness	1.018	1.299	.018	.057
kurtosis	5.503	6.718	2.678	2.679
livetime(secs)	12842	13039	5559	11097

Table B-1 also includes the number of composite image elements used in the analysis (N), the average  $n_{\sigma}$  (expected to be zero), and the total instrument livetime used to create the image. As can be seen from the table, those images which show no strong evidence for the presence of any source emission (NGC 4151 and CG135+1) have statistics which indicate a nearly Gaussian distribution. Those images which show strong evidence for source emission (Crab and Cygnus) have very non-Gaussian statistics. This analysis, as

presented here, is not meant to be a definitive test for the presence of source emission. It is simply presented as a suggestion for possible future study.

### Source Suppression in a Composite Image

The problem of source suppression, discussed in Appendix A for a single image, must also be dealt with in a composite image. The extension to a composite image from the results of Appendix A is fairly straightforward. It is important to note that, in building the composite image, each individual image element from the snapshot images has been divided by 16. This means that both the source height and the DC level per image element is reduced by the same factor of 16.

In order to resolve the source suppression problem, the prescription given at the end of Appendix A can be followed. The source is first fit with a Gaussian function using the DC level as a baseline. As in the case of a single image, the average DC level of the composite image must then be subtracted off. The fitting function is then,

$$f(x,y) = \frac{R_{fit}}{2\pi \alpha_x \alpha_y} \exp \left\{ -\frac{1}{2} \left[ \left( \frac{x-\mu_x}{\alpha_x} \right)^2 + \left( \frac{y-\mu_y}{\alpha_y} \right)^2 \right] \right\} + \Delta \quad (B.14)$$

where we now define  $\Delta$  to be,

$$\Delta = \frac{1}{16} \left( \frac{-S_T}{N-1} \right) \quad (B.15)$$

Equation (A.10) still holds in this case, so we can write equation (B.15) as,

$$\Delta = \frac{1}{16} \left( \frac{-R_{fit}}{N} \right) = -\frac{R_{fit}}{560} \quad (B.16)$$

This leads to the result which was presented in Chapter IV,

$$f(x,y) = \frac{R_{fit}}{2\pi \alpha_x \alpha_y} \exp \left\{ -\frac{1}{2} \left[ \left( \frac{x-\mu_x}{\alpha_x} \right)^2 + \left( \frac{y-\mu_y}{\alpha_y} \right)^2 \right] \right\} - \frac{R_{fit}}{560} \quad (B.17)$$

where, from Equation (A.10), we derive the total source response ( $S_T$ ) from,



$$S_T = (34/35) R_{\text{fit}} \quad (\text{B.18})$$

Alternatively, one may substitute  $S_T$  directly into equation (B.17) to avoid the last step represented by equation (B.18).

## APPENDIX C

### Bootstrap Sampling Statistics

Bootstrap sampling is a method which permits the extraction of allowable parameter ranges directly from the measured data. It is potentially a very powerful technique in that it is independent of any assumptions about the nature of the parent population of the parameter being investigated. It is, however, a computationally intensive technique. As such, it has only recently begun to receive serious attention from statisticians. A good general review can be found in Diaconis and Efron (1983). A more detailed treatment is given by Efron (1979). Simpson and Mayer-Hasselwander (1986) have discussed the application of the bootstrap technique to the analysis of the COS-B database. Here we shall present the basic concepts of bootstrap sampling and then describe the way in which this technique has been applied to the DGT database.

#### Basic Concepts

Bootstrap sampling is based on the idea that the parent distribution of a statistic (or model parameter) can best be estimated by repeating the experiment a large number of times. In this case, the experiment is "repeated" by deriving a large number simulated datasets from the single measured dataset. Each of these simulated datasets (also called a *bootstrap sample*) is obtained from the measured dataset by random sampling with replacement. To illustrate this procedure, consider a measured dataset with  $N$  data points. Each bootstrap sample also consists of  $N$  data points. Each point in the bootstrap sample is drawn at random from the measured set of data regardless of whether or not that point has already been selected (i.e., sampling with replacement). In this manner, it is possible for a given data point to be selected any number of times (including not at all) in each bootstrap sample. Once the bootstrap sample is collected, the statistic (or model parameter) of

interest is measured for that sample. The distribution of the measured statistic (or model parameter) which results from a large number of bootstrap samples is taken to represent the best available estimate for the parent distribution of that statistic (or model parameter).

One of the most powerful aspects of the bootstrap procedure is that it does not rely on any assumptions about the parent distributions involved in the data analysis. For example, the use of the classical  $\chi^2$  statistic for parameter range estimation involves varying the parameter of interest until some specified change in the associated  $\chi^2$  is effected. In this case, it is important to know the form of the denominator in the expression,

$$\chi^2 \equiv \sum_{i=1}^N \left( \frac{y_i - y_M}{\sigma_M} \right)^2 \quad (\text{C.1})$$

where the  $y_i$  are the measured data points, the  $y_M$  are the values predicted by the model being tested and the  $\sigma_M$  are the variances predicted by the model. An accurate prediction for the denominator (i.e.,  $\sigma_M$ ) generally requires a detailed propagation-of-error analysis for the experiment. This analysis may become very involved depending on the complexity of the experiment. Furthermore, this type of error analysis can only account for errors which are known and can be quantified. Any unknown errors may easily be overlooked. Obviously, any method which can avoid these difficulties and still provide reliable results (e.g., the bootstrap approach) may be of great value.

The bootstrap does not provide any new information regarding the most likely value for a given parameter. The most likely value of the parameter is simply that which is originally observed. The sole purpose of the bootstrap approach is to provide information regarding the *distribution* of the given parameter.

#### **Application to the DGT Database**

In the case of the DGT imaging data, the parameters of interest include the source location ( $\mu_x$  and  $\mu_y$ ), the point-spread-function ( $\sigma_x$  and  $\sigma_y$ ), and the measured intensity (i.e., the number of observed counts) for each of a number of different energy intervals.

The quantities  $\mu_x$ ,  $\mu_y$ ,  $\sigma_x$  and  $\sigma_y$  are measured from an image which is integrated over an energy range which is large enough to provide good source statistics (160 keV to 1 MeV). These results (which are independent of energy) are then used in determining the source intensity in each of the individual energy intervals.

Originally, a  $\chi^2$  approach was used in order to extract the associated confidence intervals for each parameter. Two difficulties arose with this procedure. Although a model had been developed to predict the element variances for a single DGT image, the extension of such a model to the composite DGT images was a more complicated problem. A second difficulty was encountered in the utilization of the errors in  $\mu_x$ ,  $\mu_y$ ,  $\sigma_x$  and  $\sigma_y$  when extracting the various image intensities. Should these values be allowed to vary from their best-fit results? If so, should they be constrained to within their derived parameter ranges? Also, what value should be used for  $\Delta\chi^2$ ? Should it correspond to two degrees of freedom or five? This problem of incorporating the errors on "calibration" data appears not to have been dealt with in the literature, at least in the context of a  $\chi^2$  analysis. At the time, it was noted that the resolution of these difficulties would be greatly facilitated if a second, independent means of determining the confidence intervals could be developed. This need led to an investigation of the bootstrap sampling procedure.

The bootstrap process provided an ideal alternative to the  $\chi^2$  approach. Not only was it independent of any model of the composite image statistics, it also could, in a very natural way, incorporate the uncertainties in the point-spread-function parameters which were used to extract the intensity information from the various energy intervals. Bootstrap sampling provided an alternative approach which permitted verification of results obtained with the  $\chi^2$  analysis. The power and simplicity of the bootstrap led to its use as the primary tool for the determination of parameter confidence levels.

We define a DGT bootstrap sample as follows. The "data points" in the measured dataset are represented by the individual snapshots which make up the database for a given source. Let there be  $N_S$  snapshots in the database being analyzed. (For the Crab data,  $N_S$

= 236.) Furthermore, let there be  $N_{\text{NRG}}$  energy intervals to be analyzed; each energy interval is associated with its own set of  $N_{\text{S}}$  snapshot intervals.. For each energy interval, we create a composite bootstrap image by assembling  $N_{\text{S}}$  snapshots which are selected from the database using the sampling with replacement technique discussed above. We then have a set of  $N_{\text{NRG}}$  composite bootstrap images. In order to determine the source location and point-spread-function using the best available statistics, the bootstrap images covering the energy range 160 keV to 1 MeV are summed together. The imaging response to the source in the sum image is then fit using equation (IV.6) in order to determine the corresponding values of  $\mu_x$ ,  $\mu_y$ ,  $\sigma_x$  and  $\sigma_y$ . In determining the imaging response for each individual image, the values of  $\mu_x$ ,  $\mu_y$ ,  $\sigma_x$  and  $\sigma_y$  are fixed while the source intensity is varied in order to obtain the best fit. The result of this entire procedure (one bootstrap sample) consists of the position ( $\mu_x$  and  $\mu_y$ ), PSF ( $\sigma_x$  and  $\sigma_y$ ) and intensity ( $I_T$ ) as determined in the sum image (160 keV to 1 MeV), along with the intensities as measured in each of the ( $N_{\text{NRG}}$ ) individual bootstrap images. A large number of such samples (~200) are created and the resulting distributions for the each of the various parameters can be used to extract the respective confidence levels.

As an example of the results which are obtained, Figures C-1 through C-3 present some representative results from the DGT data analysis. Figure C-1 shows a histogram distribution for the total Crab intensity in the 160 keV to 1 MeV energy range. Figure C-2 displays the data in a somewhat different fashion, which more readily permits the determination of the parameter confidence levels. The determination of the source location is demonstrated in Figure C-3. This figure represents the bootstrap distribution for the parameters  $\mu_x$  and  $\mu_y$  (converted to celestial coordinates).

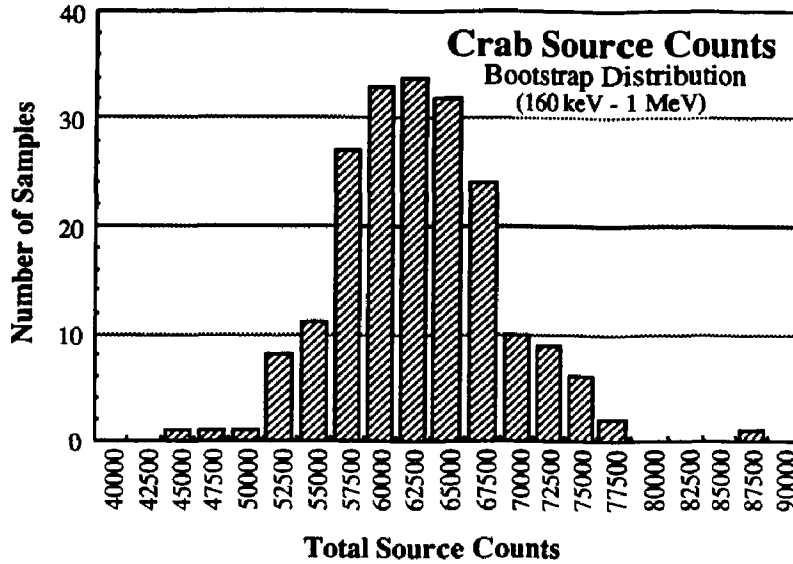


**FIGURE C-1:** The bootstrap distribution derived for the measured intensity of the Crab in the 160 keV to 1 MeV energy range, based on 200 bootstrap samples.

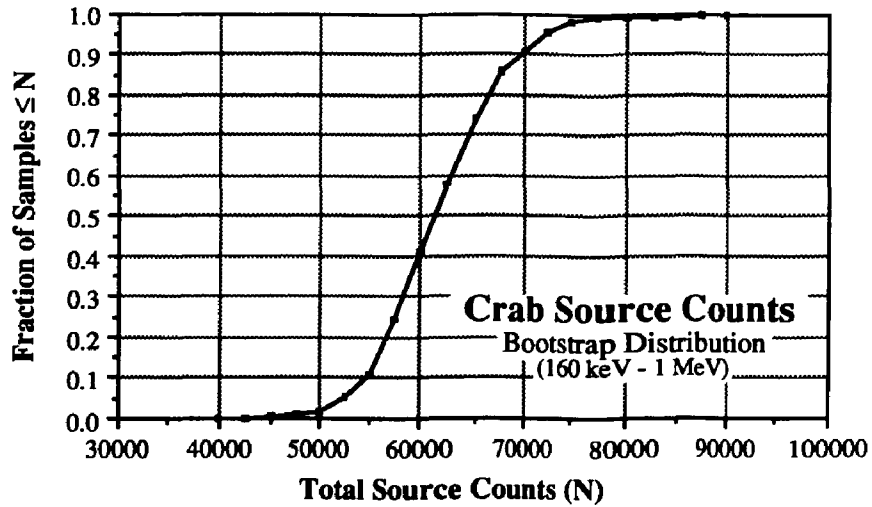


**FIGURE C-2:** A different representation of the bootstrap distribution for the Crab source counts in the 160 keV to 1 MeV range. This representation more readily permits the determination of confidence levels at any desired confidence.

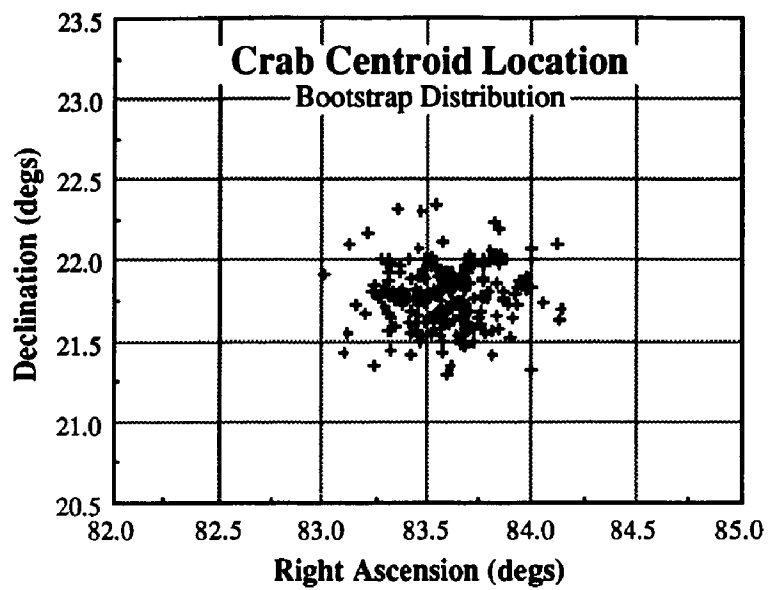


**FIGURE C-3:** The bootstrap distribution for the Crab source location, based on 200 bootstrap samples.

## **APPENDIX D**

### **DGT Response Function**

The response of a scintillation detector to a monoenergetic source of gamma-ray can be described by the following features:

- Full energy peak
- First escape peak
- Second escape peak
- Compton edge
- Compton continuum
- Backscatter peak

The response function can be thought of as a function which predicts the pulse height spectrum resulting from a given incident photon spectrum. In other words, the response function predicts the form and intensity of the above features. In modeling a pulse-height spectrum, one first determines the absolute energy-loss (or electron-deposit) spectrum using the energy-dependent parameterization of the above features. This spectrum represents the energy loss that would be observed by a detector with perfect energy resolution. In order to incorporate the finite resolution of the BGO detector array, the absolute energy-loss spectrum is folded through the energy-dependent resolution of the detector array. This smoothed spectrum represents the pulse-height spectrum which is expected to be observed by the experiment.

#### **Components of the DGT Response Function**

The response function of the DGT differs from the ideal case in a couple of important respects. First, the presence of the anticoincidence shielding acts to suppress both of the escape peaks as well as the Compton continuum. Second, the nature of the coded aperture imaging process is such that the spectra which are derived from the DGT imaging data represent the photon flux which is modulated by the mask. This means that



any scattered photon flux within the detector array (which is distributed uniformly among all of the detectors) is substantially suppressed in the reproduced spectrum.

The parameters which are used to define the DGT (imaging) response function are discussed below.

**Atmospheric attenuation.** The pointing history of the DGT during flight 1379-P is used to evaluate the energy-dependent attenuation of the gamma-ray flux incident on the top of the atmosphere. The pointing history is given in terms of the source zenith angle and the corresponding atmospheric depth of the experiment. Hence, the atmospheric attenuation is dependent on the source observation of interest.

**Lead attenuation (mask).** The lead elements of the mask perform the task of modulating the source flux so that the imaging information can be obtained. The lead elements are 1.9 cm (21.55 gm cm<sup>-2</sup>) thick. The fractional attenuation of the incident photon flux corresponding to 1.9 cm of lead is shown as a function of energy in Figure D-1. For a source within the imaging field-of-view, 17/35 (= 0.486) of the source flux incident on the mask will fall onto the lead and be attenuated.

**Aluminum transmission (mask).** Aluminum is used as a supporting structure in the coded mask assembly. Contained in the mask assembly are two sheets of aluminum which sandwich the lead elements. Each aluminum sheet is .051 cm thick. The total thickness of the aluminum is therefore .102 cm (.275 gm cm<sup>-2</sup>). The fractional transmission of this material as a function of energy is shown in Figure D-2.

**Aluminum attenuation (detector can).** Aluminum is the material which makes up the detector housing. Directly in front of the BGO array is an aluminum pressure dome .159 cm (.429 gm cm<sup>-2</sup>) thick. During the balloon flight there was also 5.08 cm (.163 gm cm<sup>-2</sup>) of Ethafoam thermal insulation surrounding the entire detector can. We approximated the attenuation of this material to be the same as that of aluminum. The combined fractional transmission of the aluminum pressure dome and the insulation is given in Figure D-3.

**BGO full energy peak efficiency.** The full energy peak efficiency of the BGO array at a given energy is determined from 1) the measured photofraction ( $P_o$ ) of a 5.08 cm diameter by 2 cm thick BGO crystal (Dunphy and Forrest 1985), 2) the known interaction efficiency of BGO ( $\epsilon_T$ ) and 3) the total geometric area ( $A$ ) of the BGO detectors in the array. More specifically,

$$\epsilon_p = P_o \epsilon_T A \quad (D.1)$$

The photofraction versus energy is shown in Figure D-4 (along with the same results for NaI(Tl) based on Berger and Seltzer 1972). The full energy peak efficiency versus energy is plotted in Figure D-5.

**First escape peak fraction.** This quantity (denoted  $P_1$ ) measures the fraction of the interacting photon flux which contributes to the first escape peak. Measurements of this quantity have been made up to an incident photon energy of 6.1 MeV. For higher energies, the function is assumed to follow the same form as that for NaI(Tl) (after Berger and Seltzer 1972). The resulting function is plotted in Figure D-6, along with the NaI(Tl) results.

**Second escape peak fraction.** This quantity (denoted  $P_2$ ) measures the fraction of the interacting photon flux which contributes to the second escape peak. Measurements of this quantity have been made up to an incident photon energy of 6.1 MeV. For higher energies, the function is assumed to follow the same form as that for NaI(Tl) (after Berger and Seltzer 1972). The resulting function is plotted in Figure D-7, along with the NaI(Tl) results.

**Compton suppression.** As mentioned previously, one effect of the anticoincidence shielding is to decrease the contribution of Compton scattered events and the escape peaks in the observed pulse height spectrum. This leads to a decrease in the height of the measured compton continuum and the escape peaks. For the DGT, this suppression factor has been estimated to be ~30%, i.e., 30% of the events which would otherwise show up in the compton continuum are rejected by the anticoincidence shielding.

**Energy resolution.** The fractional energy resolution of the gain stabilized array was measured prior to the balloon flight using a number of calibration sources with energies in the range 239 keV to 6.1 MeV. The results are shown in Figure D-8. The sources used in the DGT calibration are listed below.

ENERGY (MeV)	SOURCE
0.239	$^{228}\text{Th}$
0.511	$^{22}\text{Na}$
0.662	$^{137}\text{Cs}$
0.898	$^{88}\text{Y}$
1.275	$^{22}\text{Na}$
1.836	$^{88}\text{Y}$
2.615	$^{228}\text{Th}$
4.439	$^{241}\text{Am}$ $^9\text{Be}$ ( $^{12}\text{C}^*$ )
6.129	$^{244}\text{Cm}$ $^{12}\text{C}$ ( $^{16}\text{O}^*$ )

**Energy calibration.** The energy calibration provides a relationship between pulse height channel and the corresponding photon energy-loss. This data was obtained prior to the flight by measurements with a number of calibration sources as listed above.

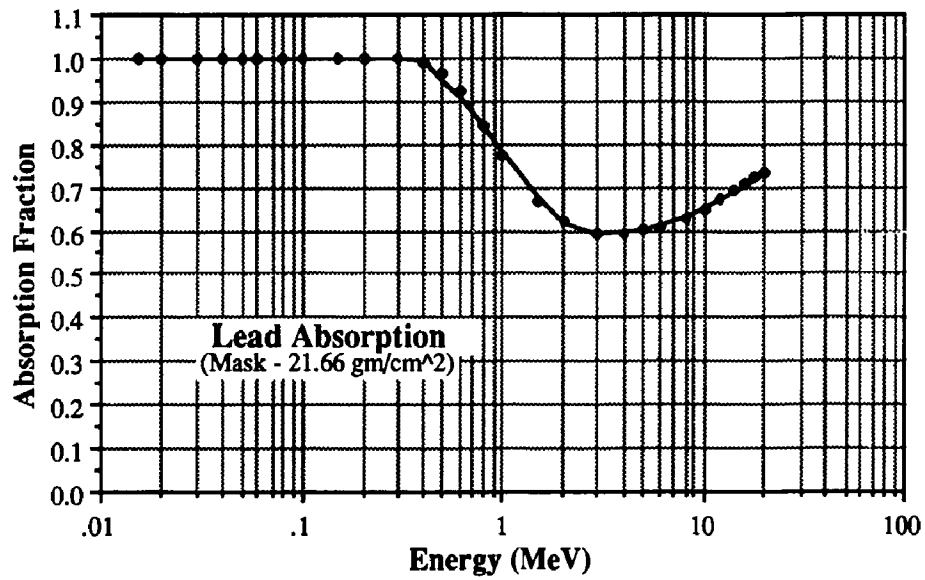


**FIGURE D-1:** The absorption of incident photon flux by the lead contained in the DGT mask. The points are based on tabulated values of the total mass attenuation coefficient (Tsoulfanidis 1983). The solid line represents the analytic fit which was used in the response function calculations.

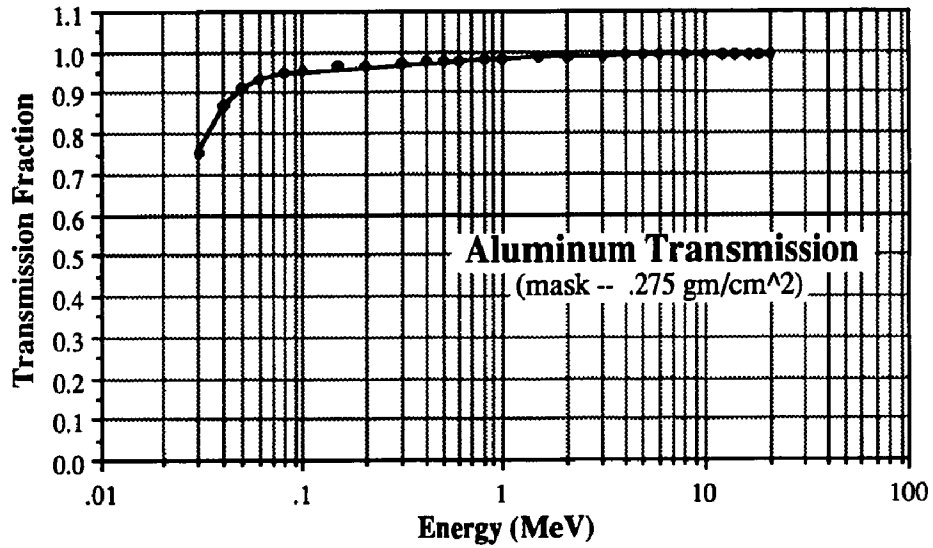


**FIGURE D-2:** The transmission of incident photon flux through the aluminum material contained in the DGT mask. The points are based on tabulated values of the total mass attenuation coefficient (Tsoulfanidis 1983). The solid line represents the analytic fit which was used in the response function calculations.

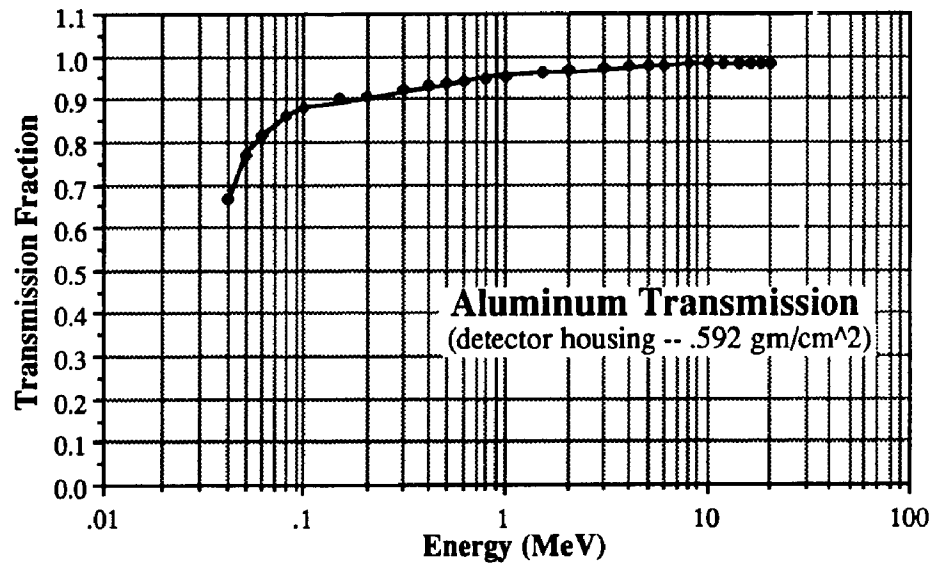


**FIGURE D-3:** The transmission of the incident photon flux through the aluminum in the detector housing. The points are based on tabulated values of the total mass attenuation coefficient (Tsoufanidis 1983). The solid line represents the analytic fit which was used in the response function calculations.

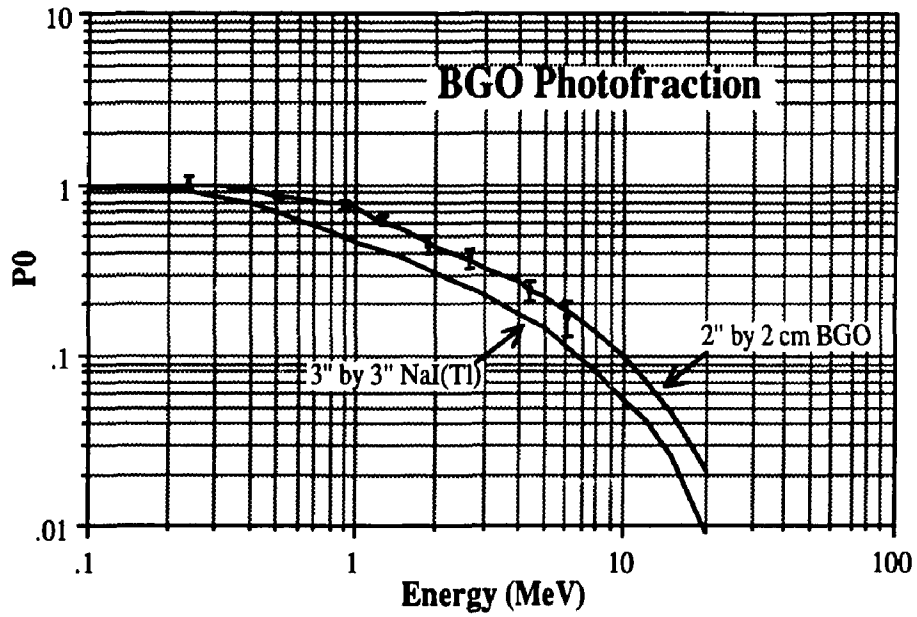


**FIGURE D-4:** The photofraction of a 2" by 2 cm BGO crystal as compared to that of a standard 3" by 3" NaI(Tl) detector (Berger and Seltzer 1972). The data points are from Dunphy and Forrest (1985).

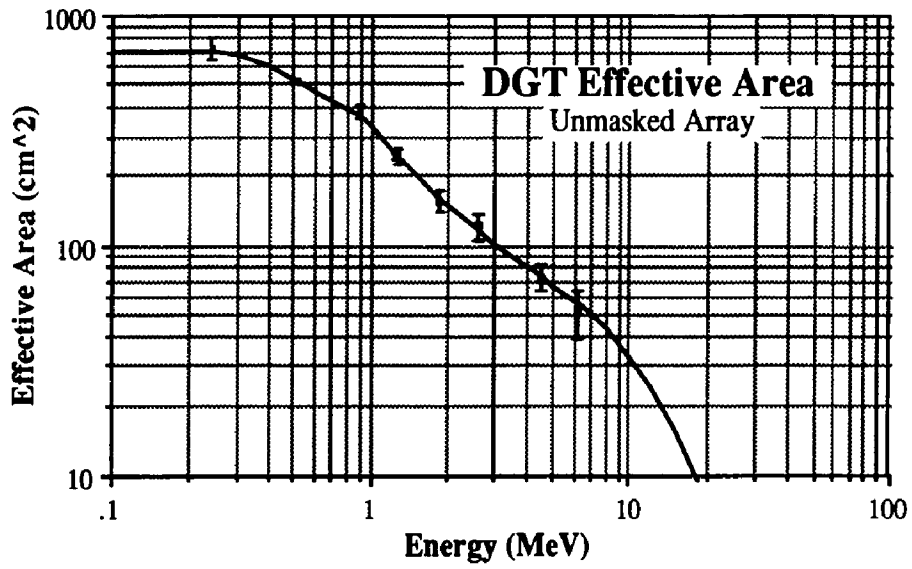


**FIGURE D-5:** The full-energy-peak efficiency of the BGO array. The data points are based on the results of Dunphy and Forrest (1985).



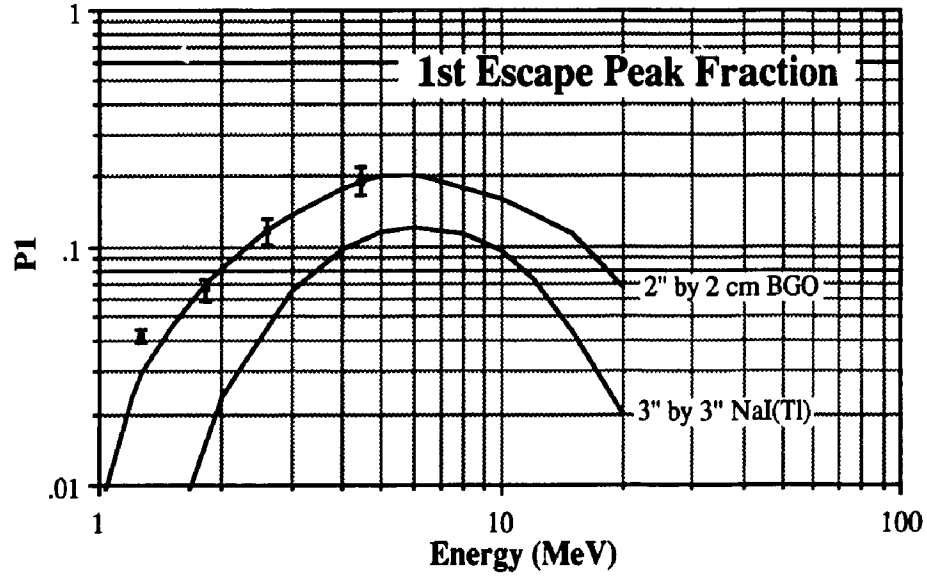


**FIGURE D-6:** The first escape peak fraction ( $P_1$ ) of BGO as a function of energy. The data points are measured points. The results for NaI are shown for comparison (Berger and Seltzer 1972).

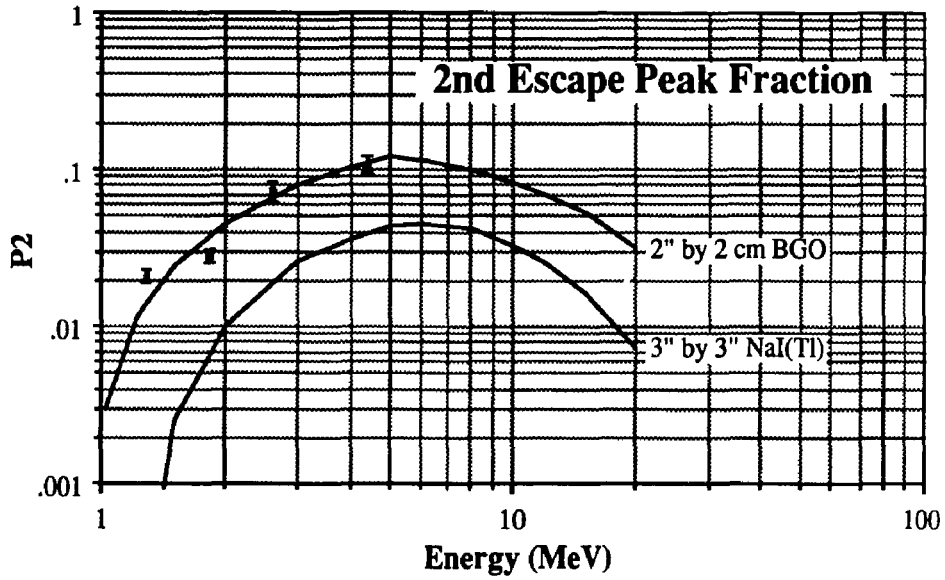


**FIGURE D-7:** The second escape peak fraction ( $P_2$ ) for BGO as a function of energy. The data points are measured points. The results for NaI are also shown for comparison (Berger and Seltzer 1972).

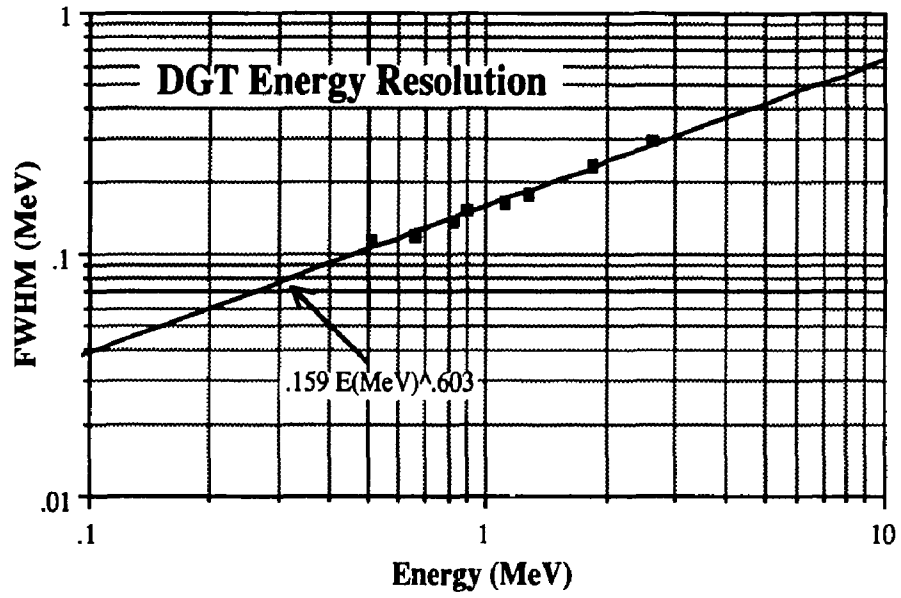


**FIGURE D-8:** The measured energy resolution of the gain stabilized BGO array.

## APPENDIX E

### Statistics of the Source Spectra

In this appendix, we provide detailed statistical information regarding the observed spectra of the Crab and of Cygnus X-1. In addition, the statistical details of source model fits are also provided.

#### The Observed Energy-Loss Spectra

As discussed in Chapter IV, the best-fit value for the source counts in each energy interval is determined by a minimization procedure which fits the measured point-spread-function to the imaging response of the source. The uncertainties in those data points are evaluated via a bootstrap analysis (Appendix C). The bootstrap provides a means to incorporate uncertainties in the data which may not otherwise be easily accounted for by the experimenter.

For an *ideal* imaging system, the statistical uncertainty of a single image element is given by (c.f., eq. II.14),

$$\sigma_o = \sqrt{(S+B)} \quad (E.1)$$

where  $S$  refers to the total number of modulated source counts in the array and  $B$  refers to the total background counts (which also includes unmodulated source counts). In the context of the DGT terminology, this expression applies to an ideal snapshot image (i.e., a single 7 by 5 element image). The need to deal with the problem of background systematics results in a degradation of the source statistics. In this case, equation (II.27) applies, and we can write,

$$\sigma^2 = \sigma_o^2 \left( 1 + 1.029 \frac{T_{\text{obs}}}{T_{\text{sys}}} \right) \quad (E.2)$$

where  $T_{\text{obs}}$  and  $T_{\text{sys}}$  refer to the time spent collecting source data and systematics data, respectively. Again, this results refers to the statistical uncertainty of an element in a single snapshot image. If a source were located at the center of an image element, then these expressions would correspond to the statistical uncertainty in the source measurement. If the source is not at the center of an image element, then the statistical uncertainty ( $\sigma$ ) will be greater by a factor of  $\sqrt{N}$ , where  $N$  represents the number of image elements involved in the source response. We can therefore generalize Equation (E.2) as,

$$\sigma^2 = \sigma_0^2 N \left( 1 + 1.029 \frac{T_{\text{obs}}}{T_{\text{sys}}} \right) \quad (\text{E.3})$$

In a situation in which the source is moving through the field-of-view,  $N$  in the above equation should be replaced by some "effective"  $N$ , which would represent the time-averaged number of source elements in the image.

Now let us turn to the case of a source measurement in a composite image (Appendix B). For this situation (with the DGT), we can use equation (E.3) with some  $N_{\text{eff}}$  in order to determine the statistical uncertainty of a composite image source measurement. Rather than attempt to calculate  $N_{\text{eff}}$ , we shall estimate  $N_{\text{eff}}$  based on the statistical results obtained from the bootstrap analysis.

Tables E-1 and E-2 present the statistical results for the Crab and Cygnus X-1 spectra. The background and source counts represent the total for the entire observation period. The statistical uncertainty based on equation (E.1) is given in column 3. Column 4 displays the uncertainty as given by equation (E.2). The bootstrap results [ $\sigma(\text{meas})$ ] are listed in column 5. Finally, an estimate of  $N_{\text{eff}} = \sigma^2(\text{meas}) / \sigma^2$  is given in column 6.

These results show that the average  $N_{\text{eff}}$  for the Crab observation is 1.96. For the Cygnus data, the average  $N_{\text{eff}}$  is 3.32. This difference between the Crab and Cygnus data would imply that, on average, the imaging response to Cyg X-1 was split amongst more elements than the imaging response to the Crab. Note also that some of the results for Cygnus X-1 are greater than four, the maximum possible number of source elements which

can be involved in the response at any given time. This indicates that there may be other effects contributing to the statistical uncertainties as derived by the bootstrap analysis.

**TABLE E-1**  
**CRAB SPECTRUM STATISTICS**

ENERGY (keV)	BCKGND	SOURCE	$\sigma_0$	$\sigma(\text{calc})$	$\sigma(\text{meas})$	$N_{\text{eff}}$
160-200	$1.2025 \times 10^6$	12359	1102	1447	1931	1.77
200-250	$1.0985 \times 10^6$	16231	1056	1387	2175	2.46
250-300	$7.9209 \times 10^5$	8640	895	1175	1596	1.85
300-400	$1.1187 \times 10^6$	8037	1062	1395	1828	1.72
400-800	$2.4052 \times 10^6$	12887	1555	2042	2839	1.93
800-2000	$1.6937 \times 10^6$	7850	1304	1712	2650	2.40
2000-9300	$7.9312 \times 10^5$	1172	891	1170	1479	1.59

**TABLE E-2**  
**CYGNUS SPECTRUM STATISTICS**

ENERGY (keV)	BCKGND	SOURCE	$\sigma_0$	$\sigma(\text{calc})$	$\sigma(\text{meas})$	$N_{\text{eff}}$
160-200	$1.2210 \times 10^6$	23800	1116	1471	2750	3.50
200-250	$1.1154 \times 10^6$	19560	1065	1403	3138	5.02
250-300	$8.0425 \times 10^5$	9549	902	1188	2198	3.42
300-400	$1.1358 \times 10^6$	13255	1072	1412	2454	3.03
400-600	$1.7918 \times 10^6$	7824	1342	1768	3425	3.76
600-1000	$1.0875 \times 10^6$	4922	1045	1377	3120	5.15
1000-2000	$1.2825 \times 10^6$	-3815	1133	1492	2695	3.28
2000-4000	$4.5962 \times 10^5$	2135	680	896	1430	2.56
4000-5000	$1.0953 \times 10^5$	1193	333	439	699	2.53
5000-6000	$7.7191 \times 10^4$	1265	280	369	535	2.10
6000-9300	$1.5947 \times 10^5$	805	400	527	783	2.22

## Model Spectra Statistics

It is instructive to look at the statistics pertaining to the model source spectra which are fit to the observed energy loss spectra. In determining the best fit source spectrum, a model spectrum is processed through the DGT response function (Appendix D) in order to determine the corresponding energy loss spectrum. The model energy loss spectrum is then compared to the observed energy loss spectrum using a  $\chi^2$  test. Here, we present a comparison of the model energy loss spectrum and the observed energy loss spectrum for four cases presented in Chapter V: a single power law spectrum for the Crab, a single power law spectrum for Cyg X-1, a single-temperature inverse Compton model for Cyg X-1, and a power law plus Compton model for Cyg X-1. In each case, the data are tabulated below. Table E-3 presents the power law fit to the observed Crab spectrum. The power law is of the form  $5.1 \times 10^{-3} E_{\text{MeV}}^{-1.88}$  photons  $\text{cm}^{-2} \text{s}^{-1} \text{MeV}^{-1}$ . Table E-4 provides the same data for Cyg X-1, with a power-law model extending from 160 keV to 10 MeV. The power law in this case is given by  $3.73 \times 10^{-3} E_{\text{MeV}}^{-2.35}$  photons  $\text{cm}^{-2} \text{s}^{-1} \text{MeV}^{-1}$ . Table E-5 gives the results from fitting a single-temperature inverse Compton model to the entire Cyg X-1 energy loss spectrum. The corresponding Compton parameters are  $kT_e = 177$  keV and  $\tau = 0.6$ . Finally, Table E-6 shows the results for a two-component fit to the Cyg X-1 data. The two components consist of an inverse Compton model (with  $kT_e = 80$  keV,  $\tau = 2.0$ ) and a power-law of the form  $1.8 \times 10^{-3} E_{\text{MeV}}^{-0.6}$  photons  $\text{cm}^{-2} \text{s}^{-1} \text{MeV}^{-1}$ .

**TABLE E-3**  
**CRAB POWER-LAW MODEL**

ENERGY (keV)	SOURCE COUNTS	$n_{\nu}$	MODEL COUNTS	$\Delta\chi^2$
160-200	12359±1931	6.40	13767	0.53
200-250	16231±2175	7.46	11825	4.10
250-300	8640±1596	5.41	8263	0.06
300-400	8037±1828	4.40	10351	1.60
400-800	12887±2839	4.54	13294	0.02
800-2000	7850±2650	2.96	4811	1.32
2000-9300	1172±1479	0.79	1536	0.06

**TABLE E-4**  
**CYG X-1 POWER LAW MODEL**

ENERGY (keV)	SOURCE COUNTS	$n_{\nu}$	MODEL COUNTS	$\Delta\chi^2$
160-200	23800±2750	8.65	23433	0.02
200-250	19560±3138	6.23	18058	0.23
250-300	9549±2198	4.34	11208	0.57
300-400	13255±2454	5.40	12703	0.05
400-600	7824±3425	2.28	9752	0.32
600-1000	4922±3120	1.58	5001	0.00
1000-2000	-3815±2695	-1.41	1745	4.26
2000-4000	2135±1430	1.49	411	0.42
4000-5000	1193±699	1.71	65	2.60
5000-6000	1265±535	2.36	41	5.23
6000-9300	805±783	1.03	62	0.90



**TABLE E-5**  
**CYG X-1 COMPTON MODEL**

ENERGY (keV)	SOURCE COUNTS	$n_{\nu}$	MODEL COUNTS	$\Delta\chi^2$
160-200	23800±2750	8.65	24598	0.08
200-250	19560±3138	6.23	18406	0.14
250-300	9549±2198	4.34	10981	0.43
300-400	13255±2454	5.40	11706	0.40
400-600	7824±3425	2.28	7696	0.00
600-1000	4922±3120	1.58	2544	0.58
1000-2000	-3815±2695	-1.41	250	2.28
2000-4000	2135±1430	1.49	1	2.23
4000-5000	1193±699	1.71	0	2.91
5000-6000	1265±535	2.36	0	5.59
6000-9300	805±783	1.03	0	1.06

**TABLE E-6**  
**CYG X-1 POWER LAW PLUS COMPTON MODEL**

ENERGY (keV)	SOURCE COUNTS	$n_{\nu}$	MODEL COUNTS	$\Delta\chi^2$
160-200	23800±2750	8.65	22253	0.32
200-250	19560±3138	6.23	18690	0.08
250-300	9549±2198	4.34	11885	1.13
300-400	13255±2454	5.40	12562	0.08
400-600	7824±3425	2.28	7158	0.04
600-1000	4922±3120	1.58	2549	0.58
1000-2000	-3815±2695	-1.41	2021	4.69
2000-4000	2135±1430	1.49	1995	0.01
4000-5000	1193±699	1.71	728	0.44
5000-6000	1265±535	2.36	625	1.43
6000-9300	805±783	1.03	1509	0.81

## REFERENCES

- Ables, J. G. 1968, *Proc. Astron. Soc. Aust.*, **4**, 172. "Fourier Transform Photography: A New Method for X-Ray Astronomy."
- Aharonian, F. A. and Sunyaev, R. A. 1984, *Mon. Not. R. Astr. Soc.*, **210**, 257. "Gamma-Ray Line Emission, Nuclear Destruction and Neutron Production in Hot Astrophysical Plasmas. The Deuterium Boiler as a Gamma-Ray Source."
- Aharonian, F. A. and Vardanian, V. V. 1985, *Astro. Space Sci.*, **115**, 31. "On the Origin of Soft Gamma-Rays from Cyg X-1."
- Akimov, V. V., *et al.* 1985, *Proc. 19th Internat. Cosmic Ray Conf.*, La Jolla, **3**, 330. "The Gamma-Ray Telescope GAMMA-1."
- Albats, P., Frye, G. M., Zych, A. D., Mace, O. B., Hopper, V. D., and Thomas, J. A. 1972, *Nature*, **240**, 221. "Detection of 10-100 MeV  $\gamma$ -rays from the Crab Nebula Pulsar NP 0532."
- Althouse, W. E., Cook, W. R., Cummings, A. C., Finger, M. H., Prince, T. A., Schindler, S. M., Starr, C. H., and Stone, E. C. 1985, *Proc. 19th Internat. Cosmic Ray Conf.*, La Jolla, **3**, 299. "A Balloon-Borne Imaging Gamma-Ray Telescope."
- Apparao, K. M. V. 1973, *Ap. Space Sci.*, **25**, 3. "The Crab Nebula."
- Avni, Y. 1976, *Ap. J.*, **210**, 642. "Energy Spectra of X-Ray Clusters of Galaxies."
- Ayre, C. A., Bhat, P. N., Ma, Y. Q., Myers, R. M., and Thompson, M. G. 1983, *Mon. Not. R. Astr. Soc.*, **205**, 285. "Gamma-Ray Line Features from the Crab Nebula in the Energy Range 50-2000 keV."
- Baker, R. E., Lovett, R. R., Orford, K. J., and Ramsden, D. 1973, *Nature Phys. Sci.*, **245**, 18. "Gamma-Rays of 1 to 10 MeV from the Crab and Cygnus Regions."
- Barr, P., White, N. E., and Page, C. G. 1985, *Mon. Not. R. Astr. Soc.*, **216**, 65P. "The Discovery of Low-Level Iron K Line Emission from Cyg X-1."
- Bennett, K., Bignami, G., Hermsen, W., Mayer-Hasselwander, H. A., Paul, J. A., and Scarsi, L. 1977a, *Astr. Ap.*, **59**, 273. "Search for Gamma-ray Emission with 4.8 h Periodicity from Cygnus X-3."
- Bennett, K., *et al.* 1977b, *Astr. Ap.*, **61**, 279. "COS B Observations of Pulsed  $\gamma$ -ray Emission from PSR 0531+21 and PSR 0833-45."
- Berger, M. J. and Seltzer, S. M. 1972, *Nucl. Instrum. Methods*, **104**, 317. "Response Functions for Sodium Iodide Scintillation Detectors."
- Bevington, P. R. 1969, *Data Reduction and Error Analysis for the Physical Sciences* (New York: McGraw-Hill).

- Blake, R. L., Burek, A. J., Fenimore, E. E., and Puetter, R. 1974, *Rev. Sci. Instrum.*, **45**, 513. "Solar X-Ray Photography with Multiplex Pin-hole Camera."
- Bleach, R. D., Boldt, E. A., Holt, S. S., Schwartz, D. A., and Serlimitsos, P. J. 1972, *Ap. J.*, **171**, 51. "X-Ray Spectra of Discrete Sources in Cygnus."
- Boella, A., *et al.* 1984, *Nuovo Cimento*, **7**, 805. "Low-Energy Gamma-Ray Sources Observed by the *MISO* Telescope."
- Bolton, C. T. 1972, *Nature*, **235**, 271. "Identification of Cygnus X-1 with HDE 226868."
- Bolton, C. T. 1975, *Ap. J.*, **200**, 269. "Orbital Elements and an Analysis of Models for HDE 226868 = Cygnus X-1."
- Bowyer, S., Byram, E. T., Chubb, T. A., and Friedman, H. 1965, *Science*, **147**, 394.
- Bregman, J., Butler, D., Kemper, E., Koski, A., Kraft, R. P., and Stone, R. P. S. 1973, *Ap. J. (Letters)*, **185**, L117. "On the Distance to Cygnus X-1 (HDE 226868)."
- Butler, R. C., *et al.* 1985, *Proc. 19th Internat. Cosmic Ray Conf.*, La Jolla, **3**, 322. "An Experimental Assessment of the Imaging Quality of the Low Energy Gamma-Ray Telescope ZEBRA."
- Carpenter, G. F., Coe, M. J., and Engel, A. R. 1976, *Nature*, **259**, 99. "New X-Ray Measurements of the Crab Spectrum in the Range 26 keV-1.2 MeV."
- Chadwick, P. M. *et al.* 1985, *Nature*, **318**, 642. "A 12.6ms Pulsar in Cygnus X-3."
- Charalambous, P. M., Dean, A. J., Stephen, J. B., Young, N. G. S., and Gourlay, A. R. 1984, *Nucl. Instrum. Methods*, **221**, 56. "Aberrations in Gamma-Ray Imaging Systems."
- Cheng, A.F. and Ruderman, M.A. 1977, *Ap. J.*, **216**, 865. "A Crab Pulsar Model: X-Ray, Optical, and Radio Emission."
- Cheng, K.S., Ho, K., and Ruderman, M. 1986a, *Ap. J.*, **300**, 500. "Energetic Radiation from Rapidly Spinning Pulsars. I. Outer Magnetosphere Gaps."
- Cheng, K.S., Ho, K., and Ruderman, M. 1986b, *Ap. J.*, **300**, 522. "Energetic Radiation from Rapidly Spinning Pulsars. II. Vela and Crab."
- Chupp, E.L. 1976, *Gamma-Ray Astronomy* (Dordrecht, Holland: D. Reidel).
- Clayton, D. D. and Craddock, W. L. 1965, *Ap. J.*, **142**, 189. "Radioactivity in Supernova Remnants."
- Clayton, D. D., Colgate, S. A., and Fishman, G. J. 1969, *Ap. J.*, **155**, 75. "Gamma-Ray Lines from Young Supernova Remnants."
- Clear, J., Bennett, K., Buccheri, R., Grenier, I.A., Hermsen, W., Mayer-Hasselwander, H.A., and Sacco, B. 1986, *Ap. J.* In Press. "A Detailed Analysis of the High Energy Gamma Ray Emission from the Crab Pulsar and Nebula."

- Cline, D. and Lesser, P. M. S. 1970, *Nucl. Instrum. Methods*, **82**, 291. "Error Estimation in Non-Linear Least Squares Analysis of Data."
- Cocke, W.J., Disney, H.J., and Taylor, D.J. 1969, *Nature*, **221**, 525. "Discovery of Optical Signals from Pulsar NP 0532."
- Coe, M. J., Carpenter, G. F., Engel, A. R., and Quenby, J. J. 1975, *Nature*, **256**, 630. "Hard X-Ray Measurements of Nova A0535+26 in Taurus."
- Collins, M. S. 1979, *Astr. Ap.*, **74**, 108. "Gamma Rays from Accretion onto Rotating Black Holes."
- Colpi, M., Maraschi, L., and Treves, A. 1984, *Ap. J.*, **280**, 319. "Two-Temperature Model of Spherical Accretion onto a Black Hole."
- Colpi, M., Maraschi, L., and Treves, A. 1986, *Ap. J.*, **311**, 150. "Gamma-Ray Emission from Accretion onto a Rotating Black Hole."
- Cook, W. R., Finger, M., Prince, T. A., and Stone, E. C. 1984, *IEEE Trans. Nucl. Sci.*, **31**, No. 1, 771. "Gamma-Ray Imaging with a Rotating Hexagonal Uniformly Redundant Array."
- Cook, W. R., Finger, M., and Prince, T. A. 1985, *IEEE Trans. Nucl. Sci.*, **32**, No. 1, 129. "A Thick Anger Camera for Gamma-Ray Astronomy."
- Costa, E., Massaro, E., Salvati, M., and Appolloni, A. 1984, *Astr. Space Sci.*, **100**, 165. "An Approximate Analytical Representation of the Atmospheric Gamma-Ray Flux at Balloon Altitudes."
- Dahlbacka, G. H., Chapline, G. F., and Weaver, T. A. 1974, *Nature*, **250**, 36. "Gamma Rays from Black Holes."
- Danaher, S., Fegan, D. J., Porter, N. A., and Weekes, T. C. 1981, *Nature*, **289**, 568. " $\gamma$ -Ray Observations of Cygnus X-3 at Energies of  $10^{12}$  eV."
- Daniel, R. R. and Stephens, S. A. 1974, *Rev. of Geophys. Space Sci.*, **12**, 233. "Cosmic-Ray-Induced Electrons and Gamma-Rays in the Atmosphere."
- Dean, A. J. and Dipper, N. A. 1981, *Mon. Not. R. Astr. Soc.*, **194**, 219. "An Evaluation of the Background Effects in Actively Shielded Hard X-Ray Telescopes at Balloon Altitudes."
- Dean, A. J. and Ramsden, D. 1981, *Phil. Trans. R. Soc. Lond.*, **A 301**, 577. "Extragalactic  $\gamma$ -Rays."
- Diaconis, P. and Efron, B. 1983, *Scientific American*, May, 96. "Computer-Intensive Methods in Statistics."
- Dicke, R. H. 1968, *Ap. J. (Letters)*, **153**, L101. "Scatter-Hole Cameras for X-Rays and Gamma-Rays."
- Doi, K. 1980, *Nature*, **287**, 210. "Short-Term Variability and the Accretion Disk Temperature Fluctuation."

- Dolan, J. F. 1986, *Comments Astrophys.*, **11**, 135. "Polarization in X-Ray Binaries."
- Dolan, J. F., Crannell, C. J., Dennis, B. R., Frost, K. J., Maurer, G. S., and Orwig, L. E. 1977, *Ap. J.*, **217**, 809. "The High-Energy X-Ray Spectrum of the Crab Nebula Observed from OSO-8."
- Dolan, J. F., Crannell, C. J., Dennis, B. R., Frost, K. J., and Orwig, L. E. 1982, *Astrophys. Letters*, **22**, 147. "High-Energy X-Ray Observations of Cyg X-3 from OSO-8: Further Evidence of a 34.1 day Period?"
- Dowthwaite, J. C., *et al.* 1984, *Astr. Ap.*, **126**, 1. "Ultra-High Energy Gamma Rays from Cygnus X-3."
- Duffett-Smith, P. 1981, *Practical Astronomy with Your Calculator* (Cambridge: Cambridge University Press).
- Dunphy, P. P., Forrest, D. J., Chupp, E. L., Cherry, M. L., and Ryan, J. M. 1981, *Ap. J.*, **244**, 1081. "Limit on a Galactic 6.13 MeV  $\gamma$ -Ray Line."
- Dunphy, P. P. and Forrest, D. J. 1985, *IEEE Trans. Nucl. Sci.*, **32**, 538. "Photofraction of a 5 cm  $\times$  2 cm BGO Scintillator."
- Durouchoux, P., Hudson, H., Hurford, G., Hurley, K., Matteson, J., and Orsal, E. 1983, *Astr. Ap.*, **120**, 150. "Gamma-Ray Imaging with a Rotating Modulator."
- Eardley, D. M., Lightman, A. P., Payne, D. G., and Shapiro, S. L. 1978, *Ap. J.*, **224**, 53. "Accretion Disks around Massive Black Holes: Persistent Emission Spectra."
- Efron, B. 1979, *SIAM Review*, **21**, 460. "Computers and the Theory of Statistics: Thinking the Unthinkable."
- Eichler, D. and Vestrand, W. T. 1984, *Nature*, **307**, 613. "Implications of  $10^{16}$  eV  $\gamma$  Rays from Cyg X-3."
- Eilek, J. A. 1980, *Ap. J.*, **236**, 664. "Pair Production and Gamma-Ray Luminosities in Hot Accretion Disks."
- Eilek, J. A., and Kafatos, M. 1983, *Ap. J.*, **271**, 804. "The High-Energy Spectrum of Hot Accretion Disks."
- Erickson, R. A., Fickle, R. K., and Lamb, R. C. 1976, *Ap. J.*, **210**, 539. "Search for Pulsed Gamma Rays of  $\sim 10^{13}$  eV from NP 0532."
- Fazio, G. G. 1967, *Ann. Rev. Astr. Astrophys.*, **5**, 481. "Gamma Radiation from Celestial Objects."
- Fenimore, E. E. 1978, *Appl. Opt.*, **17**, 3562. "Coded Aperture Imaging: Predicted Performance of Uniformly Redundant Arrays."
- Fenimore, E. E. 1980, *Appl. Opt.*, **19**, 2465. "Coded Aperture Imaging: The Modulation Transfer Function for Uniformly Redundant Arrays."

- Fenimore, E. E. 1987, preprint. "Time-Resolved and Energy-Resolved Coded Aperture Images with URA-Tagging."
- Fenimore, E. E. and Cannon, T. M. 1978, *Appl. Opt.* **17**, 337. "Coded Aperture Imaging with Uniformly Redundant Arrays."
- Fenimore, E. E., Cannon, T. M., Van Hulsteyn, D. B., and Lee, P. 1979, *Appl. Opt.*, **18**, 945. "Uniformly Redundant Array Imaging of Laser Driven Compressions: Preliminary Results."
- Fenimore, E. E., Klebesadel, R. W., and Laros, J. G. 1983, in *Adv. Space Res.*, **3**, 207. "Problems in the Analysis of Gamma-Ray Burst Spectra."
- Ferguson, D. C. 1981, in *IAU Symposium No. 95, Pulsars*, eds. W. Sieber and R. Wielebinski (Dordrecht: Reidel), p. 141. "Pulse Emission from the Light Cylinder."
- Fichtel, C. E., Hartman, R. C., Kniffen, D. A., Thompson, D. J., Bignami, G. F., Ögelman, H., Özel, M. E., and Tümer, T. 1975, *Ap. J.*, **198**, 163. "High-Energy Gamma-Ray Results from the Second Small Astronomy Satellite."
- Fichtel, C. E. and Trombka, J. I. 1981, *Gamma Ray Astrophysics : New Insight into the Universe* (NASA SP-453).
- Finger, M. H. and Prince, T. A. 1985, *Proc. 19th Internat. Cosmic Ray Conf.*, La Jolla, **3**, 295. "Hexagonal Uniformly Redundant Arrays for Coded-Aperture Imaging."
- Fishman, G. J. 1972, *Ap. J.*, **171**, 163. "Cosmic-Ray Effects on Diffuse Gamma-Ray Measurements."
- Forrest, D. J., *et al.* 1980, *Solar Phys.*, **65**, 15. "The Gamma Ray Spectrometer for the Solar Maximum Mission."
- Frank, J., King, A. R., and Raine, D. J. 1985, *Accretion Power in Astrophysics* (Cambridge: Cambridge University Press).
- Frontera, F., Dal Fiume, D., Dusi, W., Morelli, E., Spada, G., and Ventura, G. 1982, in *Accreting Neutron Stars*, eds. W. Brinkman and J. Trumper, 112. "Hard X-Ray Observation of the Transient X-Ray Pulsar A0535+26."
- Frontera, F., Dal Fiume, D., Morelli, E., and Spada, G. 1985, *Ap. J.*, **298**, 585. "The X-Ray Pulsar A0535+26: Pulse Profile and Its Time Variability in Hard X-Rays."
- Frye, G. M., Jenkins, T. L., Owens, A., Carter, J. N., Hall, C. J., Ramsden, D., Agrinier, B., and Gouiffes, C. 1985, in *Proceedings of the Workshop on Cosmic-Ray and High-Energy Gamma-Ray Experiments for the Space Station Era*, eds. W. V. Jones and J. P. Wefel, 462. "CAMTRAC, a High Energy Gamma-Ray Telescope Utilizing a Coded Aperture Mask and Drift Chambers."
- Gehrels, N., *et al.* 1985, *Proc. 19th Internat. Cosmic Ray Conf.*, La Jolla, **3**, 303. "A Coded Aperture Imaging System Optimized for Hard X-Ray and Gamma-Ray Astronomy."

- Gies, D. R. and Bolton, C. T. 1982, *Ap. J.*, **260**, 240. "The Optical Spectrum of HDE 226868 = Cygnus X-1. I. Radial Velocities and Orbital Elements."
- Gies, D. R. and Bolton, C. T. 1986a, *Ap. J.*, **304**, 371. "The Optical Spectrum of HDE 226868 = Cygnus X-1. II. Spectrophotometry and Mass Estimates."
- Gies, D. R. and Bolton, C. T. 1986b, *Ap. J.*, **304**, 389. "The Optical Spectrum of HDE 226868 = Cygnus X-1. III. A Focused Stellar Wind Model for He II  $\lambda 4686$  Emission."
- Giles, A. B. 1981, *Mon. Not. R. Astr. Soc.*, **195**, 721. "Observations of Sub-Millisecond Bursts from Cygnus X-1."
- Ginzburg, V. L. and Syrovatskii, S. I. 1964, *The Origin of Cosmic Rays* (Oxford: Pergamon).
- Gleske, I. U., Forrest, D. J. 1980, *IEEE Trans. Nucl. Sci.*, **27**, No. 1, 313. "A Nuclear Detector Gain Stabilizing Technique with Only One Stable Gain Position."
- Gold, T. 1968, *Nature*, **218**, 731. "Rotating Neutron Stars as the Origin of the Pulsating Radio Sources."
- Gold, T. 1969, *Nature*, **221**, 25. "Rotating Neutron Stars and the Nature of Pulsars."
- Goldreich, P. and Julian, W.H. 1969, *Ap. J.*, **157**, 869. "Pulsar Electrodynamics."
- Graser, U. and Schonfelder, V. 1982, *Ap. J.*, **263**, 677. "Gamma-Ray Emission from the Galactic Anticenter at MeV Energies."
- Greisen, K. 1971, *The Physics of Cosmic x-Ray,  $\gamma$ -Ray and Particle Sources* (New York: Gordon and Breach).
- Gruber, D. E., and Ling, J. C. 1977, *Ap. J.*, **213**, 802. "Evidence for Detection of 1-10 MeV Emission from the Taurus Region in 1971 August."
- Gunn, J.E. and Ostriker, J.P. 1969, *Nature*, **221**, 454. "Magnetic Dipole Radiation from Pulsars."
- Hameury, J. M., Boclet, D., Durouchoux, Ph., Cline, T. L., Paciasas, W. S., Teegarden, B. J., Tueller, J., and Haymes, R. C. 1983, *Ap. J.*, **270**, 144. "Hard X-Ray Observations of the Crab Nebula and A0535+26 with a High Energy Resolution Spectrometer."
- Harding, A.K. 1981, *Ap. J.*, **245**, 267. "Pulsar Gamma-Rays: Spectra, Luminosities, and Efficiencies."
- Harding, A. K. and Stecker, F. W. 1981, *Nature*, **290**, 316. "Pulsar and Diffuse Contributions to the Observed Galactic  $\gamma$  Radiation."
- Harnden, F. R., and Seward, F. D. 1984, *Ap. J.*, **283**, 279. "Einstein Observations of the Crab Nebula Pulsar."

- Hasinger, G., Pietsch, W., Reppin, C., Trümper, J., Voges, W., Kendziorra, E., and Staubert, R. 1984, in *Adv. Space Res.*, **3**, No. 10-12, 63. "Hard X-Ray Observations of the Crab Pulsar."
- Haymes, R. C., Ellis, D. V., Fishman, G. J., Kurfess, J. D., and Tucker, W.H. 1968, *Ap. J. (Letters)*, **151**, L9. "Observation of Gamma Radiation from the Crab Nebula."
- Helmken, H. and Hoffman, J. 1973, *Proc. 13th Internat. Cosmic Ray Conf.*, Denver, **1**, 31. "Pulsed Gamma-Ray Flux from NP0532 at  $E \geq 15$  MeV."
- Hermesen, W. 1980, Ph.D. thesis, University of Leiden, the Netherlands. "Gamma-Ray Sources."
- Hewish, A., Bell, S. J., Pilkington, J. D. H., Scott, P. F., and Collins, R. A. 1968, *Nature*, **217**, 709. "Observation of a Rapidly Pulsating Radio Source."
- Higdon, J. C. and Lingenfelter, R. E. 1977, *Ap. J. (Letters)*, **215**, L53. "Nuclear  $\gamma$ -Ray Lines in Accretion Source Spectra."
- Holt, S. S., Boldt, E. A., Serlimitsos, P. J., and Kaluziński, L. J. 1976, *Ap. J. (Letters)*, **203**, L63. "New Results from Long-Term Observations of Cygnus X-1."
- Ichimaru, S. 1977, *Ap. J.*, **214**, 840. "Bimodal Behavior of Accretion Disks: Theory and Application to Cygnus X-1 Transitions."
- Issa, M. R. and Wolfendale, A. W. 1981, *Nature*, **292**, 430. " $\gamma$  Rays from the Cosmic Ray Irradiation of Local Molecular Clouds."
- Jacobson, A. S., Bishop, R. J., Culp, G. W., Jung, L., Mahoney, W. A., and Willet, J. B. 1975, *Nucl. Instrum. Methods*, **127**, 115. "A Balloon-Borne Ge(Li) Spectrometer for Gamma-Ray Astronomy."
- Jenkins, F. A. and White, H. E. 1950, *Fundamentals of Optics* (New York: McGraw-Hill).
- Joss, P. C. and Rappaport, S. A. 1984, *Ann. Rev. Astron. Astrophys.*, **22**, 537. "Neutron Stars in Interacting Binary Systems."
- Jung, G. V. 1986, Ph. D. thesis, University of California at San Diego. "The Hard X-Ray to Low Energy Gamma-Ray Spectrum of the Crab Nebula."
- Kaluziński, L. J., Holt, S. S., Boldt, E. A., and Serlimitsos, P. J. 1975, *Nature*, **256**, 633. "Decay of X-Ray Source A0535+26."
- Katz, J. I. 1976, *Ap. J.*, **206**, 910. "Nonrelativistic Compton Scattering and Models of Quasars."
- Kazanas, D. 1986, *Astr. Ap.*, **166**, L19. "The Two States of Cyg X-1 and Related Sources."
- Kemp, J. C., Herman, L. C., and Barbour, M. S. 1978, *Astron. J.*, **83**, 962. "Cygnus X-1: Optical and X-Ray Evidence for a 78/39-day Period."



- Kemp, J. C., *et al.* 1983, *Ap. J. (Letters)*, **271**, L65. "Cygnus X-1: Optical Variation on the 294 Day X-Ray Period."
- Kitamoto, S. 1985, Ph. D. thesis, The Osaka University. "The X-Ray Spectrum of Cygnus X-3."
- Kniffen, D. A., Hartman, R. C., Thompson, D. J., Bignami, G. F., Fichtel, C. E., Türmer, T., and Ögelman, H. 1974, *Nature*, **251**, 397. "Gamma Radiation from the Crab Nebula above 35 MeV."
- Knight, F. K. 1982, *Ap. J.*, **260**, 538. "Observations and Interpretations of the Pulsed Emission from the Crab Pulsar."
- Kompaneets, A. S. 1957, *Soviet Phys. JETP*, **4**, 730. "The Establishment of Thermal Equilibrium Between Quanta and Electrons."
- Kundt, W. and Krotschek, E. 1980, *Astr. Ap.*, **83**, 1. "The Crab Nebula - A Model."
- Kurfess, J. D. 1971, *Ap. J. (Letters)*, **168**, L39. "Observation of Low-Energy Gamma Radiation from NP 0532."
- Lamb, R.C., Fichtel, C. E., Hartman, R. C., Kniffen, D. A., and Thompson, D. J. 1977, *Ap. J. (Letters)*, **212**, L63. "Observation of Gamma Rays with a 4.8 Hour Periodicity from Cygnus X-3."
- Lamb, R. C., Godfey, C. P., Wheaton, W. A., and Türmer, T. 1982, *Nature*, **296**, 543. "Cygnus X-3 Observed at Photon Energies Above 500 GeV."
- Lampton, M. L., Margon, B., and Bowyer, S. 1976, *Ap. J.*, **208**, 177. "Parameter Estimation in X-Ray Astronomy."
- Lang, K. R. 1980, *Astrophysical Formulae* (Berlin: Springer-Verlag).
- Laros, J. G., Matteson, J. L., and Pelling, R. M. 1973, *Nature Phys. Sci.*, **246**, 109. "X-Ray Spectral Features of the Crab Nebula and NP 0532."
- Leach, R. W., Murray, S. S., Schrier, E. J., Tananbaum, H. D., Ulmer, M. D., and Parsignault, D. R. 1975, *Ap. J.*, **199**, 184. "Further Observations of Cygnus X-3 with the *Uhuru* Satellite."
- Lebrun, F., *et al.* 1982, *Astr. Ap.*, **107**, 390. "COS-B Gamma-Ray Measurements, Cosmic Rays and the Local Interstellar Medium."
- Leventhal, M., MacCallum, C. J., and Watts, A. C. 1977, *Nature*, **266**, 696. "Possible Gamma-Ray Line from the Crab Nebula."
- Li, F., Rappaport, S., Clark, G. W., and Jernigan, J. G. 1979, *Ap. J.*, **228**, 893. "A0535+26: Refined Position Measurement and New Pulse Period Data."
- Liang, E. P. 1979, *Ap. J.*, **234**, 1105. "Electron-Positron Pair Production in Hot Unsaturated Compton Accretion Models Around Black Holes."
- Liang, E. P. and Nolan, P.L. 1984, *Space Sci. Rev.*, **38**, 353. "Cygnus X-1 Revisited."

- Liang, E. P. and Price, R. H. 1977, *Ap. J.*, **218**, 247. "Accretion Disk Coronae and Cygnus X-1."
- Lightman, A. P. and Eardley, D. M. 1974, *Ap. J. (Letters)*, **187**, L1. "Black Holes in Binary Systems: Instability of Accretion Disk."
- Ling, J. C. 1987, private communication.
- Ling, J. C., Mahoney, W. A., Willett, J. B., and Jacobson, A. S. 1979, *Ap. J.*, **231**, 896. "A Possible Line Feature at 73 keV from the Crab Nebula."
- Ling, J. C., Mahoney, W. A., Wheaton, W. A., Jacobson, A. S., and Kaluzienski, L. 1983, *Ap. J.*, **275**, 307. "The States of Cygnus X-1."
- Lingenfelter, R. E., Higdon, J. C., and Ramaty, R. 1978, in *Gamma-Ray Spectroscopy in Astrophysics*, eds. T. L. Cline and R. Ramaty (NASA TM-79619), p. 252. "Nuclear Gamma Rays from Compact Objects."
- Lloyd-Evans, J., Coy, R. N., Lambert, A., Lapikens, J., Patel, M., Reid, R. J. O., and Watson, A. A. 1983, *Nature*, **305**, 27. "Observation of  $\gamma$ -rays  $> 10^{15}$  eV from Cygnus X-3."
- Long, K. S., Chanan, G. A., and Novick, R. 1980, *Ap. J.*, **238**, 710. "The X-Ray Polarization of the Cygnus Sources."
- Maggioli, P. P., Caroli, E., Natalucci, L., Spizzichino, A., and Badiali, M. 1984, *Nucl. Instrum. Methods*, **221**, 82. "A Numerical Method for Recognition of Virtual Images in Coded Mask Telescopes."
- Mahoney, W. A., Ling, J. C., and Jacobson, A. S. 1984, *Ap. J.*, **278**, 784. "HEAO 3 Observations of the Crab Pulsar."
- Manchanda, R. K. 1983, *Astro. Space Sci.*, **91**, 455. "A 300-Day Periodicity of Cyg X-1."
- Manchanda, R. K., Bazzano, A., La Padula, D. C., Polcaro, V. F., and Ubertini, P. 1982, *Ap. J.*, **252**, 172. "Line Feature Around 73 keV from the Crab Nebula."
- Mandrou, P., Niel, M., Vedrenne, G., Dupont, A., and Hurley, K. 1978, *Ap. J.*, **219**, 288. "Observation of Cygnus X-1 in the Energy Range 100 keV - 3 MeV."
- Maraschi, L., and Treves, A. 1977, *Ap. J. (Letters)*, **218**, L115. "Gamma Rays from Accreting Black Holes."
- Maraschi, L., Perola, G. C., Reina, C., and Treves, A. 1979, *Ap. J.*, **230**, 243. "Turbulent Accretion onto Massive Black Holes."
- Maraschi, L., Roasio, R., and Treves, A. 1982, *Ap. J.*, **253**, 312. "The Effect of Multiple Scattering on the Temperature and Emission Spectra of Accreting Black Holes."
- Margon, B., Bowyer, S., and Stone, R. P. S. 1973, *Ap. J. (Letters)*, **185**, L113. "On the Distance to Cygnus X-1."

- Marsden, P. L., Gillett, R. E., Jennings, R. E., Emerson, J. P., De Jong, T., and Olnon, F. M. 1984, *Ap. J. (Letters)*, **278**, L29. "Far-Infrared Observations of the Crab Nebula."
- Matteson, J. L., 1971, Ph. D. thesis, University of California at San Diego. "An X-Ray Survey of the Cygnus Region in the 20 to 300 keV Energy Range."
- Matteson, J. L., *et al.* 1985, *Proc. 19th Internat. Cosmic Ray Conf.*, La Jolla, **3**, 326. "Advanced Techniques for High Resolution Spectroscopic Observations of Cosmic Gamma-Ray Sources."
- Maurer, G. M. 1979, Ph. D. thesis, The Catholic University of America. "Satellite Observations of Rapidly Varying X-Ray Sources."
- Mayer-Hasselwander, H. A., *et al.* 1982, *Astr. Ap.*, **105**, 164. "Large-Scale Distribution of Galactic Gamma Radiation Observed by COS-B."
- McConnell, M. L., Forrest, D. J., Chupp, E. L., and Dunphy, P. P. 1982, *IEEE Trans. Nucl. Sci.*, **29**, No. 1, 155. "A Coded Aperture Gamma-Ray Telescope."
- Meekins, J. F., Wood, K. S., Hedler, R. L., Byram, E. T., Yentis, D. J., Chubb, T. A., and Friedman, H. 1984, *Ap. J.*, **278**, 288. "Millisecond Variability of Cygnus X-1."
- Melzer, D.W. and Thorne, K.S. 1966, *Ap. J.*, **145**, 514. "Normal Modes of Radial Pulsation of Stars at the End Point of Thermonuclear Evolution."
- Meehan, C. A., Fishman, G. J., and Haymes, R. C. 1979, *Ap. J. (Letters)*, **234**, L123. "Observations of Cygnus X-3 Above 50 keV."
- Mertz, L. and Young, N. 1961, in *Proceedings of the International Conference on Optical Instruments and Techniques* (London: Chapman and Hall), p. 305.
- Mészáros, P. 1975, *Nature*, **258**, 583. "A Spherical Accretion Model of Cyg X-1."
- Mészáros, P. 1983, *Ap. J. (Letters)*, **274**, L13. "A Thermal Interpretation of the X-Ray Spectra of Quasars, AGN, and Cyg X-1."
- Michel, F.C. 1982, *Rev. Mod. Phys.*, **54**, No.1, 1. "Theory of Pulsar Magnetospheres."
- Molteni, D., Rapisarda, M., Robba, N. R., and Scarsi, L. 1980, *Astr. Ap.*, **87**, 88. "34.1 Day Periodicity in Cyg X-3."
- Morrison, P. 1958, *Nuovo Cimento*, **7**, 858. "On Gamma-Ray Astronomy."
- Narlikar, J. V. 1983, *Introduction to Cosmology* (Boston: Jones and Bartlett).
- Nolan, P. L. and Matteson, J. L. 1983, *Ap. J.*, **265**, 389. "A Feature in the X-Ray Spectrum of Cygnus X-1: A Possible Positron Annihilation Line."
- Nolan, P. L. *et al.* 1981a, *Nature*, **293**, 275. "Hard X-Ray Spectrum of Cygnus X-1."
- Nolan, P. L. *et al.* 1981b, *Ap. J.*, **246**, 494. "Rapid Variability of 10-140 keV X-Rays from Cygnus X-1."

- Novikov, I. D. and Thorne, K. S. 1973, *Black Holes, Les Houches 1972*, ed. C. DeWitt and B. DeWitt (New York: Gordon and Breach).
- Oda, M. 1977, *Space Sci. Reviews*, **20**, 757. "Cyg X-1 / A Candidate of the Black Hole."
- Ogawara, Y., Doi, K., Matsuoka, M., Miyamoto, S., and Oda, M. 1977, *Nature*, **270**, 154. "Temporal and Spectral Variation of Cyg X-1."
- Oort, J. and Walraven, Th. 1956, *Bull. Astron. Inst. Neth.*, **12**, 285.
- Orwig, L. E., Chupp, E. L., and Forrest, D. J. 1971, *Nature Phys. Sci.*, **231**, 171. "Gamma Rays (250 keV - 2.3 MeV) from NP 0532."
- Ostriker, J.P. and Tassoul, J.L. 1968, *Nature*, **219**, 577. "Pulsation Periods of Rotating White Dwarf Models."
- Owens, A., Myers, R. M., and Thompson, M. G. 1985a, *Proc. 19th Internat. Cosmic Ray Conf.*, La Jolla, **1**, 145. "Detection of Gamma-Ray Lines from the Direction of the Crab Nebula."
- Owens, A., *et al.* 1985b, *Proc. 19th Internat. Cosmic Ray Conf.*, **3**, 314. "Secondary Gamma-Ray Production in a Coded Aperture Mask."
- Owens, A. 1986, private communications.
- Owens, A., Bhattacharya, D., Chupp, E. L., Dunphy, P. P., Forrest, D. J., McConnell, M. L., and Bui Van, A. 1987, to be presented, *20th Internat. Cosmic Ray Conf.*, Moscow. "Evaluation of the Background Counting Rate in a Balloon Borne Coded Aperture Mask Telescope."
- Pacini, F. 1967, *Nature*, **216**, 567. "Energy Emission from a Neutron Star."
- Pacini, F. 1968, *Nature*, **219**, 145. "Rotating Neutron Stars, Pulsars and Supernova Remnants."
- Parsignault, D. R., Grindlay, J., Gursky, H., and Tucker, W. 1977, *Ap. J.*, **218**, 232. "Observational Constraints on the Models for Cygnus X-3."
- Pelling, M.R., Paciesas, W.S., Peterson, L.E., Makishima, K., Oda, M., Ogawara, Y., and Miyamoto, S. 1986. Submitted to *Ap. J.* "A Scanning Modulation Collimator Observation of the High Energy X-Ray Source in the Crab Nebula."
- Perotti, F., *et al.* 1986, *Ap.J.*, **300**, 297. "Hard X-Ray Observations of Cygnus X-1 with the MISO Telescope."
- Persi, P., Ferrari-Toniolo, M., Grasdalen, G. L., and Spada, G. 1980, *Astr. Ap.*, **92**, 238. "Infrared Photometry of HDE 226868 (Cyg X-1) from 2.3 to 10 $\mu$ : Mass Loss Rate."
- Piddington, J. H. 1957, *Australian J. Phys.*, **10**, 530. "The Crab Nebula and the Origin of Interstellar Magnetic Fields."

- Pietsch, W., Kendziorra, E., Staubert, R., and Trümper, J. 1976, *Ap. J. (Letters)*, **203**, L67. "The 4.8 Hour Variation of Cygnus X-3 at High X-Ray Energies."
- Polcaro, V. F., Bazzano, A., La Padula, C., Ubertini, P., Vialetto, G., and Manchanda, R. K. 1982, in *Accreting Neutron Stars*, eds. W. Brinkman and J. Trümper, 117. "Hard X-Ray Measurements of A0535+26 During Low State."
- Priedhorsky, W. C., Terrell, J., and Holt, S. S. 1983, *Ap. J.*, **270**, 233. "Evidence for an ~300 Day Period in Cygnus X-1."
- Proctor, R. J. 1981, in *X-Ray Astronomy in the 1980's*, ed. S. S. Holt, NASA TM 83848, 335. "Temporal Aperture Modulation."
- Proctor, R. J., Skinner, G. K., and Willmore, A. P. 1978, *Mon. Not. R. Astr. Soc.* **185**, 745. "The Design of Optimum Coded Mask X-Ray Telescope."
- Ramaty, R. and Lingenfelter, R. E. 1982, *Ann. Rev. Nucl. Part. Sci.*, **32**, 235. "Gamma-Ray Astronomy."
- Ramaty, R. and Mészáros, P. 1981, *Ap. J.*, **250**, 384. "Annihilation Radiation from a Hot  $e^+e^-$  Plasma."
- Rankin, J. M., Comella, J. M., Craft, H. D., Richards, D. W., Campbell, D. B., and Counselman, C. C. 1970, *Ap. J.*, **162**, 707. "Radio Pulse Shapes, Flux Densities and Dispersion of Pulsar NP 0532."
- Rappaport, S., Joss, P.C., Bradt, H., Clark, G. W., and Jernigan, J. G. 1976, *Ap. J. (Letters)*, **208**, L119. "Evidence for the Binary Nature of A0535+26."
- Reppin, C., Pietsch, W., Trümper, J., Voges, W., Kendziorra, E., and Staubert, R. 1979, *Ap. J.*, **234**, 329. "Hard X-Ray Observation of Cygnus X-3."
- Ricketts, M. J., Turner, M. J. L., Page, C. G., and Pounds, K. A. 1975, *Nature*, **256**, 631. "Observations of A0535+26 with the Leicester Sky Survey Experiment."
- Rocchia, R., Rothenflug, R., Boclet, D., and Durouchoux, Ph. 1969, *Astr. Ap.*, **1**, 48. "Observation of Five Sources of Cosmic X-Rays in the 15-150 keV Energy Range."
- Roques, J. P., Mandrou, P., Lebrun, F., and Paul, J. 1985, *Proc. 19th Internat. Cosmic Ray Conf.*, La Jolla, **1**, 193. "Low-Energy Gamma-Rays from Cygnus X-1."
- Rosenberg, F. D., Eyles, C. J., Skinner, G. K., and Willmore, A. P. 1975, *Nature*, **256**, 628. "Observations of a Transient X-Ray Source with a Period of 104 s."
- Rothschild, R. E., Boldt, E. A., Holt, S. S., and Serlimitsos, P. J. 1974, *Ap. J. (Letters)*, **189**, L13. "Millisecond Temporal Structure in Cygnus X-1."
- Rothschild, R. E., Boldt, E. A., Holt, S. S., and Serlimitsos, P. J. 1977, *Ap. J.*, **213**, 818. "Submillisecond Measurements of the Low State of Cygnus X-1."
- Ruderman, M.A. and Sutherland, P.G. 1974, *Ap. J.*, **196**, 51. "Theory of Pulsars: Polar Gaps, Sparks and Coherent Microwave Radiation."

- Rybicki, G. B. and Lightman, A. P. 1979, *Radiative Processes in Astrophysics* (New York: Wiley).
- Sacher, W. and Schonfelder, V. 1983, *Sp. Sci. Rev.*, **36**, 249. "Origin of the Diffuse Galactic Gamma-Ray Emission at Low and Medium Gamma-Ray Energies."
- Salvati, M. and Massaro, E. 1978, *Astr. Ap.*, **67**, 55. "Gamma Ray Emission from Pulsars."
- Samorski, M. and Stamm, W. 1983, *Ap. J. (Letters)*, **268**, L17. "Detection of  $2 \times 10^{15}$  to  $2 \times 10^{16}$  eV Gamma-Rays from Cygnus X-3."
- Scharlemann, E.T., Aarons, J., and Fawley, W.M. 1978, *Ap. J.*, **222**, 297. "Potential Drops Above Pulsar Polar Caps: Ultrarelativistic Particle Acceleration Along the Curved Magnetic Field."
- Schlickeiser, R. 1979, *Ap. J.*, **233**, 294. "Astrophysical Gamma-Ray Production by Inverse Compton Interactions of Relativistic Electrons."
- Schlickeiser, R. 1980, *Ap. J.*, **236**, 945. "Astrophysical Gamma-Ray Production by Inverse Compton Interactions of Relativistic Electrons. II. Constraints on Compton Emission Models for NGC 4151, NP 0532, and PSR 0833-45 From Gamma-Ray Data."
- Schönfelder, V., Lichti, G., and Moyano, C. 1975, *Nature*, **257**, 376. "No Indication of Excess MeV Gamma Radiation from the Crab Nebula."
- Schönfelder, V., Graml, F., and Penningsfeld, F. P. 1980, *Ap. J.*, **240**, 350. "The Vertical Component of 1-20 MeV Gamma Rays at Balloon Altitudes."
- Shakura, N. I., and Sunyaev, R. A. 1973, *Astr. Ap.*, **24**, 337. "Black Holes in Binary Systems. Observational Appearance."
- Shapiro, S. L. and Teukolsky, S. A. 1983, *Black Holes, White Dwarfs, and Neutron Stars. The Physics of Compact Objects* (New York: Wiley).
- Shapiro, S. L., Lightman, A. P., and Eardley, D. M. 1976, *Ap. J.*, **204**, 187. "A Two-Temperature Accretion Disk Model for Cygnus X-1: Structure and Spectrum."
- Shklovsky, I. S. 1978, *Stars: Their Birth, Life, and Death* (San Francisco: W. H. Freeman).
- Simpson, G., and Mayer-Hasselwander, H. 1986, *Astr. Ap.*, **162**, 340. "Bootstrap Sampling: Applications in Gamma-Ray Astronomy."
- Skinner, G. K., *et al.*, 1986, *Bull. AAS*, **18**, 675. "Observations with the Spacelab 2 X-ray Telescope."
- Smart, W. M. 1972, *Textbook on Spherical Astronomy* (Cambridge: Cambridge University Press).
- Smith, F.G. 1970, *Mon. Not. R. Astron. Soc.*, **149**, 1. "The Beaming of Radio Waves from Pulsars."

- Smith, F.G. 1971, *Mon. Not R. Astron. Soc.*, **154**, 5P. "Relativistic Beaming of Pulsars - the Effect of the Emission Spectrum."
- Smith, F.G. 1977, *Pulsars* (Cambridge: Cambridge University Press).
- Staelin, D.H. and Reifenstein, E.C. 1968, *Science*, **162**, 1481. "Pulsating Radio Sources Near the Crab Nebula."
- Steinle, H., Voges, W., Pietsch, W., Reppin, C., Trümper, J., Kendziorra, E., and Staubert, R. 1982, *Astr. Ap.*, **107**, 350. "The Hard X-Ray Spectrum of Cygnus X-1."
- Strickman, M. S., Kurfess, J. D. and Johnson, W. N. 1982, *ApJ. (Letters)*, **253**, L23. "The Hard X-Ray Spectrum of the Crab Nebula."
- Strong, A. W., *et al.* 1982, *Astr. Ap.*, **115**, 404. "The Local Interstellar Medium as Traced by Gamma Rays."
- Sturrock, P. A. 1971, *Ap. J.*, **164**, 529. "A Model of Pulsars."
- Sunyaev, R. A., and Titarchuk, L. G. 1980, *Astr. Ap.*, **86**, 121. "Comptonization of X-Rays in Plasma Clouds. Typical Radiation Spectra."
- Sunyaev, R. A., and Trümper, J. 1979, *Nature*, **279**, 506. "Hard X-Ray Spectrum of Cygnus X-1."
- Svensson, R. 1984, in *X-Ray and EUV Emission from Active Galactic Nuclei*. "Physical Processes in Relativistic Plasmas."
- Tananbaum, H., Gursky, H., Kellogg, E., Giacconi, R., and Jones, C. 1972, *Ap. J. (Letters)*, **177**, L5. "Observations of a Correlated X-Ray - Radio Transition in Cygnus X-1."
- Teegarden, B. J., *et al.* 1985, *Proc. 19th Internat. Cosmic Ray Conf.*, La Jolla, **3**, 307. "The Gamma-Ray Imaging Spectrometer (GRIS): A New Balloon-Borne Experiment for Gamma-Ray Line Astronomy."
- Terrell, N. J. 1972, *Ap. J. (Letters)*, **174**, L35. "Shot-Noise Character of Cygnus X-1 Pulsations."
- Thorne, K. S. and Price, R. H. 1975, *Ap. J.*, **195**, L101. "Cygnus X-1: An Interpretation of the Spectrum and Its Variability."
- Trümper, J., Pietsch, W., Reppin, C., Voges, W., Staubert, R., and Kendziorra, E. 1978, *Ap. J. (Letters)*, **219**, L105. "Evidence for Strong Cyclotron Emission in the Hard X-Ray Spectrum of Hercules X-1."
- Tsoufanidis, N. 1983, *Measurement and Detection of Radiation* (New York: McGraw-Hill).
- Tucker, W. H. 1975, *Radiation Processes in Astrophysics* (Cambridge, Mass.: MIT Press).
- Turner, M. J. L., Smith, A., and Zimmermann, H. U. 1981, *Space Sci. Rev.*, **30**, 513. "The Medium Energy Instrument on EXOSAT."

Ulmer, M. P., Baity, W. A., Wheaton, W. A., and Peterson, L. E. 1974, *Ap. J.*, **192**, 691. "Observations of the 4.8-Hour Variations of Cygnus X-3 Above 7 keV from the OSO-7."

Varma, C. M. 1977, *Nature*, **267**, 687. "Electron-Positron Flux at the Surface of the Pulsar in the Crab."

Vestrand, W. T. and Eichler, D. 1982, *Ap. J.*, **261**, 251. "On the Ultrahigh-Energy Gamma Rays from Cygnus X-3."

Walraven, G. D., Hall, R. D., Meegan, C. A., Coleman, P. L., Shelton, D. H., and Haymes, R. C. 1975, *Ap. J.*, **202**, 502. "Measurements of Low-Energy Gamma Radiation from the Crab Nebula and from Pulsar NP 0532."

Watanabe, H. 1985, *Astro. Space Sci.*, **111**, 157. "Line Features from Cygnus X-1 and the Crab Nebula in the Energy Range 30-270 keV."

Webber, W. R. 1982, presented at the *Intern. School of Cosmic Ray Astrophys.*, Erice, Sicily.

Webber, W. R., Simpson, G. A., and Cane, H. V. 1980, *Ap. J.*, **236**, 448. "Radio Emission, Cosmic-Ray Electrons, and the Productyion of  $\gamma$ -Rays in the Galaxy."

Weekes, T. C. 1983, *Astr. Ap.*, **121**, 232. "A Search for Very High Energy Gamma-Ray Transients from Cygnus X-3 and PSR 0531."

Wheaton, W. A., 1976, Ph. D. thesis, University of California at San Diego.

Wheaton, W. A., *et al.* 1979, *Nature*, **282**, 240. "An Absorption Feature in the Spectrum of the Pulsed Hard X-Ray Flux from 4U 0115+63."

Wheeler, J. A. 1966, *Ann. Rev. Astron. Astrophys.*, **4**, 393. "Superdense Stars."

White, R. S., Dayton, B., Gibbons, R., Long, J. L., Zanrosso, E. M., and Zych, A. D. 1980, *Nature*, **284**, 608. "Observations and Search for  $\gamma$  rays 1-20 MeV from the Crab, Cyg X-1, Cyg X-3, CG135+1 and 3C273."

White, R. S., Sweeney, W., Türner, T., and Zych, A. 1985, *Ap. J.*, **299**, L23. "Low-Energy and Medium-Energy Gamma Rays from PSR 0531+21."

Willingale, R., King, A. R., and Pounds, K. A. 1985, *Mon. Not. R. Astr. Soc.*, **215**, 295. "EXOSAT MEDA Observations of Cygnus X-3."

Wilmore, A. P., Skinner, G. K., Eyles, C. J., and Ramsey, B. 1984, *Nucl. Instrum. Methods*, **221**, 284. "A Coded Mask Telescope for the Spacelab 2 Mission."

Yoshimori, M., Watanabe, H., Okudaira, K., Hirasima, Y. and Murakami, H. 1979, *Aust. J. Phys.*, **32**, 375. "A Balloon Investigation of Galactic Gamma-Ray lines with a High Resolution Ge(Li) Spectrometer."

Zheleznyakov, V.V. and Shaposhnikov, V.E. 1972, *Astrophys. Sp. Sci.*, **18**, 166. "Mechanisms of Optical, X-Ray and Gamma-Radiation from Crab Pulsar."